Experimental investigation of supersonic plasma jets colliding with thin metallic foils

Louisa Alyce Pickworth

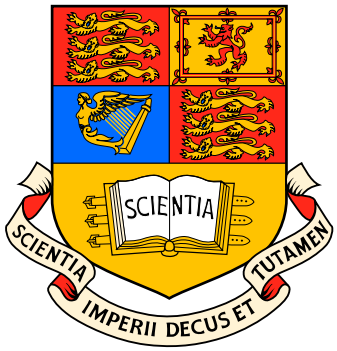

Imperial College London

Department of Physics

Plasma Physics Group

Submitted in partial fulfilment of the requirements for the degree of Doctor of Philosophy of Imperial College London

January 2013

Declaration

I hereby certify the material in this thesis, which I submit for the degree of Doctor of Philosophy, is entirely original unless otherwise cited or acknowledged in the text.

Louisa Alyce Pickworth

11/01/2013

Acknowledgments

I would like to thank both my supervisors, Sergey Lebedev and Simon Bland for their support and encouragement during my PhD. Without their enthusiasm and guidance this work would not have been possible.

Everyone on the MAGPIE team provided me with good humour and invaluable insights from the start of my PhD to the finish. Personal thanks to Alan Finch, Jerry Chittenden, Gareth Hall, Francisco Suzuki-Vidal, Adam Harvey-Thompson and George Swadling for showing me how to do all the useful things in and out of the lab and being there when it went awry. For taking this PhD journey with me, I would like to thank Guy Burdiak and Essa Khoory, it was a pleasure to learn the ropes with you. For all the wonderful physics and life discussions I would like to thank Nicolas Niasse. Thank you to Sid Patankar, Jon Skidmore, Lee Suttle, Matt Bennett and Phil de Grouchy for their help with my experiments.

I would also like to thank all the people who encouraged me to pursue my studies in Physics, especially my supervisors at JET, Phillip Andrew and Wojtek Fundamenski who showed me how exciting research can be.

Thanks to my good friends in Imperial who were always there for a coffee or dinner; Diego Anderson and Sam Bayliss. Adam Donen, thank you for keeping me sane.

Lastly I would like to thank Johan Paulsson for his patience, encouragement and love. Thank you for being by my side.

Dedicated to Mom and Dad

Abstract

An experimental investigation of collisions between supersonic plasma jets with metal foils and head-on collisions of two jets will be presented. The jets are produced by ablation of thin aluminium foils driven by 1.4MA, 250ns current pulse in a radial foil Z-pinch configuration. The jets propagate with velocity of 50-100km/s, showing a high degree of collimation (opening angle 2° to 5°) and are radiatively cooled (cooling time << hydrodynamic times). Collisions of the jets with foils, as well as inter-jet collisions, create a system of strong shocks both in the central dense part of the jet and in the lower density halo plasma which surrounds the jet and moves with the same speed. The formed shock features are sustained for 300ns, and are diagnosed with laser interferometry, optical and XUV imaging, and Thomson scattering diagnostics. Interpretation of the results indicates that dynamically significant magnetic fields are present in the system, balancing the ram pressure of the flow and supporting extended stationary shock structures. The results are relevant to the studies of astrophysical phenomena in the laboratory, in particular internal shocks in jets from young stars, accretion shocks, and for the understanding of magnetised high energy density plasma flows.

Contents

1 Introduction to the investigation of shocks and supersonic jets in the laboratory **20**

1.1 Investigating astrophysical plasmas in the laboratory 20

1.1.1 Scaling factors: From the lab to the interstellar medium . . . 23

1.2 Supersonic jets and strong shocks in astrophysics 26

1.3 Producing supersonic jets and strong shocks in the laboratory 30

1.3.1 Laboratory produced strong shocks 31

1.4 Investigation aims 32

1.5 Content of thesis 34

1.6 Contribution of the author 35

2 Shock physics related to supersonic plasma flows **37**

2.1 Basic shocks in ideal fluids 37

2.2 Effects of radiative cooling in shocks 42

2.3 Magnetised shocks 45

2.3.0.1 Single fluid model for magnetised shocks 45

2.3.0.2 Jump conditions for a magnetised shock 46

2.3.0.3 Magnetised shocks with a perpendicular magnetic field and $B_{||} = 0$ 47

3 Experimental equipment and diagnostics **49**

3.1 The MAGPIE pulsed power facility 49

3.1.1 The fast-pinch pulsed-power device 49

3.1.1.1 Marx banks 50

3.1.1.2 The pulse forming line . . . 52
3.1.2 The MAGPIE generator . . . 53
3.1.2.1 Characteristics of the MAGPIE current . . . 54
3.2 The MAGPIE diagnostic suite . . . 56
3.2.1 Monitoring the current in the experimental load . . . 56
3.2.2 The laser imaging suite . . . 57
3.2.3 Free electrons in a plasma and the plasma refractive index . . . 59
3.2.3.1 Laser shadowgraphy . . . 61
3.2.3.2 Laser imaging interferometry . . . 63
3.2.4 Thomson scattering . . . 69
3.2.4.1 Plasma temperature and ionisation from the scattered spectrum . . . 70
3.2.4.2 Macroscopic flow velocity measurements . . . 72
3.2.5 Self-emission imaging of the plasma . . . 76
3.2.5.1 Optical imaging system . . . 76
3.2.5.2 XUV imaging system . . . 77
3.2.6 Localised magnetic field measurements using B-dots . . . 77
3.2.7 The Faraday Cup . . . 79

4 Summary of previous investigations on the production of supersonic, radiatively cooled jets 82
4.1 Experimental setup . . . 83
4.2 Overview of the jet formation and propagation . . . 84
4.3 The electron density of the jet . . . 87
4.4 The jet velocity and temperature . . . 89
4.5 Numerical simulations of the jet in vacuum . . . 91

5 Interaction of a supersonic plasma jet with a thin aluminium foil target 95
5.1 Experimental set up . . . 95
5.2 Overview of the jet-target interaction . . . 99
5.3 Formation of the jet in the presence of the target foil . . . 102

5.3.1 The dynamical properties of the jet . . . 103
5.3.2 The density profile of the jet . . . 107
5.3.3 Thomson scattering measurements for the jet and halo plasma 112
5.3.3.1 Experimental setup for the Thomson scattering measurement . . . 112
5.3.3.2 Results of the Thomson scattering measurement in the jet . . . 117
5.4 The stationary shock in the halo plasma . . . 124
5.4.1 The evolution of a stationary shock in the flow of the halo plasma from the jet . . . 126
5.4.2 The electron density contrast between the halo plasma and the material above the stationary shock . . . 130
5.4.3 Temperature of material above the stationary shock from Thomson scattering . . . 135
5.4.4 The effect from the material flow from the jet and the flow from the halo plasma . . . 142
5.4.5 Electron beam emission from the jet-forming foil cathode . . . 146
5.5 The reverse shock in the jet . . . 149

6 Reverse Polarity Aluminium Jet 154
6.1 Experimental set up . . . 154
6.2 Overview of the jet-target interaction . . . 157
6.3 The formation of the jet in the reversed current polarity . . . 161
6.3.1 The dynamical properties of the jet . . . 162
6.3.2 The electron density profile of the reversed current polarity jet 164
6.4 Stationary shock formation in reversed current polarity . . . 167
6.4.1 The evolution of the stationary shock in the flow from the halo plasma in reversed current polarity . . . 168
6.4.2 The electron density contrast between the halo plasma and the material above the stationary shock . . . 172

6.5 Summary of the conditions observed in the reversed current polarity jet and the interaction with a foil target . . . 174

7 Colliding Aluminium Supersonic Jets 175

7.1 Experimental setup . . . 175

7.2 Overview of the jet-jet interaction . . . 177

7.2.1 from the optical self-emission . . . 179

7.2.2 from the XUV self-emission . . . 182

7.2.3 from interferometry . . . 183

7.3 The dynamic behaviour of the jets . . . 186

7.3.1 Formation of the jets . . . 186

7.3.2 Density profile of the jets . . . 188

7.4 The bow shock . . . 190

7.4.1 Density profile of the bow shock . . . 191

7.4.2 The bow shock as a working surface . . . 194

7.5 The stationary shock feature . . . 195

7.5.1 Evolution of the stationary shock feature . . . 196

7.5.2 Density contrast across the stationary shock feature . . . 198

7.6 A comparison of the stationary shock structures . . . 201

7.6.1 The plasma properties in the stationary shock estimated from the experimental data . . . 203

7.6.1.1 Heating of the ions and equilibration length . . . 203

7.6.1.2 The ion mean free path . . . 205

7.6.1.3 The hydrodynamic and radiative cooling times . . . 207

7.6.2 The ram pressure from the colliding halo plasmas surrounding the jet . . . 208

7.6.3 A magnetic field pressure that separates the two shock fronts in the colliding jet system . . . 209

8 Conclusions and future work 212

8.1 The formation of the supersonic jet . . . 212

8.1.1 The effect of reversed polarity on the formation of the jet . . . 214

8.2 The observed shock structures from the interaction of the jet and target foil . . . 217
8.2.1 The reverse shock . . . 217
8.2.2 The stationary shock . . . 218
8.3 Colliding jets . . . 219
8.3.1 The bow shock . . . 220
8.3.2 Collision of the counter propagating halo plasmas . . . 221
8.4 Supporting analysis for a magnetic field above the stationary shocks . 222
8.5 Comparing the observed shock structures to astrophysical shocks . . . 224
8.6 Future work . . . 224
8.6.1 Imaging the ion line density with X-ray radiography . . . 224
8.6.2 Imaging the magnetic field with Faraday rotation . . . 226
8.6.3 Axial velocity of the plasma . . . 227
8.6.4 Effect of radiative cooling in the jet though varying the jet material . . . 228

A Processing the interferometry images to find the electron line density 230

Bibliography 234

List of Figures

1.1 Temperature and density map of high energy density conditions in the laboratory and astrophysics [1] . . . 22
1.2 HH47 . . . 27
1.3 A cataclysmic variable star system . . . 27
1.4 Interaction of accretion disk with magnetic field of the star. (Camenzind 1990). . . . 28
1.5 Shock in a accretion column as it impacts a star surface . . . 29
1.6 A laboratory produced jet and HH object comparison . . . 31
1.7 Experimental setup for production of reverse shocks using a laser and vacuum filled tube (Busschaert, 2011 [2]). . . . 32
1.8 experimental sketch of expected interactions from a supersonic jet and target . . . 33

2.1 The hard ball model . . . 38
2.2 An idealised shock front, in the reference frame of the shock . . . 39
2.3 The density, temperature and velocity in the frame of the strong radiative shock [3]. . . . 43
2.4 Simulation of a supersonic jet with varied cooling parameter (Blondin, 1990) . . . 44

3.1 The MAGPIE generator at Imperial College London. . . . 50
3.2 circuit diagram of a Marx bank . . . 51
3.3 Effective electrical circuit for a Marx bank . . . 52

3.4 A cross section sketch of the MAGPIE pulsed power facility showing a Marx, PFL, transfer line MITL and the discharge chamber. 53
3.5 Diagram of the MITL and discharge chamber 54
3.6 The characteristic current discharge of MAGPIE 55
3.7 current signal from a Rogowski groove 56
3.8 Schematic showing the laser imaging systems used during the experiments. 58
3.9 A shadowgraph system (a) direct technique (b) focused technique . . 62
3.10 Experimentally obtained interferograms before and during the experiment 64
3.11 Schematic of the Mach-Zender Interferometer. 65
3.12 Numerically generated scattered and broadened spectrums from Thomson scattering 72
3.13 Wave scattering diagram 73
3.14 The direction of $\vec{k}_s$ from $\vec{k}_{out} - \vec{k}_{in}$ shown graphically 75
3.15 Manufactures graphic showing the function and structure of microchannel plate photo multiplier. The top left image shows a sketch of the channels, the top right image shows the application of the bias to the plate, the bottom left image is an electron microscope image of the MCP and the bottom right image shows the multiplication of electrons along one channel. 78
3.16 Faraday cup scheme used during experiments. 80
3.17 Attenuation curve for a 50keV electron beam through Aluminium. . 81

4.1 Experimental set up of the jet in vacuum experiment 83
4.2 Illustration of jet and halo plasma formation 85
4.3 Self emission time sequence of the jet propagating in vacuum 86
4.4 Finding the half opening angle at from the jet 87
4.5 Density maps of the jet produced from interferometry at 429ns 88
4.6 experimental set-up for the axial velocity measurement with Thomson scattering 90

4.7 Observed spectrums for the Thomson scattering measurement 91
4.8 simulated density map for the jet in vacuum from GORGON 92
4.9 Comparison of observed and simulated density profiles for the jet . . 93

5.1 Experimental set-up for the jet into a target experiment 96
5.2 The assembled target and jet foils before placement in the discharge chamber. 97
5.3 The jet foil as assembled in the discharge chamber. 98
5.4 Time sequence from optical emission of the interaction of the jet and target 100
5.5 Interferometry and shadowgraphy images of the jet and target at 260ns 104
5.6 Velocity from optical emission of the jet tip and radial expansion . . . 105
5.7 The half opening angle of the jet from optical emission 106
5.8 Density profile through the jet at 267ns 108
5.9 Radial density profile of the jet at 464ns 109
5.10 Electron density jump at the jet boundary 111
5.11 The average N_e in the jet at 490ns 111
5.12 Experimental setup of the Thomson scattering measurement in the jet 113
5.13 Position of the optical fibres with respect to the jet 114
5.14 Expected doppler shift on the fibres 116
5.15 Scattered spectrum in the jet for fibres 1 - 7 118
5.16 Scattered spectrum in the jet for fibres 8 - 14 119
5.17 The observed doppler shift from the scattered spectrum 120
5.18 Shadowgraph of the jet at 411ns 121
5.19 Radial and azimuthal velocity of the plasma from Thomson scattering 122
5.20 Fitting constraints for the estimation of ion and electron temperature 123
5.21 XUV and optical self-emission of the stationary shock 125
5.22 Interferometry of the stationary shock at 260ns and 280ns 126
5.23 The shape of the stationary shock front from laser imaging 127
5.24 Movement of the stationary shock from optical emission 128
5.25 Density map with axial line outs at 286ns 129

5.26 High reproducibility of the stationary shock as seen in interferometry 130
5.27 Density map with axial profiles at 434ns 131
5.28 Density map with axial profiles at 464ns 132
5.29 Density map with axial profiles at 490ns 133
5.30 Jump in electron density across the stationary shock. From experiments s052912, s040212 and s032812. 134
5.31 The 'width' of the shock as measured form the axial line outs through the stationary shock. From experiment s032812 and s052912. 135
5.32 Alignment of the optical fibres to observe the region above the stationary shock 136
5.33 Scattered spectrum seen above the shock for fibres 1 to 7 137
5.34 Scattered spectrum seen above the shock for fibres 8 to 13 138
5.35 Accuracy of the temperature fit for the scattered broadening 139
5.36 Ion and electron temperature as a function of radius. 140
5.37 Ionisation of shocked plasma as function of radius 141
5.38 Ionisation levels for Aluminium 141
5.39 Target-forming foil with hole on axis 142
5.40 The assembled mesh target 143
5.41 Optical emission comparison between a solid, mesh and target with a hole on axis 144
5.42 532nm laser interferometry image at 405ns. From experiment s060112. 145
5.43 Comparison of target with and without hole on axis 146
5.44 Experimental setup of the Faraday cup 147
5.45 Results from the Faraday cup 148
5.46 355nm interferometry of the region in the reverse shock 150
5.47 Velocity of the reverse shock from optical emission 151
5.48 Averaged axial profiles in electron line density through the reverse shock 152

6.1 Experimental setup for reverse polarity jet 155
6.2 Foil assembly for the reverse polarity jet 156

6.3 Time sequence of optical emission from the reverse polarity jet experiments . . . 158
6.4 XUV self emission from the reverse polarity jet . . . 161
6.5 Velocity of the anode-centric jet tip and radial expansion velocity . . . 162
6.6 Opening half-angle for the anode-centric jet . . . 164
6.7 Electron density line outs through the reverse polarity jet . . . 165
6.8 Average election density in the body of the jet . . . 166
6.9 Position in time of the optical emission from the reverse polarity stationary shock . . . 168
6.10 The shape of the stationary shock in reversed polarity . . . 169
6.11 Laser interferometry of the stationary shock at 475ns . . . 170
6.12 Laser interferometry of the stationary shock taken at 495ns . . . 170
6.13 comparison of 355nm and 532nm interferometry though the stationary shock . . . 171
6.14 Density map of the stationary shock produced in the reversed polarity experiments with axial line outs . . . 172

7.1 Experimental setup for the colliding jet experiment . . . 176
7.2 A sketch of the jet-jet interaction . . . 178
7.3 Time sequence of optical emission from the fast-framing camera showing the jet-jet interaction . . . 180
7.4 Time sequence of XUV self emission images for the colliding jets. . . . 182
7.5 532nm interferometry images of the jet-jet interaction . . . 184
7.6 353ns optical emission frame of the two jets . . . 186
7.7 Radial expansion velocity of the jets in the colliding jet system . . . 187
7.8 Radial line out through the jets in the colliding jet system . . . 189
7.9 Average electron density in the colliding jets . . . 190
7.10 velocity of the bow shock . . . 191
7.11 Electron line density map at 408ns of the colliding jet system . . . 192
7.12 Electron line density map at 428ns of the bow shock . . . 193

7.13 The working surface ahead of a supersonic jet propagating into an ambient medium. Reproduced from Hartigan, 1989. 195
7.14 The position of the two stationary shock fronts at 509ns from shadowgraphy in experiment s080312. Note that the laser images show the two shock fronts curving away from each other, in contrast to the optical images which appears to show a curve in the same direction towards the anode. It is assumed the line of sight in the optical emission forms this initial impression. 196
7.15 Separation and movement of the stationary shocks 197
7.16 Density map and axial profiles of the stationary shock at 509ns 199
7.17 The stationary shock width 200
7.18 n_e jim across the stationary shocks 201
7.19 comparison of the stationary shock systems with target and colliding jets by interferometry 202
7.20 Possible current path in the plasma 210
7.21 Preliminary simulation results of the colliding jet system 211

8.1 Preliminary investigations with different jet foil materials 229

A.1 Raw interferograms and traced fringes 231
A.2 The traced fringes are numbered, then interpolated. 232
A.3 The final electron line density, $n_e l$ map as calculated from the phase map. 233

List of Tables

1.1 Scaling factors for a young stellar object and a laboratory jet 25

8.1 Comparison of the experimentally observed properties of the jets . . 216

Chapter 1

Introduction to the investigation of shocks and supersonic jets in the laboratory

This thesis describes an experimental 'test bed' for the study of shocks in flows of supersonic, high energy density plasma. Examples of such shocks occur in outflows of young stars and binary star systems. The understanding of how these shocks form and propagate is vital to stellar modelling. This chapter introduces the astrophysical shocks that have been previously investigated through high energy density (HED) plasma physics experiments on both Z-pinches and high power, pulsed laser systems.

1.1 Investigating astrophysical plasmas in the laboratory

The production of supersonic flows and strong shocks in the laboratory is part of a wider field of investigation termed laboratory astrophysics. There are two distinct aspects to laboratory astrophysics, the reproduction of the material conditions seen in astrophysical phenomena and the reproduction of the dynamics observed in the astrophysical objects. The interaction of the material constituting stars and galaxies involves high pressures and temperatures of plasma. When these materials

interact shocks are often produced. This section will introduce the motivation to create plasmas in the laboratory that have similar properties to plasmas seen in astrophysics.

The study of laboratory astrophysics has expanded as an area of research in recent years. High power pulsed laser systems and fast dense Z-pinches can now reach plasma conditions in density and temperature that are comparable to the conditions found in stellar atmospheres, accretion disks and ejections of material from young stellar objects.

Figure 1.1 shows a temperature-density map of modern HED plasma physics. The mechanisms of plasma generation (Z-pinch, laser etc.) are shaded as areas on the plot and the areas of astrophysical investigation are overlaid. It can be seen that the conditions inside the Sun and giant planets, such as Jupiter, can be created by large experiments such as the National Ignition Facility (NIF) and the 'Z' Z-pinch at Sandia laboratories. New experiments may be able to produce the conditions found in the core of the Sun, this allows the experimental verification of spectroscopic models that predict the emission and absorption of radiation.

Z-pinches and lasers can also create relevant HED dynamical systems, which can be compared to a supersonic jet or colliding solar winds, for example. The ability to directly connect the laboratory plasma to the astrophysical plasma allows for deeper investigation of the underlying dynamics of the observed structures than is possible with direct observation alone.

It is initially difficult to envision how a laboratory produced plasma can be linked to the core of the sun or the outflow from a young star. The laboratory produced plasmas are short lived, existing for fractions of a second and on the spatial scale of millimetres. In comparison, the astrophysical plasmas exist for thousands (to billions) of years and can be many astronomical units long. Gravity, which acts to confine and accelerate the astrophysical plasma cannot be directly reproduced in the lab and its effect is replaced with other accelerating or confining fields, normally electromagnetic.

Magneto-hydrodynamics (MHD) provides the link between the laboratory and the astrophysical. In the description of a dynamical plasma system it is found the

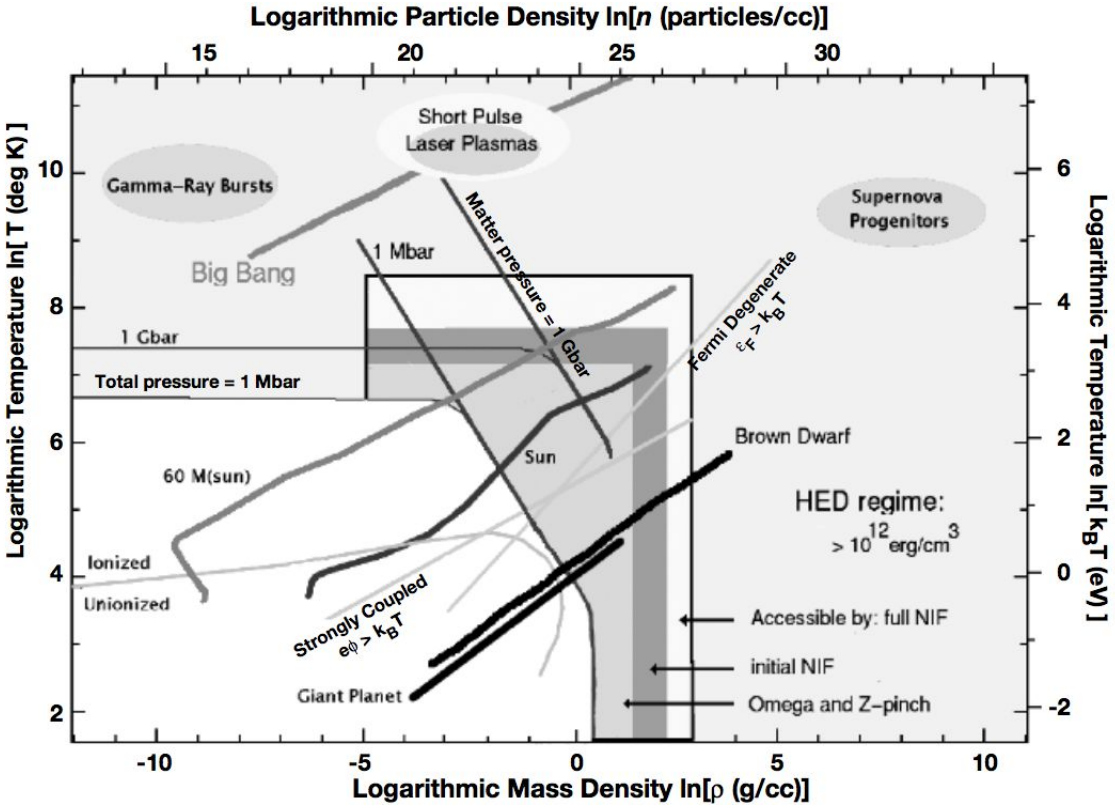

Figure 1.1: A temperature and density map showing the reachable plasma conditions from current experiments and the possible avenues of investigation relevant to astrophysics and the equation of state for materials. Taken from Drake [1].

equations of its motion are associated to several scaling factors. These scaling factors govern the interaction of the system however large or small it is. If the scaling factors are matched in the laboratory system it will then produce the same shocks, collisions and instabilities as found in an astrophysical plasma [4].

Advancements in numerical computation techniques and processing power have allowed the modelling of complex astrophysical plasmas and systems. These models aim to reproduce what is seen in astrophysical observations by developing a system governed by the MHD equations. This can require specific knowledge of the starting state, or boundary conditions, in the system. However, direct astrophysical observation can only provide a snapshot in the lifetime of an object and the conditions which created it have to be hypothesised. Laboratory astrophysics can provide a scaled model of how a system develops in time and structure. This is invaluable to building understanding surrounding the formation of astrophysical structures and

informing avenues of investigation in both observation and numerical study.

This thesis will focus on the characterisation of a dynamical shock system in a supersonic flow of plasma produced in the laboratory. Some examples of astrophysical supersonic flows can be found in binary star systems and in jets of plasma from young stars. These supersonic flows readily interact with their surroundings, which include the low density interstellar medium, the surface of stars and other supersonic flows of plasma. These interactions produce beautiful and readily observable shock structures. The shocks discussed in this thesis may provide the basis for future work that links them to a specific astrophysical context.

1.1.1 Scaling factors: From the lab to the interstellar medium

In order to create the shocked system that is investigated in this thesis the collision of a supersonic jet with perpendicular thin foil targets, or an opposing jet will be used. The jet that is used has previously been shown to match the scaling parameters for jets seen emerging from young stars [5]. For context, the scaling factors used to characterise the laboratory jet and the astrophysical system will now be introduced.

In the MHD equations there are six dimensionless parameters that need to be matched between the laboratory system and the astrophysical system [6]. This can be broken into the scaling factors that govern global properties of the jet and the scaling factors concerned with the microphysical properties of the plasma flow.

The properties of the plasma flow describe how the particles inside the structure interact with each other, these interactions determine if the two systems can be described by the same equations.

The scaling factors below govern how the temperature in the plasma is transported and how closely it resembles a continuous fluid or a collisional system of particles.

- The *localisation parameter*, a measure of the fluid like nature of the plasma relative to the scale of the jet radius: $\delta_{||} = \lambda_{mfp,||}/r_j$. Where $\lambda_{mfp,||}$ is the mean free path of the particles describing the average distance they can move before colliding with another particle. r_j is the jet radius.

- The *Reynolds number* is a ratio of the viscosity, $R_e = r_j v_j/\nu$, where ν is viscosity in the medium the jet is propagating in and v_j is the velocity of the jet. The magnetic Reynolds number, $R_{eM} = r_j v_j/\eta$ gives the permeability of the plasma to magnetic fields, where η is the magnetic diffusivity.

- The *Péclet number* $P_e = r_j v_j/\nu_h$ which measures the importance of heat convection in comparison with heat conduction, where ν_h is thermal diffusivity of the jet plasma.

The global properties describe the interaction of the flow as it moves though the surrounding medium and how readily plasma in the flow transmits heat to its surroundings. These factors are summarised below.

- The MHD *Mach number*, $M = v_j/c$, where c is the speed of sound in the medium the jet is propagating in.

- The jet to ambient density ratio or *density contrast*, $\eta = \rho_j/\rho_a$. Where ρ_j is the density of the jet and ρ_a is the density of the medium the jet is propagating in.

- The ratio of cooling length to jet radius or *cooling parameter* , $\chi = d_c/r_j$. Where d_c is cooling length and r_j is the jet radius. This can also be found by comparing the hydrodynamic and cooling times.

The scaling of a laboratory plasma to an astrophysical proportion can be achieved if the scaling parameters above are matched and the two systems can be described by Euler's fluid equations [4]. The scaling can break down when fluid instabilities become significant in the plasma, as these can relate to the viscosity in the plasma and the physical size of the system, in this case the jet radius.

The comparison of these scaling factors between a young stellar object and laboratory produced supersonic jets is given in table 1.1. It can be seen that the laboratory plasma can quite closely simulate the observed astrophysical jet. The values for the laboratory plasma for the localisation, Péclet and Reynolds numbers are smaller than seen in the astrophysical systems, but are in the same regime as

Flow Variables	**Units**	**Young Stellar Object**	**Laboratory**
Length	[mm]	10^{18}	20-40
Radius	[mm]	10^{18}	50
Dynamical age	[ns]	10^{22}	200-400
Temperature	[eV]	0.5 - 100	5-200
Fluid velocity	[km/s]	100 - 500	100-400
Density	[g/cm^3]	$10^{-18} - 10^{-20}$	10^{-4}- 10^{-6}
Radiative cooling time	[ns]	10^{18}	4-40
Mean free path	[mm]	10^{9}	10^{-4}
Dimensionless parameters	**Symbol**		
Mach number	M	5 - 40	4-40
Density contrast	η	1 - 2	0.1-10
Cooling parameter	χ	0.01 - 100	0.01-10
Localisation parameter	δ	$< 10^{-6}$	$< 10^{-4}$
Péclet number	Pe	$> 10^{7}$	50-10^{4}
Reynolds number	Re	$> 10^{8}$	$> 10^{4}$
Magnetic Reynolds number	Re_M	$> 10^{15}$	10-10^{3}

Table 1.1: Comparisons between a young stellar object and a laboratory produced plasmas. Adapted from a table presented in the lecture notes for the JetSet school [7]

the astrophysical systems (radiatively dominated, magnetically permeable etc.) and this forms an area of improvement for future experimental work.

In a shocked system the mechanism of energy transfer between the particles in the plasma, from the material before the shock to the material behind the shock governs the nature and behaviour of the shock on the macro scale. The scaling factors used to characterise the laboratory jet can also be used to find the nature of a laboratory shock. Shocked systems will be discussed in greater detail in chapter 2.

1.2 Supersonic jets and strong shocks in astrophysics

This section will introduce some examples of strong shocks and supersonic jets seen in astrophysical plasmas. These are indicated as a motivation for the experiments conducted in this thesis, though the experiments do not aim to directly match any one specific astrophysical system.

In astrophysics highly collimated flows of plasma on the parsec (1 parsec = 3.08×10^{16}m) scale are ubiquitous. These jets form from a variety of astrophysical objects, from young stellar objects (YSO) to active galactic nuclei (AGN). These jets propagate into the interstellar medium or surrounding star-forming nebula producing many shock structures that radiate in such a way to allow observation. The supersonic material comprising the jet is not seen in the telescope images, it is the radiation from shocks internally in the jet and between the jet and the interstellar medium that allow their observation.

Of particular interest are Herbig-Haro (HH) objects, pictured in figure 1.2. Associated with newly born stars, these patches of nebulosity are observed emanating from the rotational axis of the star and develop on the timescale of thousands of years. HH objects were first observed in the late 19th-cenuary and are very common in star forming regions. Figure 1.2 shows HH47, observed by the Hubble space telescope in 1999. Shock structures can be seen along the entire length of the jet

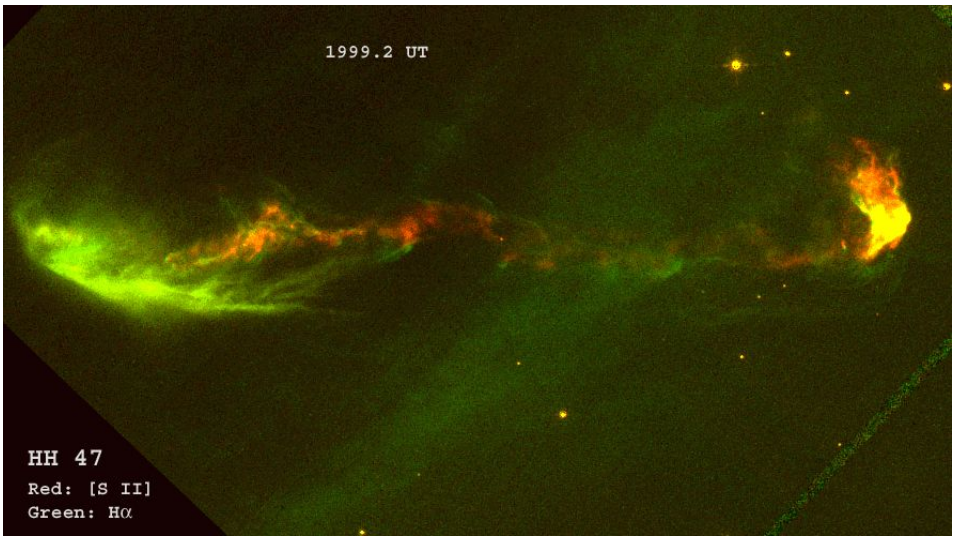

Figure 1.2: Hubble telescope image of HH47 (NASA Image Library, 1999).

shown in figure 1.2. At the tip of the jet is a prominent shock as it penetrates in to the low density material surrounding it, called a bow shock.

The analysis of these highly collimated HH jets, provides indirect and important insights into the nature of the mass-loss processes that govern the formation of stars [8]. HH objects typically have velocities of approximately 200 km/s, Temperatures of approximately 5000K and Mach numbers upwards of M=20 (Reipurth 1997).

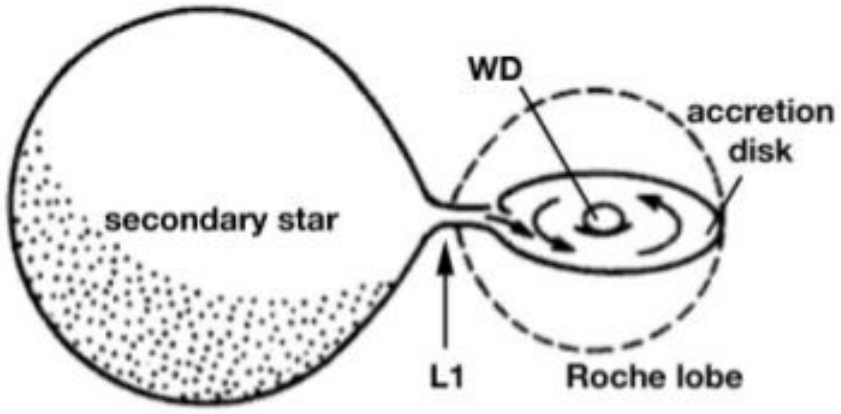

Figure 1.3: Adapted from 'The physics of fluids and plasmas' by A. Choudhuri, The secondary star transfers mass to the white dwarf (WD) and an accretion disk is formed. 'L1' marks the site of the hot spot where the mass from the secondary star impacts the accretion disk.

Another astrophysical example is the binary star system termed a 'cataclysmic

variable'. A cataclysmic variable system is shown in figure 1.3. The figure shows a sketch of a massive 'secondary' type star whose material is being pulled away by a smaller white dwarf. As the material in the secondary star is pulled away it forms an accretion disk around the white dwarf.

The material that is pulled away from the secondary star is accelerated to supersonic speeds by the gravitational pull of the white dwarf. This supersonic stream of plasma then impacts on the edge of the accretion disk producing an observable 'hot spot'. This hot spot is akin to a reverse shock in the supersonic flow from the secondary star. A reverse shock occurs when a supersonic flow encounters a sharp increase in density and a shock is reflected back into the supersonic flow.

Stars with accretion disks can form columns of gravitationally accelerated, supersonic plasma close to their magnetic poles, as shown in figure 1.4. Under the correct configuration of the magnetic field and the angular frequency of the accretion disk, two gravitationally accelerated columns of plasma, from the accretion disk, can form and impact upon the surface of the star, this is the accretion column.

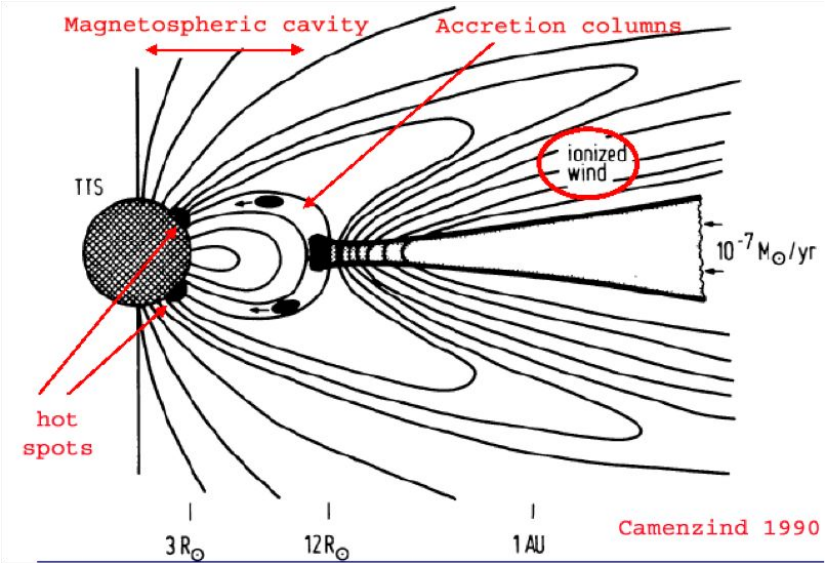

Figure 1.4: Interaction of accretion disk with magnetic field of the star. (Camenzind 1990).

The accretion column then produces a shock, some distance from the surface of the star, in the flow of material that forms the accretion column. This shock is observed primarily in X-ray emission, which forms the majority of the emission from

the shock [9, 10]. Figure 1.5 shows a schematic of this interaction, highlighting the large magnetic fields estimated to be involved in the system [11]. The magnetic field is parallel to the flow of the plasma in the column and perpendicular to the shock. The magnetic field increases dramatically in the material after the shock, near the star surface. The accretion shock is highly magnetised and radiative. As the accretion shocks are observable only by spectroscopic measurement, dynamical studies of comparable magnetised shock systems are of great interest to the astrophysical community.

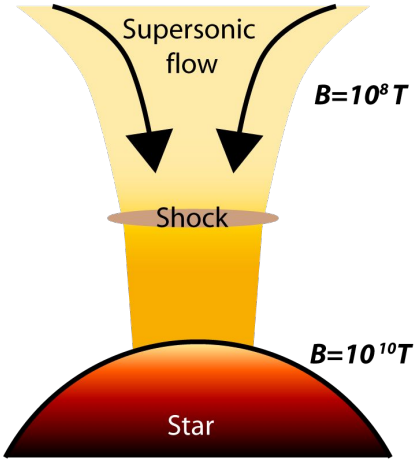

Figure 1.5: The shock produced from the impact of a supersonic flow from the accretion column onto the surface of a star.

The solar wind from a star is an emission of low density plasma, that flows away from the star surface. In massive binary star systems this wind can be supersonic in nature, and the two stars produce a system where two supersonic flows collide. Initial numerical simulation of such systems shows the development of a shock structure where magnetic fields are produced that are strong enough to counter the flow of plasma from the two stars, this effect produces a double shock front [12, 13].

1.3 Producing supersonic jets and strong shocks in the laboratory

Many successful experiments have been documented that reproduce supersonic flows and jets in the laboratory. A small selection of the many astrophysically relevant jet experiments will be showcased below.

By closely matching the Mach number M, cooling parameter χ, and density contrast η, HH objects and other astrophysical jets have been successfully modeled in the plasma physics laboratory. The field of laboratory astrophysics has shed light on the mechanism of creation for these supersonic jets as well as allowing experiments to investigate their interaction with surrounding mediums.

Both laser and Z-pinch experiments can create the plasma conditions required to produce supersonic jets of plasma. Laser experiments produce astrophysically relevant jets through the irradiation of a metallic foil with a high intensity short pulse laser [14–17] or with the conical collision of two supersonic flows from irradiated foils at an angle to each other [18]. The advantage of laser produced jets is the high repetition rate of the experiment and good diagnostic access. The laser produced jet is on the scale of millimetres and observable for timescales on the duration of the driving laser pulse, which is typically nanoseconds to picoseconds.

The MAGPIE Z-pinch has produced several mechanisms for driving supersonic jets. A conical arrangement of wires driven by a 1MA current, produces an ablation of material on to the axis of the cone of wires. This produces a conical shock driving forward a dense supersonic jet [6,19–21]. This jet was successfully used to investigate the interaction of a jet with a cross wind of low density plasma [22].

A configuration of wires arranged radially, similar to a bike wheel, was used to drive a magnetised jet which has a complex and twisted magnetic field structure similar to collimated outflows from accretion disks [23–25].

A radial foil arrangement has been more recently investigated for the production of supersonic jets, the XUV self emission of this jet is shown next to an HH jet in figure 1.6. This radial foil jet will be discussed extensively in chapter 4 and used during the experiments of this thesis as a tool for driving shocks. The relevance

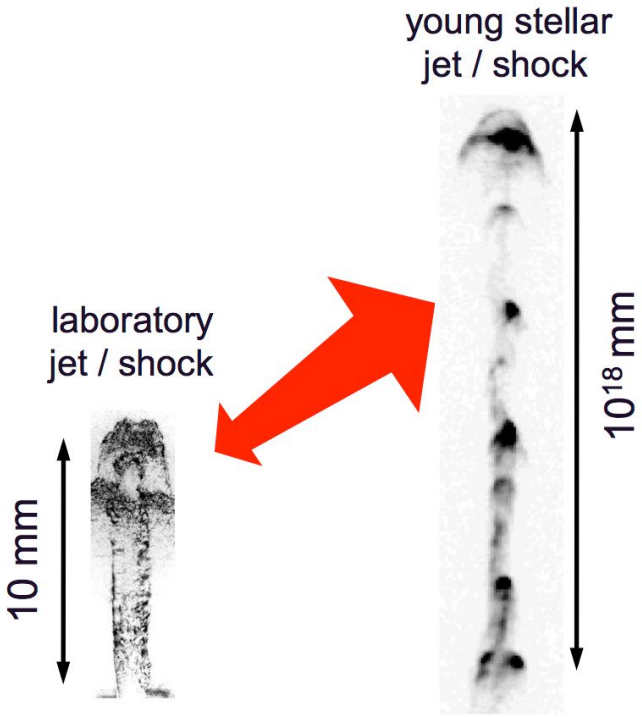

Figure 1.6: Comparison of a laboratory produced jet on the MAGPIE Z-pinch and a HH object, image reproduced from F. Suzuki-Vidal's presentation at ICOPS 2012, Edinburgh, UK.

to HH objects of the radial foil jet has been investigated in both vacuum and in collisions with ambient and localised gas clouds [26–28].

1.3.1 Laboratory produced strong shocks

The production of astrophysically relevant and strong shocks in the laboratory is a new field, and as such there are a limited number of investigations that produce shocks driven by continuous, long lasting, supersonic flows of plasma.

Investigations involving high energy lasers have produced systems comparable to astrophysical shocks, with particular mention to Prof. P. Drake's group at Michigan University. Figure 1.7 shows the set up for the production of a reverse radiative shock in a vacuum filled tube from the LULI2000 laser [2]. The laser irradiates a layer of titanium which produces a supersonic flow of material into the tube. This then interacts with a solid target producing a reverse shock. This system produces a hydrodynamical reverse shock which can be used as a model for cataclysmic variables

[29] and also as an analogy for the accretion coulmn shock [2].

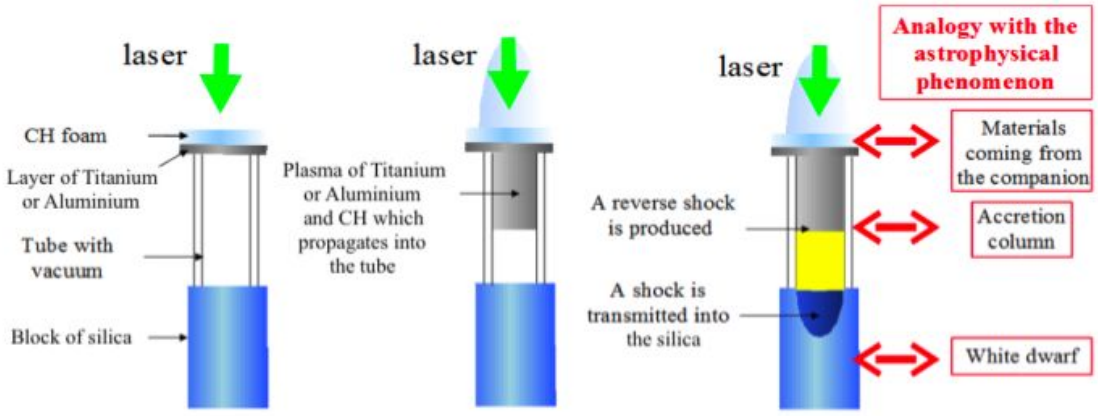

Figure 1.7: Experimental setup for production of reverse shocks using a laser and vacuum filled tube (Busschaert, 2011 [2]).

Recent work published in Nature physics [30] has looked at the collision of two supersonic laser produced jets with the aim to produce collisionless shocks (termed collisionless because the particles do not collide with each other on the same spatial scale as the shock occurs on). At the collision point of the counter-streaming jets, strong electromagnetic fields were observed which were long lived for the time scale of the experiment and spatially extended to be on the scale of the separation of the two counter streaming jets. The authors have yet to find an explanation of the origin or nature of the observed field. The experiment shows some superficial similarities to the results that will be presented in chapter 7 on the collision between two supersonic jets, though it is not at this time clear if there is a deeper connection between these two experiments.

1.4 Investigation aims

This thesis aims to produce a shock in a supersonic flow that will be relevant to astrophysical shocks. It is proposed that the supersonic jet, produced from a radial foil pinch on the MAGPIE generator, will be placed under a solid target, as sketched in figure 1.8.

It is expected that a shock will be created in the flow of the jet which is similar to the systems created in the radiative reverse shock experiments conducted with

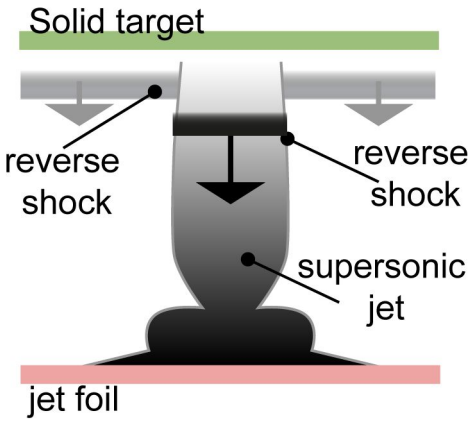

Figure 1.8: A simplified experimental set up where a supersonic flow is produced from a thin foil in the MAGPIE Z-pinch and collides with a target that is perpendicular to the flow of the jet. The dark regions show an expected density increase that may form a reverse shock in both the jet and a surrounding low density plasma termed the 'halo plasma'. It is expected that this shock will move towards the jet-forming foil.

high power lasers. The jet is also accompanied by a low density plasma which is moving at the same velocity as the jet, it is expected that this material will produce a secondary shock on interaction with the target which will be different in nature to the the shock in the flow of the jet. It is expected that both of these shocks will be a reverse shock, as the flow from the jet or halo plasma is expected to build up on the target surface, increasing the density and then reflecting a shock counter to the flow of the jet and halo plasma. Previous investigations with the radial foil jet have suggested that the magnetic field which accelerates the jet is 'frozen' into the plasma forming the jet and halo plasma, this mechanism will be discussed as the driving mechanism for a shock with dynamically significant perpendicular magnetic fields.

This investigation aims to discuss the observed shock structures that result from the interaction of the supersonic material from the jet and the material forming the target and to diagnose the plasma conditions in the shocks observed. Initial experiments investigating counter streaming jets will also be presented and discussed in the context of the jet-target experiment.

1.5 Content of thesis

Chapter 1 has introduced the concept and background of the thesis with reference to previous work done to produce shocks in supersonic flows.

Chapter 2 will introduce the equations used to describe shocks in both idealised fluids and magnetised fluids.

Chapter 3 will introduce the MAGPIE pulsed power facility and its diagnostic suite with an emphasis on describing the diagnostics used during the experiments conducted.

Chapter 4 presents a summary of the previous work conducted with a supersonic radiatively cooled jet into vacuum, produced on the MAGPIE pulsed power facility from a radial foil configuration.

Chapter 5 presents the results of an investigation with supersonic, aluminium jets into thin metallic foil targets.

Chapter 6 presents the results of inverting the polarity of the current driving the supersonic jet and the effects of this inversion on the observed shock formation.

Chapter 7 presents preliminary results for colliding supersonic jets which are created by combining the systems described in chapter 5 and chapter 6. The shock systems observed in the collision of the two jets and their halo plasmas will be used as the basis for discussing the nature of the observed shocks and evidence of a dynamically significant magnetic field.

Chapter 8 provides a summary of the results and analysis, concluding the thesis and providing suggestions of future investigations that can extend the results presented in the thesis.

1.6 Contribution of the author

The work presented in this thesis further explores the formation of radial foil jets and presents new developments in the production of collisional, radiatively cooled shocks in the laboratory. The results presented in this thesis have been presented in several international conferences (Lebedev et al. HEDLA 2012; Pickworth et al. ICOPS 2012; Pickworth et al. APS 2012).

The radial foil array has previously been shown to produce magnetically driven, radiatively cooled plasma jets in the laboratory, which can be treated as scaled versions of jets from young stellar objects. The results obtained in this thesis have extended the use of the radial foil jets as a tool to drive shocks in supersonic flows, and made new measurements on the formation of the jet from a radial foil. These results on the formation of the jet have shown that the halo plasma that surrounds the jet has a radial velocity directed at the centre of the jet, which confirms MHD simulations that have been previously performed and presented in peer reviewed journals (Suzuki-Vidal et al., PoP 2012).

The results of the new jet-target interaction experiments have produced a dynamic system of shocks which may be further characterised to apply to astrophysical shocks seen in HH objects. A reverse shock was seen in the flow from the jet and a stationary shock, which will be the focus of the thesis, formed in the halo plasma surrounding the jet. Extensive use and analysis of the interferometry and Thomson scattering diagnostics informed the conclusions made from these experiments.

New experiments investigating the effect of reversed current polarity on the jet found that the dynamics of the system are similar to the 'normal' polarity system, however the flow parameters of the jet are different indicating that the reversed polarity jet has a higher electron density. The reversed polarity jet-target interaction also produced a stationary shock in the halo plasma which is shown to have similar parameters to the shock seen in the 'normal' polarity system.

New experiments combining the reversed polarity jet with the previously investigated system created a colliding pair of jets. This system produced a bow shock at the tip of the reversed polarity jet indicating the reversed polarity jet has a higher

ram pressure. A pair of stationary shocks were produced in the colliding halo plasmas of the two jet systems, where a hollow density profile across the two shocks is indicative of a magnetic field supporting their separation despite the ram pressure from the halo plasma. This initial speculation is supported in preliminary MHD simulations of the colliding jets performed by A. Ciardi.

All the experiments were performed on the MAGPIE pulsed-power facility at Imperial College London, and were performed with the assistance of a group of experienced, post-doctoral and postgraduate researchers, which the author was part of as a team effort in order to obtain the results presented here. In the same way, the author was involved in experimental campaigns performed in MAGPIE aimed to the study of different configurations of Z-pinches, among them liners (Burdiak et al. 2012), Inverse wire arrays and two stage wire array configurations (Harvey-Thompson et al. PRL 2012) and radial foil and radial wire arrays (Suzuki-Vidal et al. PoP 2012, IEEE ToP 2011 and Shock Waves 2011).

The author was directly involved in all the experiments that produced the data that is presented in this thesis, with the exceptions labeled with their respective reference source otherwise. In general the author was in charge of the overall experiment planning, diagnostic setup, and diagnostic improvement, taking a leading role specifically in the experiments related to jet-target interactions. The colliding jet experiments and design of the hardware for them formed the basis of a MSc project by J. Music and these experiments were lead by F. Suzuki-Vidal and the author. The author was constantly involved in testing new experimental configurations, diagnostic development, building wire and foil arrays, data compiling and safe storing, and the assistance of MAGPIE PhD students in the laboratory.

All the data was analysed by the author, and the analytical models were solved and plotted by the author with assistance and discussions from other members of the MAGPIE team. Analysis software for the interferometry was written by G. Swadling. The author wrote the analysis software used for the Thomson scattering diagnostic.

Chapter 2

Shock physics related to supersonic plasma flows

This chapter will highlight the relevant aspects of shock physics which will be used in the description of the shocks observed in the flow from the supersonic jet and halo plasma when they collide with a target or counter-streaming flow. A short introduction to general shock physics and the temperature, pressure and density jump conditions across a shock will make the basis for the theory of magnetised and radiative shocks with a perpendicular magnetic field.

2.1 Basic shocks in ideal fluids

Shocks in plasmas have additional features not present in the shocks that form in the other phases of matter due to the presence of charged particles and electromagnetic fields. Shocks are ubiquitous in astrophysical observations as well as in laboratory plasma experiments.

In a given material, a shock is defined as a compression in density moving through the material at a velocity faster than the speed of sound. The shock itself compresses the material it passes though, carrying forward energy and heating the material at the shock velocity. The Mach number M, one of the hydrodynamical scaling factors, provides a measure of how many times faster than sound speed a material or object is moving. For example, M =4 implies the material or object has a velocity four

times higher than the speed of sound in the material.

Considering a material consisting of incompressible particles, referred to as the hard ball model, the shock velocity can be visualised, shown in figure 2.1. The figure shows a row of four particles which are unable to be compressed and are confined to exist in a cell, drawn as a box. A piston moves forward into the particles at a velocity u. The piston is a representation for the fluid velocity. As the particles cannot be compressed, they bunch together, filling any free cells between them, increasing the density of the material in front of the piston. The front edge of this bunching progresses at a velocity U, as marked in the diagram and is a representation for the shock velocity. This model allows the velocity of the piston or driver creating the shock to be separated from the velocity of the compression moving through the material.

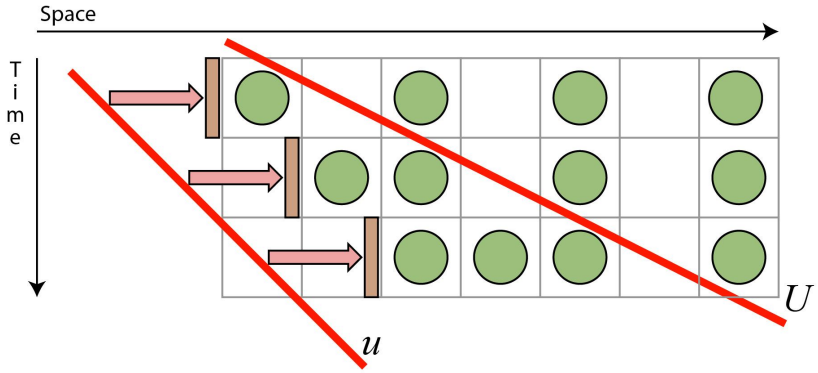

Figure 2.1: The green particles depict a lattice shocked by a piston from the left-hand side. The diagram is in space and time and shows the difference between the piston velocity, u, and and shock velocity U. The piston and particle velocity can be seen to have the same speed.

From the text, 'High-Energy-Density Physics' by Drake [1], the action of a shock wave passing through a material can be broken into three effects:

- The shock wave carries energy forward at the shock velocity.
- The shock heats and accelerates the medium it is passing through.
- The shock wave heats the material behind the shock front. This causes the motion of the shock wave relative to the heated fluid to be sub-sonic. This

heated fluid then communicates with the shock front at a new higher sound speed than the unperturbed material.

A model of a shocked system can now be presented that observes the progression of a shock front in a reference frame moving at the shock velocity. This allows us to observe the material moving into the shock front (from right to left, at the shock velocity, U) and what happens as it moves out of the shock front, shown in diagram 2.2. The figure shows an abrupt increase in the density of the material at the shock front.

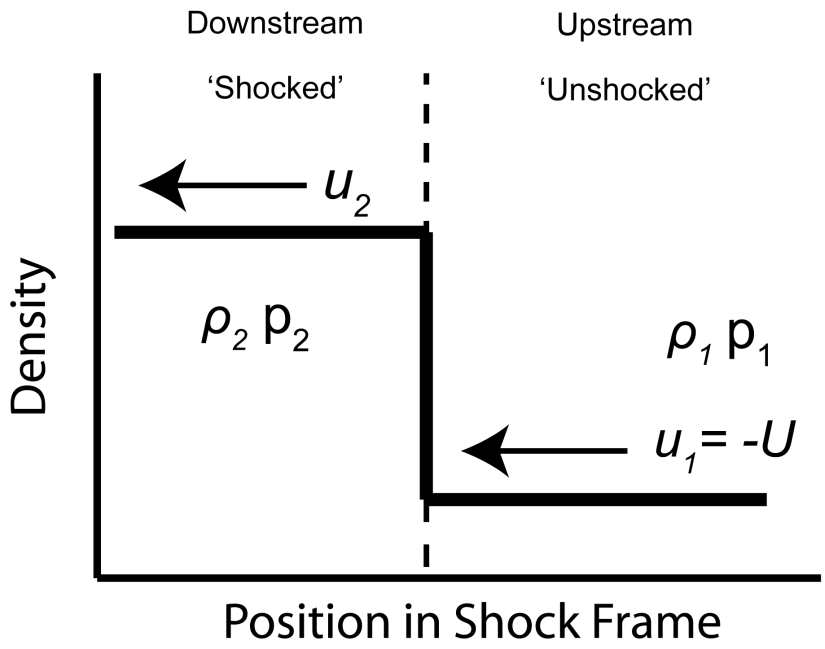

Figure 2.2: Diagram of an isolated steady shock in a reference frame moving at the shock velocity, U. p is pressure and ρ is density. Adapted from Drake [1].

It is seen that the abrupt increase in density in the material also corresponds to an abrupt change in temperature and pressure. The material moves into the shock from the right hand side of the image at a velocity u_1, which as the frame of reference is moving at the shock velocity gives $u_1 = -U$. The material then moves out of the shock at a velocity u_2.

The material will conserve mass and energy across the shock front, allowing the formulation of the Euler equations; Continuity is given in equation 2.1, momentum

in equation 2.2 and energy conservation in equation 2.3. ϵ represents the specific internal energy of the material.

$$\frac{\partial \rho}{\partial t} = -\nabla \cdot (\rho \vec{u}) \tag{2.1}$$

$$\frac{\partial}{\partial t}(\rho \vec{u}) = -\nabla \cdot (\rho \vec{u}^2) - \nabla p \tag{2.2}$$

$$\frac{\partial}{\partial t}(\frac{\rho u^2}{2} + \rho\epsilon) = -\nabla \cdot [\rho \vec{u}(\epsilon + \frac{u^2}{2}) + p\vec{u}] \tag{2.3}$$

The above equations can be integrated to find the *jump conditions* when the motion of the fluid and shock is one dimensional. This gives the change in the conditions across the shock front, due to the sharp increase in density in an infinitesimally small physical space. The subscript '1' refers to the un-shocked material, and the subscript '2' refers to the shocked material in the equations below:

$$\rho_1 u_1 = \rho_2 u_2 \tag{2.4}$$

$$\rho_1 u_1^2 + p_1 = \rho_2 u_2^2 + p_2 \tag{2.5}$$

$$\left[\rho_1 u_1 \left(\epsilon_1 + \frac{u_1^2}{2} + p_1 u_1\right)\right] = \left[\rho_2 u_2 \left(\epsilon_2 + \frac{u_2^2}{2} + p_2 u_2\right)\right] \tag{2.6}$$

This model can be successfully applied to many real world materials and the jump conditions used to predict parameters of the material after the shock front. The specific internal energy ϵ can be related to the pressure, p, in the material with the introduction of the compression factor, γ. This factor is also referred to as the 'shock gamma' and 'polytropic index'.

$$\rho\epsilon = \frac{p}{(\gamma - 1)} \tag{2.7}$$

The shock gamma is a metric of how many energy sinks exist in the material, these can be vibrational and rotational modes (such as in a diatomic gas) or the more complex radiative modes such as ionisation (as in a plasma). For the case of

the plasma in this thesis the shock gamma will be estimated at $\frac{5}{3}$. For a plasma which has more energy sinks available to it, such as radiation and magnetic fields the shock gamma approaches 1. For a physical material that has internal energy and pressures that change in a complex way the assumption that γ is constant is not always valid, though this assumption will be made in the case of the experimental plasmas in this thesis. For a more detailed discussion on the nature of γ and the estimation of its value see section 3.3.1 in High-Energy-Density Physics by Drake [1]. Experimental determination of the shock gamma is an interesting avenue of further work.

The jump conditions can be evaluated again with equation 2.7 to find a useful relation between the density before and after the shock front when $p_2 >> p_1$. This limit is called a strong shock. For a material with $\gamma \sim 5/3$ and a known large Mach number, M, the density ratio can be evaluated to be four to one across the shock from the following equations:

$$\frac{\rho_2}{\rho_1} = \frac{M^2(\gamma+1)}{M^2(\gamma-1)+2} \tag{2.8}$$

$$\frac{\rho_2}{\rho_1} = \frac{(\gamma+1)}{(\gamma-1)} \tag{2.9}$$

In the shock front the kinetic energy of the ions prior to the shock is converted to thermal energy in the shock through collisions. The temperature T, in a shock front can be estimated by the following equation assuming the shock is strong, where Z is the ionisation in the shock, A is the atomic number, m_p is the proton mass, u_1 is the velocity of the ions and k_B is Boltzmann's constant.

$$k_B T = \frac{A m_p}{(1+Z)} u_1^2 \frac{2(\gamma-1)}{(\gamma+1)^2} \tag{2.10}$$

It can be seen that as the ionisation of the shocked material increases the temperature in the shock decreases. After the initial heating at the shock front, energy is transferred between the electrons and ions in the plasma though collisions or radiation. Radiation will be dominant, as a mechanism of energy transfer, if the plasma is optically thick and this falls under the treatment of radiative shocks. Assuming

an optically thin plasma, where any radiation passes out of the shock as an energy loss, the collisions between the ions and electrons have the largest interaction cross section. The collision rate of the ions with electrons τ_{ei}, can be estimated as:

$$\tau_{ei} = \frac{AT_e^{\frac{3}{2}}}{3.2 \times 10^{-9} n_e Z^2 \ln \Lambda} \tag{2.11}$$

Where n_e is the electron density of the material in the shock and $\ln \Lambda$ is the Coulomb logarithm which can be estimated from $ln\Lambda = MAX[1, \{24 - ln(\sqrt{n_e}/T_e)\}]$ which means the Coulomb logarithm is evaluated as the larger of 1 or $24 - ln(\sqrt{n_e}/T_e)$, for most plasmas produced in the experiments of this thesis, $\ln \Lambda = 6$. The collision rate can be combined with a post shock velocity of the material to find a temperature equilibration length, which is the distance over which the ions are expected to match the electron temperature. The velocity used in combination with the electron-ion collision rate can be found from the strong shock limit to be:

$$\frac{u_2}{u_1} = \frac{(\gamma - 1)}{(\gamma + 1)} \tag{2.12}$$

This equation implies in the strong shock limit that the ratio of velocities is the inverse of the ratio of density, therefore the velocity of the material flowing into the shock will be reduced by a factor of 4 after the shock, in the frame of motion where the shock velocity is zero.

2.2 Effects of radiative cooling in shocks

In a strong shock the material is compressed and heated, and in the case of a plasma this may cause the shocked material to become radiative through increasing the ionisation in the plasma. The effect of radiation in the shock depends on whether the radiation escapes the system (the plasma is optically thin) or if the radiation is absorbed to some extent in the system (an optically thick plasma). Figure 2.3 shows a radiatively cooled shock where the pre-shocked plasma (to the left in the diagram) is heated by radiation from the shocked material, causing a radiative precursor. For an optically thin material the radiation will escape and no radiative precursor will

be formed.

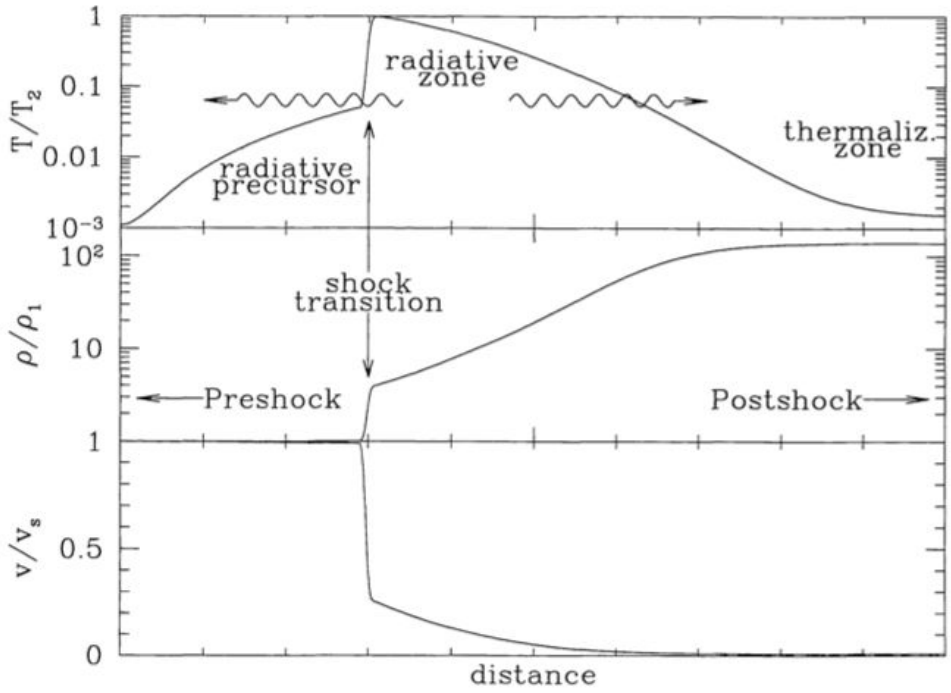

Figure 2.3: The density, temperature and velocity in the frame of the strong radiative shock [3].

The effect of escaped radiation behind the shock is that the material is cooled, reducing the thermal pressure in the material, which allows a higher compression. This is shown in the density profile in figure 2.3 where the density after the shock transition is seen to continue increasing.

The degree to which radiative effects are present in a shock is described by a dimensionless MHD scaling parameter, χ, termed the cooling parameter, which is the ratio between the hydrodynamic time scale of the plasma and the cooling time, which for a radiatively cooled plasma $\chi << 1$. The hydrodynamic time describes the rate at which the particles in the shock are moving energy through the structure and the cooling time describes how quickly the same energy can escape the structure in the form of radiation.

When cooling effects are very large a 'thin layer' instability can develop which appears as an unstable or knotted shock front. This effect is discussed for a supersonic jet propagating in a ambient material by Blondin, 1990 [31]. The mechanism and nature of the shock formed at the front of the supersonic jet is discussed fully in

Drake, section 10.5 [1], for this discussion the effect of varying the cooling parameter in the jet to produce an instability is shown in the figure 2.4.

Figure 2.4 shows the change in the shock front of a jet with a Mach number of 20 when the cooling parameter χ is varied from an adiabatic system, Figure 2.4a, to a very radiatively cooled system, figure 2.4d, where the boundary of the shock front is no longer seen to be smooth and well defined.

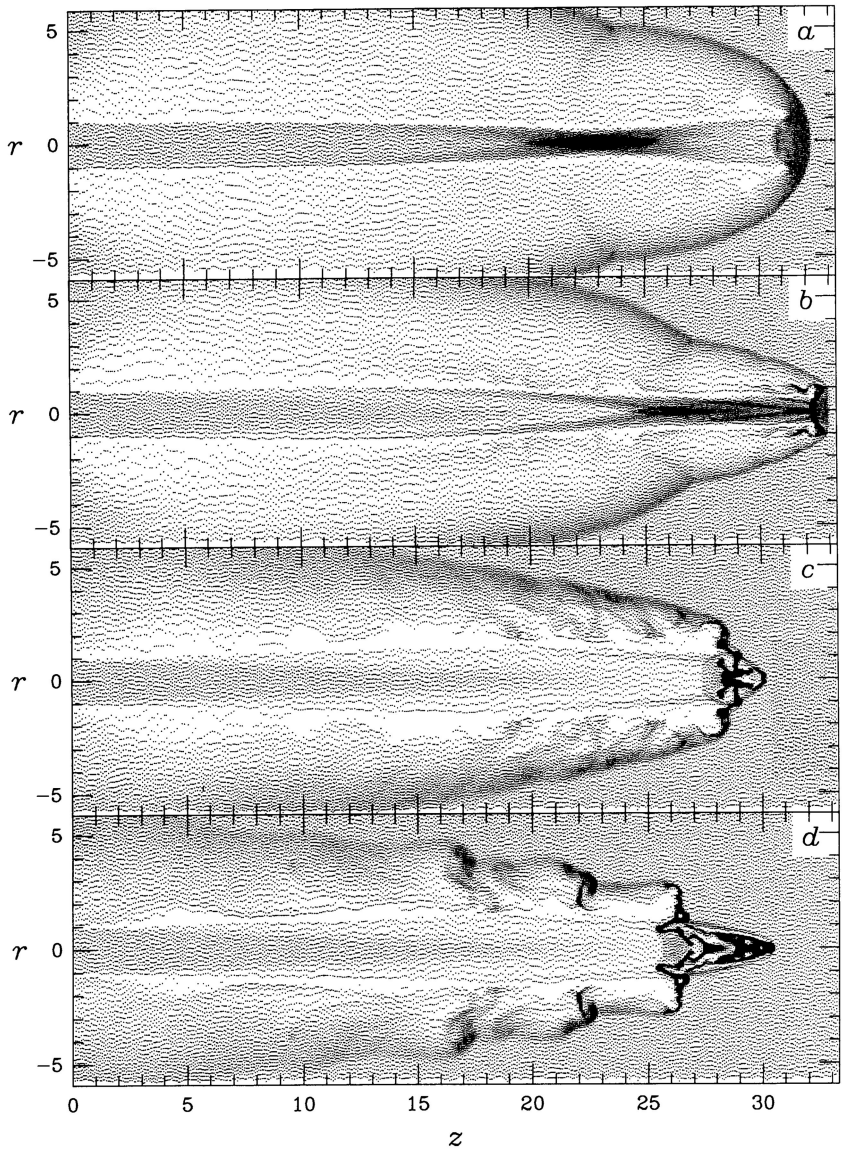

Figure 2.4: Effect of cooling on shock front of a supersonic jet. (a) an 'adiabatic' shock front, no effect from cooling. (b), (c) and (d) a decreasing cooling parameter for χ =2.2, 0.55 and 0.2 respectively. Effects of radiative cooling are dominant when $\chi < 1$. From Blondin, 1990 [31].

2.3 Magnetised shocks

The fluid model outlined for a shock does not account for the effects of electric and magnetic fields that appear in a plasma as found in astrophysics or in the laboratory. The energy conservation equation outlined in equation 2.1, 2.2 and 2.3 needs to be reformulated to take into account the effects of radiation and the electromagnetic conservation of energy. This will form the basis of a single fluid model for magnetised and radiative shocks, following the derivation of Draine, 1993 [3].

2.3.0.1 Single fluid model for magnetised shocks

The single fluid model can provide an insight into the idealised behaviour of a magnetised shock. For the single fluid, the laws of mass, momentum and energy conservation are given as:

$$\frac{\partial \rho}{\partial t} + \frac{\partial}{\partial x_k}(\rho \nu_k) = 0 \tag{2.13}$$

$$\frac{\partial}{\partial t}(\rho \nu_j) + \frac{\partial}{\partial x_k}(\rho \nu_j \nu_k + p\delta_{jk} - \sigma_{jk} + \frac{B^2}{8\pi}\delta_{jk} - \frac{1}{4\pi}B_j B_k) = 0 \tag{2.14}$$

$$\frac{\partial}{\partial t}(u) + \frac{\partial}{\partial x_k}(u\nu_k + q_k) + (p\delta_{jk} - \sigma_{jk})\frac{\partial \nu_j}{\partial x_k} + \frac{\partial F_k}{\partial x_k} = 0 \tag{2.15}$$

Where:

- $\rho, \vec{\nu}$ and p are density, velocity and pressure
- $\vec{B}$ is the magnetic field
- u is the fluid energy density ($u = (3/2)p + u_{int}$) where u_{int} is internal energy density
- $\vec{q}$ is the heat flux due to thermal conduction
- $\vec{F}$ is the radiative heat flux
- σ_{jk} is the viscous stress tensor

The electrical conductivity of the fluid is assumed to be infinite, such that the fluid is everywhere electrically neutral. Summation over the repeated indices, j and k, is implied in the equations for mass momentum and energy conservation. The divergence of the radiative flux is $\vec{\nabla} \cdot \vec{F} = \Lambda$ where Λ is the net rate per volume of energy removal due to radiative cooling.

Λ_{eff} is defined as the effective loss function which includes energy 'losses' such as ionisation and dissociation in the fluid (this then eliminates u_{int}, the internal energy density, from the formulation), then the energy conservation equation will become:

$$\frac{\partial}{\partial t}(\frac{3}{2}p) + \frac{\partial}{\partial x_k}(\frac{3}{2}p\nu_k + q_k) + (p\delta_{jk} - \sigma_{jk})\frac{\partial \nu_j}{\partial x_k} + \Lambda_{eff} = 0 \tag{2.16}$$

If it is assumed the electric field in this frame will vanish (as we have already assumed the fluid is everywhere electrically neutral), then $\vec{E} + (\frac{1}{c}\vec{\nu} \times \vec{B}) = 0$. The magnetic field is then given by:

$$\frac{\partial}{\partial t}\vec{B}_j + \frac{\partial}{\partial x_k}(\nu_k B_j - \nu_j B_k) = 0 \tag{2.17}$$

An alternative form of the energy equation may then be found:

$$\begin{aligned}\frac{\partial}{\partial t}(\frac{1}{2}\rho\nu^2 + u + \frac{B^2}{8\pi}) + \frac{\partial}{\partial x_k} \\ \times [(\frac{1}{2}\rho\nu^2 + u + p + \frac{B^2}{4\pi})\nu_k - \sigma_{kj}\nu_j - \frac{B_j B_k}{4\pi}\nu_j + F_k] = 0\end{aligned} \tag{2.18}$$

The above equations are restricted to flows where all plasma elements (the ions and electrons are separate elements or species in the plasma) have a common flow velocity $\vec{\nu}$ for that element. The ions and electrons may have different temperatures or even different anisotropic velocity distributions ($\sigma_{jk} \neq 0$).

2.3.0.2 Jump conditions for a magnetised shock

The single fluid equations given above can be integrated to find the jump conditions across a smooth shock front. The 'parallel' direction is assumed to be perpendicular to the shock front and parallel to the material flow. These equations will give the jump conditions for a magnetised shock in the general case.

The notation $[f] = f(x_2) - f(x_1)$ where the subscript '1' denotes the 'upstream' from the shock and subscript '2' denotes 'downstream' is used as short hand in the jump conditions below:

$$[\rho\nu_{||}] = 0 \tag{2.19}$$

$$[B_{||}] = 0 \tag{2.20}$$

$$[\nu_{||}\vec{B}_{\perp} - B_{||}\nu_{\perp}] = 0 \tag{2.21}$$

$$[\rho\nu_{||}^2 + P + \frac{1}{4\pi}B_{\perp}^2] = 0 \tag{2.22}$$

$$[\rho\nu_{||}\vec{v}_{\perp} - \frac{1}{4\pi}B_{||}\vec{B}_{\perp}] = 0 \tag{2.23}$$

$$[\nu_{||}(\frac{1}{2}\rho\nu^2 + p + u) + \frac{1}{4\pi}(B_{\perp}^2\nu_{||} - B_{||}\vec{B}_{\perp}\cdot\vec{\nu}_{\perp}) + F_{||}] = 0 \tag{2.24}$$

2.3.0.3 Magnetised shocks with a perpendicular magnetic field and $B_{||} = 0$

In the special case where a fluid has $u = p/(\gamma - 1)$ and $B_{||} = 0$ (the only component of the field is parallel to the front of the shock) the solution to the magnetised shock equations becomes simpler. The compression, given in the general case in equation 2.24, is found to be:

$$\frac{\rho_2}{\rho_1} = \frac{2(\gamma+1)}{D + [D^2 + 4(\gamma+1)(2-\gamma)M_A^{-2}]^{1/2}} \tag{2.25}$$

where:

$$D = (\gamma - 1) + (2M^{-2} + \gamma M_A^{-2}) \tag{2.26}$$

where $M_A = \nu_s/\nu_{A1}$ is the Alfvén Mach number, and the Mach number is defined as $M = \nu_s/c_{s1}$. The Alfvén Mach number relates the Alfvén velocity ν_{A1} of the plasma to the speed of sound in the plasma.

The sound speed in a plasma is proportional to the square root of the electron temperature T_e, and ionisation Z, and can be found by:

$$c_{s1} = \sqrt{\frac{\gamma Z k_B T_e}{m_i}} \tag{2.27}$$

For an aluminium plasma where $T_e = 30$eV and $Z = 3$ and $\gamma = 5/3$ the sound speed can be evaluated as $\sim$20km/s which is typical of the parameters found in the jets that will be used throughout this thesis.

The Alfvén velocity is related to the ratio of the magnitude of the external magnetic field and the square root of the ion density n_i, in the plasma:

$$\nu_{A1} = \frac{B}{\sqrt{4\pi n_i m_i}} \tag{2.28}$$

For an aluminium plasma with $n_i = 2 \times 10^{18}\text{cm}^{-3}$ and an external magnetic field of 10T, $\nu_{A1} \sim 30$km/s. For a plasma with the sound and Alfvén velocities given here which is moving with a flow velocity of 50km/s, $M = 2.5$ and $M_A = 1.7$. D can be evaluated (with $\gamma = 5/3$) and is found to be $D = 1.6$, then the density ratio for a shock with these velocities would be $\frac{\rho_2}{\rho_1} \sim 1.5$.

The role of the magnetic field can dominate when the collisional mean free path of the particles in the shock is much larger than the measured interaction region, or width of the shock front. In the astrophysical case the mean free path for collisions of the particles can be on the order of the distance between the Earth and the Sun, however a shock is seen to form in the solar wind interacting with the Earths magnetic field. In this case the mechanism of the shock formation is very complex, the magnetic field is strong enough to heat and compress the solar wind material through localised turbulent magnetic fields. This is said to be a collisionless shock due to the lack of collisions between the compressed particles.

Chapter 3

Experimental equipment and diagnostics

This chapter outlines the experimental equipment used in the investigations presented in this thesis. The MAGPIE pulsed power facility will be discussed along with the elements of its diagnostic suite used in these experiments.

3.1 The MAGPIE pulsed power facility

The experiments outlined in this thesis took place on the MAGPIE pulsed power facility with the use of its diagnostic suite. MAGPIE is a fast Z-pinch built in 1994 with the aim of performing single fibre implosion experiments to study the effect of radiative collapse. It has been used successfully for the investigation of wire array physics and laboratory astrophysics. With a shot capability of 1 to 4 a day, depending on the load configuration, it is fully run by the students and researchers in the plasma physics group at Imperial College London. The MAGPIE pulsed power facility is shown in figure 3.1.

3.1.1 The fast-pinch pulsed-power device

The fast Z-pinch is a subset of pulsed power devices. Pulsed power compresses electrical energy into a short time period, or pulse. The pulse is then driven into an

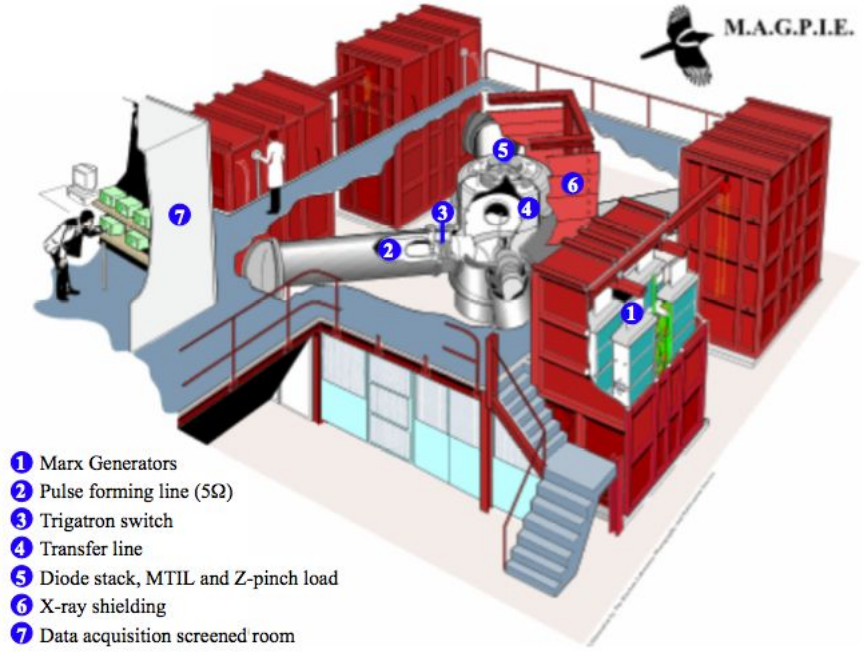

Figure 3.1: The MAGPIE generator at Imperial College London.

experimental load. In the fast pinch a large (>MA) electrical current is compressed into sub-microsecond time scales and passed through a load with dimensions on the order of centimetres.

Z-pinches are named due the mechanism of compression they produce on their load. The current J, flows in the z axis producing a large azimuthal magnetic field B, as is seen in 'the current carrying wire'. The current interacts with this magnetic field though the Lorenz force, referred to as the '$J \times B$' force. This then acts on the material accelerating it in the direction of the $J \times B$ force. Very large pressures, densities and temperatures can be produced via this mechanism.

3.1.1.1 Marx banks

The Marx bank is a device that allows the generation of high voltages and high current in a short discharge time. The circuit diagram for an 8 stage Marx is shown in figure 3.2. The Marx bank achieves high voltages through the use of gas switches allowing the capacitors to be charged in parallel and discharged in series as the gas switches can 'hold off' the charging voltage and be triggered independently with the application of an external voltage to induce the discharge of the Marx bank.

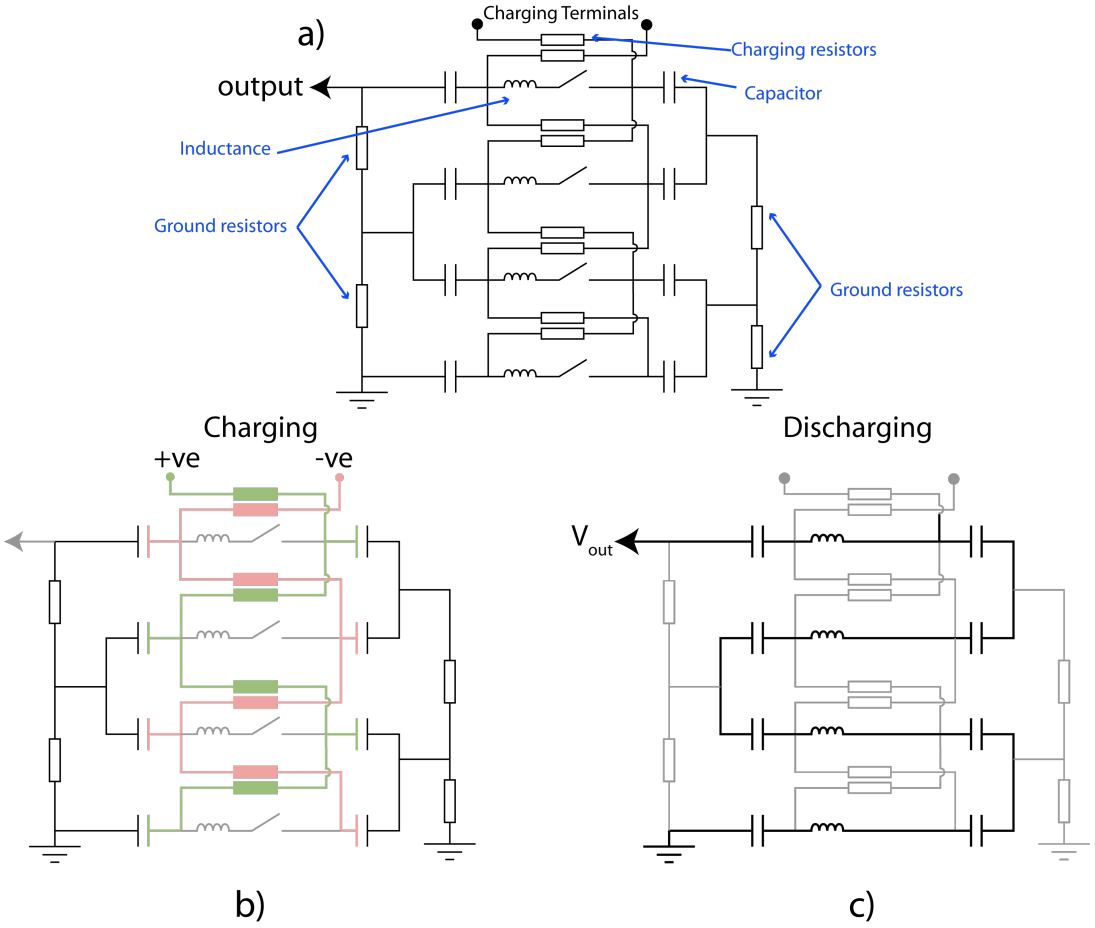

Figure 3.2: The electrical circuit for an 8 stage Marx bank, with the charge (b) and discharge (c) cycles shown. The marked inductance is the combined inductance of the switch and capacitors.

The discharge of the Marx bank can be drawn as an effective circuit, shown in figure 3.3, of a capacitor, resistor and an inductor in series creating a weakly damped oscillatory current [32].

The Marx bank arrangement allows the generator to drive larger loads as the discharge takes the form $V \propto L\frac{dI}{dt}$. When the banks are added in parallel it increases the peak current by a factor equal to the number of banks, but the inductance the generator can drive will be reduced.

Marx banks typically discharge in the μs timescale, which is still too long a discharge time for driving fast Z-pinches. The discharge of the Marx bank is therefore further compressed through a pulse forming line.

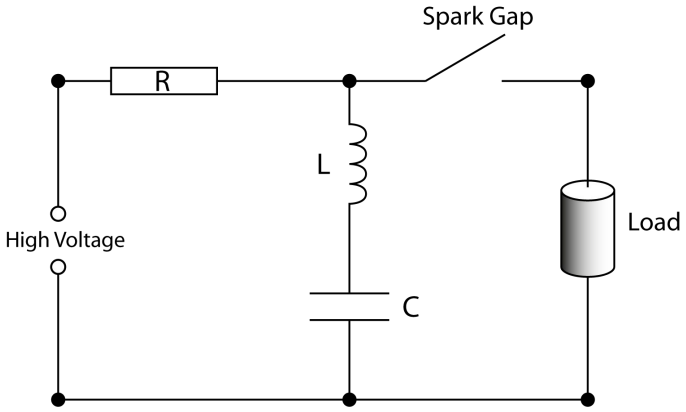

Figure 3.3: Effective electrical circuit for a Marx bank connected to a load using idealised electrical components.

3.1.1.2 The pulse forming line

A deionised water filled pulse forming line (PFL) can be used to compress the electrical pulse produced by the Marx bank. The PFL can be modeled as a coaxial cable, acting as a storage capacitor and inductor. The length and outer radius of the PFL is related to its discharge time by the following equations, where R_{inner} is the inner radius of the coaxial PFL and R_{outer} is its outer radius. L is inductance and C is the capacitance.

$$L_{Coax} = \frac{\mu_0 \mu_r}{2\pi} \ln\left(\frac{R_{outer}}{R_{inner}}\right) \tag{3.1}$$

$$C_{coax} = \frac{2\pi\epsilon_0\epsilon_r}{ln(\frac{R_{outer}}{R_{inner}})} \tag{3.2}$$

At the frequencies of interest deionised water has an extremely large dielectric constant ($\epsilon_r = 80$), due to the polarisability of the water molecules. This makes it an ideal dielectric medium for high current pulsed power applications. Deionised water is only capable of holding off electrical breakdown in the PFL for short periods, on the order of microseconds. The discharge of the Marx bank can then be used to charge the PFL, which in turn compresses the electric pulse temporally.

3.1.2 The MAGPIE generator

MAGPIE stands for Mega Ampere Generator for Plasma Implosion Experiments. The MAGPIE generator consists of 4 Marx banks, 4 pulse forming lines, a magnetically-insulated transfer line (MITL) and vacuum chamber where the experimental load is situated. Figure 3.4 shows a cross section of one Marx, one PFL and the transfer line. The generator design is discussed in detail in Mitchell et al. 1996 [33].

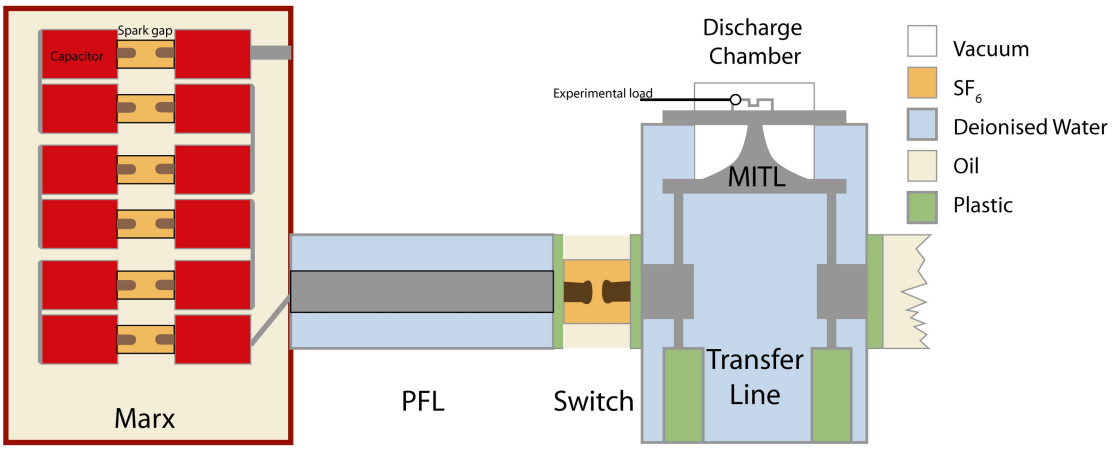

Figure 3.4: A cross section sketch of the MAGPIE pulsed power facility showing a Marx, PFL, transfer line MITL and the discharge chamber.

Each of MAGPIE's four Marx banks consist of 24×1.3μF capacitors. A charging voltage of ±65kV and a charging current of 6mA is applied. The nominal energy E_n, for one MAGPIE Marx can be found [32], this is the theoretical limit of energy stored by a Marx bank assuming 100% efficiency, given by $E_n = \frac{1}{2}nCV^2$ where n is the number of stages, C is capacitance and V is the charging voltage. This gives a stored total maximum energy for MAGPIE of $4 \times 66kJ = 264kJ$.

Each Marx bank discharges into a PFL, which behaves as a capacitor with a discharge time of 250ns. The current pulse from the four Marx generators is combined by the simultaneous triggering of the line gap switches. The line gap switch is a large spark gap, which is triggered with an external voltage applied to a pin in the centre of one of the electrodes. The gap contains ∼3.5Bar of SF_6 which will hold off the charge on the PFL until it is triggered.

The four current pulses from the PFL's are combined and delivered to the load

via the MITL which is situated at the top of the transfer line. The discharge chamber is located above the MITL. The discharge chamber and MITL are shown in figure 3.5, the inner diameter of the discharge chamber is 80cm.

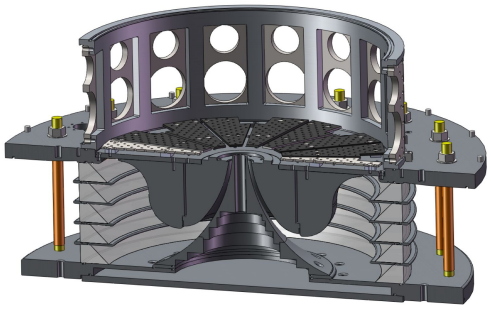

Figure 3.5: Cross section of the MITL and discharge chamber on MAGPIE. Inner diameter of the chamber is 80cm. Image courtesy of Dr. G. Hall

The MITL acts to reduce the physical size of the transfer section to the experimental load (which has a typical diameter of 5 to 40mm). This section also provides an interface between the deionised water section of the transfer line and the vacuum in the load chamber. This is achieved with a diode-stack consisting of a series of insulator rings designed to inhibit the breakdown between the MITL and the anode. The shape of the MITL conserves the magnetic field density as the current is spatially concentrated which inhibits the likelihood of breakdown through confinement of any produced free charges.

3.1.2.1 Characteristics of the MAGPIE current

The current is delivered into the load chamber with a characteristic current shape. Figure 3.6 shows the current at at the MITL section in the discharge chamber as measured by a 'B-dot' probe. The B-dot is an inductive loop of wire which measures $\frac{dI}{dt}$ via the fluctuations in the magnetic field. The pulse shape is sinusoidal at the load and can be modeled by the following equation:

$$I(t) = I_{MAX} sin^2(\frac{\pi t}{2t_{MAX}}) \tag{3.3}$$

The maximum current, I_{MAX} is typically between 1.2-1.4MA and the discharge

time, t_{MAX}, is between 240-250ns. The signal shown in figure 3.6 has a 250ns rise time.

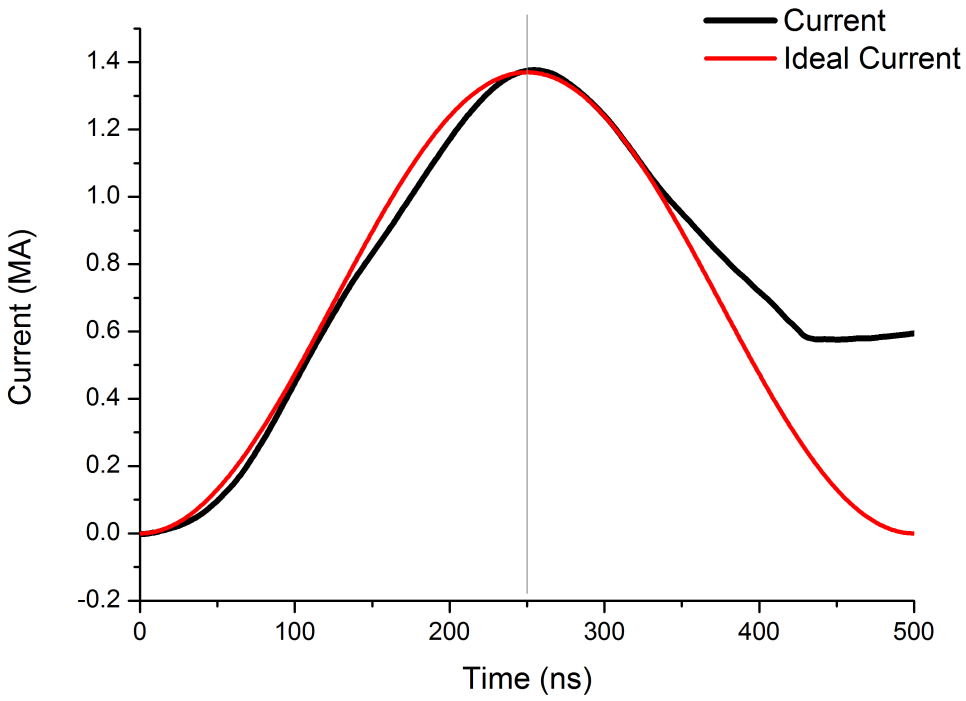

Figure 3.6: The current measured at the MITL section by an inductive probe called the 'B-dot'. The current is seen to rise smoothy and reach its peak at 250ns from the start of the current in the MITL. This gives the characteristic 250ns current rise time. The divergence from the ideal current after 400ns is termed 'crow baring' of the magnetic probe. Current trace from experiment s052312.

3.2 The MAGPIE diagnostic suite

3.2.1 Monitoring the current in the experimental load

The current delivered to the experimental load can be monitored with the use of a Rogowski coil or groove [34]. The Rogowski coil measures a current induced in the coil by a changing magnetic field. The groove is placed on one of four current return posts at the experimental load which are attached to the anode electrode of the generator. The current observed in the experimental load depends on the current profile delivered by the generator and also on the inductance of the experimental load.

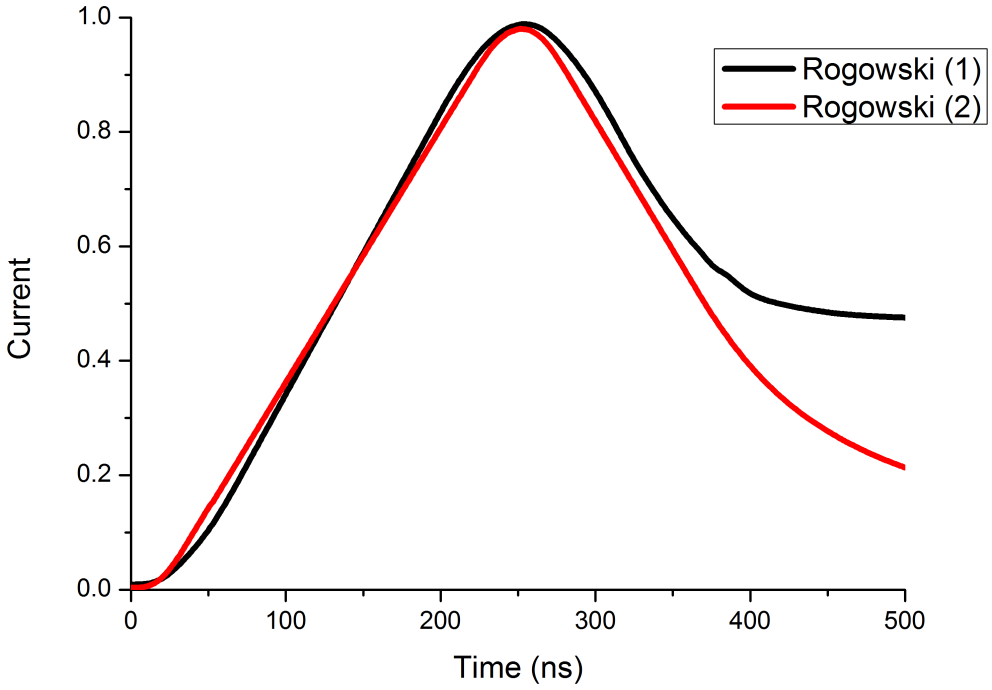

Figure 3.7: The integrated signal, which gives the current in the load, from the two Rogowski coils positioned on the return posts of the experimental hardware. The current is normalised for each signal. The current is seen to have the characteristic 250ns rise time seen on the MITL B-dot signal shown in figure 3.6. From experiment s052312.

Figure 3.7 shows the current derived from the voltage signal produced by the Rogowski groove. The current observed on the oscilloscope is proportional to equa-

tion 3.4 where V_{groove} is the voltage seen from a groove with a cross section such that the outer diameter is B and the inner diameter is A and a height of C. L_{probe} is the inductance of the probe, Φ is the flux and I is the observed current.

$$V_{groove} = -\frac{d\Phi}{dt} = -\left[\frac{C\mu_0}{2\pi} ln\left(\frac{B}{A}\right)\right]\frac{dI}{dt} = -L_{probe}\frac{dI}{dt} \tag{3.4}$$

The current in the experimental load is measured on two return posts which allows the symmetry of the current in the load to be monitored. The time that the current is observed to start from the Rogowski coil is used as the reference time for all other timed diagnostics, such that the time current starts is the zero nanosecond point in the experiment.

3.2.2 The laser imaging suite

The laser imaging suite of MAGPIE comprises of two shadowgraph systems and four interferometry systems. The imaging system uses three viewing angles in the discharge chamber which allows the azimuthal symmetry of the experimental system to be assessed. The laser path is delayed for two of the beam lines by 20ns allowing two different time points in the same experiment to be captured. The laser can be externally timed to fire at a desired point in the experimental development relative to the current start time. The imaging systems take advantage of two of the harmonic frequencies generated by the probe laser, at 532nm and 355nm.

Figure 3.8 shows a schematic of the laser imaging system. The discharge chamber is marked in the image with the laser beam paths shown in green for the 532nm wavelength and in blue for the 355nm wavelength. There are three optical benches which are shown in the diagram and named 'GreenSide', 'ChrisCam' and 'SwadCam'. The laser has a delay built into the imaging systems on 'ChrisCam' and 'SwadCam' which is achieved by increasing the path length of the laser. 'ChrisCam' and 'SwadCam' are delayed from 'GreenSide' by 20ns. The laser path of 'SwadCam' uses an optical table positioned on the ceiling above the diagnostic chamber to deliver the combined 355nm and 532nm beams through the chamber, and pass the reference beams for 'SwadCam' above the chamber.

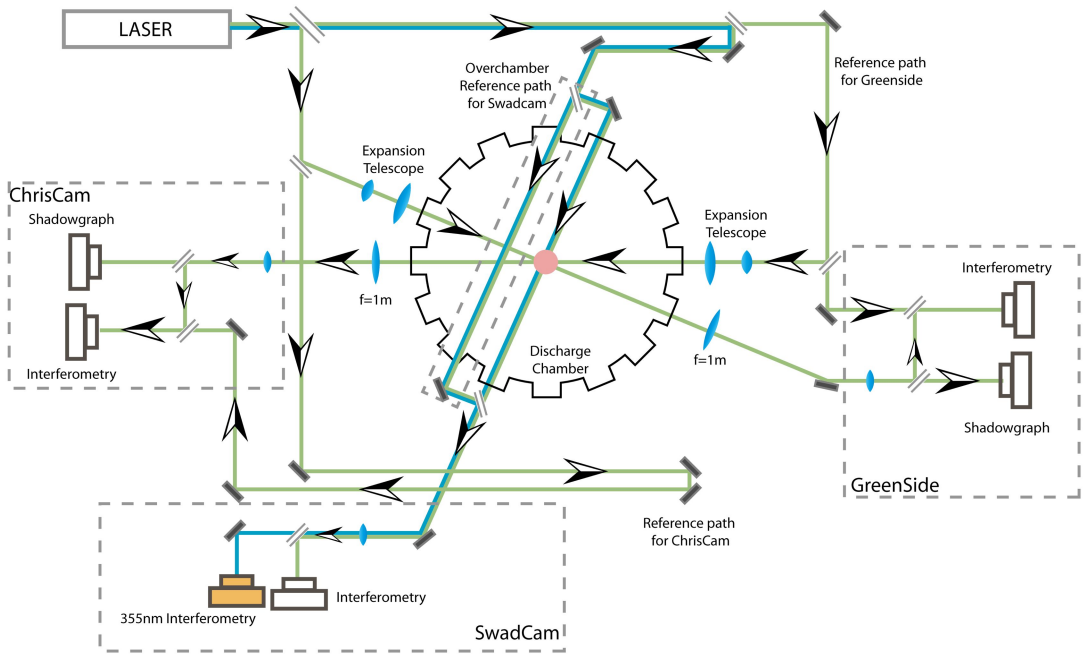

Figure 3.8: Schematic showing the laser imaging systems used during the experiments.

'ChrisCam' and 'GreenSide' both have a shadowgraph system and an interferometry system from the 532nm laser beam. 'SwadCam' has two interferometer systems, one of which is from the 355nm laser beam. The filter at the camera and the beam splitters used to construct the 355nm imaging system require different coatings to the 532nm system which currently limits the number of beam lines using the 355nm probe beam, due to expense. The images are captured on Cannon digital SLR cameras with 8 or 15MP resolution. The SLR used for the 355nm interferometry is modified to remove the UV filter fitted as standard on the sensor.

The laser used for imaging is a EkSPLA SL312P. The lasing medium is Nd:YaG which is flash-lamp pumped. The pulse length of the laser is compressed to produce a ~500ps pulse duration. The beam is coupled with non-linear crystals which combine the natural lasing frequency of the laser to produce the second and third harmonics which are the 532nm and 355nm beams.

The laser beam is expanded prior to entering the discharge chamber with a telescopic lens system to produce a collimated beam profile of ~150mm diameter which then passes though the experimental load. The collimated probe beam then

passes though a f=1m lens before the beam is passed to one of the imaging systems on the three optical benches and re-magnified onto the SLR camera detector. Each camera is fitted with a filter that blocks emission that is not at the frequency of the laser.

3.2.3 Free electrons in a plasma and the plasma refractive index

The free electron density in a plasma will effect the refractive index. As a probe beam passes though the plasma the change in refractive index along the path will result in a deflection of the beam. The refractive index of a plasma is formed of two components, the dominating component in the experiments discussed in this thesis is the free electrons in the plasma which contributes a negative component to the refractive index. The second component is the contribution from the neutral gas, made up of electrons still bound to the ions, which contributes a positive component to the refractive index. The refractive index can be derived by considering the movement of the electrons in the electromagnetic field of the probing or driving laser.

$$-e\vec{E} - v_{col} m_e \vec{V_e} = m_e \frac{d\vec{V_e}}{dt} \tag{3.5}$$

Where e is the electronic charge and m_e is the electronic mass, $\vec{E}$ is the optical electrical field, given in equation 3.6, v_{col} is the rate of collision for the electrons and $\vec{V_e}$ is the electron velocity. The optical electric field is given by the following equation where ω is the frequency and k is the wave vector. t and z are the time and distance variables respectively.

$$\vec{E} = \vec{E_0} e^{i(\omega t - kz)} \tag{3.6}$$

The motion of the electron is driven by the incident electromagnetic field of the probing laser. The motion of the electrons will then take on the same form as the optical electrical field incident upon them, shown in the following equation; where V_0

is the complex amplitude containing both the amplitude of the electron oscillation and their phase shift from the optical field of the laser.

$$\vec{V_e} = \vec{V_0} e^{i(\omega t - kz)} \tag{3.7}$$

The equation of the electron motion can be substituted into (3.5) and rewritten for the electron velocity and complex amplitude as follows, giving the equation of motion for a single electron.

$$\vec{V_e} = \frac{ie\vec{E}}{m_e(\omega - iv_{col})} \tag{3.8}$$

$$\vec{V_0} = \frac{ie\vec{E_0}}{m_e(\omega - iv_{col})} \tag{3.9}$$

The current density in the plasma is found, assuming there are no collisions and the velocity lags behind the laser by a phase of $\frac{\pi}{2}$:

$$\vec{J} = \frac{-in_e e^2 \vec{E}}{m_e(\omega - iv_{col})} \tag{3.10}$$

Amperes law depends on the current density and the electric field and is given by the following:

$$\nabla \times \vec{B} = \mu_0 \left(\vec{J} + \epsilon_0 \frac{\partial \vec{E}}{\partial t} \right) \tag{3.11}$$

The equations for the current density and electric field can be substituted into Amperes law to give the following:

$$\nabla \times \vec{B} = \mu_0 \left(\frac{-in_e e^2 \vec{E}}{m_e(\omega - iv_{col})} + \epsilon_0 \frac{\partial \vec{E}}{\partial t} \right) \tag{3.12}$$

$$\nabla \times \vec{B} = -\mu_0 \epsilon_0 \omega \left(1 - \frac{n_e e^2}{\omega_0 \epsilon_0 m_e(\omega - iv_{col})} \right) \vec{E} \tag{3.13}$$

Using the identity for the plasma frequency, $\omega_p = \sqrt{\frac{n_e e^2}{\epsilon_0 m_e}}$, and assuming $\omega >> v_{col}$:

$$\nabla \times \vec{B} = -\mu_0 \epsilon_0 \omega \left(1 - \frac{\omega_p^2}{\omega^2} \right) \vec{E} \tag{3.14}$$

Differentiating this equation and substituting into the Faraday-Maxwell equation gives a wave equation, assuming $c^2 = \frac{1}{\mu_0 \epsilon_0}$;

$$\nabla^2 \vec{E} = \frac{1}{c^2}\left(1 - \frac{\omega_p^2}{\omega^2}\right)\frac{d^2\vec{E}}{dt^2} \tag{3.15}$$

The wave velocity and the refractive index can then be found:

$$\frac{1}{v^2} = \frac{1}{c^2}\left(1 - \frac{\omega_p^2}{\omega^2}\right) \tag{3.16}$$

Using the identity $v = \frac{c}{\eta}$, where η is the refractive index then:

$$\eta = \sqrt{1 - \frac{\omega_p^2}{\omega^2}} \tag{3.17}$$

This can be rewritten in terms of the electron density in the plasma such that:

$$\eta = \sqrt{1 - \frac{n_e}{n_c}} \tag{3.18}$$

The limiting electron density that the laser can pass through is n_c, which is the cut off density. For a laser wavelength of λ this is given by:

$$n_c = \left(\frac{4\pi c^2 m_e \epsilon_0}{e^2}\right)\frac{1}{\lambda^2} = \frac{1.1 \times 10^{15}[\mathrm{m}^{-1}]}{\lambda^2} \tag{3.19}$$

For the 532nm laser this cut off density is equivalent to $n_e \sim 4 \times 10^{21}\mathrm{cm}^{-3}$ and for the 355nm laser beam the cut off density is $n_e \sim 9 \times 10^{21}\mathrm{cm}^{-3}$. If it is assumed the electron density of the plasma will be much smaller than the cut off density, then equation 3.18 can be approximated though a Taylor expansion to be:

$$\eta \approx 1 - \frac{n_e}{2n_c} \tag{3.20}$$

3.2.3.1 Laser shadowgraphy

The spatial gradients in refractive index of the plasma will deflect light as it passes through it. This effect is used to produce a shadowgraph by passing an expanded and collimated laser beam, which initially has a uniform beam intensity, through the plasma. The refractive index gradients will brighten and darken the intensity

profile of the beam according to the degree of deflection. The angle of deflection due to the refractive index in the plasma is given by (Hutchinson 2002):

$$\theta_z = \int \frac{d}{dz}\eta(z)dl = \int \eta' dl \tag{3.21}$$

It can be seen from the equation that the angle of deflection is sensitive to the derivative of the refractive index, η'. This sensitivity is shown for the direct shadowgraph technique in figure 3.9a. When the gradient of the refractive index is negative in a plasma, brightening occurs in the beam intensity profile. Where the refractive index gradient is positive in the plasma darkening occurs. This direct imaging technique is impractical for these experiments as the plasma is not expected to be optically thin in all regions and the camera detector requires that the magnification of the beam profile be decreased. Therefore the shadowgraph system used in these experiments is a focused system as described in Settles, 2001 [35] as shown in figure 3.9b.

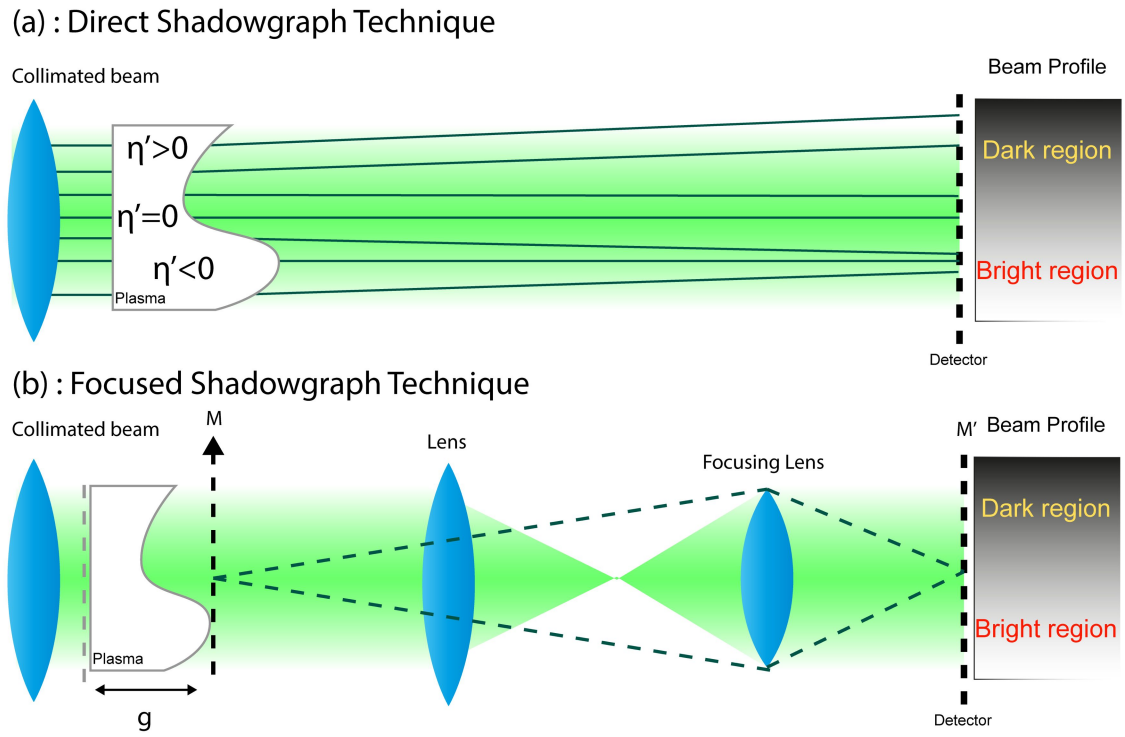

Figure 3.9: A schematic of a shadowgraphy system (a) direct shadowgraph technique (b) the focused system used in the experiments, where the shadowgraph effect at plane M is imaged to plane M'.

The shadowgraph effect is produced in the collimated beam at the object plane marked M in the diagram 3.9b. The collimated beam is then demagnified onto the detector, which would initially seem to loose the shadowgraph information. However, the imaging system is arranged to image the beam at the plane M onto the image plane (or detector plane) M'. The plasma outside of the object plane, by a distance marked as g in the diagram, is out of focus at the image plane, but will contribute to the brightening and darkening of the shadowgraph by the following relation:

$$\frac{\Delta I}{I} = \int g(l) \left[\frac{d^2}{dx^2} + \frac{d^2}{dy^2} \right] \eta dl \tag{3.22}$$

Where I is the beam intensity and l is the path length of the beam through the plasma. This technique requires a strong effect from the second derivative of the refractive index and neither technique is valid for an infinitesimally thin plasma. Further darkening can be caused by very large density gradients in the plasma which deflect the light ray outside of the aperture of the imaging system. This is a schlieren effect, which can be utilised to create a higher sensitivity system than the shadowgraph by the positioning of a knife edge, narrow aperture or block at the Fourier plane of the imaging system. The effects of large gradients can interfere with the analysis of the interferograms (which will be discussed in the next section) by obscuring the fringe pattern. These effects can be minimised by focusing the system as sharply as possible onto the object plane, or by increasing the aperture of the imaging system.

3.2.3.2 Laser imaging interferometry

Laser imaging interferometry can be used to directly measure the areal electron density distribution in the plasma. By a combination of two coherent light sources an interference pattern is produced. When the path length of the two beams is matched, the pattern of bright and dark lines produced in the interference pattern traces the lines of constant phase difference between the two beam paths. When a plasma is placed in the path of one of the two beams, the phase of the light in this beam will be changed with respect to the beam that does not pass through the

plasma. The change in phase is directly related to the free electron density in the plasma.

An example of the experimental interferometry pattern observed is shown in figure 3.10. The pattern of fringes observed before the experiment and during the experiment can be compared to find the 'fringe shift' caused by the presence of the plasma. As the plasma is dominated by free electrons, in the case of this experiment, it will be assumed that the refractive index of the plasma is also dominated by the free electron component.

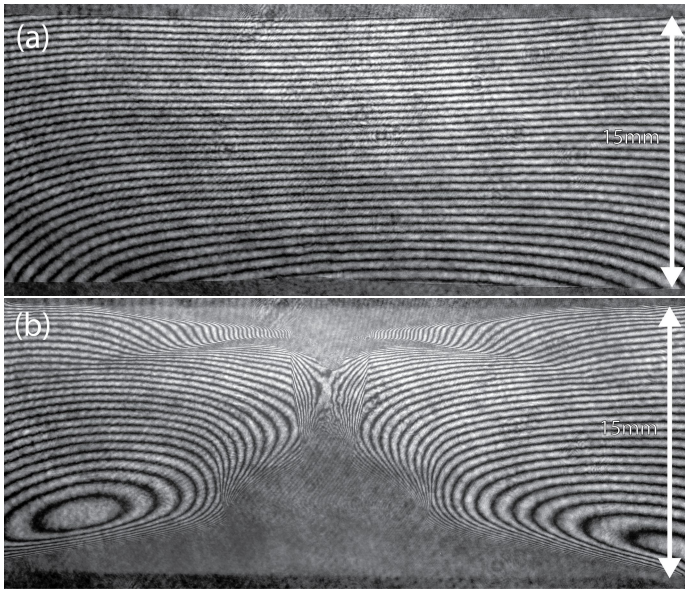

Figure 3.10: The interferometry before the experiment and during the experiment for a 'jet into target' set up which will be described in chapter 5. The image is from experiment s032812.

The interferometry scheme used for the experiments is a Mach-Zender interferometer, a schematic for the Mach-Zender interferometer is shown in figure 3.11. The figure shows the laser beam is split on a beam splitter into two paths of equal length. One of these paths is passed through the experimental load, and is referred to as the probe beam. The other path matches the length of the probe beam but is not passed through the experiment, this is referred to as the reference beam. The two beams are recombined on a beamsplitter and interfere to produced the fringe patterns of constant phase shift shown in figure 3.10a. The recombined beams are then imaged into the camera. In the case of the experiments described in this thesis the exposure

of the image is dictated by the pulse length of the laser, which is ∼500ps.

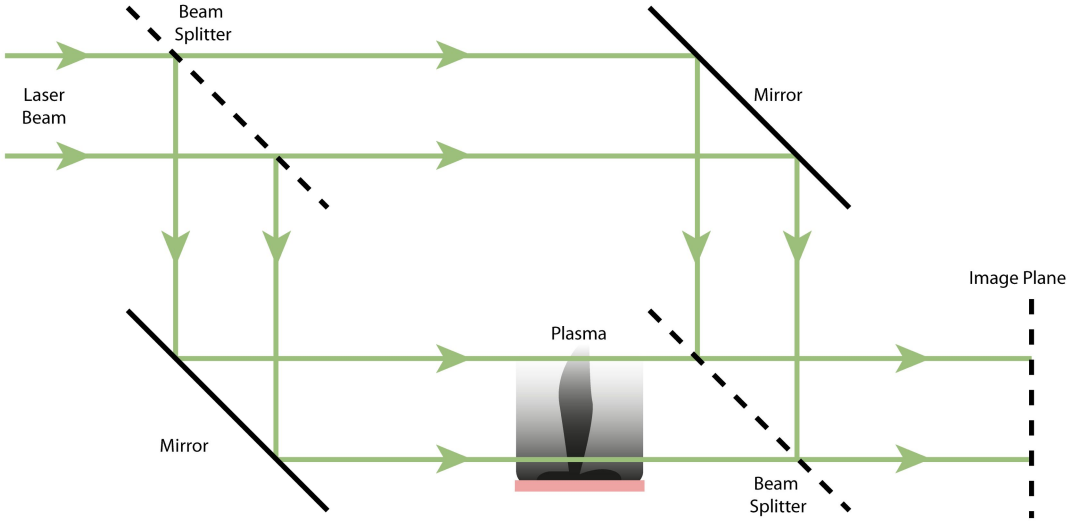

Figure 3.11: Schematic of the Mach-Zender Interferometer.

The remainder of this subsection will mathematically describe the interferometry system. The derivation is in the terms of the electric field component of the laser beam. The general equation of the electric field at the image plane:

$$E = E_0(x, y)e^{i(\omega t)}e^{i(\phi(x,y))} \tag{3.23}$$

$E_0(x, y)$ is a function that describes the cross-section intensity profile of the beam. It is assumed that the probing beam is wide and of constant intensity over the area of interest, so that we can write $E_0(x, y) = E_0$. The function $\phi(x, y)$ describes the spatial variance of the phase shift across the laser beam. For the probe beam, $\phi(x, y)$ is set by the phase delay due to the free electron density in the plasma. For the reference beam it is set by the shearing angle, θ_s, which is the angle by which the reference and probe beams are misaligned. Both beams lie in the x-z plane. If it is assumed that the shearing angle is small, then the reference beam phase is given by:

$$\phi_{ref}(y) \cong ky\theta_s \tag{3.24}$$

The combination of the reference and probe beam on the beamsplitter sets the intensity recorded at the image plane by the superposition of the reference and probe

beam electric fields:

$$E_{Total} = E_{Probe} + E_{Reference} \tag{3.25}$$

$$E_{Total} = E_0 e^{i(\omega t)} e^{i(\phi_{plasma}(x,y))} + E_0 e^{i(\omega t)} e^{i(ky\theta_s)} \tag{3.26}$$

$$E_{Total} = E_0 e^{i(\omega t)} (e^{i(\phi_{plasma})} + e^{i(ky\theta_s)}) \tag{3.27}$$

The detector is sensitive only to the light intensity, which is a function of the electric field at the detector. This is found by:

$$I = \langle E^2 \rangle = EE^* = E_0^2 (e^{i(\phi_{plasma})} + e^{i(ky\theta_s)})(e^{-i(\phi_{plasma})} + e^{-i(ky\theta_s)}) \tag{3.28}$$

$$I = E_0^2 (2 + e^{i(ky\theta_s - \phi_{plasma})} + e^{-i(ky\theta_s - \phi_{plasma})}) \tag{3.29}$$

$$I = 2E_0^2 (1 + cos(ky\theta_s - \phi_{plasma})) = 4E_0^2 cos^2 \left(\frac{ky\theta_s - \phi_{plasma}}{2} \right) \tag{3.30}$$

The fringes are observed to be dark when the intensity is zero (such that the two beams deconstructively interfere). This allows the position of the fringes to be calculated as follows, where n is the fringe number:

$$\frac{ky\theta_s - \phi_{plasma}}{2} = \pi \left(n + \frac{1}{2} \right) \tag{3.31}$$

$$y = \frac{\pi(2n+1)}{k\theta_s} + \frac{\phi_{plasma}(x,y)}{k\theta_s} \tag{3.32}$$

For a background image where no plasma is present, $\phi_{plasma} = 0$, resulting in straight fringes separated by $\frac{2\pi}{k\theta_s} = \frac{\lambda}{\theta_s}$. Fringe density increases with the shearing angle. When the plasma is in the path of the probe beam, these fringes will be distorted by ϕ_{plasma}. The displacement of the fringes observed in the image with plasma present in comparison to the background image, where no plasma is present, is proportional to the spacing of the fringes, i.e. a small fringe spacing produces a smaller fringe shift.

The difference in phase shift between the probing and reference beam is related to the areal refractive index perceived by the two beams:

$$\Delta\phi = \phi_{probe} - \phi_{plasma} = \int_l \frac{\omega}{c}(\eta_{probe} - \eta_{reference})dl \tag{3.33}$$

As the reference beam is propagating through air, the refractive index, $\eta_{reference}$ is equal to 1. The refractive index for the probe beam is equal to the refractive index of the plasma. The phase difference between the two beams can then be written as:

$$\Delta\phi = \int_l \frac{\omega}{c}(\eta_{plasma} - 1)dl \tag{3.34}$$

The refractive index was shown previously to depend on the electron density, n_e and the cut off density, n_c such that $\eta_{plasma} \approx 1 - \frac{n_e}{2n_c}$. The phase difference is then given by:

$$\Delta\phi = -\frac{\pi}{\lambda n_c}\int_l n_e dl \tag{3.35}$$

The displacement of the fringe, F, for the 532nm interferometer using the previously calculated n_c, is related to the phase shift by:

$$F = \frac{\Delta\phi}{2\pi} \approx 2.37 \times 10^{-18}(\int_l n_e dl[\mathrm{cm}^{-2}]) \tag{3.36}$$

$$F \times 4.2 \times 10^{17} = \int_l n_e dl[\mathrm{cm}^{-2}] \tag{3.37}$$

This gives a lower limit of sensitivity to the interferometry system, such that if a fringe is displaced by a fringe shift of 1, it will be equivalent to an electron density along the line of sight of $\sim 4.2 \times 10^{17}[\mathrm{cm}^{-2}]$.

The interferograms produced during the course of the experiments were analysed with a processing code for MATLAB written by Dr. G.F. Swadling. The details of processing the interferograms to find the electron line density map is given in appendix A.

Abel inversion The interferometry system looks side on at the experimental load. With this viewing angle a cylindrical symmetry observed in the experiment can be used to find the radial dependance of the electron density using an Abel

inversion. This is an algorithm that can convert from the line integrated density plot, $n_e l$ and find the density distribution that would have created it in n_e.

The basic form of the Abel inversion is given by equation 3.38 for a density function with cylindrical symmetry $f(r)$, which is integrated in the line of sight l, giving the line integrated function, $F(y)$:

$$F(y) = 2\int_y^\infty \frac{f(r)rdr}{\sqrt{r^2 - y^2}} \tag{3.38}$$

The inverse of the Abel inversion is given by equation 3.39. In the case of the interferometry, $n_e l$ can be substituted for $F(y)$ and n_e for $f(r)$.

$$f(r) = -\frac{1}{\pi}\int_r^\infty \frac{dF(y)}{dy}\frac{dy}{\sqrt{r^2 - y^2}} \tag{3.39}$$

A numerical version, written in MATLAB, of the Abel transform written by Dr. F. Suzuki-Vidal was used in the processing of the interferograms generated in the course of the experiments. This is applied to the electron density map produced from the MATLAB code written by Dr. G.F. Swadling. The Abel transform code relies on the user to select the correct line of symmetry for the experiment, and then calculates the left hand and right hand of the $n_e l$ map separately.

Experimentally the calculation of the $n_e l$ map can result in localised large fluctuations due to the iteration between the lines of constant phase, discussed in appendix A. These fluctuations can result from large density gradients in the plasma that may cause the distance between phase lines to be locally much larger than the 'background' spacing. In this case, $F(y)$ also fluctuates which can lead to the numerical calculation appearing to jump and over or under estimate the electron density n_e. Where this is the case the data has been omitted from the experimental electron density profiles, and the effects have been mitigated by averaging the $n_e l$ map prior to performing the Abel inversion. Where there is a high, but asymmetric, localised density on the axis of the inversion (such as in the body of the jet) the effect of over or under estimation is very pronounced.

3.2.4 Thomson scattering

The Thomson scattering diagnostic takes advantage of the collective effects of the ions and electrons in the plasma when they interact with an intense light source to give spatially and temporally resolved localised plasma parameters i.e. temperatures and velocities. The Thomson system requires a monochromatic and powerful probe laser which is delivered by the CERBERUS laser system. The CERBERUS laser is a 532nm Nd:Yag laser with a ∼4J, ∼7ns pulse. The probe laser is then focused to a spot size of $\sim 500 \mu m$ at the centre of the discharge chamber. During the experiment the laser light is scattered from the plasma. This scattered light is observed by a set of fibre optics which are used in conjunction with an optical spectrometer to record the spectrum of the scattered light. By comparing the observed scattered spectrum to the spectrum of the laser when no plasma is present, the shift in mean frequency and broadening can be analysed to find the velocity of the probed plasma and the plasma temperature.

This section will discuss the theory of the scattering system, and the specific instrumental set-up will be described in the relevant results chapter (section 4.4 and 5.4.3). The theory presented here provides the basis of a MATLAB code written by the author, which allows fitting to the experimentally observed spectrums with modelled scattering spectrums. This code will be used extensively in the analysis of the experimentally acquired data to find the ion and election temperatures.

The theory of the Thomson scattering will be broken into two parts. The first will discuss the origin of broadening in the scattered spectrum. The second will discuss the measurement of velocity of the plasma volume. The system discussed here is assumed to be a fully ionised plasma and the observed scattering is the result of interference between all scattering particles. The ions are much heavier than the electrons and their wave-induced acceleration is negligible. Only scattering from the electrons has to be considered.

The cross-section for the Thomson scattering is assumed to be small, and as such multiple scattered EM waves can be neglected. The Thomson cross section for the system is given below where r_0 is the electron radius [36].

$$\sigma_{Th} = 8\frac{\pi}{3}r_0^2 = 0.655 \times 10^{-24} cm^2 \tag{3.40}$$

3.2.4.1 Plasma temperature and ionisation from the scattered spectrum

The Debye length λ_D, in the plasma sets a characteristic length which determines how the light of the probe beam will interact with the electrons and ions constituting the plasma. For a plasma in thermal equilibrium the charges are randomly distributed within the scattering volume. The ratio of the wavelength of the probe beam λ_0, to the Debye length of the plasma determines if the EM field of the probe will scatter 'incoherently' or 'coherently'. Incoherent scattering occurs when $\lambda_0 < \lambda_D$, the electrons do not interfere with each other and no collective behaviour is seen in the spectrum. When $\lambda_0 > \lambda_D$ the EM field of the laser interacts with the shielded ions and electrons in a collective manner, hence the term coherent scattering. The nature of the scattering in a plasma is characterised though the alpha parameter shown in equation 3.41. When $\alpha > 1$ the scattering is coherent and the converse is the incoherent regime. Both regimes can be described by a single set of equations that use α as a dependant factor [37, 38].

$$\alpha = \frac{1}{k_D \lambda_D} \approx \frac{\lambda_0}{4\pi\lambda_D sin\frac{\theta}{2}} \propto \sqrt{\frac{n_e}{T_e}} \tag{3.41}$$

In the incoherent scattering regime the probe beam scatters off single free electrons and the shielding clouds of electrons around the ions. The sum of the individual interactions in this regime, resulting in the scattered spectrum, will be small as the scattering from the individual ion clouds and electrons will tend to cancel. This then means the scattering spectrum is dominated by the movement of the ions. In the coherent scattering regime the scattered field from the electrons and the electron-cloud add, producing a dominating effect as there is little phase difference between their movements.

The scattered spectrum, $S(\vec{k}_s, \omega)$, can be described as the sum of the contributions from the scattering of the electrons, $S_e(\vec{k}_s, \omega)$, and the scattering from the ions, $S_i(\vec{k}_s, \omega)$, such that:

$$S(\vec{k}_s, \omega) = S_e(\vec{k}_s, \omega) + S_i(\vec{k}_s, \omega) \tag{3.42}$$

$S_e(\vec{k}_s, \omega)$ is termed the electron component and $S_i(\vec{k}_s, \omega)$ is termed the ion component, though it will be shown this still depends on electron fluctuations.

The following derivation is a formulation for an idealised scattered spectrum from a weakly coupled, collisionless plasma in thermal equilibrium, with no magnetic field [39]. The derivation is based on the Fourier transform of the charge distribution, n_e, for the electrons in a single species plasma with electron temperature T_e, ion temperature T_i, mean ionisation Z and ion mass M.

These following functions will be used to find the idealised spectrum:

$$\beta^2 = Z\frac{T_e}{T_i}\frac{\alpha^2}{1+\alpha^2} \tag{3.43}$$

The equation below is also known as Dawson's integral or the error function:

$$f(x) = 2xe^{-x^2}\int_0^x e^{t^2}dt \tag{3.44}$$

$$\Gamma_\xi(x) = \frac{e^{-x^2}}{[1+\xi^2(1-f(x))]^2 + \pi\xi^4x^2e^{-2x^2}} \tag{3.45}$$

The above theoretical functions are defined for two non-dimensional frequencies, x_e and x_i, for the electron and ion respectively, where k_B is Boltzmann's constant:

$$x_e = \frac{\omega - \omega_0}{\sqrt{2k_s^2k_BT_e/m_e}} \tag{3.46}$$

$$x_i = \frac{\omega - \omega_0}{\sqrt{2k_s^2k_BT_i/m_i}} \tag{3.47}$$

$\omega - \omega_0$ is the frequency shift, where ω_0 is the frequency of the incident EM wave. The theoretical scattering functions are given by:

$$S_e(\vec{k}_s, \omega) = \frac{1}{\sqrt{\pi}}\frac{n_e}{\sqrt{2k_s^2k_BT_e/m_e}}\Gamma_\alpha(x_e) \tag{3.48}$$

$$S_i(\vec{k}_s, \omega) = \frac{Z}{\sqrt{\pi}}\left(\frac{\alpha^2}{1+\alpha^2}\right)^2\frac{n_e}{\sqrt{2k_s^2k_BT_e/m_i}}\Gamma_\beta(x_i) \tag{3.49}$$

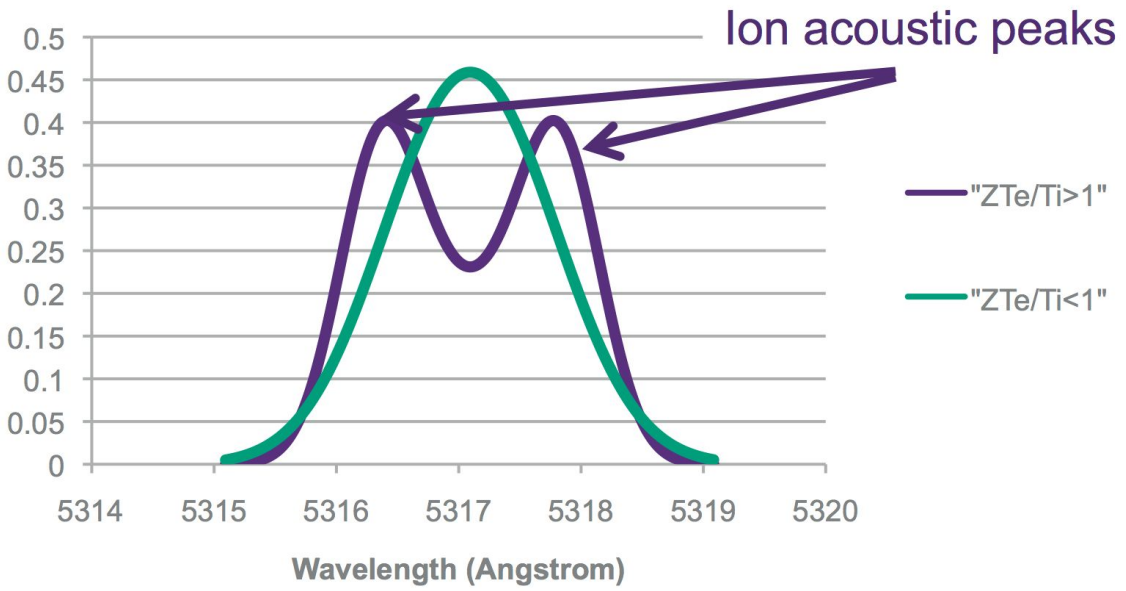

Figure 3.12: A comparison of the generated spectrums in two different regimes. When $ZT_e > T_i$ the electron component of the scattering is dominant. This results in a spectrum with a double peak, referred to as 'ion acoustic peaks'. When this effect is highly pronounced then alpha is also large.

Figure 3.12 shows the extreme of the two scattering regimes. Where α is low the scattered spectrum is Gaussian like and broad. Where α is large the spectrum become split, forming two peaks.

3.2.4.2 Macroscopic flow velocity measurements

The electrons in a plasma have a velocity with respect to the lab frame of reference, whether this is thermal or there is an additional bulk velocity. From the electron frame of reference the incident EM wave from the probe laser is Doppler shifted. As the electron is moving, the re-emitted wave will also be Doppler shifted. This is the case for every electron in the plasma, such that the cross section of electrons with their individual velocities will Doppler shift the mean frequency of the incident beam they interact with. When there is no bulk velocity in the plasma the thermal velocity of the electrons will tend to cancel resulting in an unshifted mean wavelength for the scattered light. However when the electrons are moving collectively with a bulk velocity this will result in a shifted scattered spectrum. The Doppler effect

will be shown for a single electron initially and then the working equations for the measurement of the bulk velocity from a scattered spectrum will be given.

Figure 3.13 shows a general system of scattering for a probe beam with wave vector $\vec{k}_{in}$ and observed scattering with wave vector $\vec{k}_{out}$. The observation of the scattering is at an angle $\theta = 180° - 2\chi$ from the probe beam. The coordinate system is arranged such that the x axis bisects $\vec{k}_{in}$ and $\vec{k}_{out}$. χ is the angle between the probe beam and the x-axis. The electron velocity, $\vec{V}$ is in an arbitrary direction in the x,y plane with its projection onto the x and y coordinate axis marked.

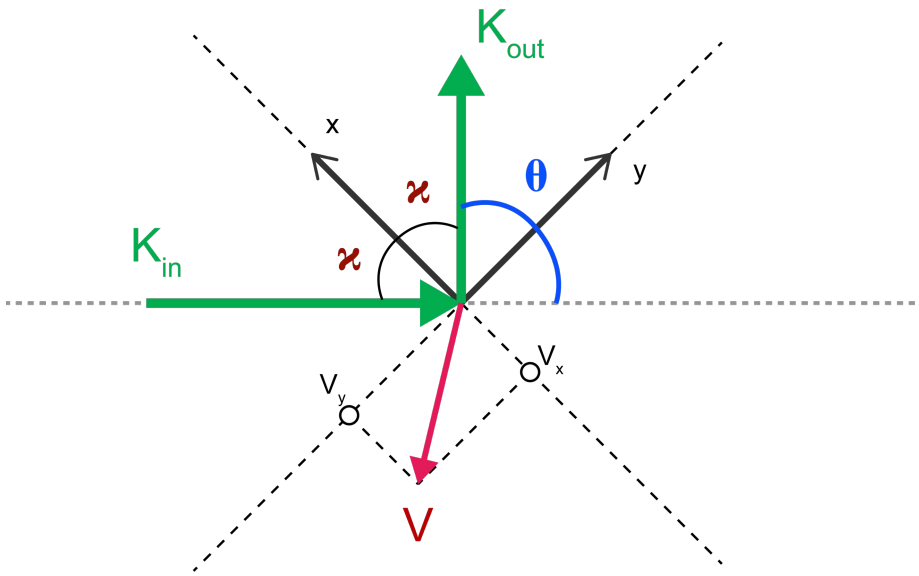

Figure 3.13: Wave scattering in 2D from a single moving electron with velocity $\vec{V}$ and an incident wave vector $\vec{k}_{in}$.

The probe beam wave vector is given by the dispersion relation for EM waves in plasmas:

$$\omega_0^2 = \omega_p^2 + \vec{k}_{in}^2 c^2 \tag{3.50}$$

Where ω_0 is the probe beams angular frequency and ω_p is the plasma frequency. The above relationship can be rearranged to express k_{in} as:

$$k_{in} = \frac{\omega_0}{c}\sqrt{1 - \left(\frac{\omega_p}{\omega_0}\right)^2} \tag{3.51}$$

This gives a density effect on the change for the probing laser wavelength. For a plasma density of $n_e \approx 5 \times 10^{18} cm^{-3}$ and laser wavelength of λ_0=532nm then the above can be evaluated to find:

$$\begin{aligned} k_{in} &\approx 0.9994 \frac{\omega}{c} \\ &\approx \frac{\omega_0}{c} \end{aligned} \tag{3.52}$$

This implies that the typical densities observed during an experiment allow the effect of plasma electron density on the wavenumber of the probe beam to be neglected. The norm of $\vec{k_{in}}$ is defined as $k_{in} = \frac{\omega_0}{c}$.

From the reference frame of the moving electron with velocity $\vec{V}$, an incident wave with shifted frequency ω' is observed:

$$\omega' = \omega_0 - \vec{k_{in}} \cdot \vec{V} \tag{3.53}$$

The Doppler shift for the wave is then given by:

$$\vec{k_{in}} \cdot \vec{V} = k_{in}(-v_x \cos(\chi) + v_y \sin(\chi)) \tag{3.54}$$

The moving electron then re-emits a wave at the shifted angular frequency ω_{out}:

$$\begin{aligned} \omega_{out} &= \omega' + \vec{k_{out}} \cdot \vec{V} \\ &= \omega_0 + (\vec{k_{out}} - \vec{k_{in}}) \cdot \vec{V} \end{aligned} \tag{3.55}$$

Where the Doppler shift is given by:

$$\vec{k_{out}} \cdot \vec{V} = k_{out}(-v_x \cos(\chi) + v_y \sin(\chi)) \tag{3.56}$$

Total doppler shift is therefore:

$$\begin{aligned} \Delta\omega &= \omega_{out} - \omega_0 \\ &= (\vec{k_{out}} - \vec{k_{in}}) \cdot \vec{V} \\ &= \vec{k_s} \cdot \vec{V} \end{aligned} \tag{3.57}$$

Where $\vec{k}_s$ is the scattering wave vector, given by $\vec{k}_s = \vec{k}_{out} - \vec{k}_{in}$ and shown graphically in figure 3.14.

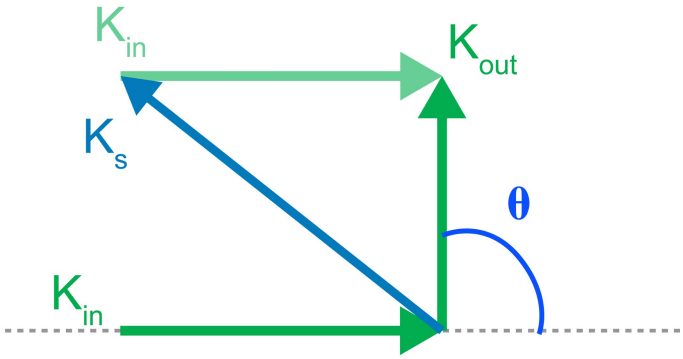

Figure 3.14: The direction of $\vec{k}_s$ from $\vec{k}_{out} - \vec{k}_{in}$ shown graphically

When the doppler shift is small $\vec{k_{in}} \approx \vec{k_{out}}$ then:

$$\begin{aligned} \vec{k_s} \cdot \vec{V} &\approx k_{in} 2 v_x \cos(\chi) \\ &= \frac{\omega_0}{c} 2 v_x \sin\frac{\theta}{2} \end{aligned} \tag{3.58}$$

The frequency shift comes from a component of velocity along the $\vec{x}$ axis in the direction of the scattered wave vector $\vec{k_s}$. When the plasma has a bulk velocity then equation can be used to find the bulk velocity of the plasma volume from the observed shift in the mean frequency of the scattered spectrum in comparison to the mean frequency of the probe laser.

The observed scattered spectrums will be measured on a spectrometer by their wavelength and not their frequency. The above equation can be rewritten for the shifted wavelength, $\Delta\lambda$ of the observed spectrum. $\vec{k}$ is related to the wavelength λ such that $k = 2\pi/\lambda$ and $k = \omega/c$, where c is the speed of light. Equation 3.58 can be rearranged for a scattering angle $\theta = 90°$ and a working equation for the scattering experiment can be found:

$$\Delta\omega = \frac{4\pi}{\lambda_0}\frac{1}{\sqrt{2}} \cdot v_x \tag{3.59}$$

$$\omega = \frac{2\pi c}{\lambda}$$
$$\Delta\omega = \frac{2\pi c}{\lambda_0^2}\Delta\lambda \tag{3.60}$$

$$\Delta\lambda = \frac{2\lambda_0}{\sqrt{2}} \cdot \frac{v_x}{c} \tag{3.61}$$

3.2.5 Self-emission imaging of the plasma

The plasma will emit in a range of frequencies from optical to hard X-ray depending on the temperature and density in the plasma body. The plasma will not uniformly emit in any one frequency as the density and temperature varies across the plasma produced in the experiment both spatially and in the time evolution of the plasma. Time and spatially resolved imaging techniques are therefore useful in diagnosing the development of the plasma as the current is discharged in the experimental load. The experiments that are discussed in this thesis will not emit in the hard X-ray spectrum as the density and temperature of the plasma will not produce sufficiently high ionisation. Two imaging systems will be discussed that take a series of time resolved images of the plasma during a single experiment in optical or XUV emission.

3.2.5.1 Optical imaging system

The optical imaging system uses a set of achromatic lenses to image the self-emission from the array on to a fast-framing camera. The fast-framing camera is controlled through a programmed interface that allows 12 images to be taken with a user defined exposure and inter-frame spacing. The gain of the camera can also be adjusted to ensure good contrast of the images. For the experiments discussed here a typical set up used a 5ns exposure and a 30ns inter-frame spacing which allows a 330ns time period of the experiment to be observed. The camera software can be independently timed to trigger at any point in the experiment.

3.2.5.2 XUV imaging system

The XUV imaging system cannot use traditional optics, as used in the optical imaging system, as the glass and coatings of the optics will absorb the XUV radiation. A demagnifying pinhole system is used to image the experimental load and coupled to a micro channel plate (MCP) detector with four frames. The use of a pin hole system allows the magnification and spacing of the four images to be easily set and has perfect focus across the image. The exposure of the MCP can be set at 5ns, 10ns or 20ns with an inter frame spacing of 10ns or 30ns. This is achieved though a cable delay from the triggering box to the MCP. The MCP can be independently timed to trigger at any point in the experiment.

The MCP is shown from a manufacturing schematic in figure 3.15 and consists of a series of channels that multiply the number of electrons created when the light is incident on the photo-cathode surface. The intensified electrons then interact with a phosphor and are reconverted into photons on the viewing screen. This image is then captured with a digital SLR though a periscope system. The pinhole and MCP system is sensitive to radiation $>$ 30eV from the plasma, which is limited by the size of the pinhole as the MCP detector alone is sensitive to $>$ 10eV emission. Each of the four frames is independently triggered with a high voltage pulse between 4-6kV. The gain of the MCP is set by the magnitude of the triggering pulse such that it is maximum at the highest triggering pulse.

3.2.6 Localised magnetic field measurements using B-dots

As the current, J, is delivered to the load, the structure of the plasma can create a complex current path. In order to determine the location of the current in the plasma the magnetic field that is induced in a loop by the flow of current can be monitored (through Faradays law). The maximum response from the detector will occur when it is placed perpendicular to the magnetic field it measures. Using a loop of wire the magnetic field will induce a current in the loop that can then be measured on an oscilloscope.

This diagnostic can be fielded close to the array when appropriately shielded and

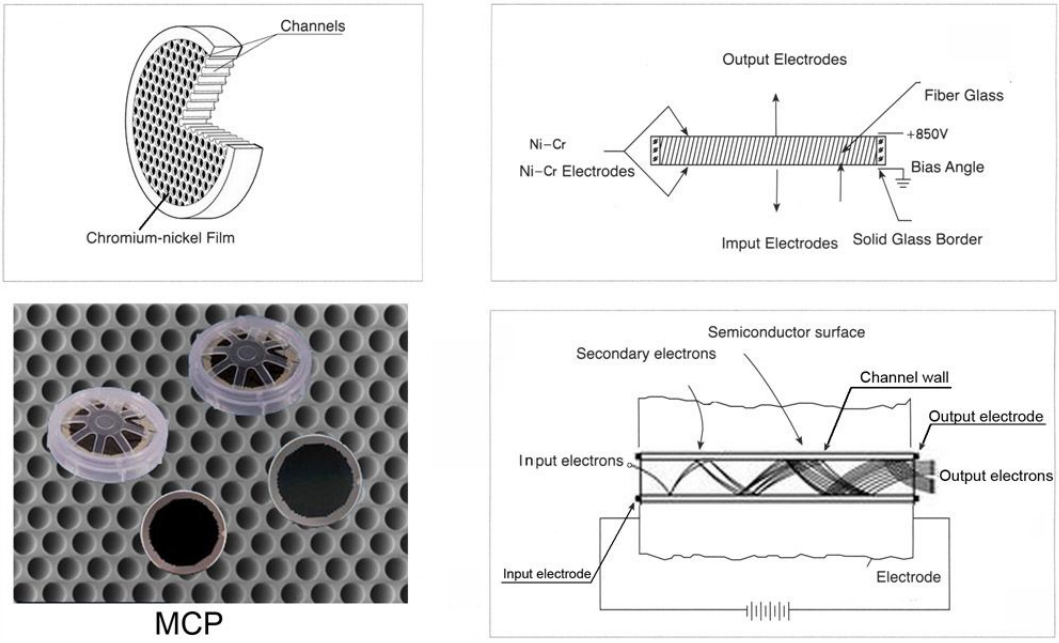

Figure 3.15: Manufactures graphic showing the function and structure of microchannel plate photo multiplier. The top left image shows a sketch of the channels, the top right image shows the application of the bias to the plate, the bottom left image is an electron microscope image of the MCP and the bottom right image shows the multiplication of electrons along one channel.

is termed a 'B-dot' probe. This name is derived from the notation of the first time differential of the magnetic field vector, $\dot{\vec{B}}$.

$$\text{Faradays Law: } \Phi_B = \iint \vec{B}(\vec{r},t) \cdot d\vec{A} \tag{3.62}$$

The following equations describe the signal seen on an oscilloscope for a N turn B-dot of area A. Φ represents the magnetic field flux and is time dependant, V is the induced voltage.

$$V = -\frac{d\Phi(t)}{dt} \tag{3.63}$$

$$\Phi(t) = \Phi_B = \iint \vec{B}(\vec{r},t) \cdot d\vec{A} = NA\vec{B}_{\perp}(t) \tag{3.64}$$

$$\frac{d\vec{B}_{\perp}(t)}{dt} = -\frac{1}{NA}V(t) \tag{3.65}$$

During the development of the plasma system the current measurement from a B-dot probe can become capacitively coupled to $\vec{E}$ fields in the plasma. This effect can be mitigated in analysis by subtracting the signal of a B-dot probe that is 'counter coiled', i.e. the opposite coiling or turning direction. The signal from these two probes will be of opposite polarity but any capacitive effects will remain the same polarity.

When fielding a B-dot inside a plasma the probe is susceptible to electrical fields from free charges. This can firstly be mitigated with use of good insulation (Kapton) and good grounding of the outer conductor. Further improvements in the shielding using a metal of high resistivity and low magnetic μ_0 such as NbCr or NbTi foil $<5\mu m$ thick, which is permeable to the magnetic field but impermeable to electric field, are of use when the probe is placed in a plasma flow.

3.2.7 The Faraday Cup

In order to detect the presence of an electron beam a modified Faraday cup can be used. A Faraday cup detects the overall transmission of electrons as a current with no sensitivity to the energy distribution within the electron beam. The Faraday cup can also be made with very low inductance allowing for sensitivity on the nanosecond time scale. When used in combination with a foil, the energy spectrum of the electrons can be discerned as the foil will absorb lower energy electrons depending on its material and thickness. One foil will not discern the energy spectrum of the incident beam, however a series of foils can be used and the current on the surface of each foil measured. This will allow the calculation, with some uncertainty, of an energy spectrum of the electron beam.

The diagnostic fielded in these experiments was developed by G. Swadling in a MSci thesis investigating the measurement of electrons generated in imploding wire arrays [40]. The Faraday cup consists of a thick metal target that is connected to an oscilloscope via $8 \times 3\Omega$ resistors connected in parallel, shown in figure 3.16. This gives a total resistance of $3/8\ \Omega$. When the electron beam is absorbed on the target a change in voltage is measured by the oscilloscope across the resistors. The voltage

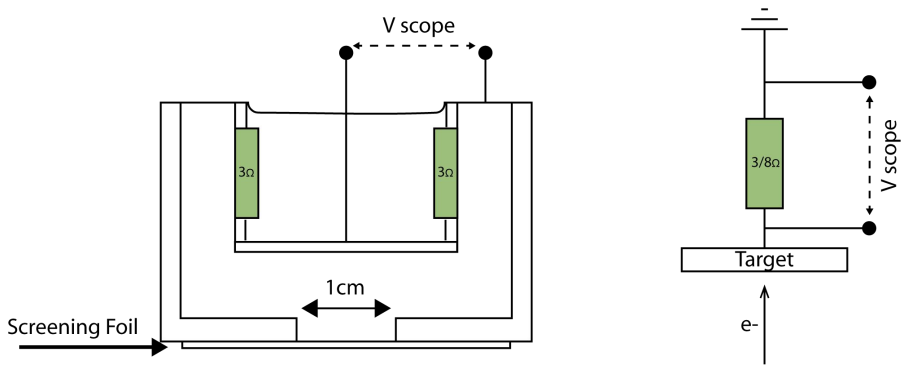

Figure 3.16: Faraday cup scheme used during experiments.

seen by the scope during the experiment is then directly proportional to this current via ohms law ($V = IR$).

By evaluating the diffusion effect due to multiple collisions of the electrons, with the material of the foil and the scattering of electrons from ions, a 'range-energy' relationship can be found which describes the absorption of the electrons within the beam through a material of thickness x [41]. For the energy range of 10-1000keV, the attenuation of a monochromatic electron beam will follow the form of equation 3.66, where I_0 is the initial intensity of the beam with measured intensity I. γ is given by $\gamma = \frac{2.97}{5\times 2^{5/3}} Z^{2/3}$.

$$\frac{I}{I_0} = e^{-\frac{\gamma x}{1-x}} \tag{3.66}$$

This equation can then be used to calculate the observed current density through a foil as seen by the oscilloscope. x is normalised against the maximum penetration of the electron beam into a solid made of the same material as the foil. This is shown in equation 3.67, where R is the range, ρ is the density of the material, E is the energy of the beam, λ_s is an empirically determined constant (see paper by K. Kanaya and S. Okayama [41]).

$$\rho R = \frac{5.025 \times 10^{-12} A E^{5/3}}{\lambda_s Z^{8/9}} \tag{3.67}$$

Taking into account the relativistic electrons the density-range equation follows

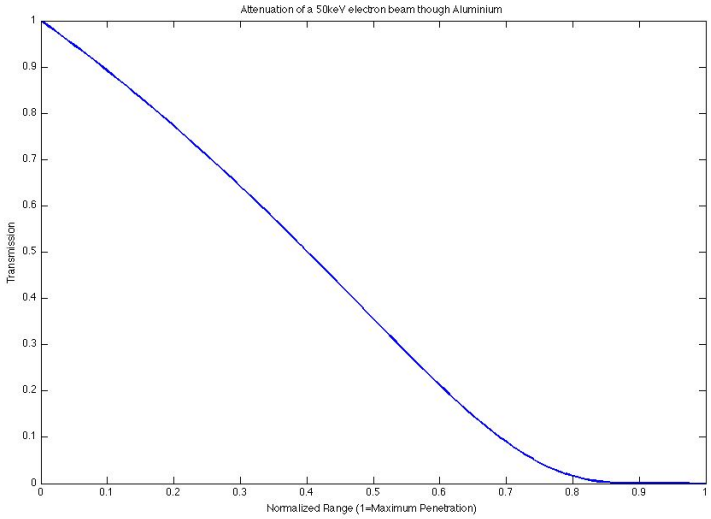

Figure 3.17: Attenuation curve for a 50keV electron beam through Aluminium.

the form in equation 3.68.

$$\rho R = \frac{2.76 \times 10^{-11} A E_0^{5/3}}{Z^{8/9}} \frac{(1 + 0.978 \times 10^{-6} E_0)^{5/3}}{(1 + 1.957 \times 10^{-6} E_0)^{4/3}} \tag{3.68}$$

The attenuation curve can now be plotted against $\frac{x}{R}$ where R will be the foil thickness at which total absorption occurs, shown in figure 3.17. The attenuation curve can be used to find the proportion of the beam absorbed into the foil. By considering the energy deposition near the surface of the foil the temperature rise T, in the material (shown in equation 3.69) can be found. The materials properties of resistivity, χ, and density, ρ, determine the efficiency of the energy deposition.

$$dE = \chi \rho dT \tag{3.69}$$

Chapter 4

Summary of previous investigations on the production of supersonic, radiatively cooled jets

This chapter will introduce the radiatively cooled, supersonic jet propagating in vacuum, produced on the MAGPIE Z-pinch by the discharge of current radially through a thin aluminium foil. The work discussed in this chapter has been published in several peer reviewed journals. The discussion will follow closely the work of F. Suzuki-Vidal et al. in Physics of Plasmas 2012, [42], unless otherwise indicated in the text.

The discussion of these experiments will lay the groundwork for the next three chapters that introduce new experiments using the jet system described here as a tool to drive shocks in a supersonic flow. The produced jet is magnetically driven and hydrodynamic, which is comparable to the astrophysical jets seen from young stellar objects and Herbig-Haro (HH) objects, discussed in chapter 1. The experimentally produced jet is supersonic, with a Mach number >1, well collimated and radiatively cooled.

4.1 Experimental setup

The jet is produced from a thin, $\sim 15\mu m$ circular metallic foil, which has a cathode electrode at its centre and anode electrode at its outer circumference which is 40mm in diameter. The current from the generator is conducted from the anode radially inwards to the cathode tube, hence this arrangement is referred to as the 'radial foil'. Figure 4.1 shows a schematic of the hardware used to create the jet. The hardware is shown in profile with the components labeled, the jet-forming foil is marked in red and the cathode in grey, the current path is marked in green by J.

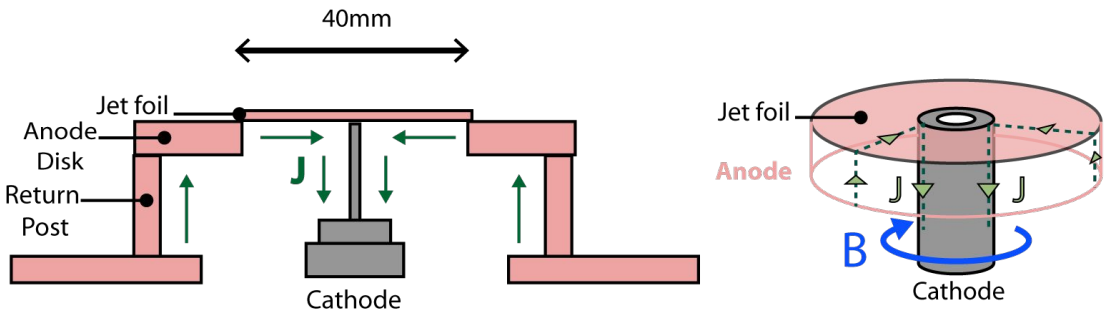

Figure 4.1: Schematic showing experimental setup for the production of jets from radial foils. The direction of current in the jet-forming foil is marked in green.

The cathode is formed from a 6.35mm diameter hollow stainless steel tube that makes electrical contact at the centre of the jet-forming foil. The jet-forming foil is clamped into a concentric pair of rings that forms the electrical anode. The base ring has a raised lip which the foil is tensioned over by attaching the upper ring to the lower ring with a set of small screws that tighten the two rings together forming a clamp. This forms a flat surface on the foil which is highly reproducible and clamps the edge of the foil into the holder ensuring good electrical contact. The assembled foil holder is placed in the anode disk, which is connected to the four current return posts of the hardware and supports the jet-forming foil as it makes contact with the cathode. Electrical contact between the foil surface and the cathode-tube is ensured by pushing the cathode into the centre of the foil forming a slightly raised profile i.e. the centre of the jet-forming foil on the cathode is higher than the edges of the

jet-forming foil by ∼1mm.

Current passes from the outer circumference of the foil to the outer diameter of the cathode-tube as indicated in the figure 4.1. The current produces an azimuthal magnetic field round the cathode-tube under the foil, which is indicated in the diagram. This magnetic field forms the driving force that will produce the jet. The jet is produced above the cathode and propagates perpendicularly away from the foil for >35mm.

The relationship between the foil thickness, jet-forming foil outer diameter and cathode diameter have been explored to fine tune the production of the jet. The outer diameter of the foil and foil thickness will dictate the amount of ablation from the foil and which will control the timing of the jet production, such that smaller foils will produced a jet earlier in time [5]. The current density at the cathode is related to the cathode radius. By decreasing the radius of the cathode the magnetic field under the foil will be increased. This changes the propagation dynamics and stability of the jet by allowing a higher current fraction into the body of the jet [43]. This produces an episodic, magnetically driven jet, [44, 45]. For the investigation of this thesis the parameters of foil thickness and cathode size were not varied from the experimental set up described above.

4.2 Overview of the jet formation and propagation

Figure 4.2 shows an illustration of the jet formation. The jet foil is shown in red with an exaggerated raised cross section between the cathode at the foil centre and the contact at the anode. The current follows the path marked by J, shown in green. When current flows though the foil it initially Ohmically heats the foil causing the foil to be partially converted into a plasma. The current along the cathode produces an azimuthal magnetic field underneath the foil. The magnitude of this field is inversely proportional to the current driven though the foil such that $B \propto \frac{I}{r}$ where I is the current in the foil and r is the foil radius. The foil is sufficiently

thin that a fraction of the magnetic field and current produced underneath the foil can diffuse upwards through the foil and drive the ablation of material from the foil surface, this ablated material is indicated by the brown arrows in the figure. The acceleration of the ablated material perpendicular to the foil surface is driven by the Lorentz $\vec{J} \times \vec{B}$ force resulting from the radial current path along the surface of the foil and the azimuthal magnetic field. The accelerating force on the material is strongest at the cathode as this is where the current density is highest.

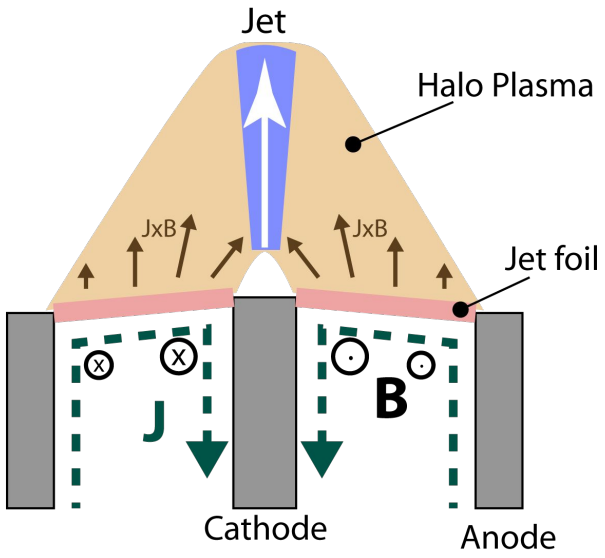

Figure 4.2: The development and acceleration of the jet from the jet-forming foil by the convergence of ablated and accelerated plasma over the cathode.

The ablation from the surface of the foil is reduced in the region directly above the cathode, where r <3.175mm, as there is no current gradient in this region. The ablated material from radii larger than the cathode radius is redirected into the the centre of the foil as shown by the angled brown arrows either side of the cathode in figure 4.2. This redirection of the ablation is due to a lack of thermal pressure directly above the cathode, the redirected flow also causes the $J \times B$ force to be angled inwards as shown by the arrows in the diagram. Stagnation of the plasma at the axis of the foil forms a standing conical shock, which redirects the flow of plasma into a column, in this way forming the jet which is marked in blue on the figure 4.2. The jet will form with a diameter of ∼1mm directly above the cathode, and the surrounding material ablated from the foil forms a 'halo plasma' that is

propagating at the same velocity as the jet.

The production of a jet by a standing conical shock was discussed in Cantó et al. 1988 [46] in the context of an astrophysical jet produced from the re-converging stellar wind of typical T Tauri stars. Numerical simulations of the laboratory produced jets have shown a similar converging flow of plasma which produces a conical shock, thus, confining a jet [19, 20, 24] for jets produced via different mechanisms to the radial foil. In the jet system discussed in this chapter experimental verification of the inward radial flow of material has not previously been performed and will be presented in chapter 5, section 5.3.3 as a new result.

Figure 4.3 shows a series of XUV self emission images showing the development in time of the jet. The sequence of images was taken with a 5ns exposure using the XUV pinhole framing camera described in section 3.2. The position of the cathode is marked in red and a scale of 35mm is marked on the right hand side of the image.

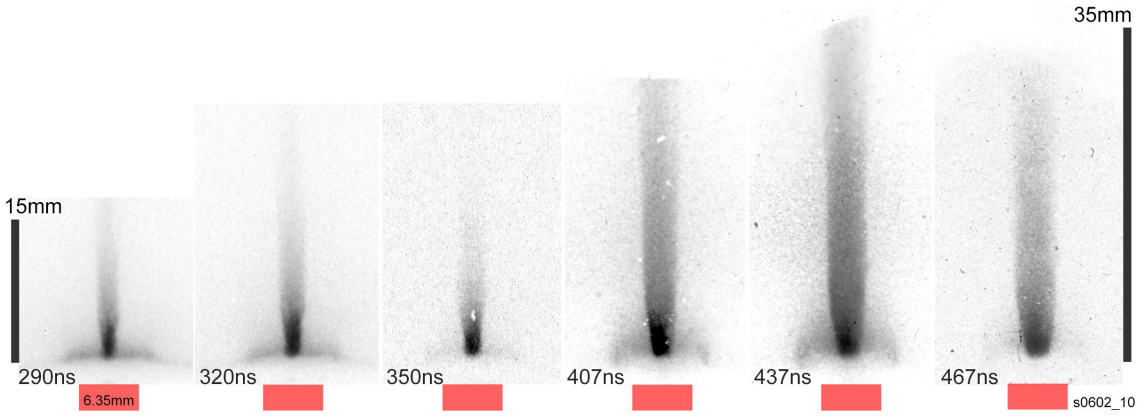

Figure 4.3: XUV self emission images of the jet at six points in its propagation away from the jet-forming foil, which is at the base of the image. The sequence is taken from the same experiment with a 5ns frame exposure. The time after current start is indicated on each frame, time increases from left to right. Image from Suzuki-Vidal et al. 2012 [42].

The jet is seen to have a well defined smooth boundary with no noticeable perturbation in shape or intensity. The jet emerges as a stable column of emission from a region of higher material density which forms at the top of the cathode. The jet is seen to be initially narrower than the cathode, with a diameter of ∼1mm, but expands outwards as time progresses, to a radius of ∼2mm. The emitting region of the jet body expands radially outwards at a velocity of ∼5km/s from the XUV

images in figure 4.3. The time period observed in figure 4.3 covers 177ns, the jet extends 35mm above the cathode by the final image which gives an upper boundary of the axial jet tip velocity from emission of ∼80km/s.

Figure 4.4 is a diagram showing how the opening angle is measured at the base of the jet. The divergence from the jet flow is exaggerated to show that the opening angle at the base of the jet is observed to be larger than at the edge of the jet in its body, which is seen to be parallel with the direction of flow of the jet.

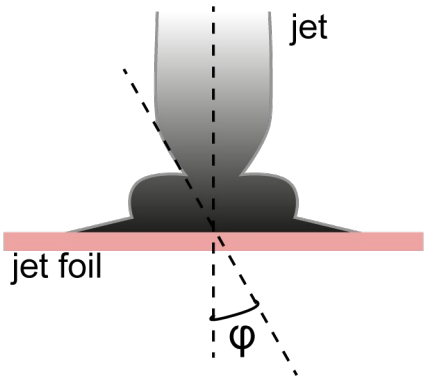

Figure 4.4: Diagram to show how the opening angle, ϕ, is measured at the base of the jet from the XUV self-emission images.

The base of the jet is observed to have an opening angle of $\sim 5°$ for a distance above the foil which is comparable to the diameter of the cathode. The opening angle is then visibly reduced in the body of the jet and is measured to be $\sim 2°$ from the XUV self emission images. The larger opening angle at the base of the jet occurs in the region above the cathode where the ablation from the jet-forming foil is reduced.

4.3 The electron density of the jet

Figure 4.5a shows a 532nm laser interferometry image taken at 429ns after the current start. The jet is visible with the same shape as observed in the XUV images shown in figure 4.3. The jet has a distinct boundary marked by a shift in the interferometry fringes. The fringes are displaced the most from their original positions at the base of the jet, and less displaced near its tip, indicating a reduction

in density axially away from the jet-forming foil. The dark region at the base of the jet is a region of plasma with high refractive index gradients near the ablated jet-forming foil which the jet emerges from, causing the probe beam to be deflected out of the imaging system.

As described in section 3.2.3.2, laser interferometry is sensitive to the refractive index of the plasma which is proportional to the electron density along the path which the laser beam passes though the system. By comparison of the phase fringes seen before and during the experiment the shift of the fringes from their original positions can be measured. This can be processed, as described in appendix A, to give a two-dimensional electron line density map of the plasma shown in figure 4.5b. Due to the high level of azimuthal symmetry seen in the jet the radial distribution of electron density can be found in the jet with the application of an Abel inversion [47] to find a two-dimensional map of electron density, n_e, shown in figure 4.5c .

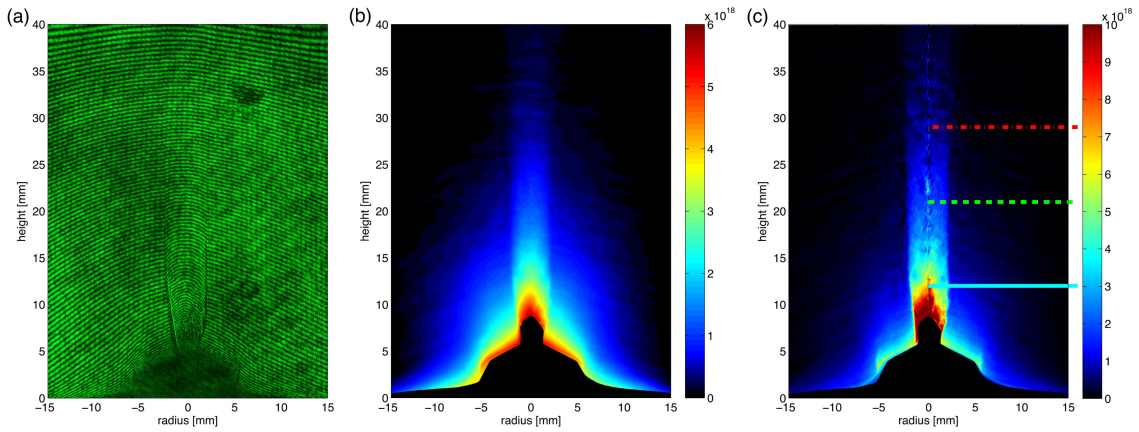

Figure 4.5: 532ns laser interferometry of the jet at 429ns (a), (b) electron line density, $n_e l$ and (c) electron density map n_e. Image from Suzuki-Vidal et.al. 2012 [42].

The electron density map in figure 4.5c shows the density in the jet reduces with height, having the largest density at its base. The electron density in the body of the jet is between 1 to $8\times10^{18}\text{cm}^{-3}$. The jet is accompanied by a halo of lower density plasma, which has an electron density of $\sim1\times10^{18}\text{cm}^{-3}$. The halo plasma is seen to decrease in density with increased distance from the axis of the jet.

4.4 The axial velocity of the jet and temperature of the jet body

The Thomson scattering diagnostic is used to measure the axial velocity of the jet and estimate the ion and electron temperature in the body of the jet. Figure 4.6b shows a schematic for the experimental set up of the Thomson scattering diagnostic using the CERBERUS probe beam. The Thomson scattering diagnostic is described in section 3.2. The probe laser provides a 532nm beam which is focused into the centre of the discharge chamber. The probe laser is focused at the centre of the jet at an axial height of 12mm or 20mm (in separate experiments). The optical fibre head, shown in figure 4.6c is made up of 7, 200μm diameter fibres with a 490μm separation. The scattered light from the laser beam is imaged onto the fibre head with an f=100mm achromatic lens. The magnification of this system allows the fibre head to observe 7 volumes of plasma with a spacing of 1.3mm. The fibres are aligned with respect to the jet as shown in figure 4.6a which allows scattered light from inside the jet body and the halo plasma to be observed.

The scattered light is observed on an optical, time-gated ANDOR spectrometer with an intensified charge coupled device (ICCD) with a gate time of 5ns. The resolution of the observed spectrum is dominated by the diameter of the optical fibres. Prior to the experiments the probe beam is scattered off of an alignment pin which provides a background spectrum at the wavelength of the probe laser. This is used for comparison to the scattered spectrum seen during the experiment and gives the resolution of the spectrometer.

Figure 4.6a shows the relationship between the probe laser wave vector, $\vec{k}_{in}$, and the observed scattered light which has a wave vector, $\vec{k}_{out}$. The observation angle of the optical fibre head is 90° directly above the jet. The velocity of the jet is related to an observed shift in the mean wavelength of the scattered spectrum from the background spectrum. This is related to the scattering vector, $\vec{k}_s$, which has the direction indicated in figure 4.6a, by the relationship $\Delta\omega = \vec{k}_s \cdot \vec{v}$ where ω is frequency and $\vec{v}$ is the velocity of the plasma volume. The measured velocity is the projection of the volume's velocity along the scattering vector $\vec{k}_s$. This system

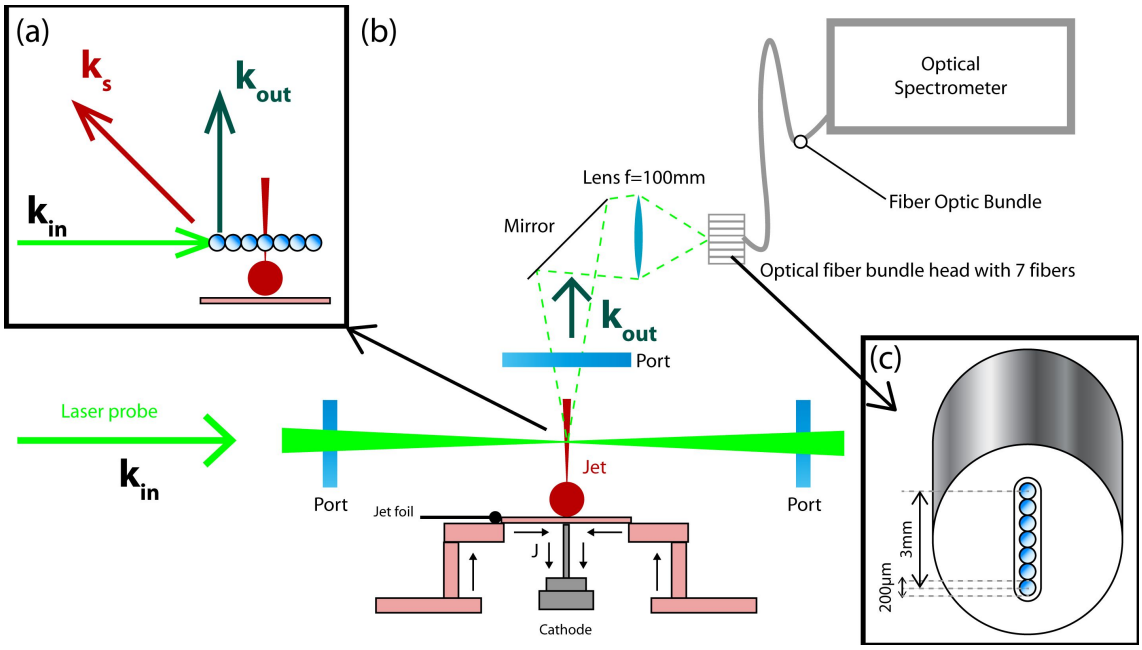

Figure 4.6: The experimental set up for the Thomson scattering measurement of the jet velocity. (a) the direction of the scattering vector and the alignment of the fibre to the jet. (b) experimental layout in the discharge chamber. (c) fibre optic head and spacing of the individual fibres.

of scattering is therefore sensitive to axial and radial velocities in the plasma. As the jet will move towards the optical fibre head it is expected that the observed scattered spectrum will be blue shifted.

The scattered light observed for the jet velocity experiments is shown in figure 4.7a. The three central positions observed by the fibres are at 1.3mm, 0mm and -1.3mm, which are inside the body of the jet. All of the scattered spectrums are observed to be blue shifted by $\Delta\lambda \sim 0.85$Å, this corresponds to an axial flow velocity of ∼50km/s. The scattering observed in the halo plasma is also blue shifted by a similar amount such that the halo plasma is moving at a comparable velocity to the jet body.

The scattered spectra observed inside the jet are broadened due to the collective scattering effect from the electrons in the plasma. Figure 4.7b shows a set of simulated fits applied to the observed scattered spectrum with a variation of electron temperatures. The fit is sensitive to electron temperature, ion temperature and the ionisation of the plasma. The fit is not sensitive to less than order of magnitude changes in the electron density. The electron density for the simulated fit is found

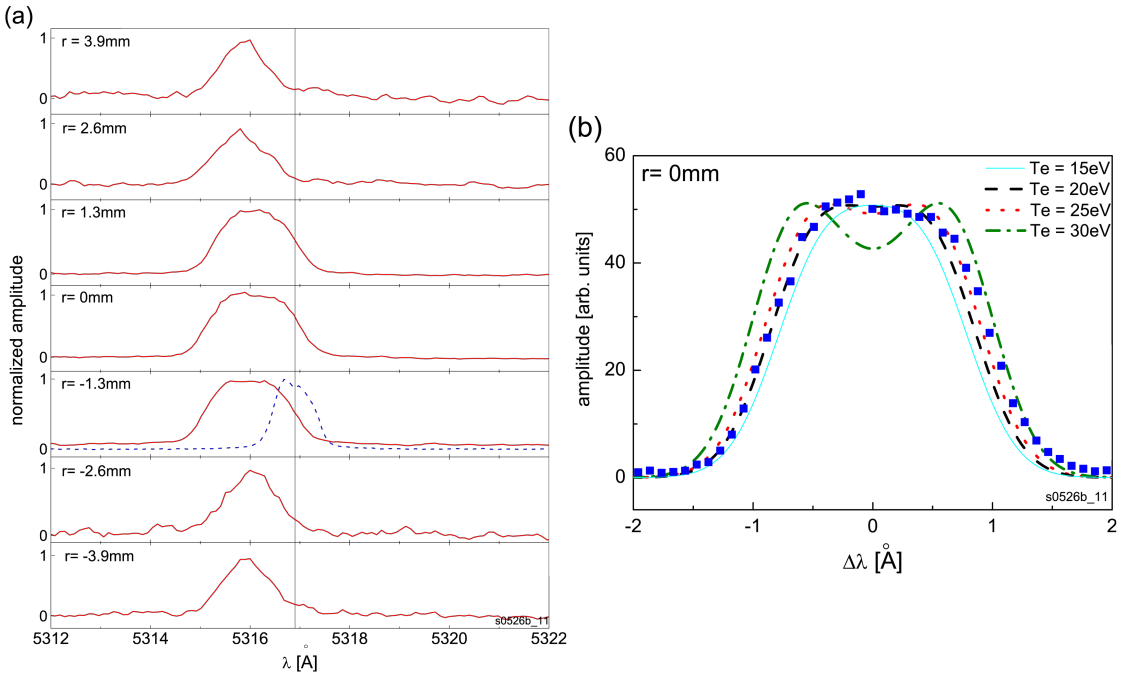

Figure 4.7: (a) scattered light observed by the optical fibres. The background spectrum is indicated at the radial position r=-1.3mm. The spectrum is seen to be red shifted. (b) the effect of variation in electron temperature T_e on the calculated fit to the measured broadened spectrum. The best fit is found to be $T_e = 25eV$, $T_i = 45eV$ and $Z = 4$. Image from Suzuki-Vidal et al. 2012 [42]

from the interferometry images taken at the same time after current start as the Thomson scattering measurement.

The electron temperature in the body of the jet is found to be ∼15 to 20eV with an ionisation of $Z \sim 4$. The ion temperature in the body of the jet is found to be $\sim 45eV$. The broadening in the halo plasma is not as pronounced but still exceeds the spectral resolution of the spectrometer. Assuming local thermodynamic equilibrium in this region an ion and electron temperature of ∼15 to 20eV is found.

4.5 Numerical simulations of the jet in vacuum

A small number of simulations have been performed attempting to numerically model the jet propagation into vacuum. This was done using the magnetohydrodynamic (MHD) code GORGON [24, 48]. GORGON is an explicit, parallel code designed to solve resistive MHD equations on a three-dimensional Cartesian grid

employing a Van Leer type algorithm. The code treats the plasma as a single fluid but allows different temperatures for the ions and electrons by solving their energy equations separately. The evolution of the system is driven by developing the vector potential, ensuring the magnetic field is solenoidal at all times. As such, the model does not drive a current through the simulated electrodes, but changes the magnetic field boundary conditions at these points to match a selonoidal current with a 250ns rise time.

Figure 4.8a shows a simulation of the jet propagating in vacuum as a density cross section. The location of the magnetic fields is indicated by the blue lines. The simulation reproduces some of the observed features of the jet, however the opening angle of the jet is seen to be slightly larger in the simulation and the collimation does not improve further from the jet base. Figure 4.8b overlays the '$J \times B$' vectors for plasma volumes, shown by the orange arrows in the image, both in the jet and surrounding halo plasma on a density map. The simulation predicts a force directed radially inwards around the jet in the halo plasma. This may correspond to a radial velocity in the halo plasma directed towards the jet axis.

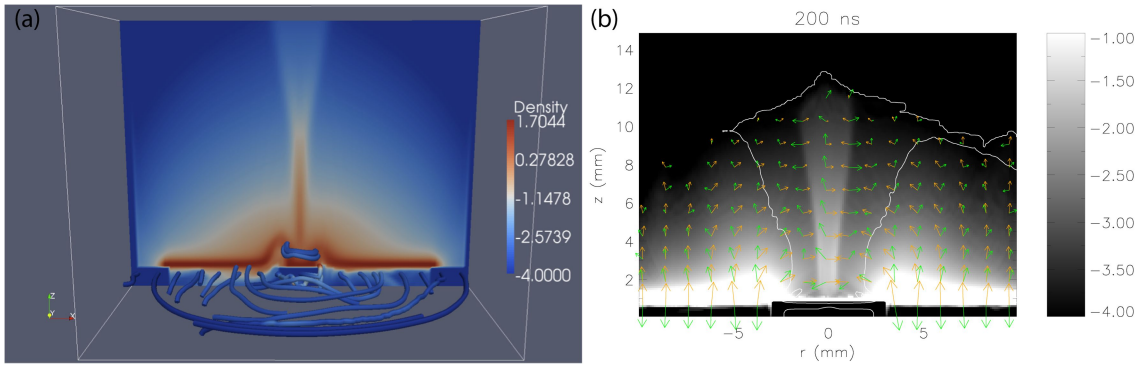

Figure 4.8: (a)A simulation of the jet at 400ns showing the predicted density distribution and the magnetic field lines (in blue) The density scale has red as a higher density than blue and is logarithmic with units of kg/m^3. The simulation treats densities below $\rho = 10^{-4} kg/m^3$ as a vacuum. (b) Orange '$J \times B$' vectors of small plasma volumes over laid on a density map at 200ns. Produced by M. Bocchi.

The velocity of the jet and electron temperature found via the Thomson scattering measurement can be used to calculated the Mach number of the jet. The ion sound speed is found to be ∼20km/s and the axial velocity of the jet is ∼50

to 60km/s. The Mach number, M, is the ratio of the plasma velocity to the ion sound speed, and for the jet this is found to be M ∼2.5 to 3. For such a flow of freely expanding plasma a half-opening angle of ∼ 20° is expected for $M = 3$. The measured half angles were smaller, at 2° to 5°, which would correspond to a much higher internal Mach number between 10 and 30, which is not experimentally observed. The expansion velocity is also expected to be higher than the observed ∼5km/s, as the sound speed calculated is ∼20km/s, which strongly suggests that there is a confinement system present azimuthally around the jet.

Figure 4.9 shows a comparison between the experimentally found electron density at three axial points along the jet from figure 4.5 to the simulation predicted densities. The electron density closer to the jet-forming foil is matched at its peak but the simulation predicts a much narrower jet. The electron density predicted further axially from the jet-forming foil (the green and red curves) is much lower than seen experimentally.

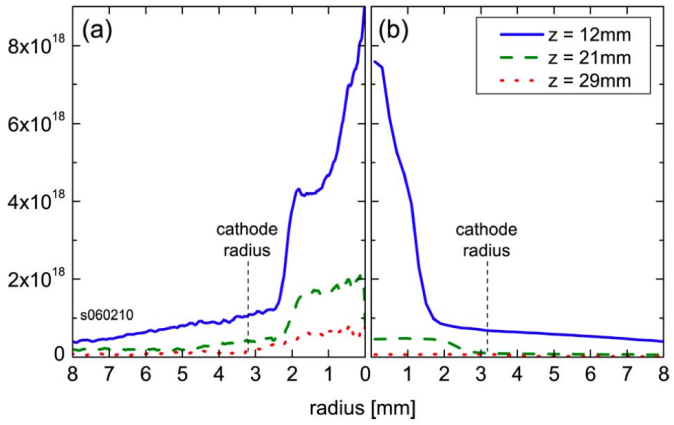

Figure 4.9: (a) Radial profiles from the electron density map shown in figure 4.5. (b) simulated density profiles at the same axial distances from the jet-forming foil. Image from Suzuki-Vidal et al. 2012 [42].

The simulations suggest that the confinement of the central dense body of the jet is provided from the ram pressure of the plasma flow from the foil which is directed at the axis of the jet. This is further reinforced by the presence of a toroidal magnetic field around the body of the jet. The GORGON simulations suggest that a fraction of the current is present in the region above the foil due to the high resistivity in the foil. Measurements of this toroidal field have been made on a different Z-pinch

device, COBRA, based at Cornell University [49] using a similar experimental set up as described above. The experiments however used a smaller cathode and thiner aluminium foil which will allow greater penetration of the magnetic field through the foil due to higher current density. Using a micro B-dot probe (described in section 3.2) azimuthal fields grater than 2kG/ns are measured at early developmental times. This measurement is expected to be larger than in the radial foil configuration as the current density at the cathode will be lower with a larger cathode.

The next chapters will discuss experiments that use the jet discussed in this chapter as a piston to produce a shock in the supersonic flow of the jet and the halo plasma. Effects of current polarity in the jet formation will also be experimentally explored in chapter 6.

Chapter 5

Interaction of a supersonic plasma jet with a thin aluminium foil target

This chapter describes experiments investigating the interaction of a radiatively cooled, supersonic jet with a thin aluminium foil target. The target foil acts as an obstacle to the supersonic flow of plasma in the jet and the surrounding halo plasma which leads to the formation of several shock features. The target foil is at ground potential while the high-voltage is applied to the cathode which is at the centre of the jet-forming foil. The next chapter will discuss the case where the polarity of the current is reversed in the jet-forming foil.

5.1 Experimental set up

A schematic of the experimental set up is shown in figure 5.1. The hardware is rendered in the figure as a schematic with the key elements labeled. The figure also shows a photograph of the hardware in the discharge chamber. In the photograph the target and jet foil can be seen installed in the discharge chamber with the cathode and return posts under the jet-producing foil.

In the schematic of the set up, shown in figure 5.1a, the jet-forming foil is marked in red, the target-forming foil and its holder are marked in green and the cathode is

in grey. The cathode is a hollow stainless steel tube with outer diameter of 6.35mm. The jet foil is positioned with its centre touching the cathode and its perimeter touching the anode disk. The anode disk connects the jet-forming foil to the anode plate via the four return posts. The target is shown suspended above the jet foil via two long posts which are also connected to the anode plate. The distance between the two foils is 15mm. The current driving the formation of the jet follows the path marked by J in figure 5.1, in a manner identical to previous jet into vacuum experiments discussed in chapter 4. A supersonic aluminium jet is formed above the cathode, projected towards the target foil.

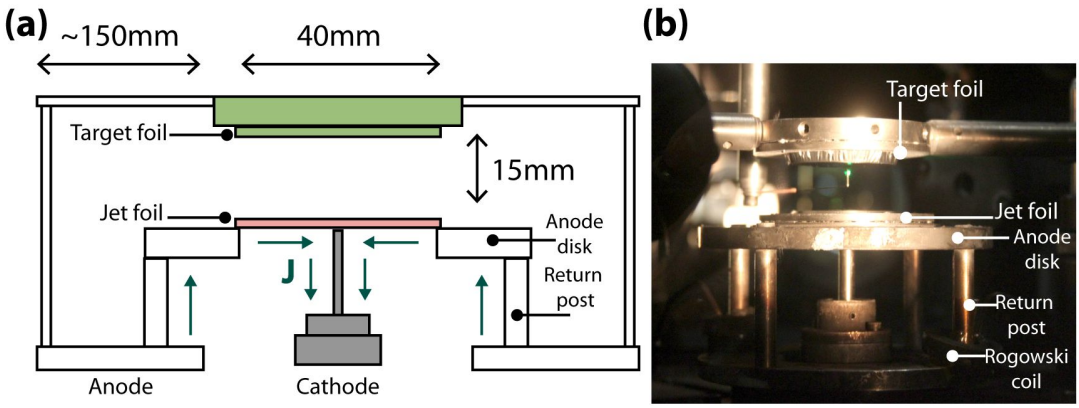

Figure 5.1: (a) schematic of the hardware used for the aluminium jet with suspend aluminium target foil. (b) is a photograph of the hardware in the discharge chamber, taken during the alignment of the Thomson scattering diagnostic (this is described in section 3.2). A 3mm tall, 200μm wide alignment pin can be seen between the target and jet foil, the alignment pin is removed prior to the experiment.

Both jet-forming and target-forming foils are 14μm thick with a diameter of 40mm. This is the same configuration as used during the jet into vacuum experiments. Previous work on the jet into vacuum found the 6.35mm diameter cathode with 40mm outer diameter, 14μm thick foil to reliably produce supersonic radiatively cooled jets, and have been extensively characterised as discussed in chapter 4 [42].

Both the jet and target foil are assembled into the hardware by pressing the foil between two stainless steel disks. A photograph of the assembled foils is shown in

figure 5.2 prior to placement in the discharge chamber. It can be seen in the figure 5.2 that the foil is tensioned between two stainless steel disks which are then fastened together with four M3 bolts. The use of four bolts allows even and controllable tension across the foil as it is clamped. The foil is tensioned over a lip in the lower of the two disks, which protrudes from the lower disk for <1mm in the jet foil and <3mm for the target foil. Assembling the target and jet foils in this manner ensures a flat surface on the foil that is reproducible from experiment to experiment.

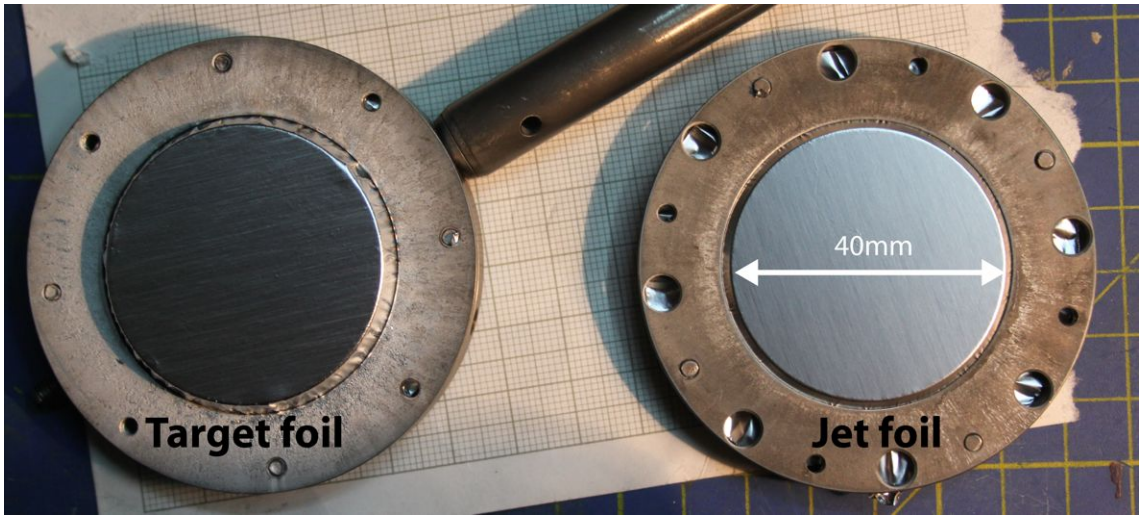

Figure 5.2: The assembled target and jet foils before placement in the discharge chamber.

The jet foil is positioned above the cathode as shown in Figure 5.3. The cathode is pressed into the foil forming a slightly humped profile which is visible in the figure. This is done to ensure good electrical contact between the foil and the cathode. The cathode protrudes <0.5mm above the rim of the hardware forming the jet foil.

The cathode is hollow and forms a cavity leading into the MITL section of MAGPIE (see chapter 3). The jet-forming foil touches the cathode and thus seals this cavity allowing only small gaps between the hardware for the air to be evacuated though. To avoid this, the part of the foil just above the cathode tube is removed, forming a hole on axis of the jet-forming foil of ∼3mm diameter. The removal of the foil allows the chamber to reach suitable vacuum pressure more rapidly than when this cavity is sealed. Experiments performed with and without the hole on axis show no difference in the formation and dynamics of the jet confirming this region of the

foil is not involved in the jet formation.

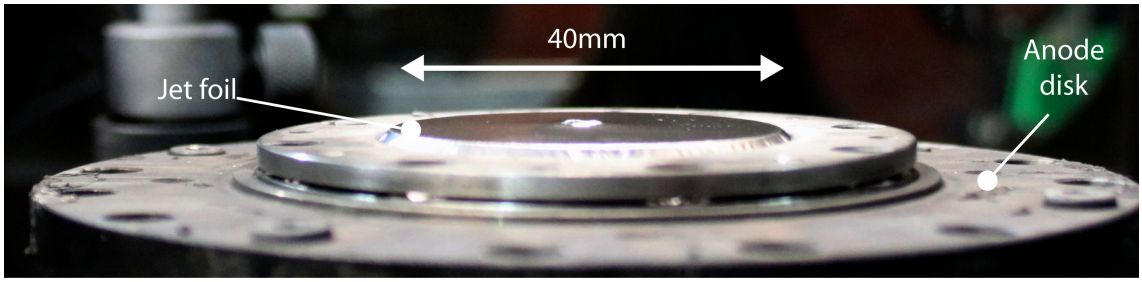

Figure 5.3: The jet foil as assembled in the discharge chamber. At the centre of the foil contact with the cathode is seen.

The jet-forming foil holder is placed in the anode disk which is connected to the generator anode via four brass return posts. A Rogowski coil is placed on two of the return posts (partially visible in figure 5.1b). Each Rogowski coil monitors a quarter of the current driven into the foil, allowing the monitoring of current symmetry in the return hardware. The signals from the coils are then used to determine the shape of the driving current and the start of the current is used as a 'zero ns' time. The timing of all images discussed in the following analysis are given in relation to the determined 0ns for each experiment.

The target-forming foil is positioned 15mm above, and parallel to, the jet-forming foil. The edge of the target foil holder is attached to two stainless steel optical posts by M4 grub screws. The posts are positioned on opposing sides of the foil holder and are clamped at 90 degrees to an height adjustable optical post. The adjustable post is then clamped to the base of the discharge chamber. The base of the discharge chamber is in electrical contact with the ground and at the same electrical potential as the anode of the jet-forming hardware. The adjustable posts are ∼150mm from the edge of the target foil holder which is a larger radius than the anode disk and return posts.

In experiments with the jet propagating into vacuum it was proposed a fraction of the current driving the jet could be present in the plasma above the jet-forming foil [42]. The presence of current above the jet-forming foil was shown primarily though MHD simulation, as was discussed in chapter 4. With the addition of a target above the foil it is possible a fraction of the current could flow into the

target-forming foil through the jet and the halo plasma. Placing the target on long posts in the manner described above increases the inductance between the target foil and the electrical ground. The increase in inductance should reduce the fraction of current flowing into the target. It is possible the variation of this inductance could control the current driven into the target and would be an interesting line of investigation for future experiments.

Twelve separate experiments were conducted with this configuration of foils and a 15mm spacing, varying the timing for the imaging diagnostics and probing time and positions for the Thomson scatting diagnostic. For each experiment the full diagnostic suite, as described in section 3.2 was used.

5.2 Overview of the jet-target interaction observed in the experiments

The fast-framing optical emission camera can be set to produce a series of images over a large interaction period in the experiment, making the fast-framing camera images useful as an overview of the experiment. The fast-framing optical emission camera diagnostic, described in section 3.2.5.1, captures a series of twelve images with a inter-frame spacing and exposure chosen before the experiment. In the case of the images discussed in this section the exposure was set to 5ns and the inter-frame spacing was 30ns. Figure 5.4c is a composite of twenty four images from two experiments charting the interaction of the jet and target-forming foil. The time period shown in the images ranges over 243ns to 708ns from current start in the jet-forming foil.

Figure 5.4a shows the frame taken at 468ns after current start. At 468ns all of the shock structures formed in the interaction of the jet and target foil are visible. These structures are highlighted in the sketch of figure 5.4b. The jet is seen as a vertical column in the middle of the image. Below the jet the dense material from the jet-forming foil appears as a round base which the jet emerges from. At the top of the jet a shock is observed in the flow from the jet moving towards the jet-forming

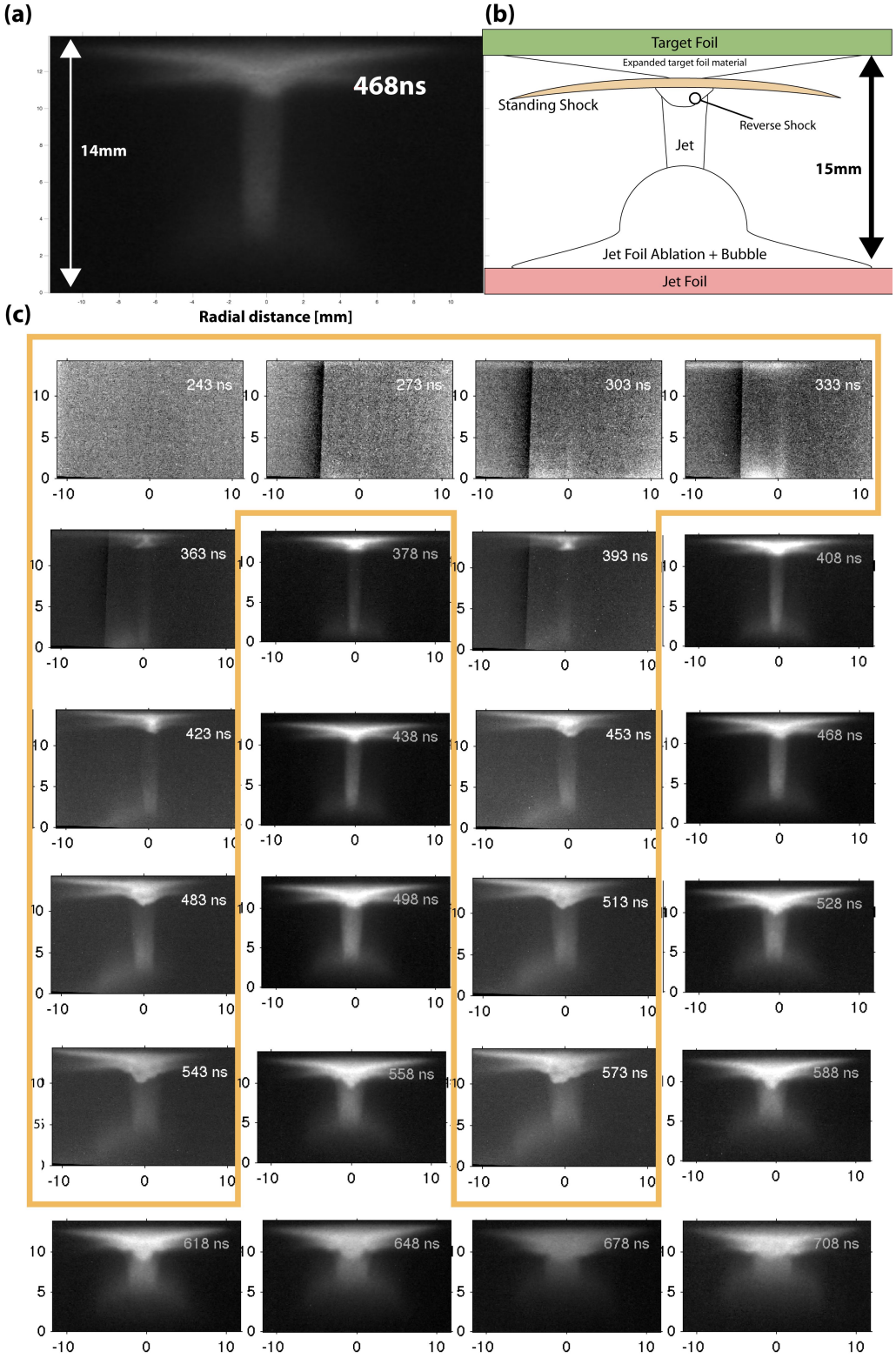

Figure 5.4: (a) Still from the optical fast framing camera at 468ns. The jet is seen in the image originating from the bottom of the image and extending upwards to the target foil. From experiment s032812. (b) Sketch of the jet-target interaction highlighting the structures which are seen in (a). (c) Composite of 24 chronological frames from the fast framing camera showing the interaction of the target and jet. The frames highlighted are at a larger magnification, from experiment s052912. The remainder are from experiment s032812. Scale in mm.

foil, this is the reverse shock. The stationary shock is highlighted in figure 5.4b in orange extending radially outward from the centre of the jet. A stationary shock forms ∼2mm below the target-forming foil and is visible for 100's of nanoseconds after its formation. Behind the stationary shock the surface of the target-forming foil is seen to expand.

Figure 5.4c charts the formation of the features highlighted in the sketch in figure 5.4b. The time each frame is captured is indicated on the image. The earliest frame, 243ns, is in the top left corner with increasing time running left to right. The last frame, 708ns, is in the bottom right hand corner of the image. A group of frames are boxed in orange to indicate they are from a different experiment, and at a larger magnification. The scale is indicated on the frames is in mm's. All the frames have been processed to improve contrast, although some artefacts of the camera (the horizontal black line on frames 243ns, 273ns, 303ns, 333ns and 393ns and a grainy texture) remain on the images.

The first four images from 243ns to 333ns, in the top row of figure 5.4c show the jet moving upwards towards the target-forming foil, which is at the top of the image. The jet is not initially visible on the first two frames, though the jet will have formed prior to this time but as yet is not emitting optically at a high enough intensity for the camera. The first optical emission observed arises from the jet and target-forming foil on frames 303ns and 333ns. By the frame at 363ns, the first frame on the second row of the image, the jet has reached the target-forming foil. The jet is seen to be well collimated and have a diameter of ∼1mm as measured from the optical emission.

In frame 363ns the jet is seen to be emitting most intensely from its base and at the interaction point of the target. The region where the jet interacts with the target appears as a bright triangle with its apex on the target-forming foil. The target foil is seen to be emitting at all points along its surface, however the brightest regions are those nearest to the jet. Frames 378ns, 393ns and 408ns show the continuation of this interaction and the formation of the stationary shock. The stationary shock appears as a horizontal line of emission below the target-forming foil which is centred on the jet axis. The stationary shock is seen to extend radially outwards in the period of

378ns to 408ns. The stationary shock has a slight downwards curvature at larger radius from the jet axis.

In the time period from 423ns to 528ns the material that formed the surface of the jet foil is seen to move upwards towards the target-forming foil and the diameter of the jet also increases in this period. The emission from the stationary shock and target-forming foil increases in this time period. Both the stationary shock and the target-forming foil appear to extend radially outwards in this time period from the observed emission. The interaction region of the jet and target foil forms a pointed 'V' shaped shock at the top of the jet, which is visible on frames 438 to 528ns. This structure is the formation of the reverse shock in the central dense flow of the jet.

In the frames from 543ns to 708ns the jet continues to expand radially and the ablated material from the jet-forming foil moves upwards towards the target-forming foil, by the 708ns frame it has reached the stationary shock. The reverse shock is seen to progress counter to the flow of the jet in this time period. The reverse shock also forms an unstable or 'bumpy' interface in the flow of material from the jet, visible on all of the frames in this time period, but particularly on frame 573ns.

The features indicated here will now be discussed in some detail in the remaining sections of this chapter. The jet will be compared to the jet observed in vacuum as a bench mark for the nature of the plasma flow interacting with the target. The two observed shock structures, the stationary shock and the reverse shock, will be investigated to find their plasma parameters and the conditions in the shock.

5.3 The formation and properties of the jet in the presence of the target foil

The jet-forming foil is expected to form a jet in the same manner as the jet in vacuum, however the presence of the target-forming foil may change the environment the jet is developing in. This section sets out to compare the jet propagating towards a target foil with the jet propagating into a vacuum and show the properties of the two systems are the same. The velocity of the jet and its radial expansion will be

found from optical emission. The electron density in the jet and halo plasma will be found from interferometry. The temperature of the jet and halo plasma will be found from Thomson scattering. The radial velocity of the halo plasma will also be found from Thomson scattering.

5.3.1 The dynamical properties of the jet

The early time development of the jet appears on first inspection to resemble the jet seen in vacuum. The development of the jet will be discussed from the laser probing images and the optical self emission images taken with the fast framing camera.

Figure 5.5 shows the laser images at 260ns after current start in the jet-forming foil. The jet is visible in both the interferometry, 5.5a, and shadowgraph, 5.5b. The images of the jet are accompanied with the pre-shot images which show the starting positions of the jet-forming foil and the target-forming foil. On first inspection the jet is seen to have smooth sides with no perturbations and appears well collimated. The tip of the jet has progressed ∼12mm towards the target foil and is ∼1.4mm in diameter. This is most visible on the interferometry image with the upwards bend in the fringes indicating the presence of plasma forming the jet.

It is observed that a plasma forms on the surface of the target foil before the dense tip of the jet has reached the foil, as can be seen in figure 5.5a. From comparison of the two images, before and during the experiment in figure 5.5a, it can be seen that the target foil is showing expansion and the presence of a plasma ∼2mm below its starting position from the change in the fringes. This indicates the foil is heated, which could be due to radiation from the jet-forming foil, a low density plasma moving ahead of the jet or electrons emitted from the surface of the jet-forming foil.

The jet-forming foil has also expanded upwards with the jet, forming a toroidal ring of plasma around the base of the jet which is darkened due to either high refractive index gradients or a large electron line density. In the laser images this appears as a ‘bump’ either side of the base of the jet due to the cylindrical symmetry. This is seen to be a similar size to the cathode (6.35mm).

Using the fast framing optical camera images shown in the previous section

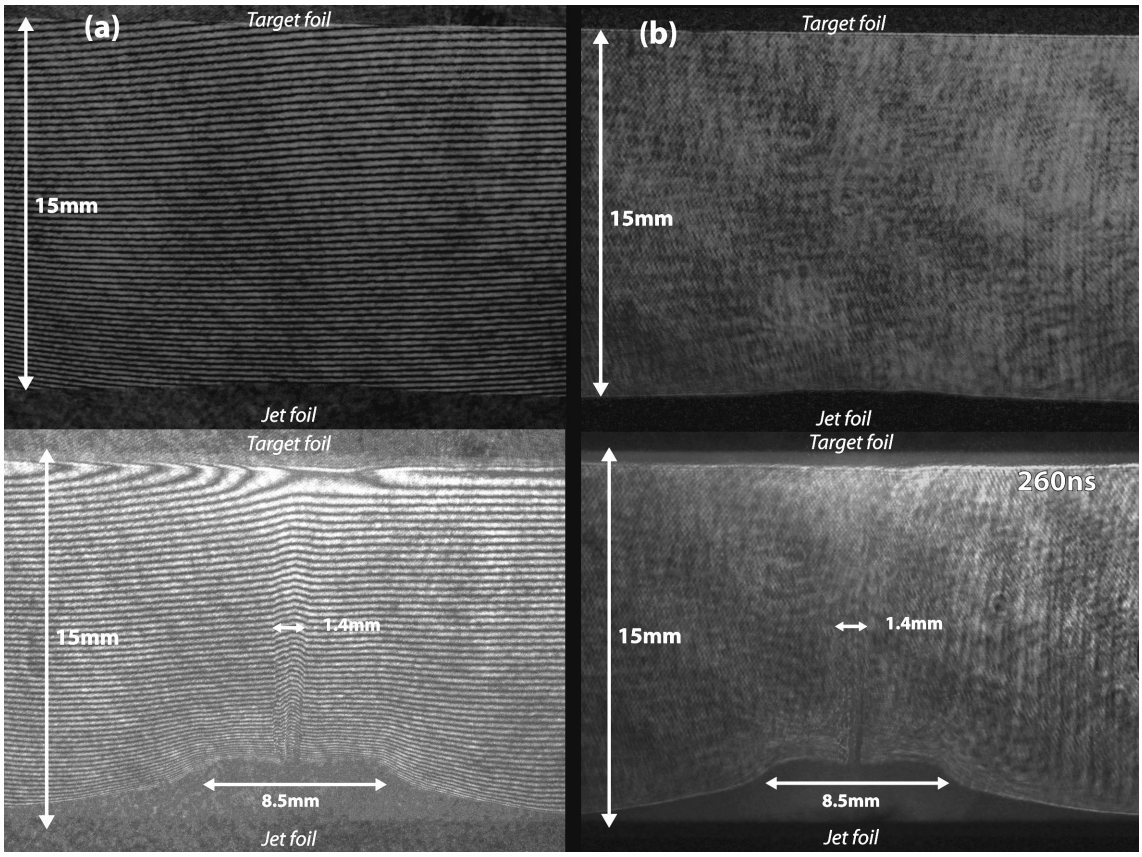

Figure 5.5: 532nm laser interferometry and shadowgraph image of the jet at 260ns after current start from experiment s052512. Both the shadowgraph and interferometry are taken from the same viewing angle through the discharge chamber. The pre-shot images are included as a comparison. It can be seen the fringes of the interferogram are shifted inside the jet and at the target surface, indicating the presence of plasma, which is not visible on the shadowgraph.

(figure 5.4) the velocity of the optically emitting tip of the jet, the material on the jet-forming foil and the radial expansion of the jet can be found. This is shown in figure 5.6. The images taken with the fast framing optical camera diagnostic have an exposure of 5ns and an inter frame spacing of 30ns. There is an error in the measurement of position of ±0.5mm. This arises from the uncertainty in finding the edge of the emission for the object being measured due to a lack of contrast or focus on the image captured by the fast framing camera.

To find the velocity of the jet, images from the fast framing camera diagnostic were found where the emission from the jet had yet to reach the foil. These are shown in the figure 5.4a and are processed to increase the contrast of the jet with

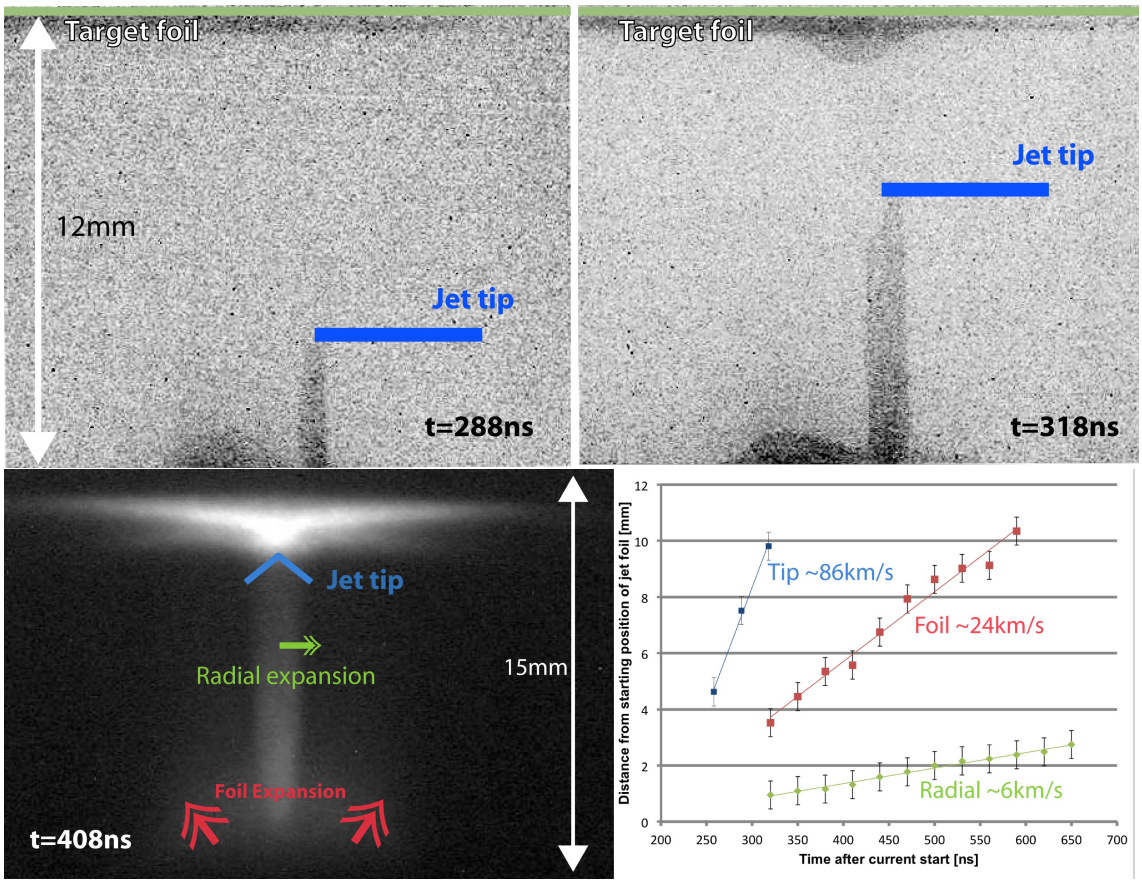

Figure 5.6: The velocity of the jet tip (prior to contact with the foil), material on the jet foil and the radial expansion of the jet are shown as measured from the fast optical framing camera. The two early time images are at a higher magnification and taken from shot s053012, they have been processed to increase the contrast of the emitting regions in the system for illustration of the velocity measurement. The annotated image taken at 408ns is from s032812.

respect to the background. The position of the emitting jet tip is marked in these images. Plotting the position of the jet tip against the time the image was taken gives a velocity of $\sim$ 85$\pm$5km/s for the emitting jet tip. This is comparable to velocities found for the jet propagating in vacuum via a similar measurement from the XUV 4-frame pin-hole camera diagnostic which showed the jet tip velocity to be $\sim$80km/s [42]. This measurement of comparable velocity is of interest as it is expected that the emission in XUV will arise from a hotter region of the jet. The jet will appear shorter in XUV images in comparison to the optical emission due to the strong radiative cooling in the jet. This result implies the emitting material is moving at the same velocity in both temperature regions.

The emission boundary at the jet-forming foil is seen to propagate upwards with a velocity of ∼25±3km/s. This was measured to be ∼20km/s for the jet into vacuum experiments [5]. It was shown that this expansion velocity matched the expected motion of a mass element in the foil accelerated by a radially dependent magnetic field pressure [5], which matches the description given in chapter 4 that indicated the ablated material from the foil is accelerated by a $\vec{J}\times\vec{B}$ force. It should be noted that this velocity is the same as the velocity observed in high-current electron-beam diodes for the expansion of plasma from the cathode electrode (Mesyats & Proskurovsky, 1988).

The radial expansion of the jet is measured by finding the diameter of the emitting region of the jet at a fixed position in z between the two foils on each frame. The diameter of the jet was measured from the fast framing camera images and then halved to find the radius. The radial expansion was found to be $\sim 6\pm2$km/s which is comparable to the radial expansion velocity measured for the jet into vacuum which was 5km/s [42].

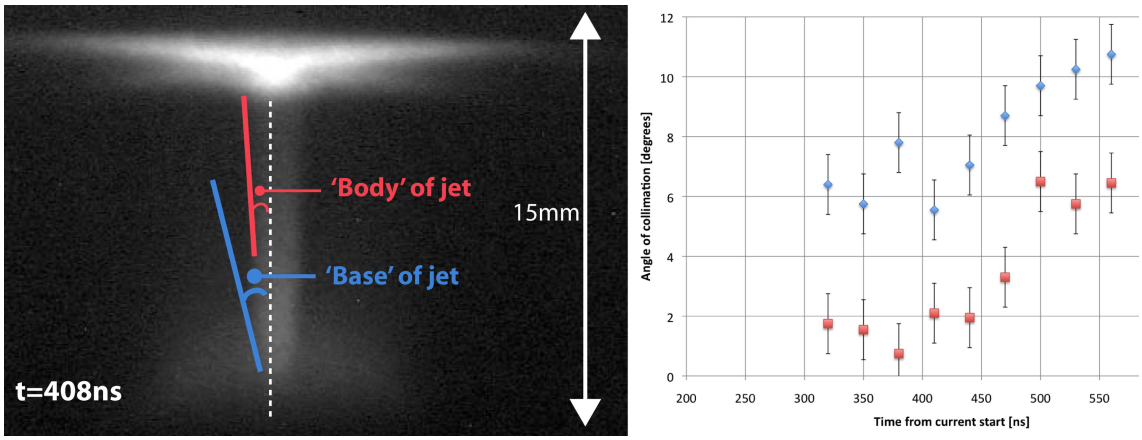

Figure 5.7: The half opening angle of the jet as seen to develop in time on the fast framing optical camera. The accompanying annotated frame is from experiment s032812.

In chapter 4 it was discussed that the jet propagating into vacuum is observed to have a high degree of collimation. For the present experiment with a target foil this can also be measured from the fast framing optical camera. Figure 5.7 shows the measured half angle of the emission from the 5mm at the base of jet closest to the cathode, and at the main body of the jet which are both marked in the figure

5.7.

Figure 5.7 shows a measured half angle over the 5mm at the base of the jet of 6° to 11°. However, in the region forming the main body of the jet extending to the target-forming foil, a half opening angle of 2° to 6° is measured. In the region where the jet is interacting with the target, the flow appears to be perpendicular to the target surface whereas the flow is clearly divergent near to the cathode. The observed improvement in the collimation of the jet is constant with the observation of the jet in vacuum where the half angle in the body of the jet was found to be 2° and 5° at the base of the jet [5].

From the comparison of the measurements made in optical emission of the jet with the measurements made in XUV of the jet in vacuum, the jet appears to behave dynamically in the same manner as the jet propagating into vacuum.

5.3.2 The density profile of the jet

It was found in previous experiments that the jet propagating into vacuum had an interior density between 1-8$\times 10^{18}$cm^{-3} [42]. This section will compare the density of the jet when forming in the presence of a target foil, to the density profile found when the jet propagates into vacuum.

The electron density can be measured with laser interferometry. The results discussed in this section are based on 532nm laser interferometry diagnostic which is described in the section 3.2. Laser interferometry is sensitive to the refractive index of the plasma, which is proportional to the electron density, this allows the electron line density map, $n_e l$ to be calculated. The images show a high degree of cylindrical symmetry. This allows an Abel transform to be performed on the $n_e l$ density map which gives an electron density map n_e. This method of analysis is described fully in appendix A.

Figure 5.8a shows part of the laser interferometry image of the jet obtained at time 267ns after current start. At this time the jet has begun its interaction with the target foil, as can be seen in the interferogram ∼1mm below the target-forming foil surface, the position of which is marked in green. Below the target the jet is

visible as a downward bend in the fringes extending 1mm either side of the axis of the jet, marked as 0mm. This gives a diameter for the jet of ∼2mm. The boundary of the jet is marked by a well defined, sharp bend in the fringes and the fringes that can be followed though the body of the jet are smooth. This indicates there is no turbulence in the body of the jet prior to interaction with the foil.

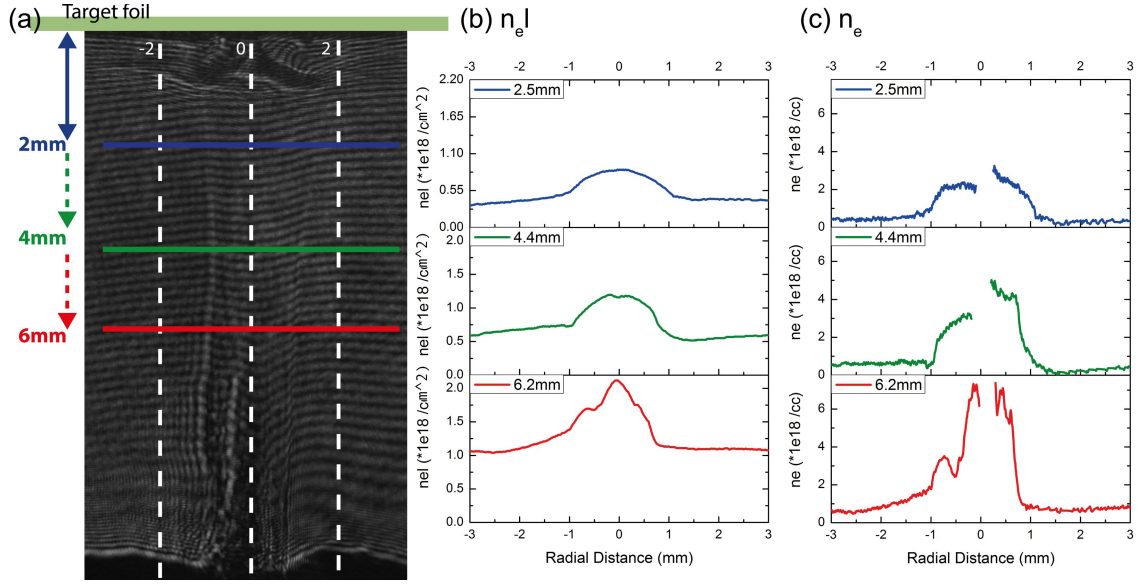

Figure 5.8: Radial line outs through the jet for experiment s060712B. t=267ns. Both the $n_e l$ and calculated n_e are shown. Both profiles are averaged over 10 pixel rows from the $n_e l$ density map, which is not shown, using the Abel inversion as discussed in section 3.2.3.2. The absence of the data points on axis in (c) is also briefly discussed in section 3.2.3.2.

Figure 5.8c shows three electron density profiles taken at 2mm, 4mm and 6mm below the target-forming foil surface, which is at 0mm, Figure 5.8b shows the averaged $n_e l$ from which the n_e line out is calculated. The line outs shown are an expanded range of the full $n_e l$ and n_e which is calculated to a large radius away from the jet to where no fringe shift is observed implying the plasma density is below the sensitivity of the interferometer.

The jet has the highest electron density near to the jet-forming foil, as can be seen in the 6mm line profile. At 6mm below the target-forming foil the jet has a density of $\sim 7\times10^{18}\mathrm{cm}^{-3}$. This density is not continuous axially along the jet towards the target, as shown by the two further profiles. At 2mm below the target the density is $\sim 2\times10^{18}\mathrm{cm}^{-3}$. The results are consistent with previous electron density

measurements of the jet propagating into vacuum [50].

Figure 5.9a shows an interferogram and three electron line density profiles taken at 464ns after the current start. At this time in the jet-target interaction the stationary shock is fully formed and the reverse shock is also forming, both are visible in the interferogram. The stationary shock is visible in the top portion of the interferogram to either side of the jet-target interaction region, ∼2mm below the target foil. The reverse shock is visible as a very tightly packed and knotted fringes at ∼3mm below the target foil forming in the body of the jet. This configuration of fringes indicates the reverse shock is dense and contains large localised density gradients.

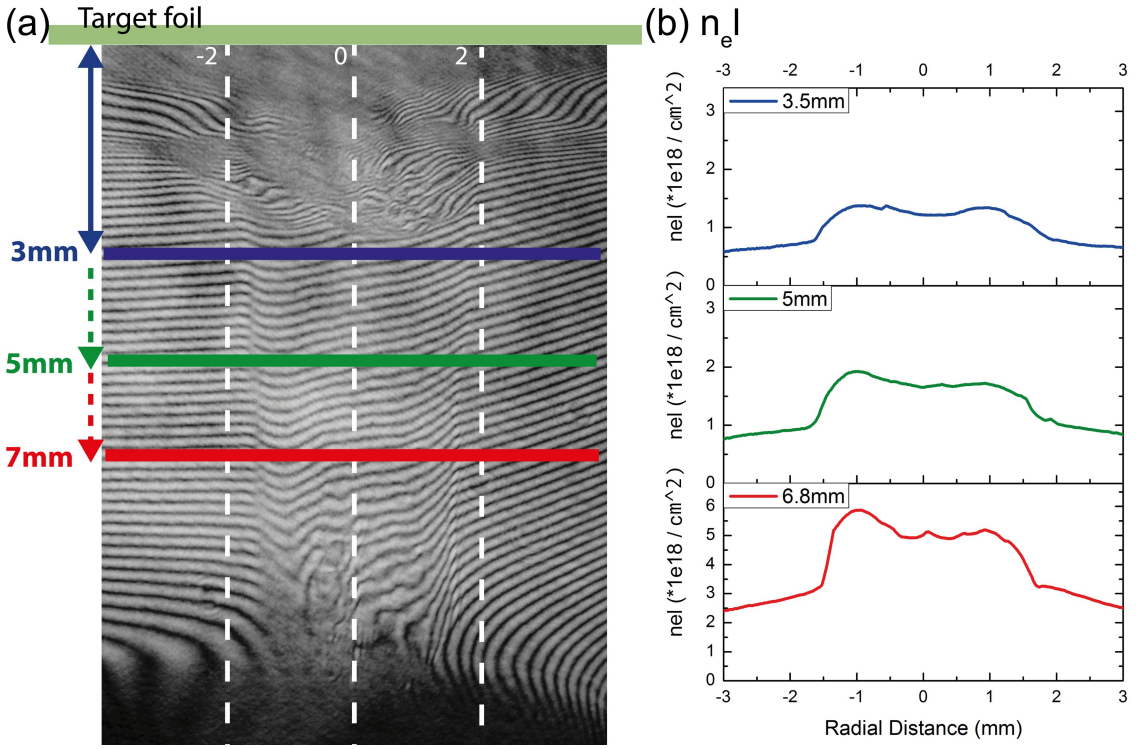

Figure 5.9: Radial averaged line outs from the $n_e l$ density map for experiment s040212 taken at 464ns after current start. Due to asymmetry in the jet an Abel inversion was not performed.

The jet is visible as a smooth downward curve in the fringes with a distinct boundary. On close inspection it can be seen the fringes are discontinuous at the boundary of the jet. This indicates a jump in the electron density that occurs in a very short spatial scale. The jet is not observed to be turbulent, though the jet in this experiment was found to be asymmetric.

Figure 5.9b shows three electron line density profiles taken at 3mm, 5mm and7mm below the surface of the target-forming foil. Close to the jet-forming foil the 7mm profile has a line density of $\sim 8\times10^{18}\text{cm}^{-2}$ in its interior. The density of the jet is seen to decrease towards the target-forming foil. The density profile at 3mm below the target gives an electron line density of $\sim 1.5\times10^{18}\text{cm}^{-2}$.

The jet is observed to have a larger radius closer to the target-forming foil. The jet in the line density profiles taken at 464ns is of a larger diameter than the jet observed at 267ns, the jet in figure 5.9 has a diameter of ~3.5mm. The edge of the jet is more distinct in the radial profiles shown in figure 5.9 with the jump in line density from the halo plasma to the edge of the jet occurring in <0.2mm.

In both figures, 5.8 and 5.9, the jet is moving through a lower density plasma termed the halo plasma. The density of the halo plasma decreases axially towards the target-forming foil and radially away from the jet axis. The observed density of the halo plasma ranges between 0.5 to $5\times10^{18}\text{cm}^{-3}$ with the highest observed values closest to the jet body and cathode.

The ratio between the electron density at the edge of the jet and the halo plasma is plotted in figure 5.10. This is calculated from the electron density in the halo plasma directly next to the jet, and then compared to the value of the electron density at the edge of the jet. In the electron density profiles this is observed as a step or jump in density occurring in a short spatial distance (<1mm). The material in the interior of the jet has a 2 to 4 times higher electron density than the surrounding halo plasma.

The jet body observed in vacuum was said to have a electron density of 1 to $8\times10^{18}\text{cm}^{-3}$ and a halo plasma electron density of $1\times10^{18}\text{cm}^{-3}$, on inspection of the figure 4.5 the halo plasma is also seen to decrease axially with the jet in vacuum. The electron density ratio in the jet body to the halo plasma at similar axial positions is seen to be the same between the two systems.

The average electron density axially along the jet at 490ns is shown in figure 5.11. This is calculated by integrating the electron line density in the body of the jet, then dividing by the jet diameter. The figure shows that the number of electrons in the jet decreases along its axial length.

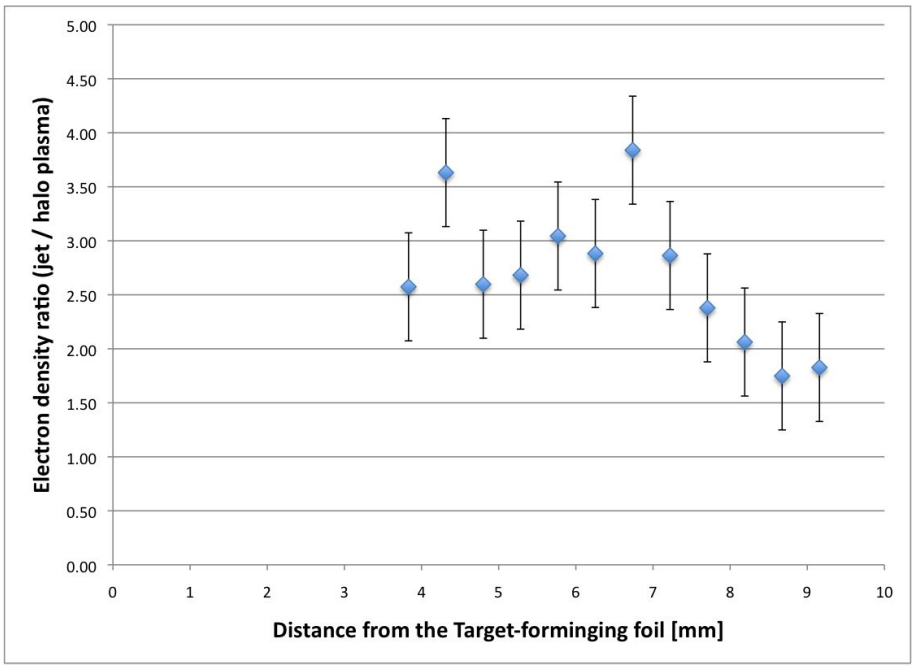

Figure 5.10: The ratio between the electron density at the edge of the jet and in the halo plasma. The area of the jet closest to the target shows the largest contrast of an $\sim 3\times$ density increase between the halo plasma and jet. Calculated from s040212

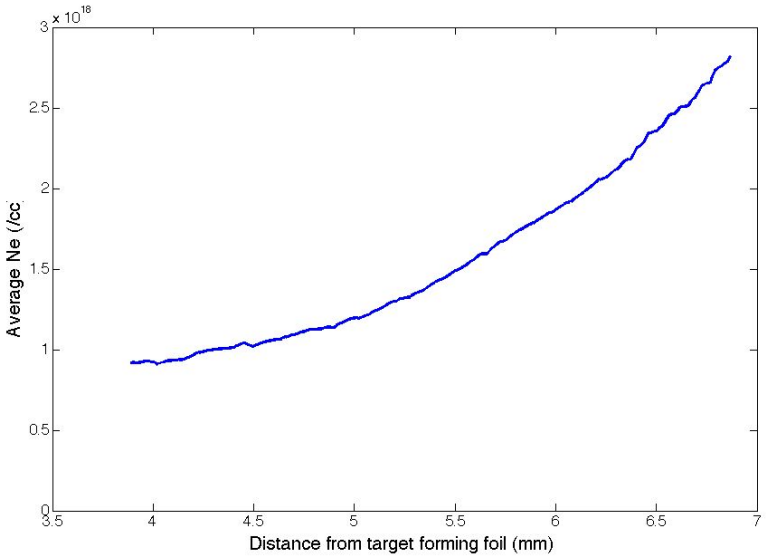

Figure 5.11: the average electron density, N_e axially distributed in the jet at 490ns. Calculated from s032812.

5.3.3 Thomson scattering measurements for the jet and halo plasma

The Thomson scattering diagnostic is used to find the plasma parameters in the jet and the radial velocity of the jet and halo plasma. Figure 5.12b shows the experimental set up for the Thomson scattering measurement, as viewed from above the discharge chamber. The Thomson scattering diagnostic was discussed in section 3.2.4. A description of the experimental set up for the Thomson scattering experiment will be given in section 5.3.3.1 for completeness and the results will be presented in section 5.3.3.2.

5.3.3.1 Experimental setup for the Thomson scattering measurement

Figure 5.12b shows the path of the probe laser through the discharge chamber, which forms the probe beam for the Thomson scattering diagnostic. The laser is focused into the centre of the discharge chamber using an f=2.5m lens. This provides a focal spot of $\sim 500\mu m$ diameter that remains approximately constant through the jet and halo plasma. This narrow and long focal region is where the light from the laser will be scattered, this is focused on to the optical fibre head as described in section 4.4. The fibres are aligned parallel to the radial axis of the jet-forming foil along the probe laser beam path and observes the scattered light at a 'scattering angle' of 90°. This provides a measurement of the scattered light from several spatial points along the laser beam at a separation determined by the magnification of the optical set up and spacing of the fibres. There are two fibre bundle heads positioned on opposite sides of the chamber and the individual fibres are aligned to view the same scattering volumes (at ±90°) with a vertical alignment error of ±0.5mm.

The laser beam is aligned prior to the experiment with respect to the target-forming foil and the jet-forming foil through moving the focal spot of the beam on to an alignment pin. The pin is $200\mu m$ diameter, held on a translation stage that can be moved (up, down, left, right) when the diagnostic chamber is under vacuum. It is moved out of the experimental hardware before the experiment. The translation stage has a micrometer scale allowing the measurement of the movement

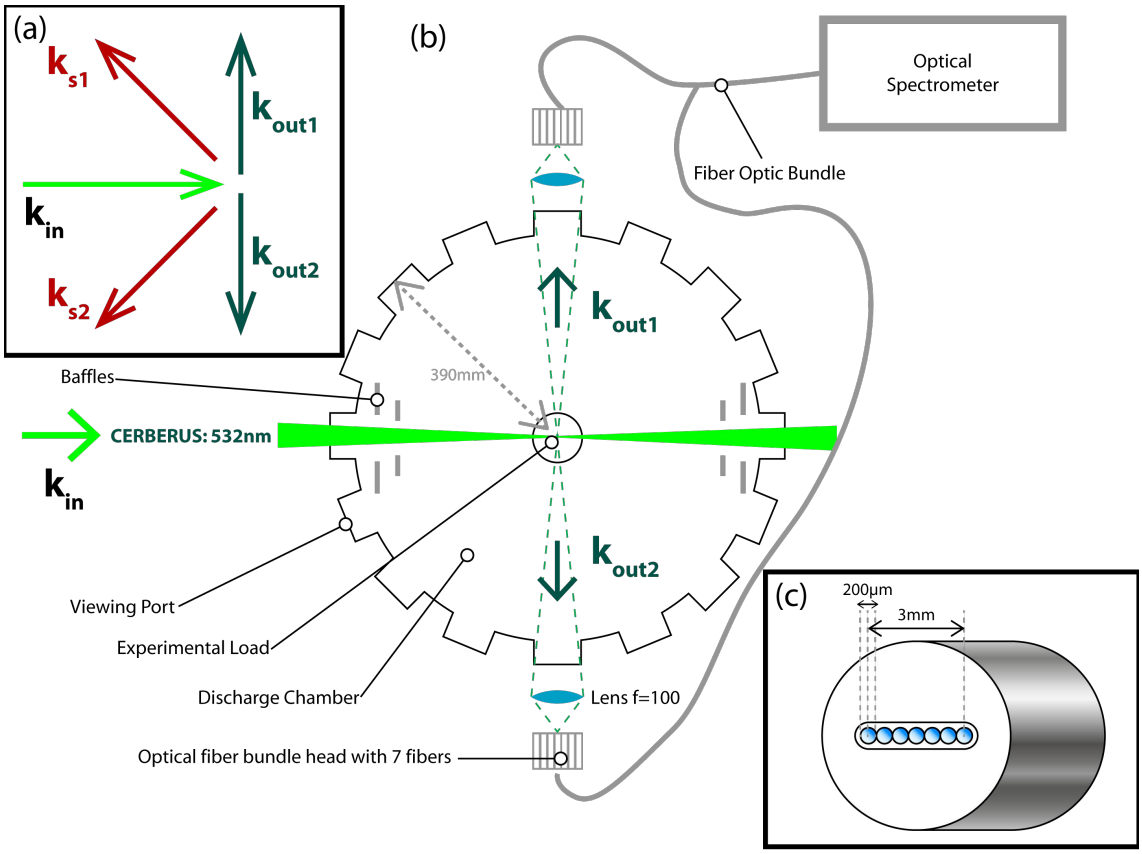

Figure 5.12: The experimental setup for the Thomson scattering measurement in the jet. (a) relationship of the $\vec{k}$ wave vectors in the scattering scheme which uses a 90° scattering angle. (b) experimental setup in the chamber with the input laser and two optical fibre heads at 90° from the laser. (c) close up of one optical fibre head bundle with seven 200μm diameter fibre optics. The fibres deliver the scattered light to an optical spectrometer. A time gated ANDOR camera attached to the optical spectrometer captures the spectrum from all 14 fibres.

of the pin tip during alignment. The pin tip is positioned at the axial height below the target-forming foil where the plasma parameters are to be measured, which in this experiment is ∼5mm (shown in figure 5.13) below the target-forming foil. When the lasers focal spot is aligned to the pin, the light scatters from the tip of the pin, and produces a diffraction pattern observable in the output of the laser beam. The beam is scanned radially until a strong diffraction pattern is present in the output, imaged onto a paper through the viewing port opposite the entry port for the laser. The scattered light from the tip of the pin is also seen to be brightest when the centre of the focal spot is correctly aligned as viewed from the other ports around

the discharge chamber. The laser beam can be positioned with an error of ±0.5mm with respect to the experimental load.

The scattered laser light from the pin tip is imaged on to the optical fibre bundle heads and is used to position the fibre with respect to the pin. A single fibre is chosen to look at the pin tip from each of the two fibre heads. In the case of this experiment, fibres 5 and 10 were positioned to look at the pin which is nominally on the axis of the jet. The fibre positions with respect to the jet are shown in figure 5.13. The volumes observed by each fibre have an effective spacing of 1.3mm for the magnification in the imaging system. The spatial resolution is determined by the size of the fibre and the imaging system magnification which in this case gives a collection area from a 700μm diameter plasma volume. It is seen in figure 5.13 that fibres 1,7,8 and 14 are positioned outside of the jet and will observe the halo plasma.

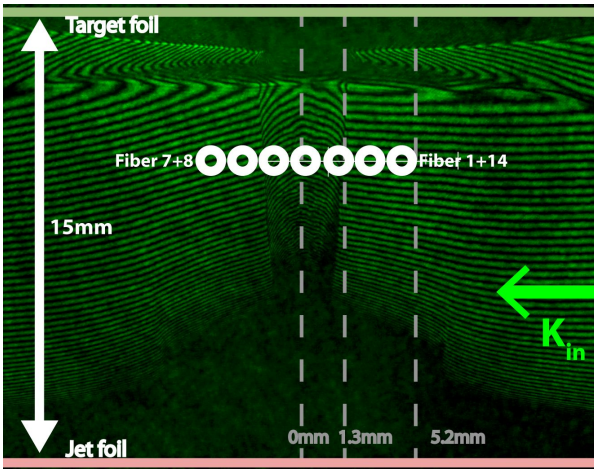

Figure 5.13: The position of the fibre bundle head in relationship to the jet viewed from the perspective of fibres 1 to 7 which view the scattering vector $\vec{k}_{out1}$, as shown in diagram 5.12. The spacing of the fibres is ∼1.3mm and the error on spatial position both vertical and horizontal is 0.5mm. From s053012.

The optical fibres are connected to a 0.5m imaging ANDOR spectrometer with a 2400 lines/mm grating and 5ns exposure. The scattered light from the alignment pin is used to find the spectrometer resolution for the fibre-optic setup and the measured frequency of the laser prior to the experiment. The resolution of the spectrometer is determined by the grating used and the size of the fibre optic (as no

slit is used with the spectrometer). The scattered light from the pin is termed the background spectrum. This gives a resolution for the spectrometer of 0.045nm which is the standard deviation, σ, of a Gaussian profile fit to the observed background spectrum [51].

Previous experiments, using Thomson scattering, found the axial velocity of the jet body to be 50km/s [42], these results and the experimental scheme used to obtain them are discussed in section 4.4. The experimental scheme described in this section and shown in figure 5.12 is sensitive only to the radial and azimuthal velocity of the plasma, as shown by the projection of the scattering wave vector for each fibre bundle position shown in figure 5.12a, which means the axial velocity of the jet cannot be found. This scheme will allow a new measurement of the radial velocity in the halo plasma and jet which can be used together with the previous measurement to estimate the direction of material flow in and around the jet.

The light from the probe laser and the scattered light observed by the fibres have wave vectors associated to them as shown in figures 5.12a and 5.12b. This produces a scattering wave vector, k_s, at 45° between the laser, k_{in} and the scattered light, k_{out}. If the volume of plasma observed has a radial or azimuthal velocity with respect to the jet-forming foil this will be seen as a Doppler shift in the mean frequency of the scattered light from the laser. This relationship is given by $\Delta\omega = \vec{k}_s \cdot \vec{v}$. The velocity directly measured from the Doppler shift in the scattered spectrum will be the projection of the velocity v along the direction of $\vec{k}_s$, this will be termed $v_{||}$. In this experiment $\Delta\omega$ can be observed as a shift in the wavelength, $\Delta\lambda$, and related to the velocity parallel to $\vec{k}_s$ by equation 5.1. Where λ_0 is the unshifted wavelength of the laser and c is the speed of light in a vacuum. The calculation of the Doppler shift in Thomson scattering is discussed in more detail in chapter 3.2. The error in the detectable mean wavelength, $\Delta\lambda$, shift between the scattered spectrum and the background spectrum is ±0.004nm which corresponds to a velocity of 1.6km/s in the direction of the scattering wave vector, $\vec{k}_s$ [51]. The velocity parallel to the scattering wave vector is found by evaluating equation 5.1 to give a parallel velocity, $v_{||1}$ and $v_{||2}$, for each fibre head.

$$\frac{\Delta\lambda}{\lambda_0} = \frac{2}{\sqrt{2}}\frac{v_{||}}{c} \tag{5.1}$$

Figure 5.14 shows the relationship between the scattered wave vector observed by each fibre to a flow of plasma directed radially inwards to the jet (shown as a blue circle in the centre of the image, viewed from above). The fibres view the plasma such that fibres 1 and 14, observing the same plasma volume at ±90°, will see a red shift in the scattered spectrum and fibres 7 and 8 will see a blue shift in the scattered spectrum due to the direction of the velocity in the observed plasma volume. As the fibres are arranged in a line, it is expected that there will be an observed red shift in the spectrum observed on on fibres 1, 2, 13 and 14 and an observed blue shift in the spectrum observed on fibres 6, 7, 8 and 9.

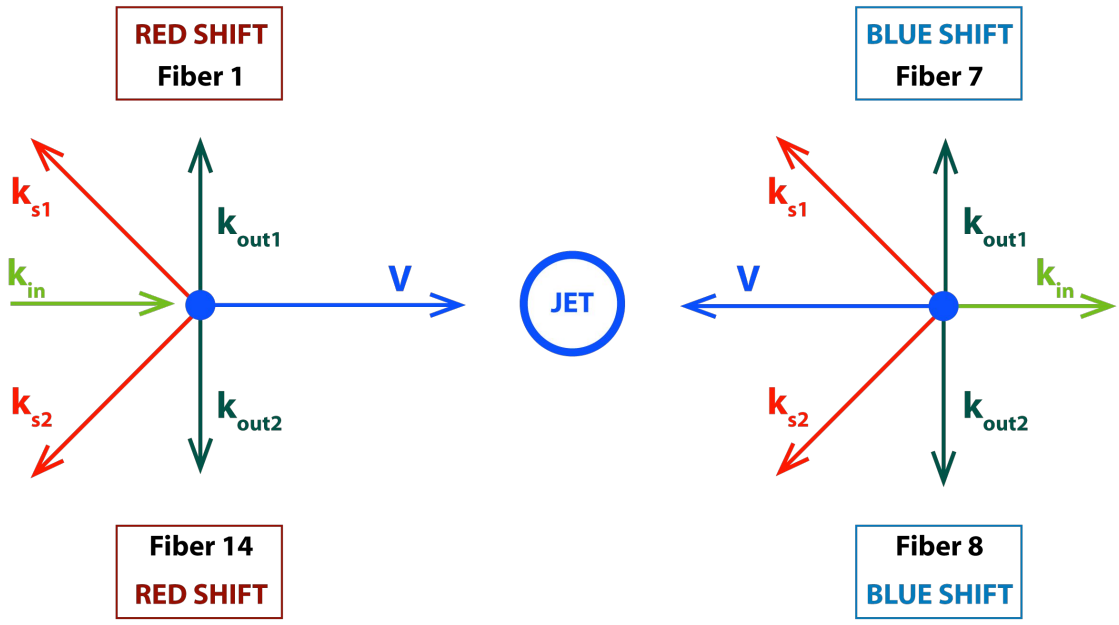

Figure 5.14: Doppler shift expected on the fibres if there is a inward flow of material from the halo plasma towards the jet. The jet is pictured in the centre of the image and the velocity vector, $\vec{v}$ of two plasma volumes on either side of the jet is marked in blue. The relative position of the fibres 1,7,8 & 14 is shown along with the scattering vectors, $\vec{k}_s$ associated with them. It is shown that the fibres viewing the halo plasma to the side of 1 &14 will see a red shifted spectrum. The fibres on the side of 7 & 8 will see a blue shifted spectrum.

5.3.3.2 Results of the Thomson scattering measurement in the jet

Figure 5.15 shows the observed spectrum from fibres 1 to 7. Figure 5.16 shows the observed spectrum from fibres 8 to 14 which is arranged from 14 to 8 to allow comparison to figure 5.15 (as fibre 1 and 14 view the same plasma volume). The background spectrum is shown in red on fibres 3 and 10 to illustrate the measured λ_0 of the laser (λ_0 =531.736nm as measured by the spectrometer which is not absolutely calibrated) and the resolution of the spectrometer. Fibres 3 to 5 and 10 to 12 show a clearly broadened spectrum with a 'flat top'. Fibres 1, 2, 6, 7, 8, 9, 13 and 14 are Doppler shifted in a direction consistent with an inward flow of plasma (as discussed in figure 5.14), but show less obvious broadening retaining a Gaussian profile. These fibres are outside the jet observing the halo plasma.

For fibre 1 the spectrum is red shifted with a change in mean wavelength of $\Delta\lambda = 0.016\pm0.004$nm. The spectrum is red shifted for fibres 1, 2, 13, 14 and blue shifted for fibres 6, 7, 8, 9. The red shift observed on the spectrum of fibre 1 corresponds to a velocity parallel to the scattering vector of 6.3±1.6km/s. There appears the be a systematic shift in the scattered spectrums observed in the halo plasma, red shifted on fibres 'before' the jet and 'blue' shifted on the fibres after the jet in the direction of the probe beam propagation through the experiments. Figure 5.17 shows a graph of the measured wavelength shifts $\Delta\lambda$, of the spectrums observed by the two fibre bundle heads. It can be seen the material in the edges of the jet, which is marked in the figure, has no observed Doppler shift, though the material at the centre of the jet appears to have a non zero velocity indicated by a large shift in the observed spectrum. Figure 5.18 shows a shadowgraph taken at 411ns. It can be seen on this image that there is some density gradient on the axis of the jet which may indicate the doppler shift seen at the axis of the jet results form an internal localised turbulence of the plasma.

The two velocities calculated from the two observation positions of the fibres can then be used to find the velocity parallel and perpendicular to the laser wave vector, $\vec{k}_{in}$, and shown in equations 5.5. The velocities correspond to the radial velocity, v_r and the azimuthal velocity, v_θ of the plasma volume.

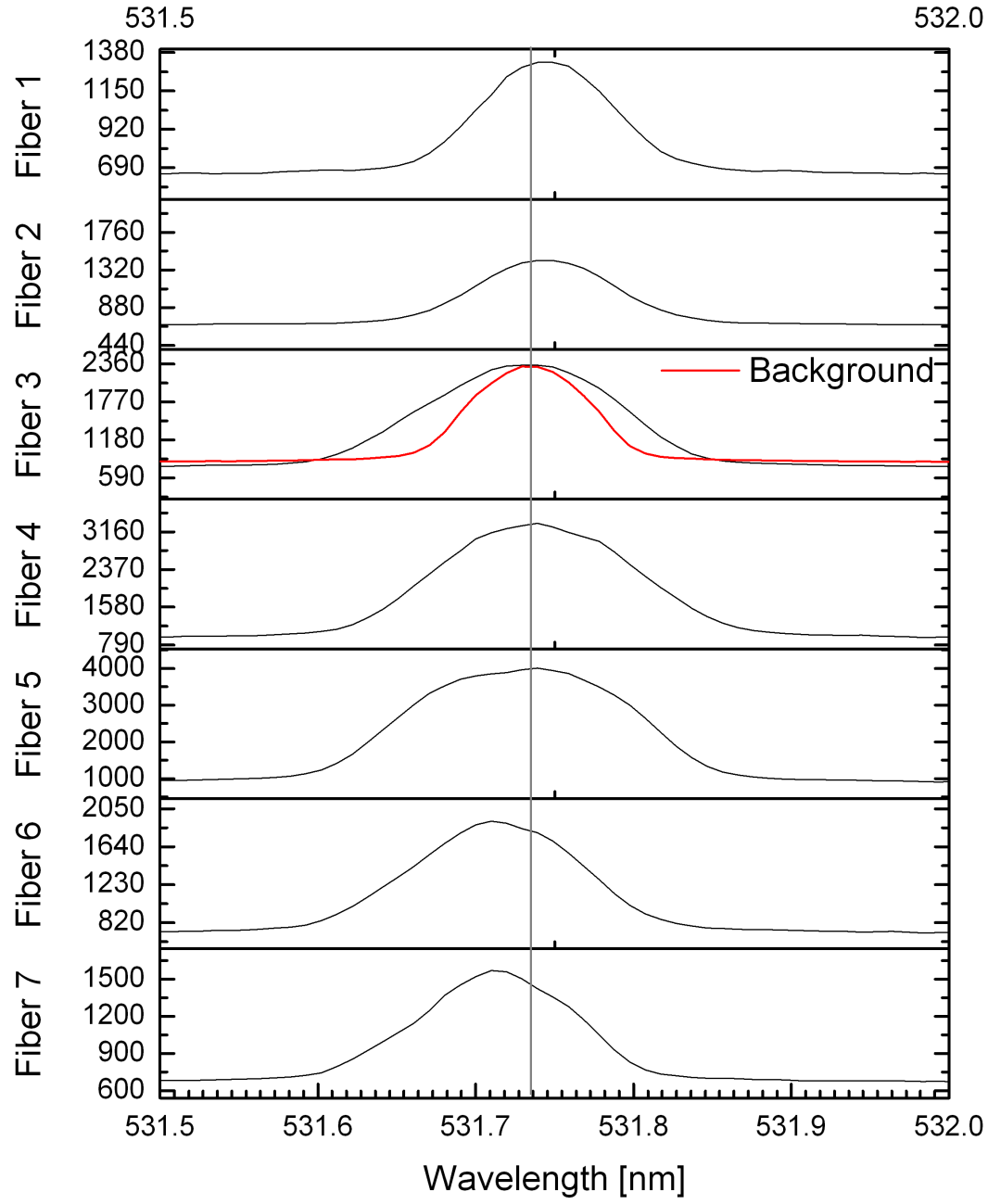

Figure 5.15: The spectrum observed by fibres 1 to 7. The unscatterd background spectrum of the probe laser is shown on fibre 3. This shows the natural frequency of the laser and the spectrometer resolution. Fibres 1 & 2 are slightly red shifted and fibers 6 & 7 are slightly blue shifted. From experiment s053012 at 423ns.

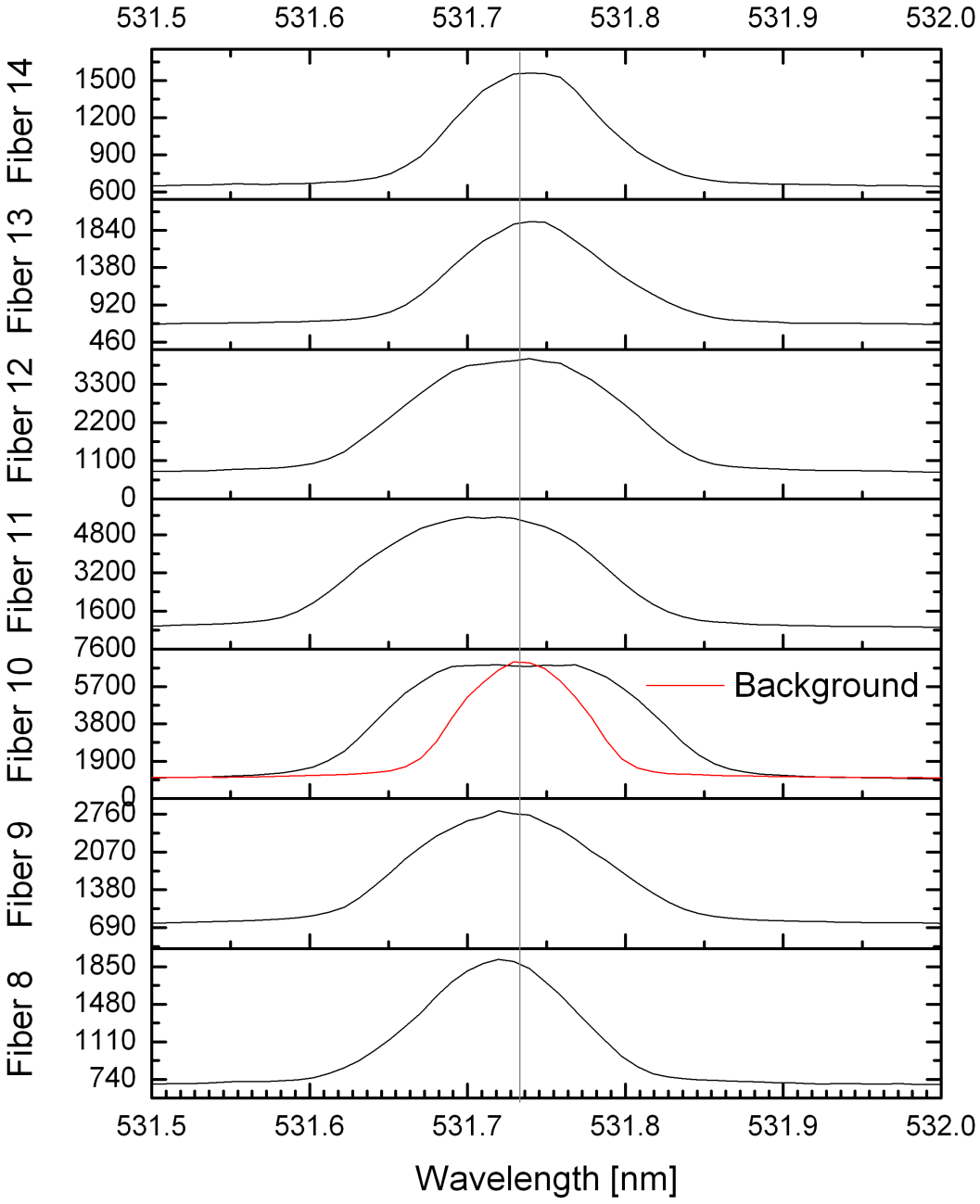

Figure 5.16: The spectrum observed by fibres 8 to 14. The unscatterd background spectrum of the probe laser is shown on fibre 10. This shows the observed frequency of the laser and the spectrometer resolution. Fibres 8 & 9 are slightly blue shifted and fibres 13 & 14 are slightly red shifted. From experiment s053012 and 423ns.

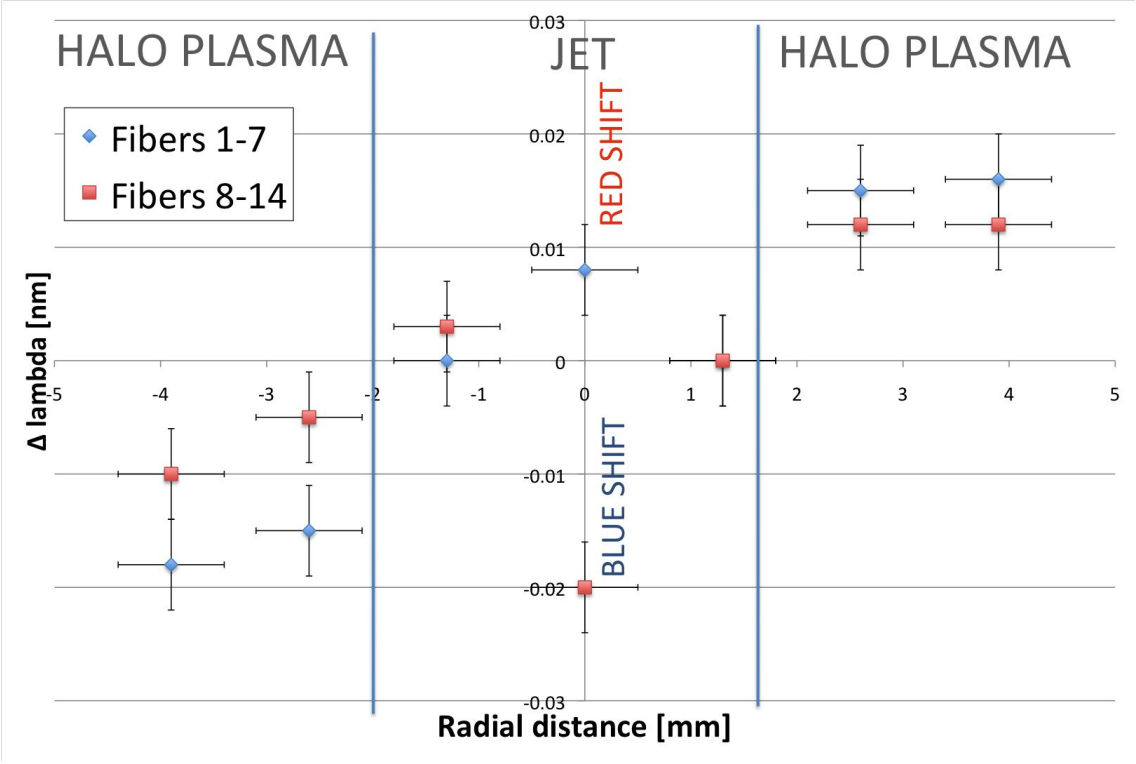

Figure 5.17: The $\Delta\lambda$ observed in the scattered spectrum. The approximate boundary of the jet during the experiment is indicated. The measured change in wavelength in the halo plasma on both sides of the jet correspond with a radially velocity towards the jet axis. From experiment s053012 at 423ns.

$$Fibers1-7: v_{||1} = v_r cos45^\circ + v_\theta cos45^\circ \quad (5.2)$$

$$Fibers8-14: v_{||2} = v_r cos45^\circ - v_\theta cos45^\circ \quad (5.3)$$

$$v_r = \frac{v_{||1}+v_{||2}}{2cos45^\circ} = \frac{v_{||1}+v_{||2}}{\sqrt{2}} \quad (5.4)$$

$$v_\theta = \frac{v_{||1}-v_{||2}}{2cos45^\circ} = \frac{v_{||1}-v_{||2}}{\sqrt{2}} \quad (5.5)$$

The calculated radial and azimuthal velocities are shown on figure 5.19. The radial velocity corresponds to the green markers and the azimuthal velocity corresponds to the red markers. For reference the direction of the laser wave vector, $\vec{k}_{in}$, is shown on the figure with a schematic of a corresponding positive radial velocity vector. The position of the jet and halo plasma is marked on the scale for reference. It is seen there is a flow of plasma moving towards the jet at an average radial velocity of 7±2km/s in the regions marked as the halo plasma. On the interior of the

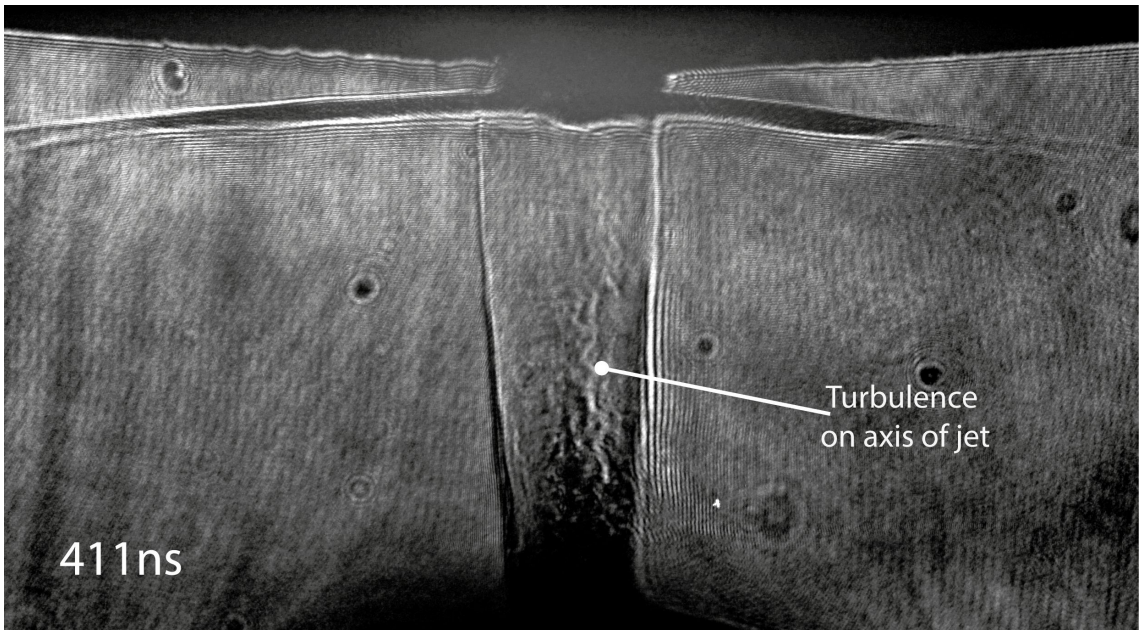

Figure 5.18: A shadowgraph of the jet at 411ns showing localised density gradients in the central region of the jet, marked as 'turbulence'. From experiment s053012.

jet the material near the jet boundaries appears to have no velocity. The large azimuthal velocity at the centre of the jet corresponds with the density gradients seen in the shadowgraph image in figure 5.18 and may indicate some localised turbulence on the axis of the jet. The azimuthal velocity in the halo plasma is averaged to be 1.7±2km/s which can be taken to be negligible within errors.

Using the axial flow velocity (50km/s) and the radial flow velocity (7km/s) the angle between the material in the halo plasma flow and the jet axis can be found. This is found to be $atan(\frac{7}{50}) = 8°$. This corresponds with the simulation results discussed in chapter 4 which indicated the material in the halo plasma had a $\vec{J} \times \vec{B}$ force directed at the axis of the jet, aiding the confinement of the jet body.

The scattered spectrum of the probe beam is also sensitive to the temperature of the ions and electrons in the plasma volume which is observed as a broadening of the scattered spectrum. The fibres looking at the region inside the jet observed a spectrum that was broadened and had a 'flat top' profile. The flat top indicates that the ZT_e is higher than T_i. Figure 5.20 shows a fitted spectrum observed by fibre 10 (r=0mm). The quality of the fit depends strongly on the value of the ratio between T_i and ZT_e. The electron density is needed for the fit, but the fitting is not

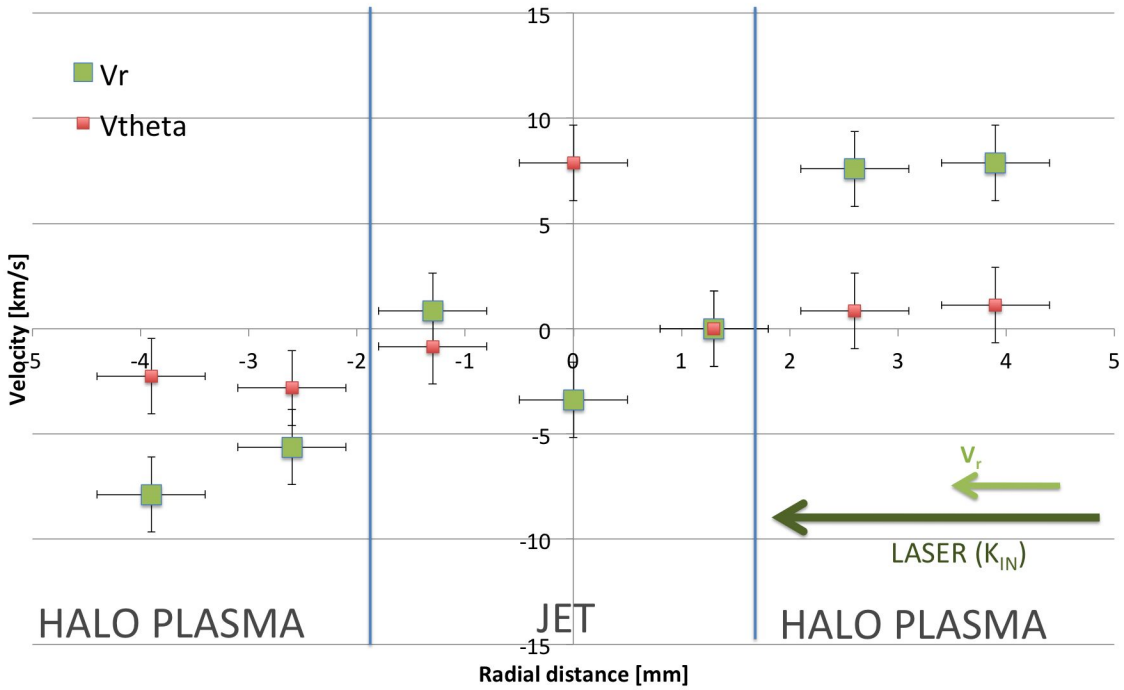

Figure 5.19: The calculated radial and azimuthal velocity with respect to the probe laser wave vector. The negative velocities correspond to plasma moving towards the laser light source, and positive velocities are moving along the direction of the light. This corresponds with the wave vector $\vec{k}_{in}$ as shown in figure 5.13. The approximate boundary of the jet during the experiment is indicated. The measured velocities in the halo plasma on both sides of the jet are moving radially inwards towards the jet.

sensitive to this parameter. The electron densities from the interferometry taken at the same time are used. The sensitivity to temperature is demonstrated by varying the ZT_e from the 'best fit' by 20% higher and 20% lower. It is shown in the figure that the variation of $\pm 20\%$ is an inadequate fit to the spectrum in the broadening or in the displayed features i.e more pronounced double peaks instead of a flat top. The spectrum from fibre 10 was fit with the parameters of $n_e = 7 \times 10^{18}\text{cm}^{-3}$, $T_i = 50 \pm 10\text{eV}$ and $ZT_e = 80 \pm 16\text{eV}$.

Fitting for each of the spectrums obtained by the fibres observing the interior of the jet, the temperature within the jet is averaged and found to be $T_i \sim 55 \pm 10\text{eV}$ and $ZT_e \sim 50 \pm 10\text{eV}$. The ionisation of the plasma in the jet cannot be directly evaluated without knowing the ion density. The expected ionisation using a Saha model which assumes local thermodynamic equilibrium at $n_e = 7 \times 10^{18}\text{cm}^{-3}$ and

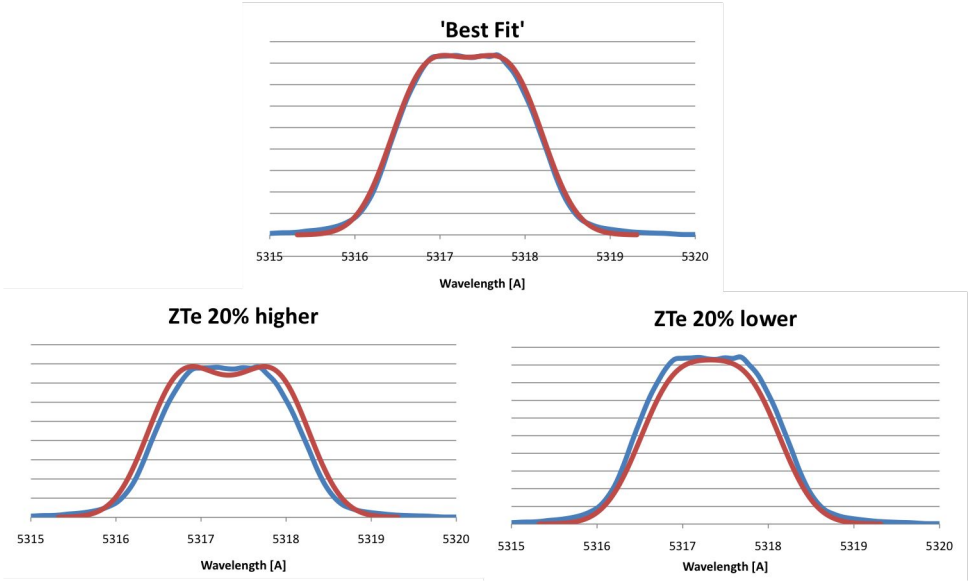

Figure 5.20: The spectrum observed by fibre 10 is shown in blue on these three charts. The red curve is a fit to the observed spectrum that accounts for the spectrometer resolution, electron density, element, ion temperature, T_i, and the product of ionisation and electron temperature, ZT_e. The middle plot shows the 'best fit' to the data and corresponds to T_i = 50eV and ZT_e = 80eV. The plots to the left and right show a variation in the ZT_e by 20% which is given as the accuracy of the fit.

$T_e = 20eV$ is found to be $Z = 6$. Using the modified Saha model by D.E. Post, [52] the ionisation is found to be $Z = 3$ for a 20eV aluminium plasma. The Post model estimates a polynomial fit for the ionisation which is based on calculations using an average ion model. In this model the plasma is treated as optically thin. Populations are determined by balancing the rate of collisional ionisation against the rates of dielectronic, radiative and three-body (collisional) recombination. The Post model is calculated for much lower density plasmas ($n_e = 1 \times 10^{16}\text{cm}^{-3}$) than is applicable in this case, however it is generally used for similar plasma parameters as observed in the jet. The value given by the modified model is in better agreement with the measured ZT_e. The jet in vacuum was seen to have T_i ~45eV, $ZT_e \sim$ 60eV to 80eV and $Z \sim 4$. It is seen the temperatures agree, although the ionisation is predicted to be higher for the jet in vacuum which may be due to the timing of the experiment or different parameters used in the estimation of the ionisation.

Using the value of T_e = 20eV and $Z = 3$ in the body of the jet the speed of sound is found to be ~20km/s. This can be used to find a Mach number in the jet

of $M = 3$ for an axial flow velocity of 50km/s, this supports the jet is supersonic.

The spectrum observed by the fibres outside of the jet is seen to retain a Gaussian profile and have less broadening when compared to the jet spectrum. This implies the broadening is dominated by T_i and the contribution from ZT_e is difficult to discern. The ion temperature can be approximated at 20eV in this region from fitting to the observed broadening but the accuracy of this estimate is not very high (Depending on the ionisation chosen for the fit, very different temperature values can be found, constraining the fitting to $Z = 1$ the accuracy is $\pm 50\%$) and should only be considered as an indication that the ion temperature in the halo plasma is lower than in the flow of the jet.

The low ion temperature outside of the jet in comparison with the interior implies the boundary of the jet is a shock front. In the radial velocity frame material from the halo plasma is flowing inwards and being heated in the shock front by ion-ion collisions. The heated ions then exchange energy with the electrons in the interior of the jet through collisions and ionisation.

From the comparison of the jet in vacuum and the jet forming in the presence of the target foil the two systems are found to be the same within experimental error, and where differences where noted they are discussed in the text. This indicates that the presence of a target does not change the mechanisms that drive the plasma forming the jet.

5.4 The stationary shock in the halo plasma

The stationary shock was seen to form in the halo plasma of the jet, ∼370ns after current start. The stationary shock extends radially outwards by ∼15mm from the centre of the jet as seen in figure 5.4. The stationary shock has a smooth front with a slight downwards curvature. As discussed in section 5.2, the stationary shock appears to maintain its position relative to the emission from the target-forming foil. The stationary shock feature is then seen to emit optically and in XUV, shown in figure 5.21. It can be seen the structure of the stationary shock is similar in both optical and XUV emission.

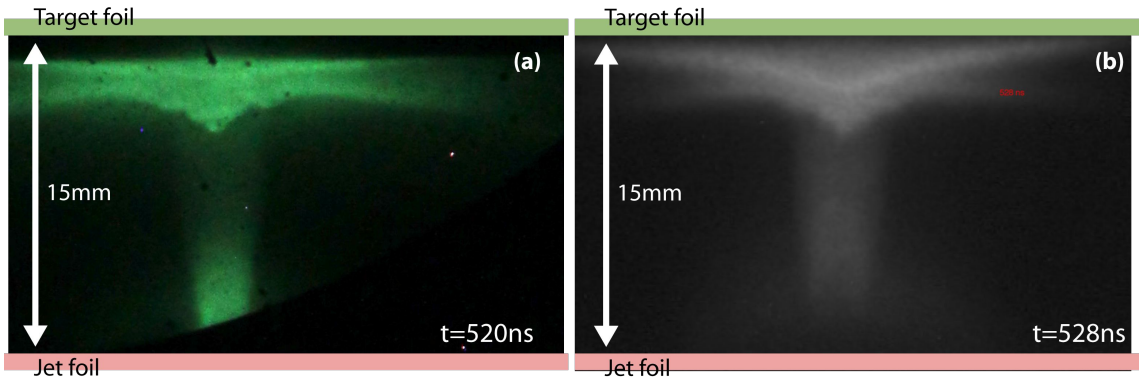

Figure 5.21: (a) shows the XUV emission at 520ns. (b) shows the optical emission at 528ns. Both images from shot s032812.

The longevity, stability and size of the stationary shock feature make it an interesting structure. From the previous section discussing the jet, it is known the bright vertical emission, seen in figure 5.4, forming the jet is accompanied by a halo plasma which extends some distance radially away from the jet. This is not seen to emit in optical emission but was measured on the interferometry diagnostic to have a density on the order of $\sim 0.5 \times 10^{18}\text{cm}^{-3}$. This halo plasma is interacting with something prior to reaching the target-forming foil surface, causing the formation of a stationary shock feature. The obstacle that the halo plasma encounters could take the form of ablation from the target foil, material accumulated at the target from the jet, a reverse shock in the halo plasma itself, or an electromagnetic field or another yet unknown cause.

The dynamics of the shock and its initial evolution will be discussed in the first subsection with the results of interferometry from the standing shock formation and the observation of its movement with respect to the emission from the target foil.

The conditions of the plasma in the shock will then be investigated. The electron density contrast between the halo-plasma and the material behind the shock front from interferometry will be found. The electron and ion temperatures behind the stationary shock will be estimated from the Thomson scattering diagnostic.

The dynamics of the stationary shock will be investigated though the variation of the target-forming foil such that some of the possible causes of the stationary shock can be eliminated.

5.4.1 The evolution of a stationary shock in the flow of the halo plasma from the jet

Material is observed to expand and emit from the target foil early in the experiment time (this was shown on the interferometry images in figure 5.5). When the jet reaches the target the stationary shock forms very quickly, on the order of 20ns, as can be seen in figure 5.22.

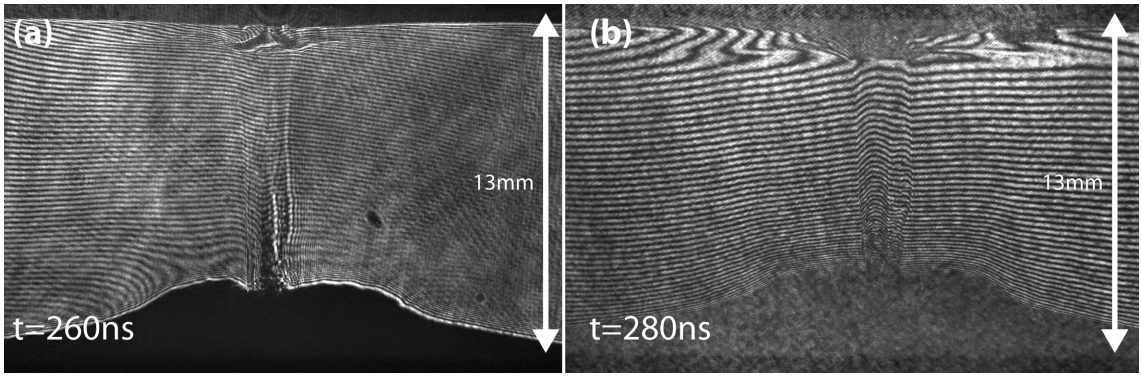

Figure 5.22: Two interferograms from experiment s060712B. The images are taken with 532nm laser imaging at 260ns and 280ns. The formation of the stationary shock occurs between the two frames indicated by the sharp bend and compression of the fringes close to the target-forming foil in (b). The spacing between the foils in this experiment is 13mm. The interaction of the jet and target was observed to be the same as with a spacing of 15mm, but the interactions happen at an earlier time as the jet arrives at the foil earlier.

The two images in figure 5.22 are from the same experiment and taken 20ns apart from each other. In figure 5.22a the jet has reached the target-forming foil and there is an interaction in the flow of material from the jet. Below the target-forming foil surface there is a bending and compression of the fringes which indicates there is plasma present ∼2mm from the target surface, and the localised compression of the fringes suggests this is the material that will form the stationary shock. In figure 5.22b the stationary shock has formed, indicated by the stronger compression of the fringes, appearing as though the line of phase turns back on itself. This is surprising as it would be expected that the shock would form on the surface of the foil and move downwards into the flow from the halo plasma forming a reverse shock. No evidence of this mechanism is seen, the shock forms ∼2mm from the surface of the

foil and stays in a very similar position for the rest of the jet-foil interaction.

Figure 5.23 shows the position and the shape of the stationary shock by plotting its radial position against its axial position. The position of the shock front is calculated from the laser shadowgraph. It is seen that for the 100ns time period the three profiles are taken in, the shock front does not move axially and retains a similar shape. The shock front is flatter closer to axis of the jet and there is a downward curvature to the shock front at larger radius. This implies the shock front forms a distorted hemisphere around the top of the jet. The width of the shock will be discussed later with context to the electron density profiles across the shock front.

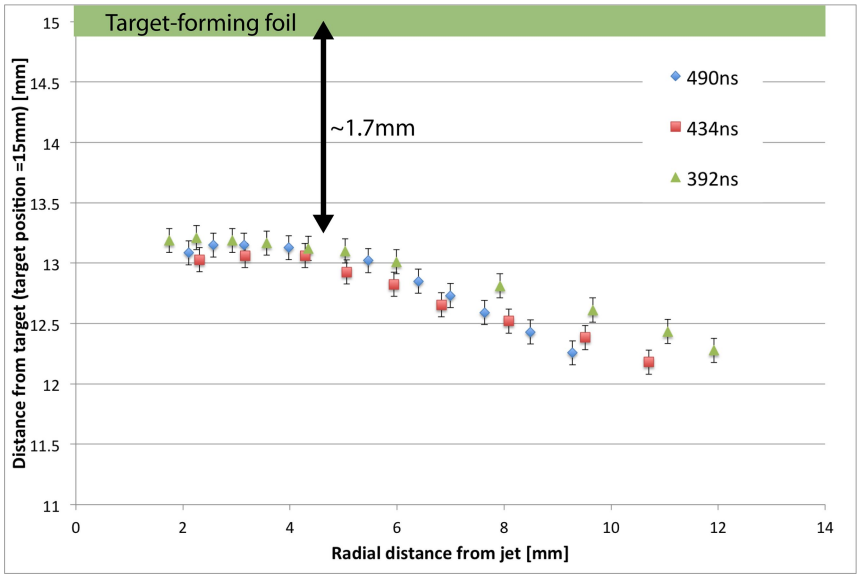

Figure 5.23: The 'edge' of the stationary shock is plotted against its radial position for three time points within a 100ns period between 392ns and 490ns. It can be seen that in this period the position of the shock does not change and that the curvature of the shock is also the same for these time points. From shadowgraph images on experiments s032812, s052412 and s052912.

The velocity of the shock front can be found from the position of the stationary shock which can be plotted in time, and compared to the ablation expansion from the target-forming foil. This is shown in figure 5.24. The standing shock is marked in red and the expanding target foil is marked in blue, the corresponding data point on the accompanying graph are also colour coded in this way.

The velocity of the emission from the expanding foil is found to be $\sim 4\pm2$km/s

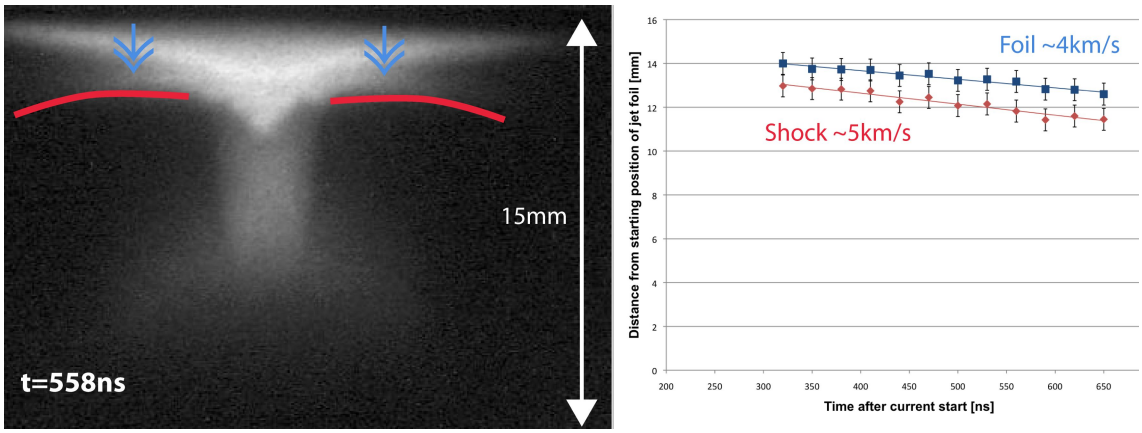

Figure 5.24: Velocity of the emitting region of the stationary shock as measured from the optical fast-framing camera diagnostic. Image from s032812.

and the velocity of the emitting region of the stationary shock is found to be ∼5±2km/s. Within the error of the experiment these are comparable velocities. It is seen from the graph in figure 5.24 that the stationary shock retains the same distance from the edge of the expanding target foil for the observed time period.

Figure 5.25a shows the electron line density, $n_e l$, figure 5.25b shows the electron density, n_e both are calculated from the interferogram shown in figure 5.22a. On both maps the position of the three density profiles is indicated and these are shown in figure 5.25c from the $n_e l$ plot and 5.25d from the n_e plot.

From inspection of the line profiles shown in figure 5.25c, the material accumulated on the target-forming foil surface increases in density gradually over z =1.5mm to 3mm in both density plots and there is not a sharp density increase associated with a shock seen in the density profiles. As will be shown in the next subsection, once the stationary shock is formed it has an abrupt change in density at the shock front, as is indicated by the compressed fringes close to the target-forming foil in figure figure 5.22b. If there is a shock in the material at this point it is a very weak shock which quickly becomes a strong shock, which is what is seen in the interferometry image of figure 5.22b.

From the time that the stationary shock is formed it is observed to maintain a similar position and shape during the experiment. It is also seen to be highly reproducible from experiment to experiment with very strong cylindrical symmetry. The fully formed stationary shock from two different experiments, at the same time

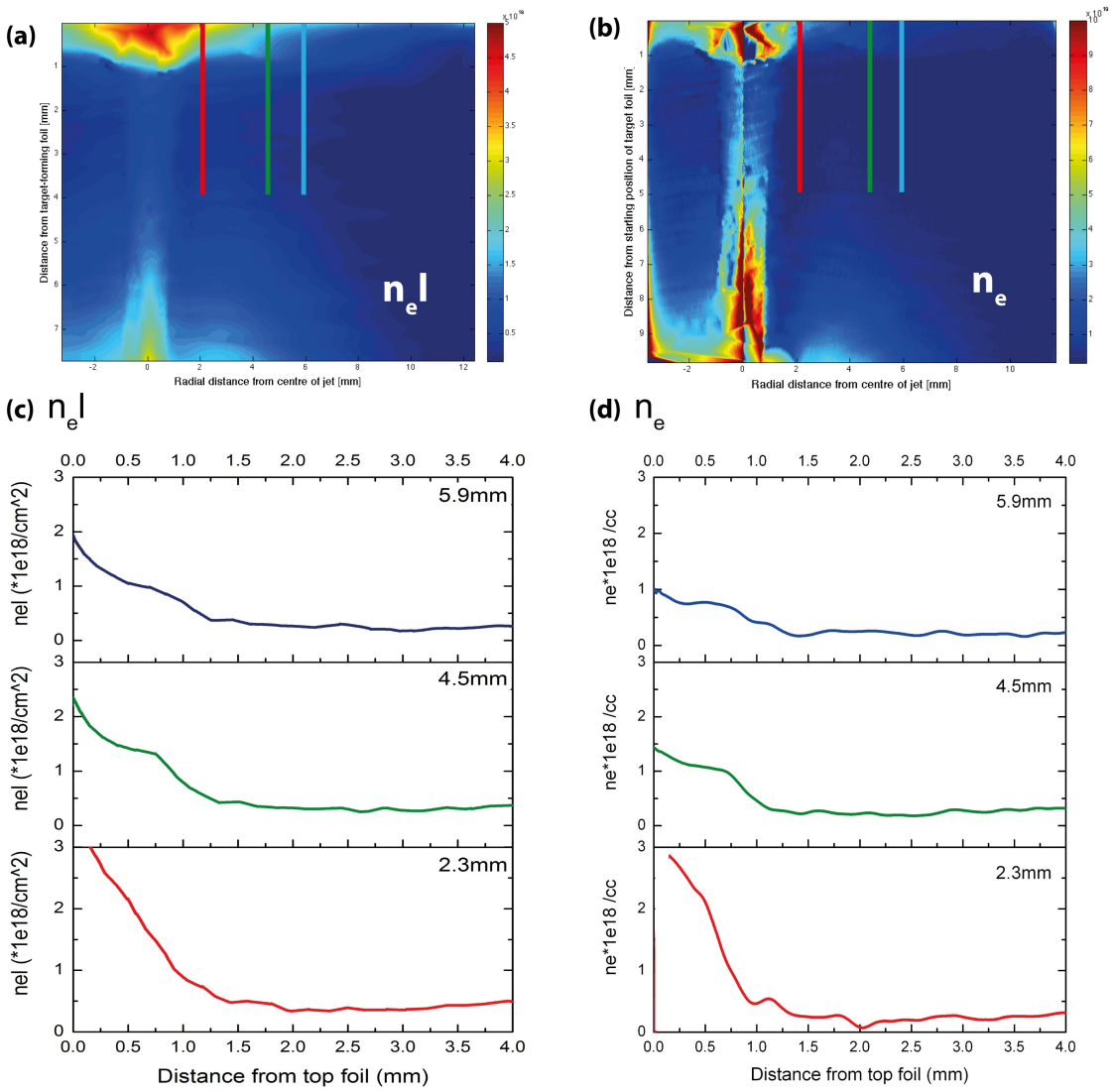

Figure 5.25: The interferogram taken at 260ns from 5.22a is processed to produce an $n_e l$ map (a) as described in appendix A. The electron density, n_e, map, (b), is found through the Abel inversion of (a). (c) $n_e l$ and (d) n_e three averaged axial line outs from the density maps, the positions of which are marked on both (a) and (b). Experiment s060712B.

after current start, is shown in figure 5.26.

The stationary shock is seen extending outwards with a slight downward curve. At the shock front the plasma is seen to be very dense causing the fringes of the interferogram to become discontinuous or obscured in localised regions, though the fringes can be traced around these areas allowing the density behind the shock front to be found. The fringe discontinuity is most apparent close to the interaction region of the jet and target-forming foil. At larger radius from the jet it is possible to follow

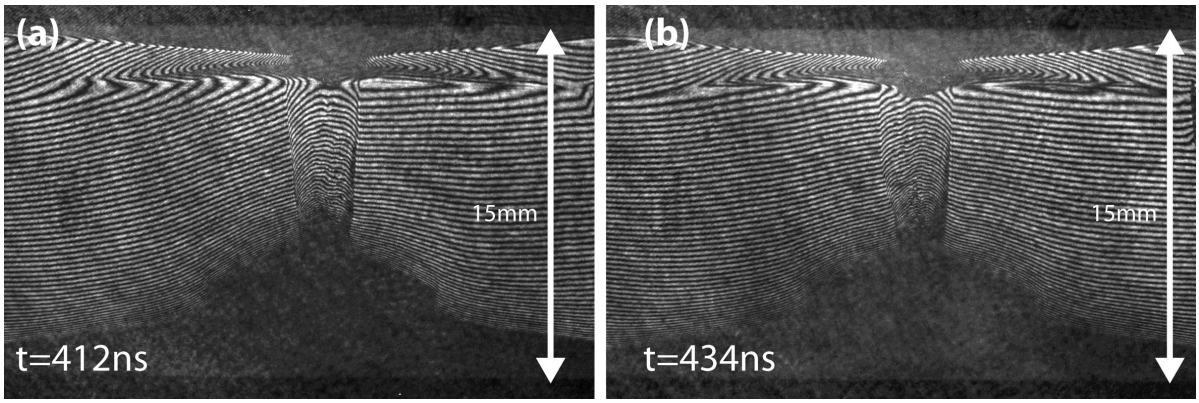

Figure 5.26: The production of the stationary shock is highly reproducible from experiment to experiment. (a) taken at 412ns from experiment s052412. (b) taken at 434ns from experiment s052912. The spacing of the jet-forming foil and the target-forming foil is 15mm. It can be seen the position and shape of the stationary shock is unchanged between the two experiments.

the fringes though the shock front.

5.4.2 The electron density contrast between the halo plasma and the material above the stationary shock

The electron density jump across the fully formed stationary shock structure will now be discussed. The interferograms are processed to produce an electron density map, $n_e l$ as is described in the appendix A. Figures 5.27, 5.28 and 5.29 show the processed interferometry from three different experiments, presenting the electron line density, $n_e l$, electron density, n_e which is obtained though Abel inversion of $n_e l$ and several line outs axially through the stationary shock. The jet-target interaction is fully formed in all of the images, which cover a time period after the current start from 434ns to 490ns. The jet can be seen on the bottom half of the images as a well defined vertical column. The stationary shock is seen as a density increase ~2mm below the target-forming foil which is in the top portion of all the images.

Figure 5.27a,b show the $n_e l$ and n_e density maps respectively for 434ns after current start. The stationary shock extends radially outwards ~15mm from the centre of the jet, visible on the $n_e l$ and n_e density map.

The five line outs in figure 5.27c are shown by a red line on figures 5.27a and

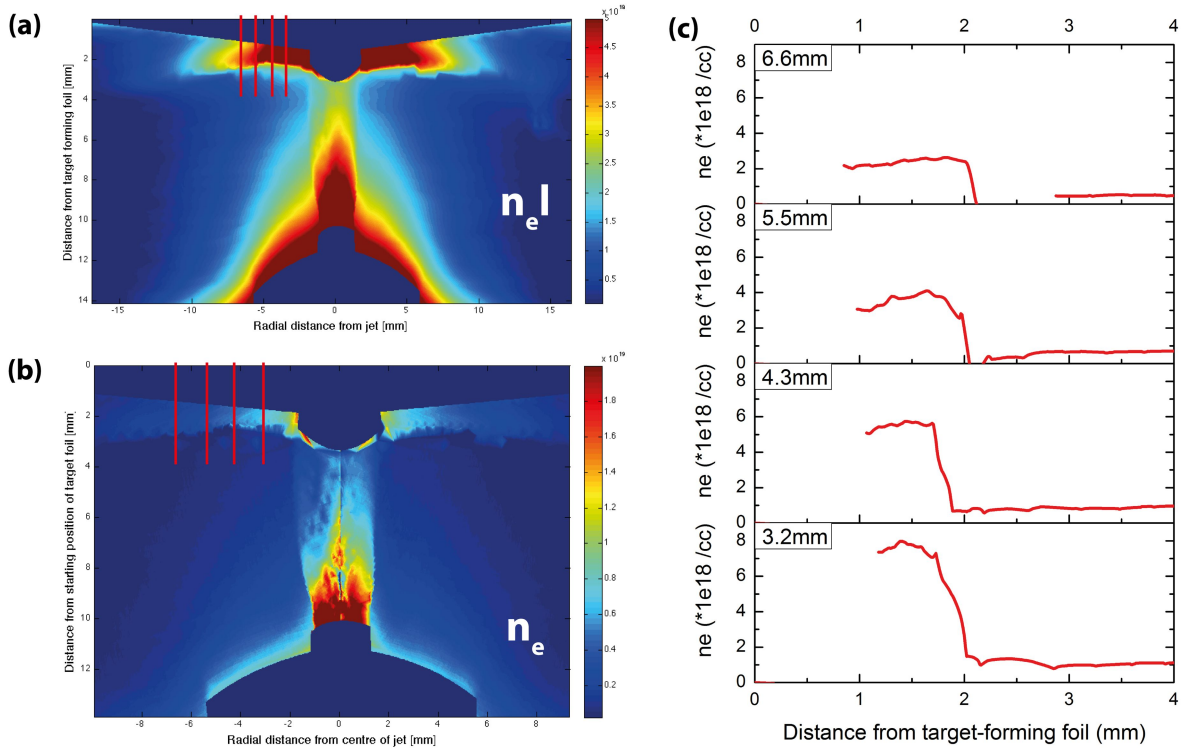

Figure 5.27: The jet-target interaction with 15mm spacing at 434ns from current start. The figure (a) the electron line density map, $n_e l$ and the electron density map of (a) in figure (b). Line outs across the stationary shock are shown in figure (c). 'Roughness' at the stationary shock from results from low resolution in the calculated phase map, discussed in section 3.2.3.2. From experiment s052912.

5.27b. The profiles show the electron density which is calculated from an averaged set of 10 adjacent columns of pixels in the n_e map, in order to smooth small errors in the n_e calculation. The stationary shock appears in figure 5.27c as a abrupt increase in the electron density at ∼2.5mm.

Figure 5.28a,b show the $n_e l$ and n_e density maps respectively for 464ns after current start, although the development of the shock and jet appears to correspond to an earlier time due to low current in this experiment, this accounts for the discrepancy in the absolute density values shown in the profiles. The jet can be seen as having distinct edges in both the $n_e l$ and n_e density maps. The electron density map in figure 5.28 appears to show a hollow profile for the jet, though this may be due to either inaccuracy in the Abel inversion or the low current in this experiment, as this is not seen in figure 5.27 or figure 5.29 taken at times both earlier and later

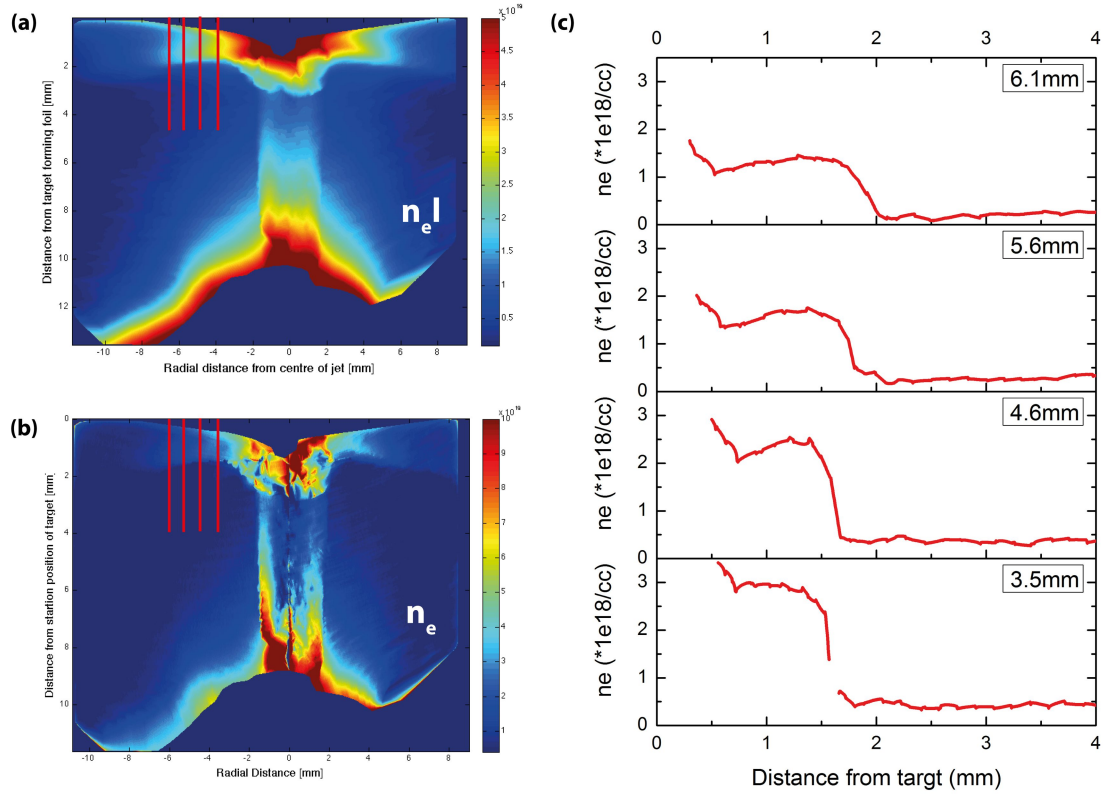

Figure 5.28: The jet-target interaction with 15mm spacing at 464ns from current start. Due to low current in the load the developmental time is effectively earlier than the electron density plots shown in figures 5.27 and 5.29. The figure (a) shows the electron line density map, $n_e l$ and the electron density map of (a) in figure (b). Five line outs across the stationary shock are shown in figure (c). From experiment s040212

than the image in figure 5.28.

Figure 5.28a and 5.28b indicate the region where the several line profiles shown in figure 5.28c are taken with a red line. The stationary shock is visible in figure 5.28c as a sharp increase in the electron density at ∼1.5mm and is seen to extend radially to the edge of both of the density maps in figures 5.28a and 5.28b. The region above the shock on the profiles can be seen to decrease in density before again increasing towards the target, this is also partially noticeable on the n_e density map in figure 5.28b.

Figure 5.29a and 5.29b show the $n_e l$ and n_e density maps respectively for 490ns after current start. It can be seen that the region of increased density forming the stationary shock extends radially outwards ∼12mm from the centre of the jet, clearly

visible on the $n_e l$ density map. The jet is seen to be denser in figure 5.29 than in the previous two n_e density maps at 434ns and 464ns. The jet is seen to have a distinct boundary with respect to the halo plasma.

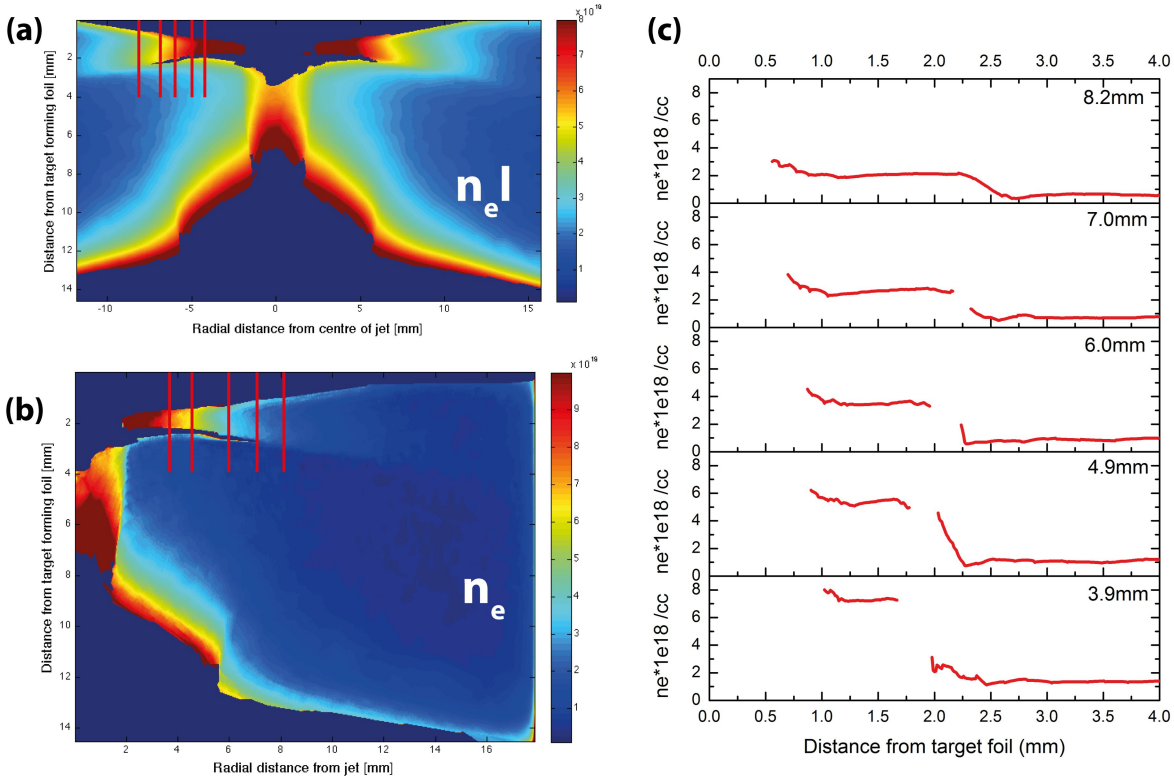

Figure 5.29: The jet-target interaction with 15mm spacing at 490ns from current start. (a) electron line density map, $n_e l$ and the electron density map for the left hand portion of (a) in figure (b). Four line outs across the stationary shock are shown in (c). From experiment s032812

The five electron density line outs shown in figure 5.29c give the position of the stationary shock as ∼2mm below the target foil surface. The position of the profiles is indicated by the vertical red lines of the density maps in figure 5.29a and 5.29b.

On the three figures shown, 5.27, 5.28 and 5.29, the electron density is seen as a large jump in density forming a stepped profile. This sharp increase in density is seen to extend radially away from the jet in the line outs shown with the figures for ∼10mm. In some of the electron density profiles there is a dip in the electron density behind the shock front before again rising in density at the target-forming foil surface.

From the density profiles shown in figures 5.27, 5.28 and 5.29 the jump in electron

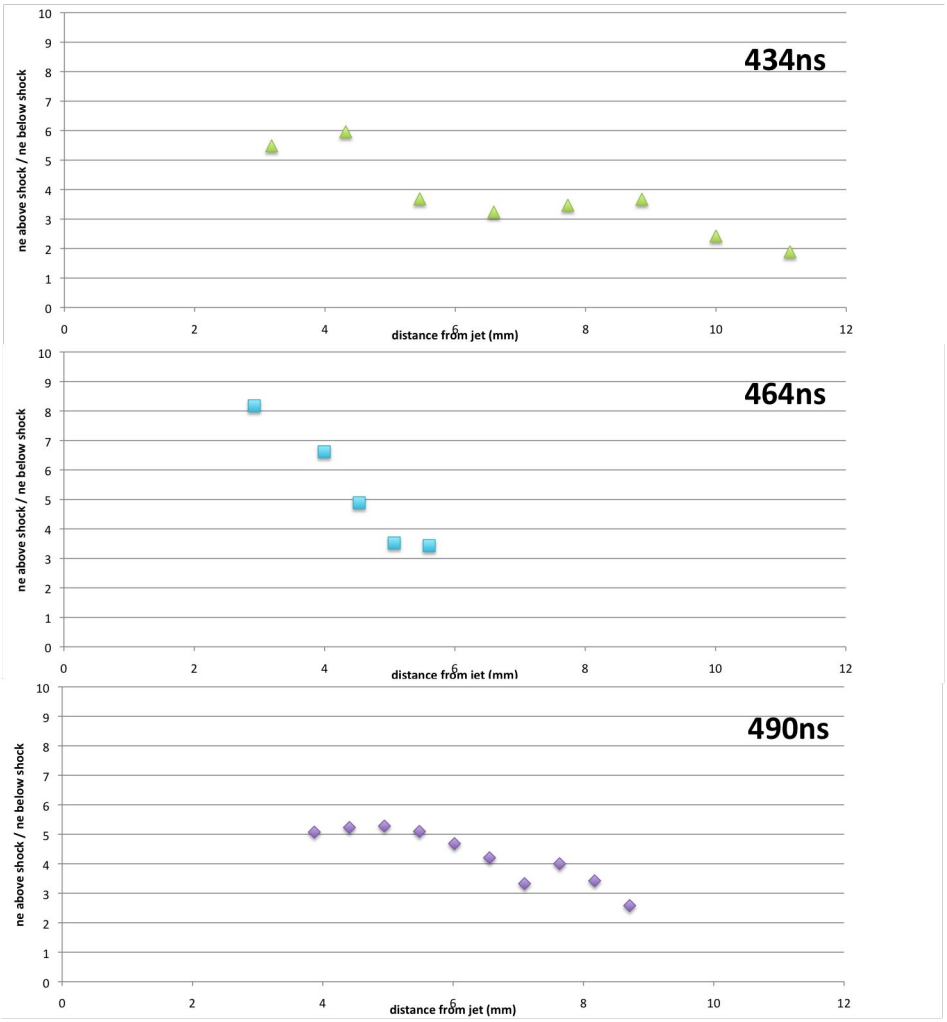

Figure 5.30: Jump in electron density across the stationary shock. From experiments s052912, s040212 and s032812.

density before and after the shock can be found, this ratio of the density conditions before the stationary shock in the halo plasma and at the peak of the stationary shock is evaluated in figure 5.30.

It can be seen from the figure that there is a very strong jump in density across the shock front that increases the electron density between 2 to 8 times the halo plasma electron density. The largest density increase is seen closest to the jet and corresponds to when the shock has shortest width. The width of the shock is defined at the distance over which the density jumps from the halo plasma density to the peak density in the shock front. This is summarised in figure 5.31.

Figure 5.31 shows that the width of the shock front is increasing with radius. As the width of the shock is seen to increase, the electron density contrast above and

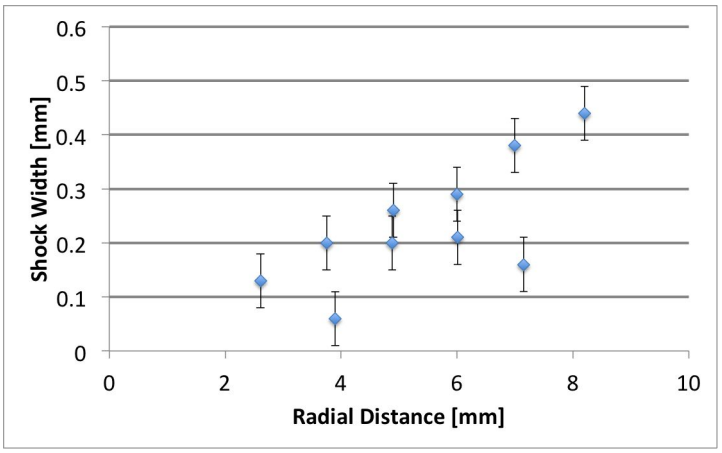

Figure 5.31: The 'width' of the shock as measured form the axial line outs through the stationary shock. From experiment s032812 and s052912.

below the shock is seen to decrease.

5.4.3 Temperature of material above the stationary shock from Thomson scattering

Using a Thomson scattering set up as described in the previous section and shown in figure 5.12, the temperature of the material above the stationary shock can be estimated.

The probe laser is aligned to scatter from a region ∼1mm below the target-forming foil using the positioning method described previously in this chapter. This region will be above the stationary shock at the time the laser probes the system which is set to be 491ns. It is expected the system will be in a similar stage of development as shown in the electron density map in figure 5.29.

Figure 5.32 shows the alignment of the optical fibre bundle heads with reference to the jet and stationary shock as seen during the experiment. Fibre 14 on the second optical fibre bundle was not used during the experiment.

Figures 5.33 and 5.34 show the observed scattered spectrum as seen on fibres 1 to 13 from the experiment. The background spectrum is shown on fibres 1 and 13 in red. With comparison to the scattered spectrum observed below the stationary shock in the jet and halo plasma, from figures 5.15 and 5.16, it is immediately apparent that the scattered spectrum above the shock is significantly broadened and ion acoustic

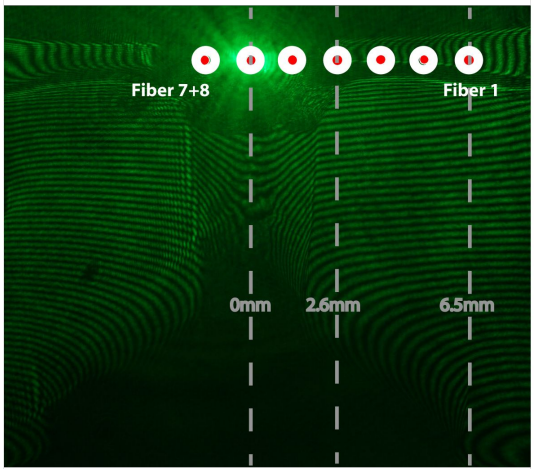

Figure 5.32: The alignment of the optical fibres to observe the region above the stationary shock as shown on an interferogram taken at 490ns which is the same time as the Thomson measurement. Experiment s032312.

effects are dominant. Fibres 7 and 8 are observing the axis of the jet and show a very complex scattered and broadened spectrum, which contains contributions from a two-temperature or two-velocity plasma volume. Due to this unusual convolution the temperature from these scattered spectrums could not easily be estimated.

The presence of the large broadening and the double peak or splitting of the scattered spectrum implies that ZT_e is larger than T_i. The scattered spectrum observed by the fibres can be fit in the manner previously described to find the temperature of the ions and the product of ZT_e.

Figure 5.35 shows the accuracy of the temperature fit for the scattered spectrum observed on fibre 6. The best fit assumes T_i=85±17eV and ZT_e=200±40eV and $n_e = 12 \times 10^{18}\text{cm}^{-3}$. The two accompanying graphs to the figure 5.35 show the variation of the two fitting parameters, ZT_e and T_i by 20% to demonstrate that the fit is accurate to this degree or better. The fit is sensitive to order of magnitude changes in n_e but not small adjustments. The n_e density map from s032812 shown in figure 5.29 was used to provide the electron density for the fit as it was taken at the same time after the current start as the Thomson measurement (490ns).

Figure 5.36 shows the calculated temperatures in the plasma volumes observed by the fibres. These temperatures are plotted against their radial position with respect to the predicted centre of the jet. Figure 5.36 shows the ionic temperature

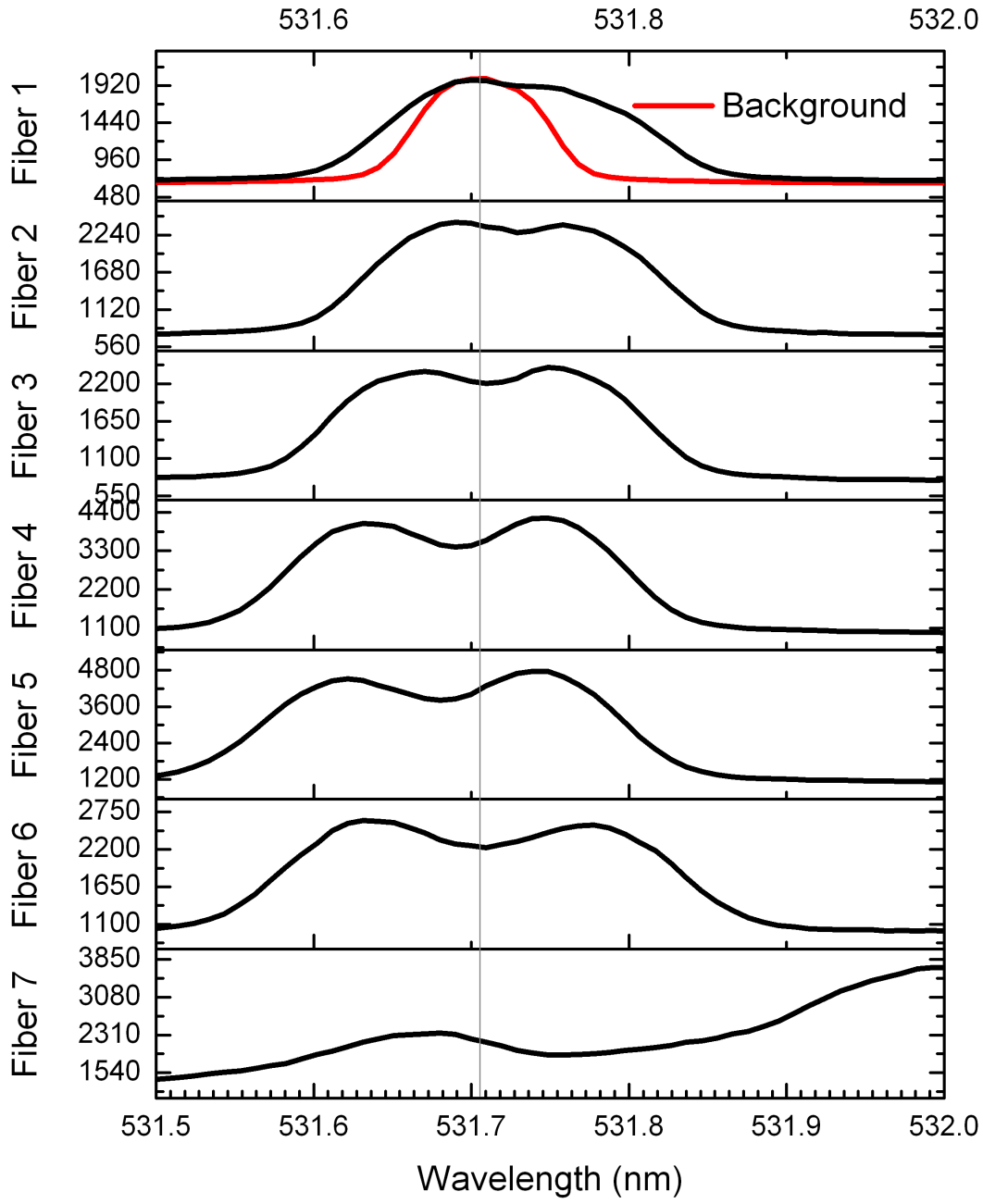

Figure 5.33: The scattered spectrum as seen on the spectrometer from fibres 1 to 7. The unscattered background spectrum is indicated in red on fibre 1. This shows the natural frequency of the laser and the spectrometer resolution. From experiment s032312 at 491ns.

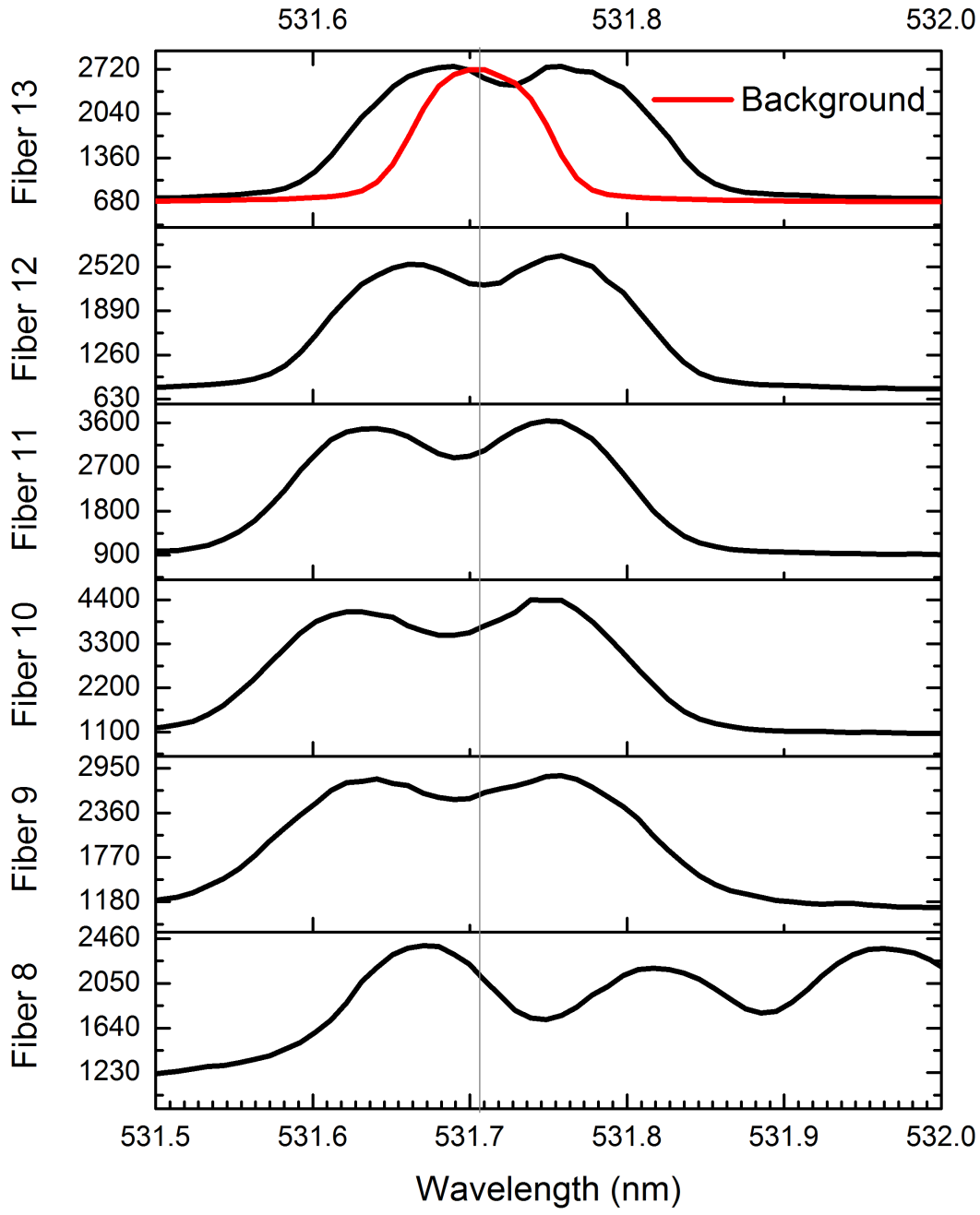

Figure 5.34: The scattered spectrum as seen on the spectrometer from fibres 8 to 13. The un scattered background spectrum is indicated in red on fibre 13. This shows the natural frequency of the laser and the spectrometer resolution. Fibre 13 views the same plasma volume as fibre 2. From experiment s032312 at 491ns.

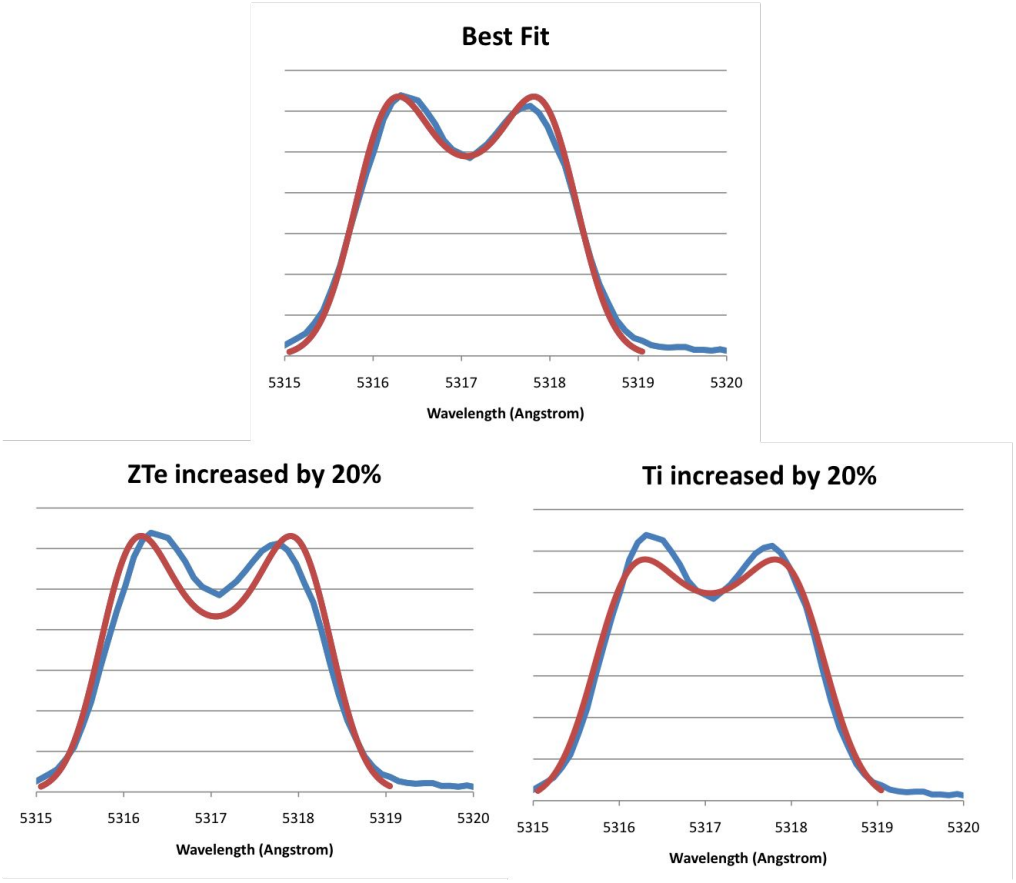

Figure 5.35: The accuracy of the fitting algorithm is sensitive to ZT_e and T_i. The figure shows the best fit for fibre 6 and a 20% increase in T_i and ZT_e showing temperature can be fit with a better than 20% accuracy.

decreases with an increase in radius, giving a range of temperatures, T_i ~40±8eV to 80±16eV. The product of the ionisation and and the electron temperature also decreases with increasing radius from the jet and gives a range of temperatures, ZT_e ~200±40eV to 80±16eV.

The ionisation and electron temperature estimated by ZT_e in the shock front cannot be easily distinguished by the Thomson scattering diagnostic. In order to find the ionisation Z, an assumption about the relationship of T_e, Z and T_i must be made.

A simple estimation of Z, shown in figure 5.37a, assumes thermal equilibrium such that $T_i = T_e$. The ionisation shown in the figure is found from ZT_e/T_i. This assumption may be valid if the scattering volume where the measurement is taken (~1mm from the shock front) is on the order of the mean free path in the plasma,

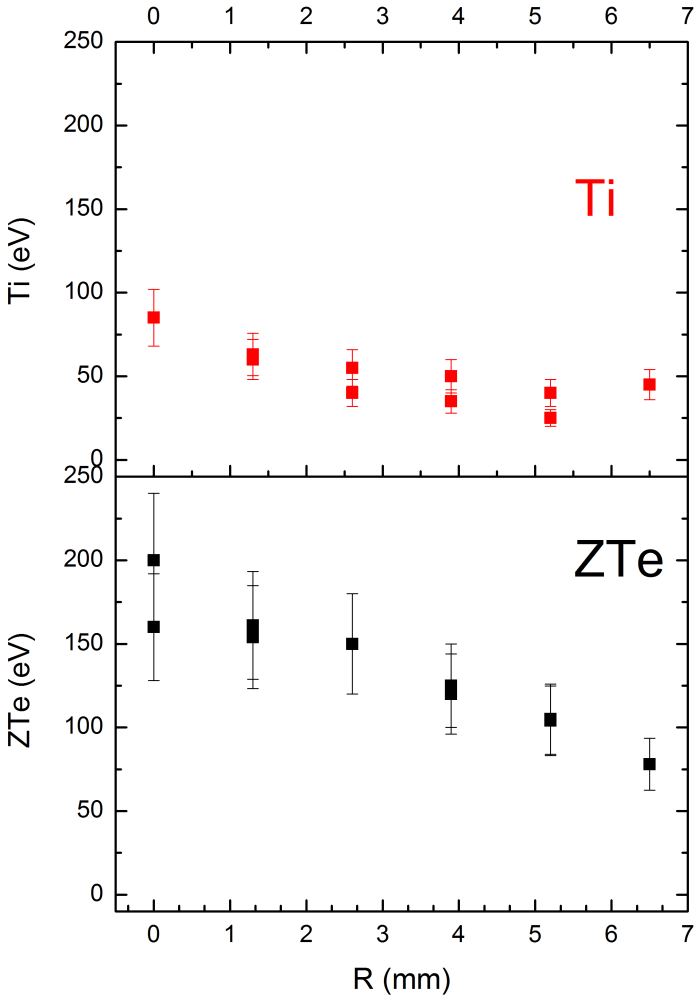

Figure 5.36: Ion and the product of ionisation and electron temperature as a function of radius. From experiment s032312 at 491ns.

the validity of this assumption will be discussed in section 7.6.

A second method of estimating the ionisation from the experimentally obtained ZT_e values uses the threshold energy required to ionise an aluminium atom $n\times$ to give a analytical relationship between the temperature of the plasma and the ionisation. Figure 5.38 shows the energy required for each ionisation level in blue and a 'fit' to these energy values given by $T = 2.5Z^{2/3}$. The experimentally obtained ZT_e value can be substituted into $T = 2.5Z^{2/3}$, to obtain an estimate for the ionisation which is shown in figure 5.37b.

The ionisation estimated from the 'energy level' model is higher than found

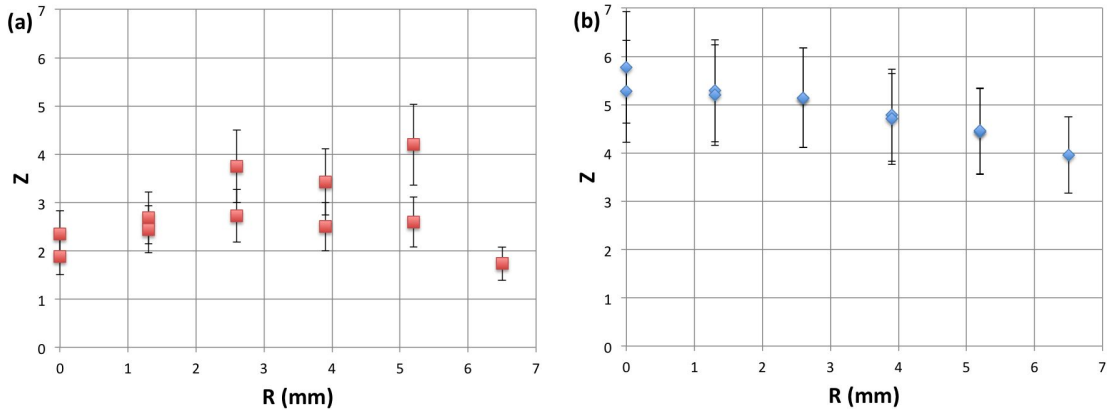

Figure 5.37: (a) Ionisation from assumption of temperature equilibration, $T_i = T_e$. (b) Ionisation from the ionisation energy levels of Al using $T = 2.5Z^{2/3}$. Error estimated at 20%. From experiment s032312 at 491ns.

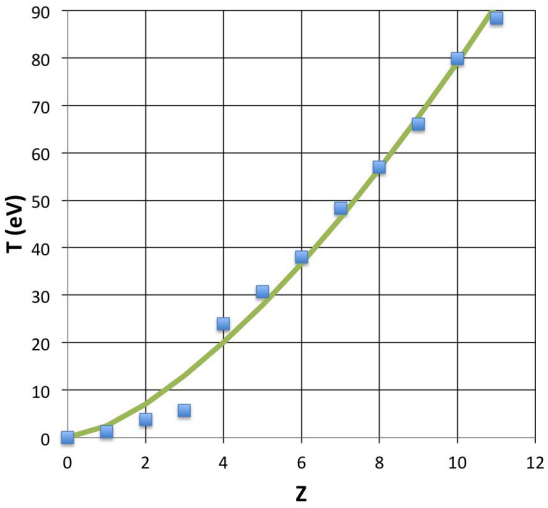

Figure 5.38: Temperature, in eV, required to ionise Al shown by blue markers. The function, $T = 2.5Z^{2/3}$ shown in green, gives a model for the ionisation-temperature relationship.

through the assumption of thermal equilibration. An ionisation of $3 < Z < 5$ can be used to estimate $T_e \sim 25 \pm 5$eV in the halo plasma shock ($R > 2$mm) from the two methods.

Due to the downward curvature of the stationary shock the temperature measurements are not at the same distance from the shock front at all observation volumes.

The stationary shock has a large electron density jump across the shock front and supports ion temperatures up to 5× higher than seen in the halo plasma. The

mechanism of its origin has not been explained through the observations made with the Thomson scattering or though the electron density maps. Two experiments will now be described that varied the topology of the target-forming foil in order to determine the driving forces in the stationary shock.

5.4.4 The effect from the material flow from the jet and the flow from the halo plasma

In investigating the mechanism driving the formation of the stationary shock and the origin of the material behind the shock it was useful to make a variation in the structure of the target which would allow the different interactions of the jet and halo plasma to be isolated.

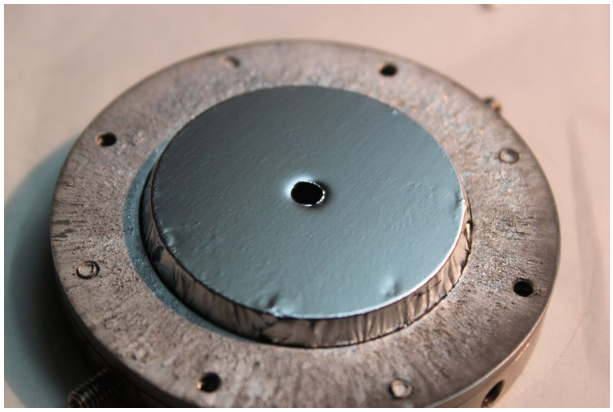

Figure 5.39: The assembled target foil with a 4mm diameter hole on axis of the foil. The hole was cut after the assembly of the target foil. The target is shown prior to instalment in the discharge chamber.

It is suspected that material from the jet does not flow radially outwards behind the shock as large radial velocities were not measured behind the shock. In order to ascertain if the material gathered behind the shock originated from the jet, a 4mm diameter hole was cut on the axis of the target foil as shown in figure 5.39. This will allow the dense flow in the body of the jet to pass through the target.

The role of the target was investigated through the use of a stainless steel mesh, as shown in figure 5.40, with a hole dimension of ∼2×2mm. The mesh target is a grid of wires that are expected to expand in the same manner as the thin foil target. However the wires will expand in all directions outwards from their cores, in

contrast to the thin foil which expands only towards the jet. The use of the mesh will reduce the density of plasma on the target at the arrival of the jet.

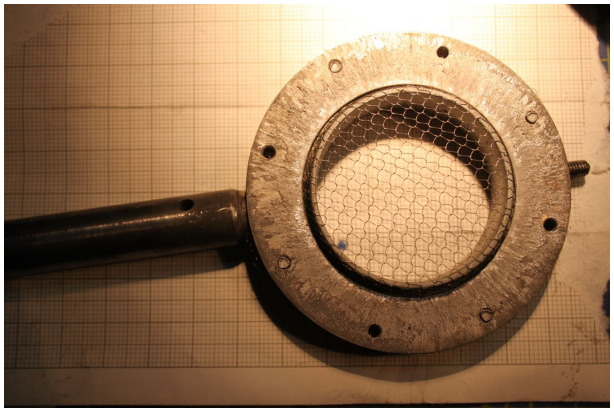

Figure 5.40: The assembled mesh target prior to instalment in the discharge chamber. The target is a stainless steel wire mesh with a ∼2×2mm hole dimension. The wire density was chosen to be low so that the expansion of the wires would be inhibited from creating a continuous surface plasma during the interaction with the jet.

Figure 5.41 gives a comparison between the three targets, thin foil (5.41a), foil with hole on axis (5.41b) and mesh (5.41c). The four frames are taken from the optical emission fast framing camera and selected to be at similar times after the current starts in the jet. The experimental set-up for the jet is unchanged in the three experiments. The target is positioned 15mm from the jet-forming foil in each experiment. The images for each experiment are presented on a millimetre scale and the time after current start is indicated on the frame.

Comparing figure 5.41b where a hole is placed on the axis of the target with the thin foil target it can be seen that the standing shock forms at the same position below the target-forming foil and at a similar time after the current start. The standing shock has a similar shape and radial length as in the thin foil experiment. On the axis of the jet, there is an absence of emission which forms the reverse shock feature. In figure 5.41a the reverse shock is seen as a bright shock moving into the flow of the jet, this is not seen on figure 5.41b.

Emission from the position of the mesh target in figure 5.41c is just visible. The jet appears unchanged from the experiments shown in figures 5.41a and 5.41b and there is no indication of an interaction in the flow of the jet. No static shock is

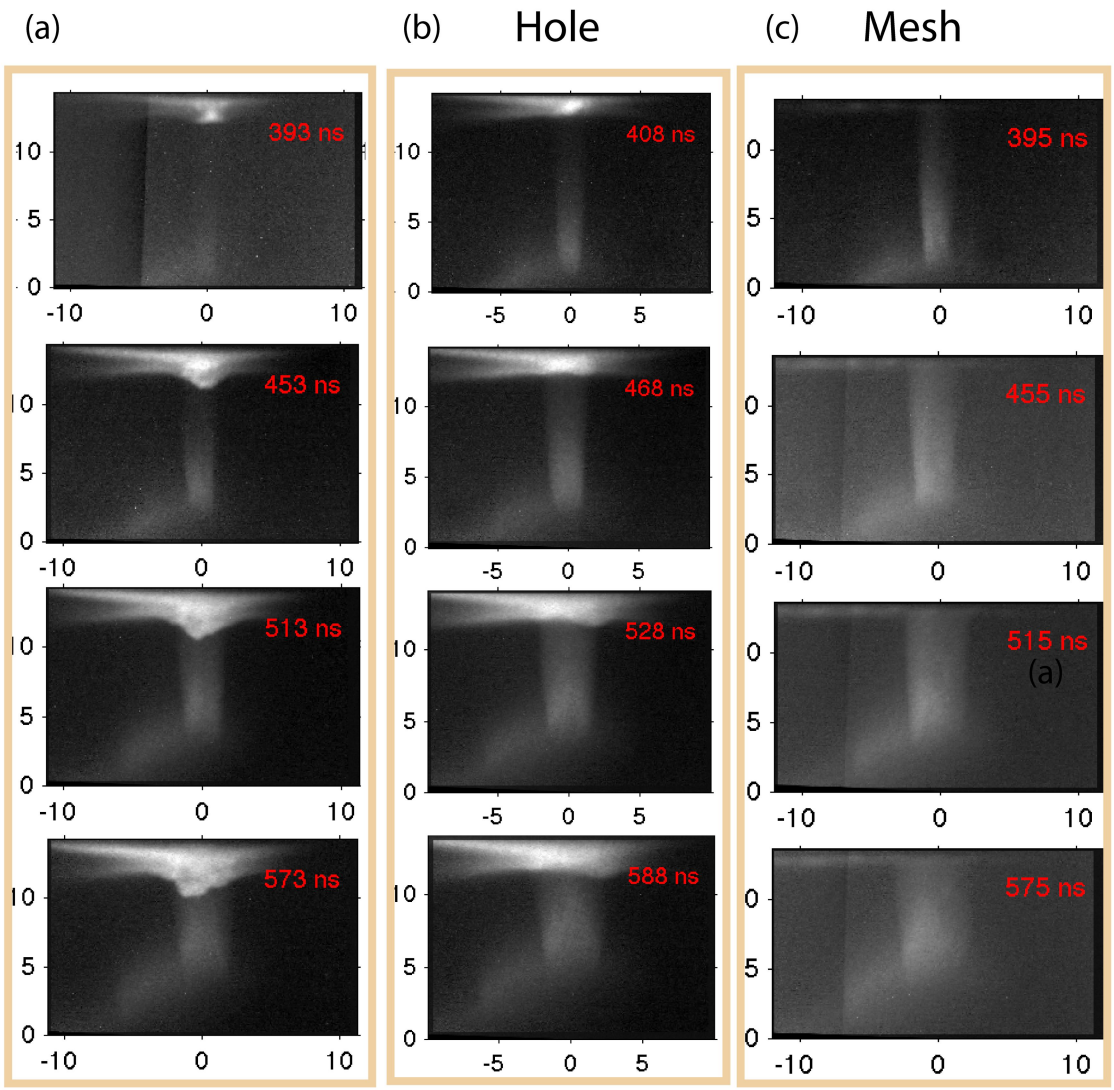

Figure 5.41: (a) shows the interaction of the jet with a target at 15mm. From experiment s052912. (b) shows the interaction of the jet with a target that has a 4mm hole on axis. From experiment s053012. (c) shows the interaction of a jet with a wire mesh target. From experiment s060112. All the images are on a millimetre scale.

visible on the fast framing optical camera, however inspection of the laser images shows that a shock forms at a large radial distance from the jet close to the target surface. This shock is seen in the interferometry image 5.42.

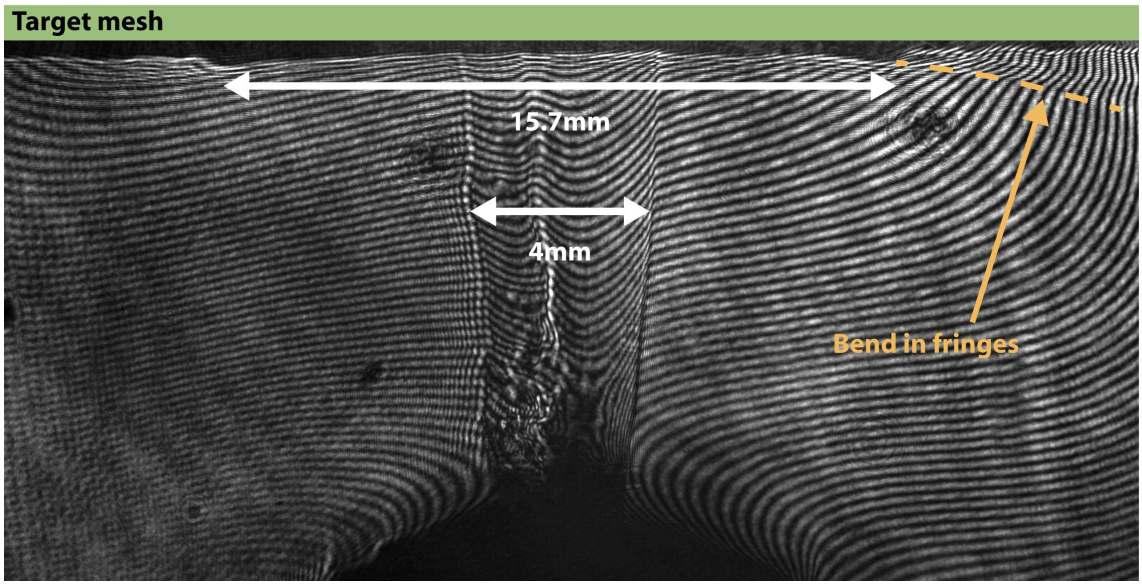

Figure 5.42: 532nm laser interferometry image at 405ns. From experiment s060112.

From inspection of figure 5.42, there is a region of the target-mesh that has expanded downwards towards the jet by 0.43mm which is 15.7mm in diameter, in comparison the jet into a solid target produces a surface plasma that extends 1mm to 1.5mm below the starting position of the target-forming foil. To the edge of this step a compression in the fringes indicates a change in density similar to the stationary shock. This shock is forming ∼0.5mm from the expanded mesh surface. The surface of the target shows a periodic undulation which is the spacing of the mesh wires. The interaction region of the jet and mesh target shows no indication of a reverse shock in the flow of the jet or of turbulence that was seen in the reverse shock.

The interaction region of the jet and target in figure 5.42 is similar to the interaction observed when a hole is placed on the axis of the thin foil. A comparison of the thin foil taken at the same time after current start and the thin foil with a hole on axis is show in 532nm laser interferometry in figure 5.43.

It can be seen in the two interferograms in figure 5.43 that the jet and the

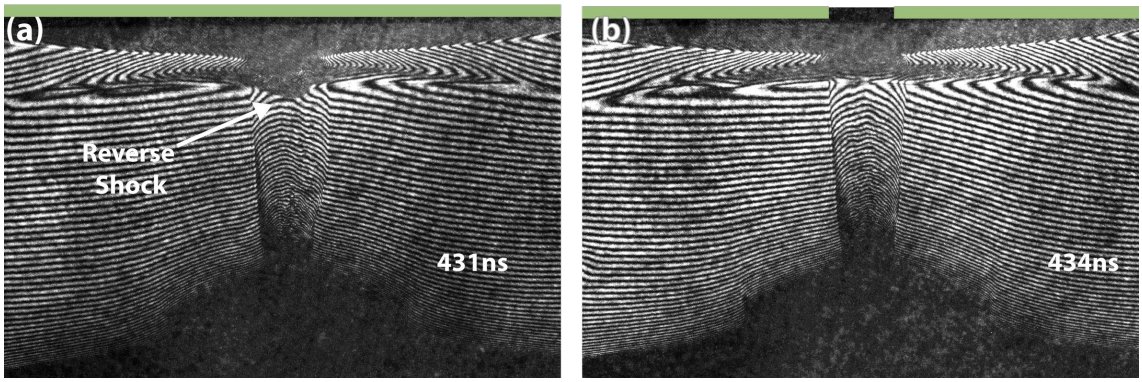

Figure 5.43: Comparison of observed structures at similar times after current start between (a) normal Al target and (b) target with a 4mm hole above the flow of the jet. From experiments s052912 and s053012.

stationary shock are unperturbed by the presence of the hole on the axis of the target foil. The jet has a comparable diameter in both interferograms and the stationary shock is the same distance from the target foil retaining its characteristic curved shape. In figure 5.43a the interaction region between the target-forming foil and the flow of the jet produces a reverse shock which is indicated on the image. It is clear that this is absent from figure 5.43b.

The formation of the stationary shock is shown to be independent from the flow in the body of the jet by the modification of the target by positioning a hole on axis. The experiment allows the conclusion that the stationary shock arises from an interaction of the halo plasma and the target, and that the observed density increase behind the shock does not originate from the jet body.

The mesh target indicates the position and strength of the shock may depend on the density of material at the target, which needs to provide a 'stopping' force to the supersonic material in the halo plasma.

5.4.5 Electron beam emission from the jet-forming foil cathode

The electron emission from the jet-forming foil and the cathode can interact with the target prior to the arrival of the jet and halo-plasma. The Faraday cup, described in section 3.2.7, directly measures a current generated by high energy electrons

impacting on a metal target after passing though a screening foil. When the electron beam is absorbed on the target a change in voltage is measured by the oscilloscope across the resistors in the cup. The voltage seen by the scope during the shot is then directly proportional to current via ohms law ($V = IR$). The screening foil acts to cut off the thermal electrons and places a low energy limit on the energy of the electrons that can pass though the foil without being absorbed.

Figure 5.44 shows a schematic and photograph of the Faraday cup fielded above the jet-forming foil. The screening foil for the Faraday cup acts as the target foil. In this case the foil is 6.5μm thick. The 6.5μm foil cuts off electrons with an energy below 27keV. Behind the screening foil there is a 10mm iris that limits the sampling area of the Faraday cup allowing the origin of the electron beam to be inferred to within this area.

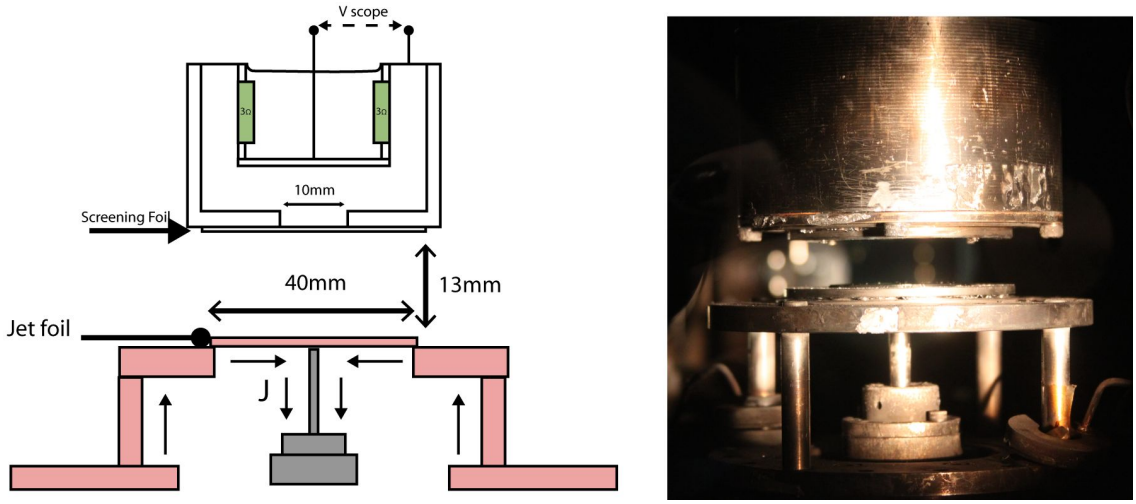

Figure 5.44: The experimental setup for the Faraday cup above the jet. The schematic shows the hardware for the jet and the Faraday cup with a screening foil and 10mm aperture. The Faraday cup is suspended from the lid of the discharge chamber. The photograph shows the hardware in the discharge chamber.

Figure 5.45 shows the electron current measured above the target foil from the Faraday cup fielded on three experiments. It can be seen a current of ~100A is measured starting at 100ns after current start in the jet-forming foil. This corresponds to the initial formation of the jet. The current is then measured to be 100A until 400ns after current start, this corresponds to the early formation of the static shock

when the jet interacts with the target-forming foil.

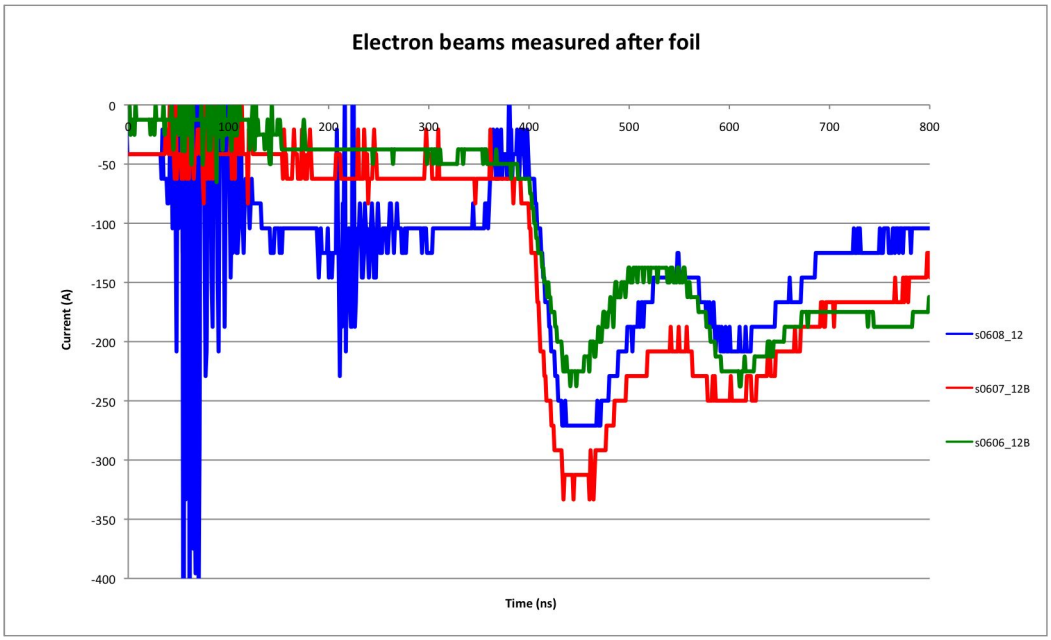

Figure 5.45: Results from 3 shots of an Al jet into a Al foil target of 6.5μm thickness with a separation of 13mm. Time is measured from current start in the jet foil.

The attenuation curve shown in figure 3.17 can be used to find the proportion of the beam absorbed into the foil. By considering the energy deposition near the surface of the foil the temperature rise T, in the material (shown in equation 3.69) can be found. The materials properties of resistivity, χ, and density, ρ, determine the efficiency of the energy deposition.

The spectrum of energies in the original beam is not known, and as the target foil is the only filter applied to the electron beam the measured currents can be used to estimate the intensity of an electron beam with a given energy.

From previous experiment with radial wire arrays, a voltage of 50kV has been measured at the cathode [53]. This can be used to assume a 50keV electron beam is created, though the current density from a radial wire array is higher at the cathode than from a radial foil array as the wires concentrate the current density locally at the cathode.

For an initial electron beam of 50keV, 44% of the beam is deposited into the foil, derived from the attenuation curve shown in figure 3.17. The 100A current

measured after the target foil corresponds to an monochromatic 50keV beam with a power of $7.8 \times 10^6 W$, for a constant 100A current for 200ns this is a deposition of 0.687J, for 300ns this is 1.03J.

This beam was collected from a 10mm diameter area, but it can be assumed the beam originates from a smaller area, on the scale of the jet. The jet has a diameter of ∼1mm at its early time formation. For this discussion it is assumed the electron beam has a cross section of 1mm. The vaporisation of Al requires $294 kJ mol^{-1}$ which for this volume of foil (assuming the whole foil is heated) requires 0.6J deposited by the beam. It can be seen that this requirement is met after the 200ns point, which corresponds to the arrival of the jet at the target.

From these measurements it is possible that the electron-beam heating of the target has some role in the early time formation of the shock structures (such as the reverse shock) directly above the cathode. This can be tested further by changing the polarity of the current in the jet, which will eliminate the effect of an electron beam at the target surface in early time and will be discussed in chapter 6.

It is unlikely that the electron beam has a significant role in preheating the target-forming foil for the development of the stationary shock as the measured energy deposition requires the beam to be concentrated in a narrow area.

The formation of the stationary shock has been determined to arise from the interaction of the halo plasma with an opposing object or field able to counter the ram pressure from the halo plasma. The ions in the halo plasma are heated as they move though the shock front and ionisation appears to increase, though this is not known as the ion density has not been measured directly. However, the electron density is seen to increase abruptly and the shock width is <1mm. Material flow from the jet accumulating at the surface of the target was ruled out as the cause for this density jump through modification of the target.

5.5 The reverse shock in the jet

In the interaction region of the jet and the target-forming foil a shock is observed to propagate counter to the flow of the jet. This is termed the reverse shock. During the

experiments there were limited diagnostics to probe this feature fully as the electron density gradients created though the shock were large. A short presentation of the results will be made here as a starting point for future work.

The reverse shock is shown in figure 5.46 in two interferogram images. The jet can be seen in both images with a diameter of $\sim$ 4mm. The stationary shock is indicated to either side of the jet $\sim$2mm below the target surface. In both images the interaction region of the jet and target-forming foil is seen to be dense, indicated by closely packed fringes, and with localised density gradients indicating instability or small scale structures in the plasma. The reverse shock is seen to have a curved profile in the flow of the jet, with the furthest penetration into the jet at its centre. The surface of the reverse shock is not smooth and it also seen to be an unstable boundary in the flow of the jet.

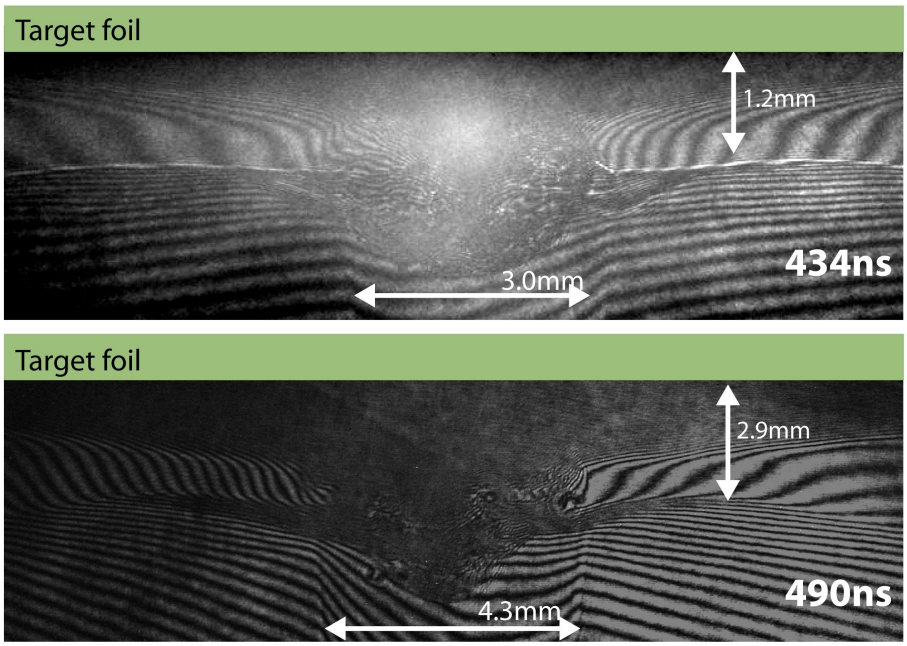

Figure 5.46: 355nm interferometry of the region in the reverse shock in the flow of the plasma. The two images zoom in on the turbulent and dense region in which the reverse shock is formed. Taken at 434ns and 490ns from experiments s052912 and s032812 respectively.

The the emission from the reverse shock can be seen on the optical emission fast-framing camera. The position of the lowest point of the emitting region of the reverse shock is plotted against the time of the frame of the camera, this is shown

in figure 5.47. Figure 5.47 shows a frame from the fast-framing camera with the reverse shock marked in green and the emission from the target-forming foil in blue. The accompanying graph shows that the emitting region of the reverse shock has a velocity of $\sim 9 \pm 2$km/s counter to the flow of the jet. In comparison, the expansion velocity of the emitting region of the target-forming foil is found to be $\sim 4 \pm 2$km/s.

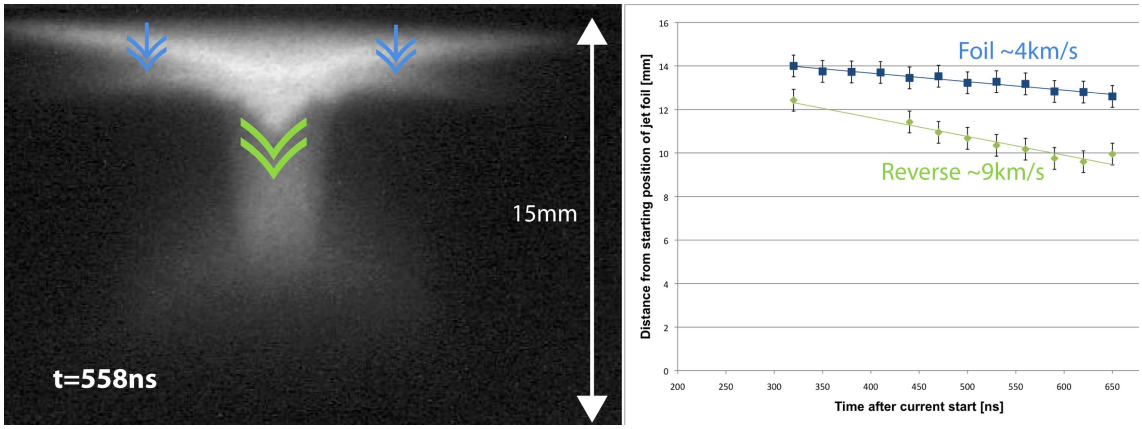

Figure 5.47: The velocity of the optically emitting region of the reverse shock feature is found from the optical fast framing camera diagnostic. Shown for reference is the expansion of the target foil. Annotated image from experiment s032812.

The plasma conditions behind the reverse shock, near the target-forming foil, have been shown in the previous section in the Thomson scattering results. The scattered spectrum observed on the fibres placed in this region is shown in figures 5.33 and 5.34. It is seen that the scattered spectrum is very difficult to fit due to the large broadening and splitting which results from a plasma volume which is very dense and possibly containing large temperature gradients and velocities. This supports the results seen in the interferometry images of this region that show the refractive index gradients in this region to be very large, and the density measurement is limited by the aperture of all of the laser imaging systems.

Figure 5.48 shows three electron line densities taken through the reverse shock region. The profiles are averaged over 10 adjacent pixels to smooth the discontinuities in the calculated $n_e l$ map. The density is seen to steeply increase in this region, and on the red and green profiles in the figure a stepped region can be seen that forms the reverse shock front.

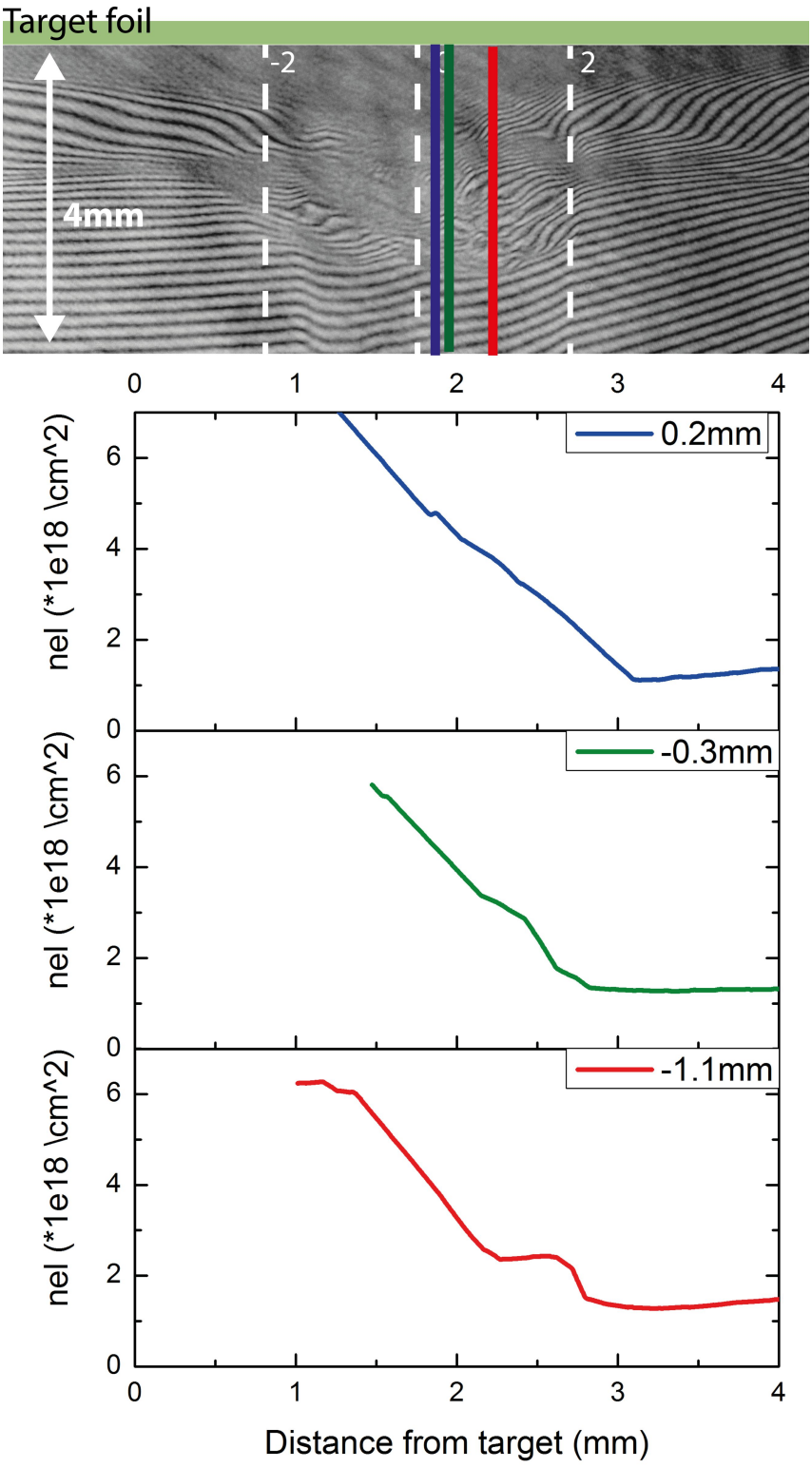

Figure 5.48: An 355nm laser interferogram marked with the position of the line outs taken from inside the jet. The electron line density profiles are shown from three radial positions and averaged over 10 adjacent columns. From experiment s040212.

As the laser interferometry shown in figure 5.48 demonstrates, the high refractive index gradients observed behind the reverse shock is inhibitive to a more detailed study of its nature with the current laser probing set up. The laser and optical emission images also suggests that the reverse shock does not have a high degree of cylindrical symmetry as it progresses into the flow of the jet. The lack of symmetry inhibits the use of Abel inversion in this region which means electron densities can only be inferred. An interferometry system with a high acceptance angle or a radiography set up may be more appropriate for the study of this structure.

The next chapter will introduce experiments investigating the effect of reverse polarity on the formation and propagation of the jet and the shock structures created at the interaction with a thin foil target.

Chapter 6

Reverse Polarity Aluminium Jet

This chapter describes experiments investigating the effect of reversed current polarity in the interaction of a supersonic plasma jet and thin foil target. According to a simple one fluid magnetohydrodynamic model, the reversal of current direction should have no effect on the dynamics of the jet. However, there are observed to be some differences between the reversed current polarity jet and the jet described in the previous chapter.

The next chapter will describe the interaction of colliding supersonic flows created by combining the jet described in the previous chapter with the reversed current polarity jet that is described here.

6.1 Experimental set up

The elements in the experimental set up of the reverse polarity jet are designed to be the same as in the standard polarity jet experiments. The difference between the two experiments is that the electrode polarity is inverted such that a cathode is now an anode in this set up. The size and thickness of the foil for both the jet and target is the same, also the size of the central electrode used for the jet-forming foil remains the same diameter with respect to the previous experiments.

The experimental set up used for the reversed polarity jets is shown in figure 6.1. The hardware is shown in a schematic form in figure 6.1a and a photograph, in figure 6.1b, shows the experimental hardware in the discharge chamber prior to the

experiment. The different components of the hardware are labeled in the schematic for reference and the path of the current is shown. The jet will propagate downwards in this diagram from the jet-forming foil towards the target-forming foil.

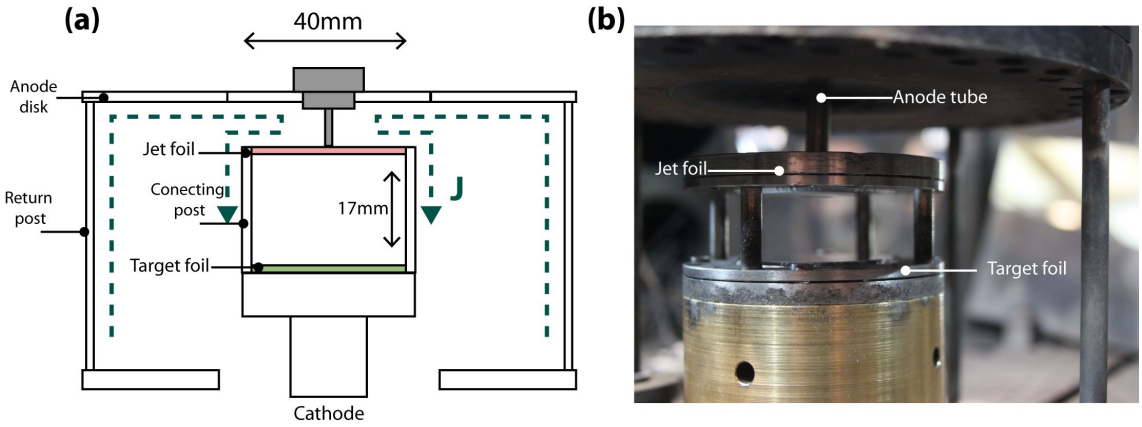

Figure 6.1: A schematic diagram of the hardware used in the experiments for the reverse polarity jet and a photograph of the hardware installed in the discharge chamber.

In figure 6.1a the jet-forming foil is shown in red, the target-forming foil is shown in green and the anode connection to the jet-forming foil is shown in grey. Both the jet-forming and target-forming foils are $14\mu m$ thick aluminium with an outer diameter of 40mm. The anode is formed of a hollow stainless steel tube with an outer diameter of 6.35mm. The anode tube is the same material and diameter as used for the cathode tube in the experiments described in chapter 5. The anode tube is positioned in the centre of the jet-forming foil, and the outer-diameter of the jet-forming foil is in contact with the cathode through a set of connecting posts attached to the foil holders of the jet-forming and target-forming foils. The current flows radially outwards from the anode connection to the cathode connection as marked by 'J' in figure 6.1a.

Figure 6.2 shows a photograph of the jet-forming and target-forming foils in the process of assembly. The foils are connected together via the connecting posts shown in figure 6.2 already attached to the left hand foil. The posts are attached to the foils once they are assembled into their holders as was described in section 5.1. In this experiment the target-forming and jet-forming foil holders are both identical to the jet-forming foil holder described in section 5.1. M3 screws are attached to both ends

of the connecting posts though the foil holders, securing them in-between the two foil holders. The initial experiment in this set up used eight connecting posts (as is shown in the figure 6.2) in order that the current density is distributed evenly across the foil. However, to improve diagnostic access the number of connecting posts was reduced to four connecting posts for the later experiments and no difference in the formation of the jet was observed.

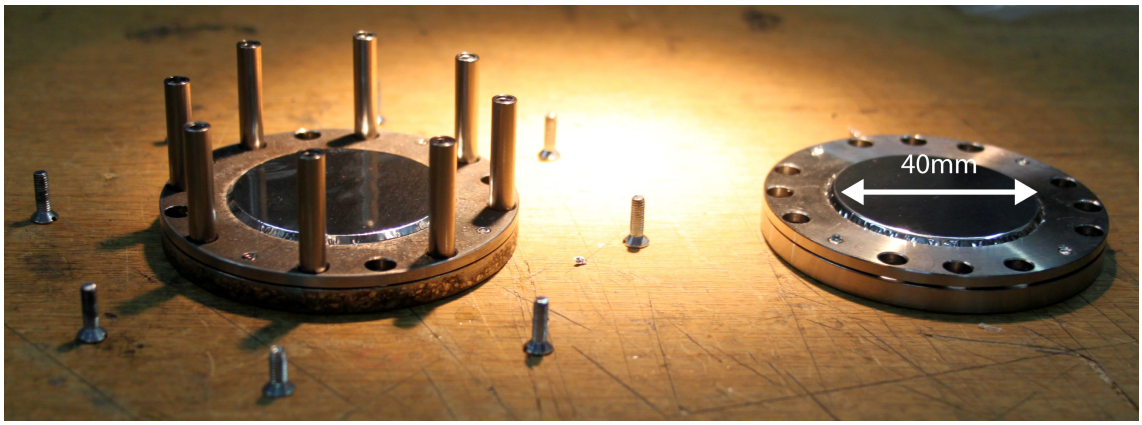

Figure 6.2: The assembled target and jet foils pictured with the connecting posts. The foil holders are identical. The number of connecting posts shown is eight, but the results reported in this chapter used four, no asymmetry to the distribution of current was observed in the jet formation with this set up.

The assembled foils are installed in the discharge chamber by connecting the target-forming foil holder to an expanded MITL (the base of which is shown in figure 6.1b) which is the same outer diameter as the target-forming foil holder. The target is at the cathode (negative) voltage, whereas it was previously at ground voltage. The connecting posts between the two foils sets the separation between the foil surfaces at 17mm. The anode tube is pressed into the jet-forming foil from above, causing a slightly raised profile to the jet-forming foil as was discussed in section 5.1 and shown in figure 5.3.

The anode tube is connected to the anode electrode of MAGPIE through four height adjustable stainless steel return posts which are attached to the anode disk which the holder for the anode tube is placed in. The current is monitored on the return posts by two Rogowski coils.

In figure 6.1 the jet-forming foil appears above the target-forming foil. For ease

of comparison with the previous jet into target experiment, the presentation of the observed jet-target interaction will continue to show the jet propagating from the bottom of the page to the top of the page. The two experiments will be distinguished by the polarity of the central electrode in the jet-forming foil. The previously described experiment, in chapter 5, will be termed the cathode-centric jet and this reversed current polarity setup, described in this chapter, will produce an anode-centric jet.

Two separate experiments were conducted with the reversed current polarity driven jet with the set up as described above. For each experiment observations were made with the optical and XUV self emission imaging cameras and the laser imaging suite as described in section 3.2.

6.2 Overview of the jet-target interaction observed in the reverse polarity experiments

This section will present an overview of the reverse polarity jet-target interaction before looking in more detail at the behaviour of the jet and the shock structures that were formed. It was observed that the major features seen in the cathode-centric jet-target interaction were reproduced in the reversed polarity set up such that the two experiments are very similar.

Figure 6.3 shows a composite image generated from the optical emission fast-framing camera described in section 3.2.5.1. Figure 6.3a shows a frame taken at 470ns after current start on a millimetre scale. The jet is seen at the centre of the image as a vertical column of emission, ∼2mm in diameter. At the base of the jet there is emission from the ablated material from the jet-forming foil. The target-forming foil is seen emitting brightly at the point where the jet is interacting with it. To either side of the interaction region there are bright spots of emission. Just visible on figure 6.3a is the stationary shock seen as a thin line of horizontal emission ∼2mm below the target-forming foil. The stationary shock is separate from the target-forming foil emission, as seen in the cathode-centric jet system. These

structures are summarised in figure 6.3b which shows a sketch of the interaction with the jet, target-foils and stationary shock which are indicated.

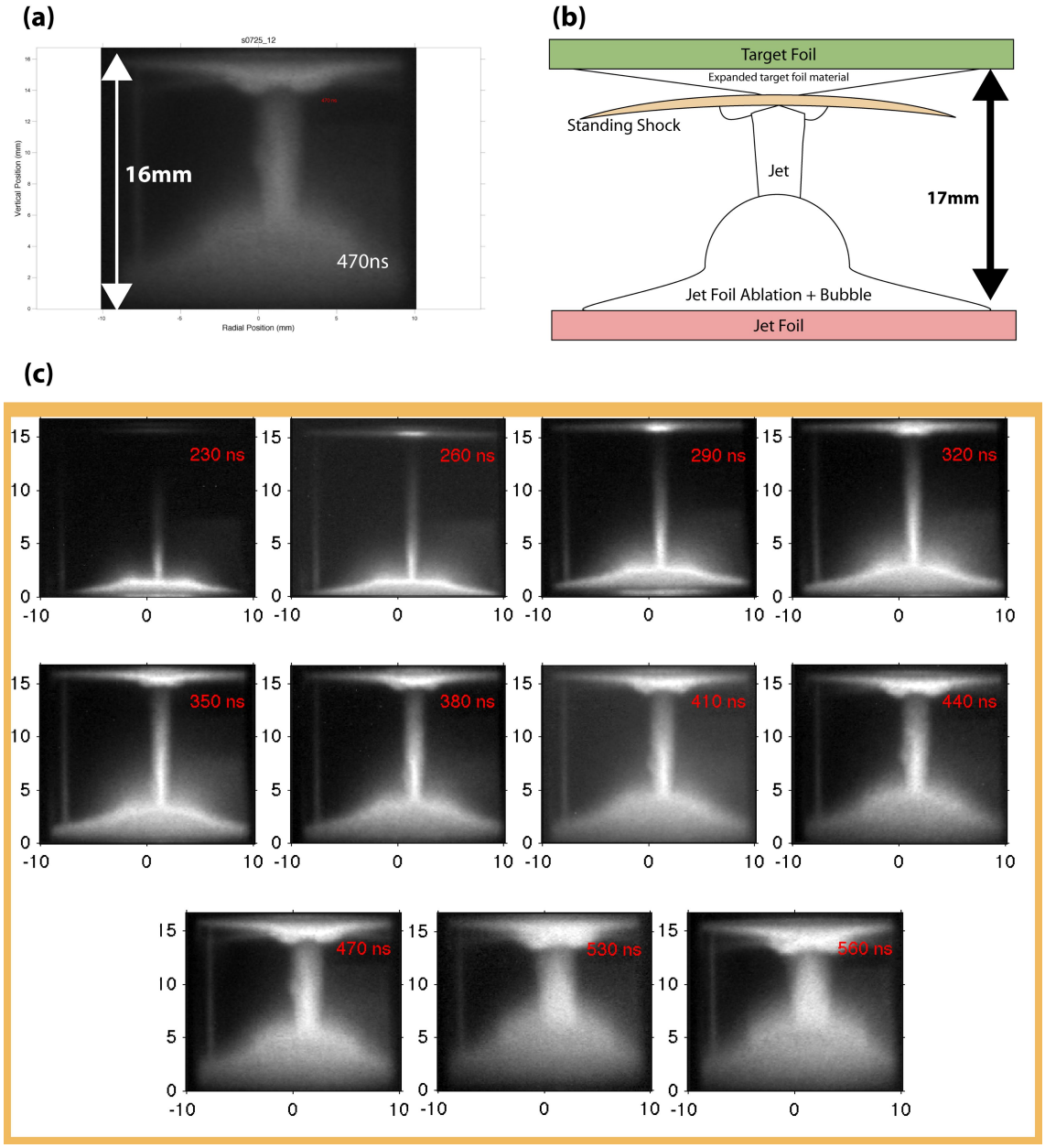

Figure 6.3: Composite image of the optical emission images as captured by the fast framing camera. (a) an enlarged image at 470ns. (b) a sketch of the features seen during the jet-target interaction. (c) a series of images with a 30ns interval and 5ns exposure. Time from current start is indicated on the image in red and time increases from left to right. From experiment s072512. Scale in mm.

Figure 6.3c shows eleven frames from the optical emission fast framing camera

that are spaced with a 30ns interval. The earliest frame is shown in the top left-hand of the image and occurs 230ns after current start. The latest frame is shown in the bottom right-hand of the figure and occurs at 560ns. Time runs along the rows from left to right and is indicated in red on the frames. The scale associated with each frame is in millimetres. The images have been post processed to increase the contrast of the emitting structures.

The first three frames taken at 230ns, 260ns and 290ns in figure 6.3c, show the jet rising towards the target-forming foil and in frame 290ns, impacting upon the target foil surface, which is similar to the time the cathode-centric jet is seen to form. The jet is seen to be narrow and well collimated. The region that is emitting most intensely in these frames is the jet-forming foil and the base of the jet, in comparison to the cathode-centric jet the emission appears brighter along the length of the jet. The emitting region of the jet appears separate from the target-forming foil in the first two frames at 230 and 260ns, however the target-forming foil is emitting in a bright spot directly above the jet. The surface of the target-forming foil is also emitting. A thin vertical line of emission can be seen on the left-hand side of the frames ∼9mm from the jet centre. This is a reflection of the emission from the jet as seen from a connection post between the target and jet foils that is behind the jet.

The three frames from 320ns to 380ns, in figure 6.3c, show the jet interacting with the target foil. At the point where the jet intercepts the target foil, two spots of emission develop on either side to the emitting region of the jet. Due to the symmetry of the interaction, this is a ring of emitting plasma which could be material moving out of the flow of the jet, or material of the target moved aside by the flow from the body of the jet. In the three frames from 320ns to 380ns the jet becomes visibly wider in diameter and the emission from the body of the jet appears uneven. The plasma ablated from the jet-forming foil moves upwards in the frames. At this point the stationary shock is not visible from its optical emission.

The final five frames, in figure 6.3c, from 410ns to 560ns show the development of the stationary shock. The stationary shock is just visible on frame 410ns as a fine line of emission to either side of the interacting region of the jet and target. Over

these five final frames the emission from the stationary shock increases in intensity and it is clearly visible in the last three frames at 470ns, 530ns and 560ns. In the final five frames the jet continues to increase in diameter, yet it retains vertical, well collimated edges to the emission region. The emission from the body of the jet is seen to be uneven and a 'lump' of emission appears to progress along the left-hand side of the jet towards the target. This indicates the flow of plasma is uneven and possibly contains localised large density gradients.

The stationary shock appears to form from 410ns onwards from the optical emission images shown in figure 6.3. In direct comparison to the optical imagery of the cathode-centric jet, section 5.2, the stationary shock in the anode-centric jet appears fainter. This may be due to the greater intensity of emission from the jet and jet-forming foil saturating the camera. The jet and the jet-forming and target-forming foils dominated the optical emission in this time period. The optical emission can be compared to XUV emission as captured by the micro-channel plate four-frame pinhole camera, described in section 3.2.5.2. Figure 6.4 shows two XUV self emission images of the jet interacting with the target foil at 464ns and 494ns. With comparison to the the optical emission at this time (frames 470 and 530ns in figure 6.3c), the emission from the jet is confined to the region closest to the jet-forming foil in both of the XUV images. Directly before the region interacting with the jet-forming foil the emission from the body of the jet is hardly visible. At the target surface the ring of optical emission around the interaction point of the jet and target is reduced in the XUV emission, however the interaction of jet and target appears to emit as brightly as the base of the jet. In the XUV the formation of the stationary shock has begun and it is visible below, and separate to, the emission from the target-forming foil surface.

In comparing the images in figure 6.3 and the optical images of the previous experiment in figure 5.4 the components of the jet-target interaction are on first inspection very similar. However the jet produced from the anode-centric jet-forming foil is seen to be narrower and more uneven in its emission. The stationary shock forms in both experiments, however the emission from the anode-centric jet dominates the optical imagery in comparison to the stationary shock formed by the cathode-centric

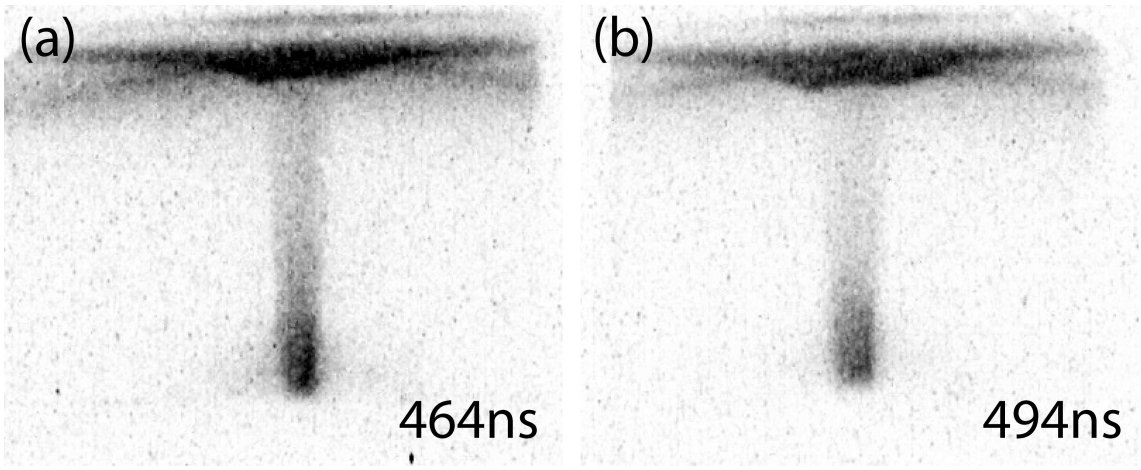

Figure 6.4: XUV pinhole camera image of the reverse polarity jet at 464ns and 494ns. Taken with a 5ns exposure and 30ns inter-frame from experiment s072612.

jet. No reverse shock is seen in the anode-centric jet-target interaction, this indicates the flow parameters in the jet are different from the cathode-centric jet system.

6.3 The formation of the jet with reversed current polarity

This section will examine the jet as it forms and interacts with the target-forming foil. The anode-centric jet is expected to be similar to the cathode-centric jet described in chapter 5 with regards to its propagation and interaction with the target-forming foil. However, it was mentioned in the previous section that there were differences when the optical imaging diagnostics from the two jets were compared, this will now be expanded on.

The section is split into two parts. The first subsection will discuss the velocity of the observed emission from the jet and its radial expansion. The collimation of the jet, also observed from optical emission, will be discussed.

The second section will show the observeations in the jet from 532nm laser interferometry. The electron density profile through the body of the jet will be shown.

6.3.1 The dynamical properties of the jet

Using the fast-framing optical emission camera images shown in figure 6.3 the velocity of the emitting features can be found. The velocity of the optically emitting regions of the jet may not be reflective of the actual velocity of the plasma as the emission could be affected by the radiative cooling within the plasma jet. The actual velocity of the plasma is probably higher than this value, but this depends on the exact conditions of the cooling.

Figure 6.5 shows the velocity of the emitting regions of the jet tip, the material ablated from the jet foil and the jet radial expansion which are found by plotting their positions in the fast-framing camera imagery against the time the frame was taken, next to the graph is a still from the fast-frame optical camera taken at 350ns after current start. The measured structures are indicated on the image in colours that correspond to their data points on the graph. The jet tip is in light blue, the radial expansion is in red and the ablated material from the jet foil is in dark blue.

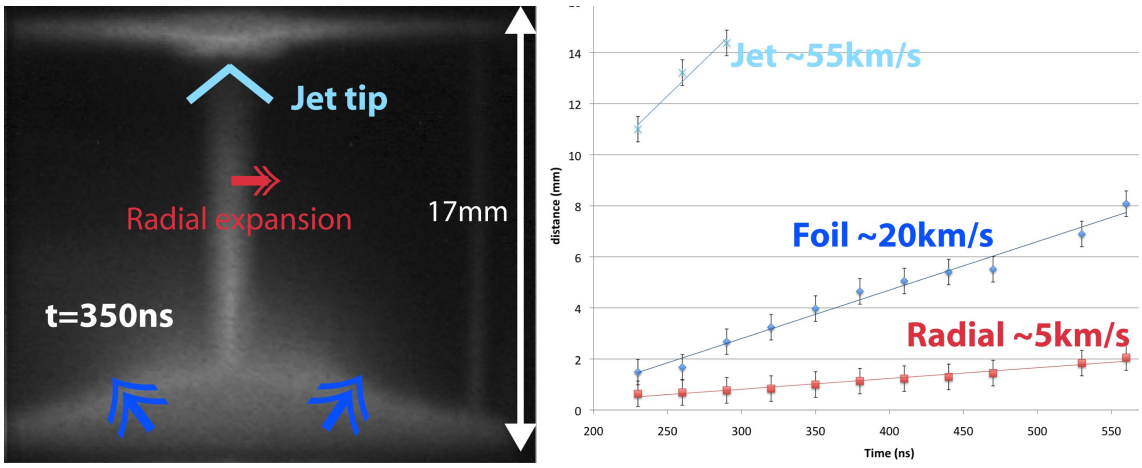

Figure 6.5: Velocity as measured from the fast framing optical camera diagnostic for the optically emitting regions of the jet, jet radial expansion and the jet foil ablation. From experiment s072512.

The velocity of the jet tip is determined using the boundary of the emitting material at the tip of the jet, as seen in the first three frames of figure 6.3. This is found to be $\sim$ 55$\pm$5km/s. The cathode-centric jet was found to have a faster jet tip velocity of $\sim$ 85$\pm$5km/s which was discussed in section 5.3.1. This suggests that the emitting region of the jet may be moving slower than in the cathode-centric jet

system, or that the radiative cooling parameters inside the jet are different.

The velocity of radial expansion of the jet is found by measuring the diameter of the jet at a fixed point relative to the target-forming foil. The diameter is then halved to find the radius and this value is plotted against the time the image was taken. The radial expansion of the emitting region of the jet body is found to be $\sim 5\pm2$km/s which is comparable to the cathode-centric jet which had a radial expansion of $\sim 6\pm2$km/s. This suggests that the mechanism providing the confinement of the jet may be similar in the two systems.

The expansion of the material ablated from the jet-forming foil is measured at the highest point of the emission near the jet. The emission from the ablated material from the jet-forming foil is found to be $\sim 20\pm3$km/s which is the same within error to the cathode-centric jet where the expansion velocity was found to be $\sim 25 \pm 3$km/s and for the jet in vacuum it was found to be $\sim$20km/s, which was measured from XUV emission. This suggests that the mechanism driving the expansion of the jet-forming foil in all three systems is the same.

It was mentioned in the previous section that from the optical emission measurements the anode-centric jet appears to be narrower and straighter than the optical emission observed for the cathode-centric jet. Further comparisons can be made from the measurements of the opening angle of the jet found from the optical emission at the boundary of the jet.

Figure 6.6 shows the measurement of the half-opening angle for the anode-centric jet against time as measured from the optical emission boundary observed on the fast-framing camera. In the $\sim$5mm at the base of the jet, marked in the figure 6.6 in blue, the emission is observed to have a larger opening angle than in the body of the jet, marked in the diagram in red. The opening angle is measured as the divergence from the axis of the jet, as shown on the diagram. The half opening angle for the base and body of the jet is compared in figure 6.6.

For the base of the jet the measured opening angle increases with time, however in the body of the jet very little increase in the half opening angle is seen. The base of the anode-centric jet is measured to have a opening angle between 6° and 8° this is comparable to the half-opening angle measured for the base of the cathode-centric

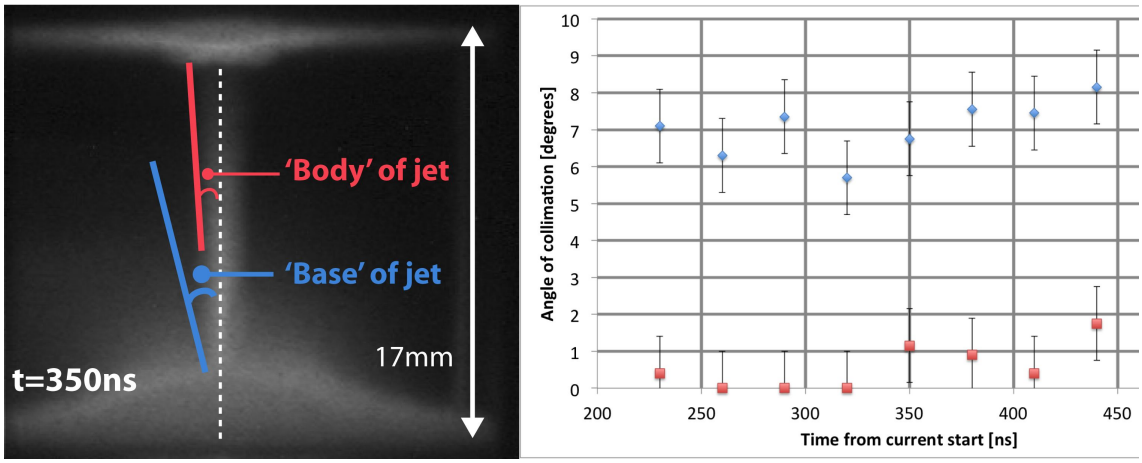

Figure 6.6: The opening half angle of the jet is measured in two places, near the base and in the body of the jet, as indicated on the diagram. The jet improves its collimation in the body of the jet, where a smaller opening angle is observed. From experiment s072512.

jet. This may indicate the mechanism for the creation of both jets is initially very similar.

The body of the anode-centric jet is observed to have an opening angle of between 0° and 2° for the duration of the measured time periods. In comparison to the cathode-centric, jet which was measured to have a opening angle between 2° and 6° for a similar time period, the anode-centric jet has a better collimation which it retains for a longer period of time. This indicates that the confinement of the body of the jet is improved in the anode-centric jet system.

6.3.2 The electron density profile of the reversed current polarity jet

Figure 6.7a shows a 532nm laser interferometry image of the anode-centric jet interacting with the target-forming foil. The region of the image between ±2mm shows sharp downward bend in the fringes marking the edge of the body of the jet. At the interaction of the jet and target there is a dark area on the interferogram marking a region of the plasma with very large refractive index gradients that deflect the probe beam out of the optical imaging system. The electron line density $n_e l$, through the two marked radial positions is shown in figure 6.7b and the electron density is calcu-

lated from these profiles and shown in figure 6.7c. The $n_e l$ line out is averaged over five pixel rows, which smooths the calculated values to account for the resolution determined by the original fringe spacing. The n_e line outs are calculated from the averaged $n_e l$ line outs using an Abel inversion discussed in section 3.2.3.2.

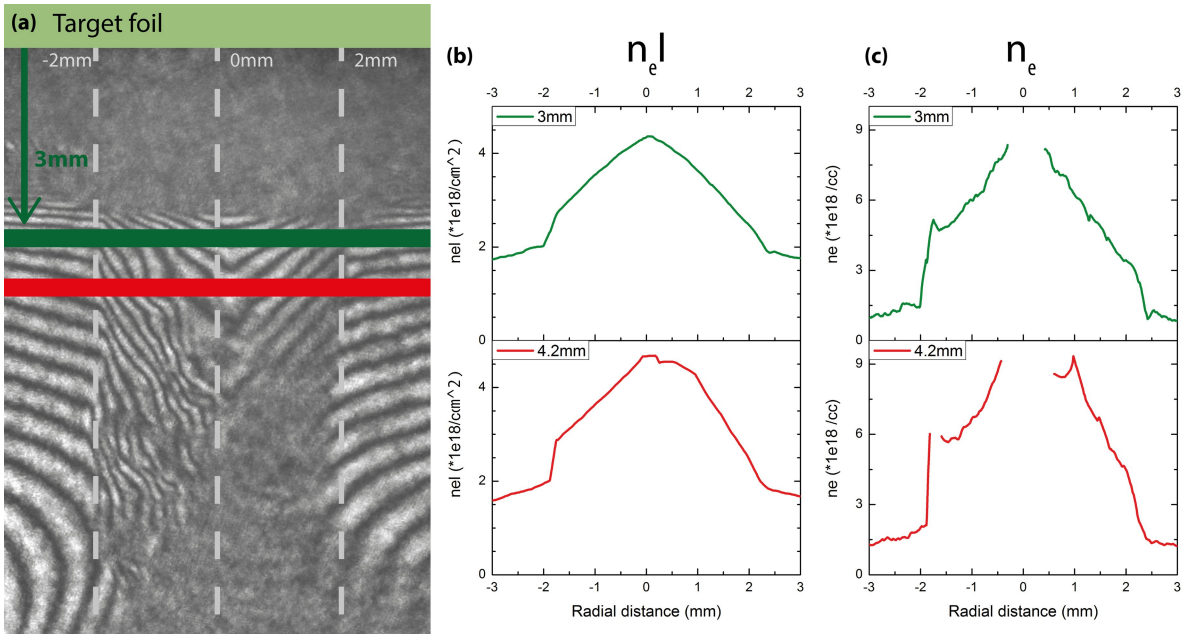

Figure 6.7: Density profiles across the jet taken at 495ns. The colour of the density profiles corresponds to the bands of colour on the interferogram showing the axial position where the profile is taken. Both the electron line density (b) and electron density (c) are shown for two axial positions. From experiment s072612.

The profiles shown in figure 6.7b show a sharp increase in electron line density marking the edges of the jet. The interior of the jet appears to increase in density radially inwards towards the jet centre. The centre of the jet has a density $n_e \approx$ 7 to $9\times10^{18}\text{cm}^{-3}$ at the axial position 4mm below the target-forming foil, marked in red. Nearer the target the density of the jet is slightly lower ranging from 5 to $8\times10^{18}\text{cm}^{-3}$. The density of the jet decreases closer to the target-forming foil. The radial profiles shown for the cathode-centric jet, shown in section 5.3.2, were taken at earlier times in the development of the jet (267ns and 464ns), however densities seen in the electron density map shown in figure 5.29, which is during the jet-target interaction, indicate at the 4mm position below the jet the cathode-centric jet has an electron density of $\sim8\times10^{18}\text{cm}^{-3}$, which is lower than observed in the anode-centric

jet system.

As seen in the cathode-centric jet, the anode-centric jet is also accompanied by a halo plasma. This is a lower density plasma in comparison to the anode-centric jet which has an electron density of $\sim 1 \times 10^{18}\text{cm}^{-3}$ directly next to the jet and this is seen to reduce with increased radial distance from the jet. This is comparable to the density seen in vacuum for the cathode-centric jet, and slightly higher than the value given for the cathode-centric jet with target, though as stated these were taken at an earlier development time.

The average electron density axially along the jet is shown in figure 6.8. This is calculated by integrating the electron line density in the body of the jet, then dividing by the jet width. The election density in the jet appears to remain roughly constant axially, in comparison to the cathode-centric jet, shown in figure 5.11, is ~ 2 to $3\times$ more dense. The average electron densities were calculated in the same manner and at similar developmental times, which indicates the anode-centric jet has a higher electron density along its length than the cathode-centric jet.

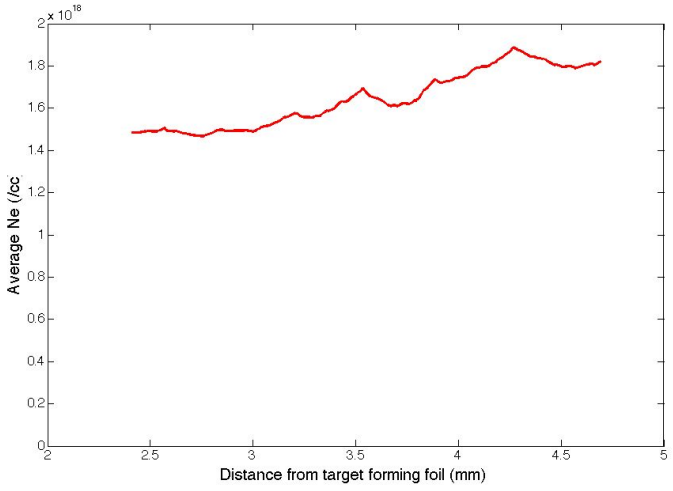

Figure 6.8: Average electron density distributed axially in the body of the jet at 495ns. From experiment s072612.

The electron density inside the jet can be compared to the electron density outside the jet in the halo plasma to give the electron density contrast between the jet and its surrounding plasma. At the edge of the jet profile, taken at 3mm below the target in figure 6.7c, the increase in density is $\sim 2\times$, and the comparison of the

halo plasma to the density in the interior of the jet gives a ∼3× density increase.

This can be compared to the ratio of densities between the cathode-centric jet and its halo plasma discussed in the previous chapter. The cathode-centric jet was found to be ∼3× increase in density at the same axial position and time (shown in figure 5.10), which indicates the two jets are comparable in terms of their density contrast.

The measured higher electron density in the anode-centric jet may provide an explanation for the observed improvement in the collimation in the anode-centric jet body. If there is a toroidal magnetic field in the plasma above the jet-forming foil, as discussed in section 4.5, the increase in electron density will correspond to an increase in the magnitude of the toroidal field at the boundary of the jet and halo plasma, as the magnetic field is 'frozen' into the electron density. This will contribute to the confinement and good collimation of both jet systems, though the anode-centric jet will have a larger toroidal field than the cathode-centric jet system due to its higher electron density.

6.4 The stationary shock formation in the halo plasma in a reversed current polarity

The stationary shock structure was seen to form in the cathode-centric jet system and was discussed in section 5.4. As shown in section 6.2, a stationary shock is seen to form in the halo plasma of the reversed polarity jet-target interaction, this will be discussed in this section.

This section is broken into two subsections. The first subsection will discuss the the observed movement of the optical emission from the fast framing camera and the shape and width of the shock.

The second section will present the electron density map of the jet-target interaction and show five electron density profiles though the stationary shock. The density contrast between the material in the halo plasma and the material behind the shock will be discussed.

6.4.1 The evolution of the stationary shock in the flow from the halo plasma in reversed current polarity

The stationary shock can be seen by its optical emission on the fast-framing camera. As described in the previous sections the stationary shock appears as a thin horizontal line of emission below the emission from the target-forming foil. Figure 6.9 shows the position of the stationary shock and the emission from the target-forming foil against the time the fame was taken. The accompanying still image from the fast framing camera shows the evolution of the jet and target interaction with the features colour coded. The stationary shock is indicated in green and the emission from the target-forming foil is indicated in purple. These colours correspond to the data points shown on the graph in figure 6.9b

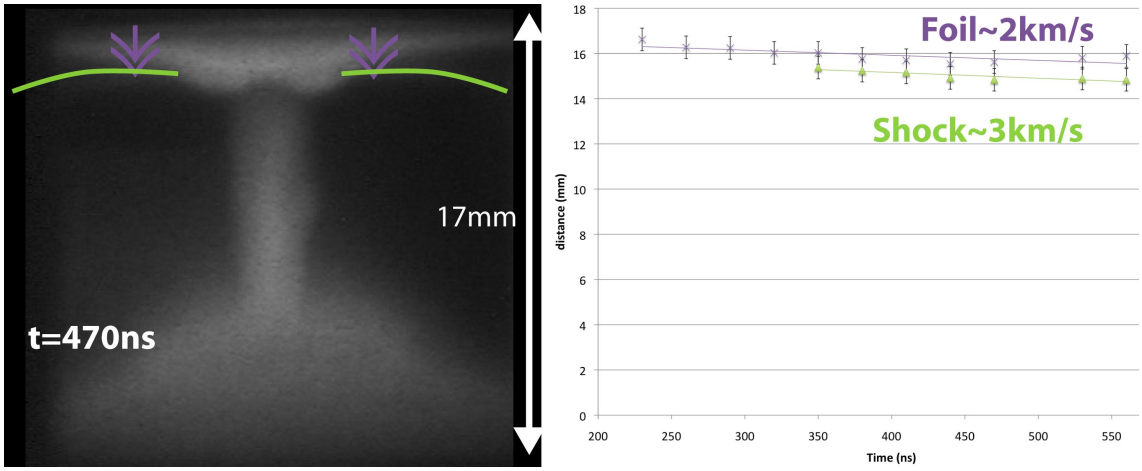

Figure 6.9: Velocity as measured from the fast framing optical camera diagnostic for the expansion of the target foil and the progression of the stationary shock feature from their optical emission. From experiment s072512.

The position of the emission from the stationary shock is seen to maintain its distance from the edge of the emission seen on the target foil. The expansion of the emitting region on the target-forming foil is seen to have a small velocity $\sim 2 \pm 1$km/s. The position of the emitting region of the stationary shock is seen to move at $\sim 3 \pm 1$km/s. In the cathode-centric jet system the stationary shock and emission from the target-forming foil was observed to move at $\sim 4 \pm 2$km/s, the stationary shock formed in the anode-centric jet system has a comparable measured velocity of 5 ± 2km/s.

The shape of the stationary shock is shown in figure 6.10 as measured from the laser imagery. The downward curve in the shape of the shock front indicates that the shock forms as a hemisphere centred on the jet. The red line shown on the figure is the section of a circle with radius of 45mm, it is seen the shock follows this curve closely, although this length does not relate directly to any distance in the system and would be centred below the jet-forming foil.

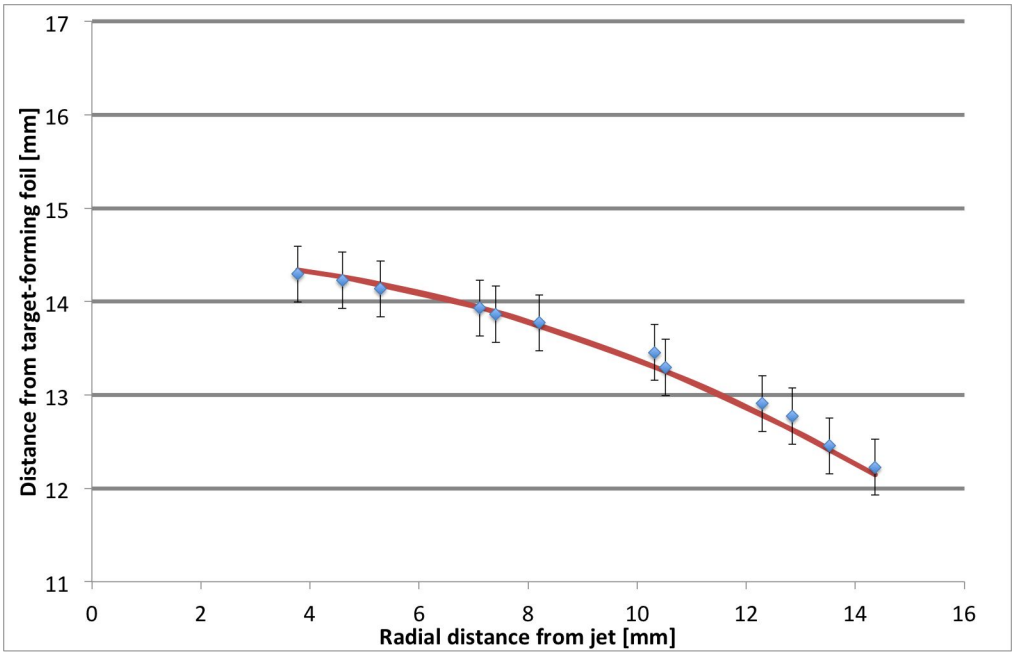

Figure 6.10: The radial position from the target-forming foil is plotted in blue. The red curve is a section of a circle with radius of 45mm. The distance between the jet-forming and target-forming foils is 17mm. From experiment s072512.

The stationary shock can also be seen in the laser interferometry and shadowgraphy. Figures 6.11 and 6.12 show the 532nm laser shadowgraph next to the interferometry image taken in the same experiment, at the same time. The pair of images were obtained at the same time and from the same viewing angle through the discharge chamber. Figure 6.11 shows the jet and stationary shock at 475ns after current start. The jet is seen to be ∼4mm in diameter at this time. The stationary shock is visible ∼3mm below the target-forming foil surface as a downward curving shadow. The stationary shock acts as a boundary line between the material below it, the halo plasma moving with the jet, and the material above it. From the

shadowgraph the shock front is seen to be dark indicating a larger refractive index gradient.

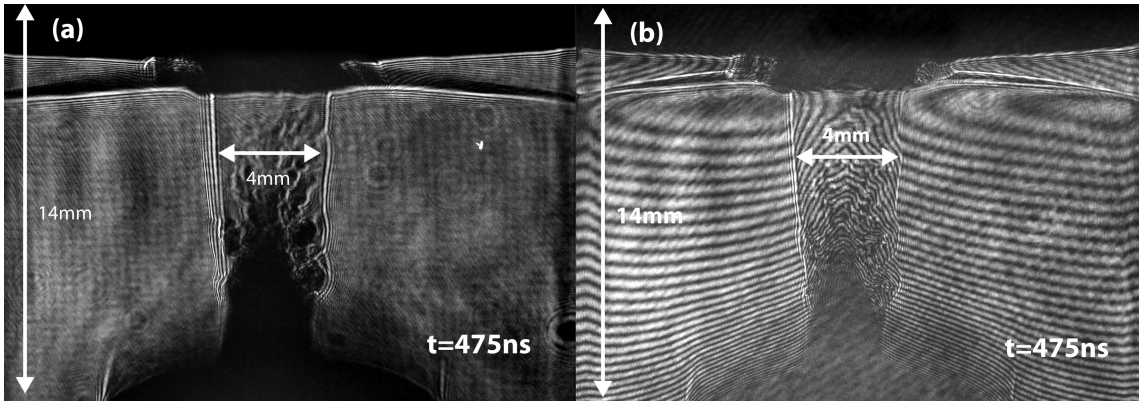

Figure 6.11: (a) 532nm shadowgraph and (b) interferogram taken at 475ns after current start. From experiment s072612.

Figure 6.11b shows the interferometry from the same time as the shadowgraph in figure 6.11a. The fringes curve upwards through the jet. The stationary shock causes the fringe lines to be displaced abruptly and in the figure 6.11b they cannot be traced though the shock front from the halo plasma into the material behind the stationary shock, though the phase of the fringes behind the shock can be found by tracing around the shock from larger radii where the fringes can be traced though the shock.

Figure 6.12 shows a shadowgraph and interferometry taken with the 532nm laser at 495ns after the current start. The jet, ablated material from the jet-forming foil and the stationary shock are visible on both the shadowgraph and the interferometry image.

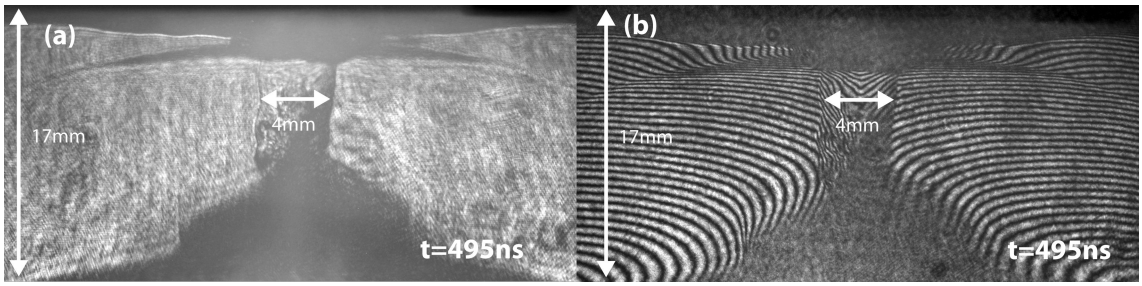

Figure 6.12: (a) 532nm shadowgraph and (b) interferogram taken at 495ns after current start. From experiment s072612 .

The shock front in figure 6.12 extend radially from the centre of the jet for

±15mm, to the edge of the image, most clearly visible in the interferometry image in figure 6.12b as a sharp bend or blocking of the fringe pattern. In the case of figure 6.12b the fringes can be followed though most of the stationary shock front from the halo plasma to the material behind it. The stationary shock is seen to have a downwards curvature as was shown in figure 6.10.

The jet in figure 6.12 has developed larger density gradients when compared to figure 6.11, as indicated by the dark region to the right hand side of the jet where the fine fringe pattern is lost. The ablated material from the jet-forming foil has also moved axially upwards retaining a spherical shape with large refractive index gradients.

Figure 6.13 compares the 532nm interferometry with the 355nm interferometry taken at the same time and from the same experiment, though they are from different viewing angles. The 355nm interferometry has a higher acceptance angle and a higher critical density which it can probe due to the shorter probing wavelength. This allows the resolution of the shock to be improved in the image shown in figure 6.13b.

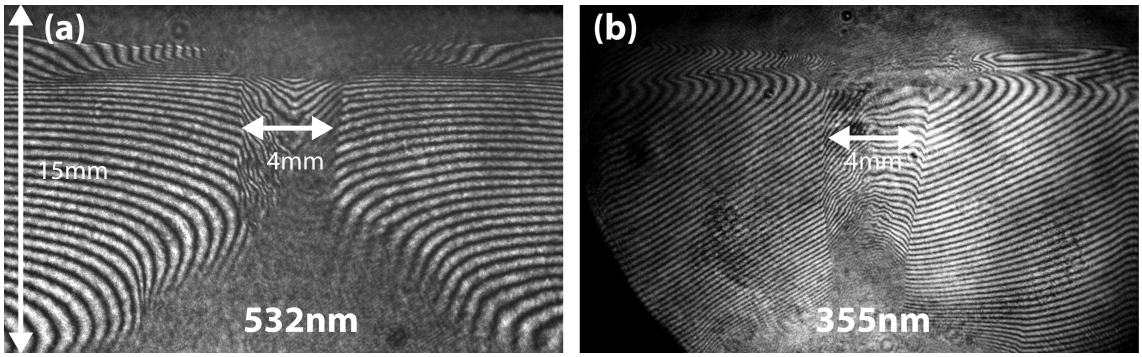

Figure 6.13: comparison of 355nm and 532nm interferometry images from the same experiment at the same time. Note well defined shock in (b) from experiment s072612.

The stationary shock in figure 6.13b is seen to be very distinct and narrow with a downwards slope. Fringes can be seen close to the interaction region of the jet and target foil, however this region still contains inhibitive density gradients to form a traceable fringe pattern at the interaction point of the jet and target with the 355nm interferometry system, despite the larger aperture and lower wavelength.

6.4.2 The electron density contrast between the halo plasma and the material above the stationary shock

Figure 6.14a shows the electron line density $n_e l$, and figure 6.14b shows the electron density n_e, as calculated from the interferogram shown in figure 6.12. Accompanying the two density maps are five electron density profiles, shown in figure 6.14c, which show the jump in electron density across the stationary shock front. These profiles are taken at the radial positions indicated by the red lines in figure 6.14a abd 6.14b.

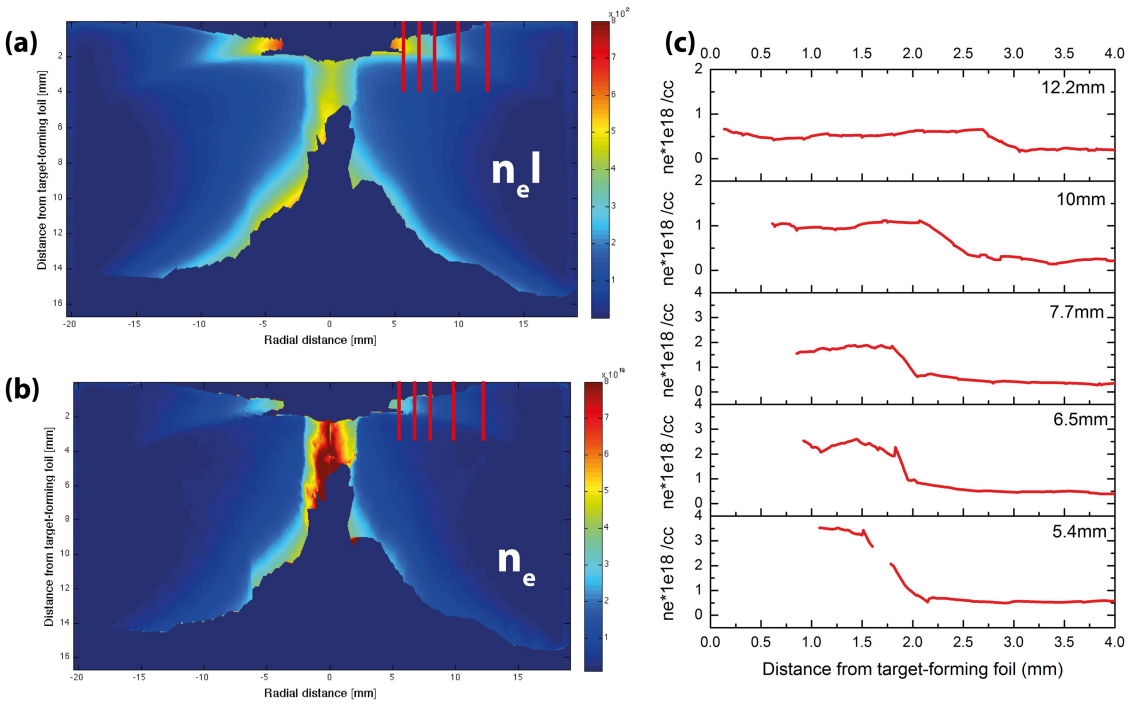

Figure 6.14: (a) the electron line density, $n_e l$, calculated from the 532ns laser interferometry. (b) the calculated electron density, n_e, from the electron line density shown in (a). (c) five density profiles from the n_e map over 4mm from the target-forming foil surface. The radial position of the profiles is indicated on (a) and (b) by red lines. The electron density jump at the stationary shock can be seen on all the profiles. From experiment s072612.

In both density maps (figures 6.14a and 6.14b), the stationary shock is seen as a jump in density from the halo plasma to the post shock material, between the shock and the target. The jet is the region of highest density in figure 6.14b. The halo plasma accompanying the jet is seen to have a lower density further from the jet.

The stationary shock is visible to ±12mm either side of the centre of the jet. Figure 6.14c shows five n_e profiles through the stationary shock. The shock front is visible in all of the profiles as a step increase in the n_e. The region before the shock is to the right-hand side of the plot.

The increase in density occurs abruptly in a short spatial distance (as is shown on figure 6.10). The density of the material both before and behind the shock decreases as the radial distance from the jet increases. In the profile at 12.2mm, from the centre of the jet the density of material behind the shock is $\sim 0.8\times10^{18}\text{cm}^{-3}$ in comparison to the material behind the shock at the radial position closest to the jet which is $\sim 4\times10^{18}\text{cm}^{-3}$.

The jump in electron density between the material behind the shock and the halo plasma at a radial position of 12mm is $\sim 3\times$. At the radial position closest to the jet at r=5.4mm the electron density jump is $\sim 4\times$. The distance over which the density increases, or shock width, is seen to be $\sim$ 0.2mm closest to the jet and $\sim$ 0.4mm furthest from the jet axis.

The increase in shock width and the corresponding decrease in the electron density jump was seen in the cathode-centric jet system. This relationship is also seen here, but the axial profiles have been taken at radial distances that are larger than the measurements made in the cathode-centric jet system. The high density gradients on the interaction point of the jet and target mean a measurement closer to the jet is not possible.

Comparing the electron density contrast seen in the cathode-centric jet system at radial distances from the jet greater than 5mm, the observed electron density jump in the anode-centric jet system is the same, between 3 and 4 times increase. Ideally a comparison should be made closer to the jet where the shock would be expected to produce a larger density contrast, this provides material for future investigations.

6.5 Summary of the conditions observed in the reversed current polarity jet and the interaction with a foil target

The anode-centric jet is initially seen to be similar to the cathode-centric jet system. Both jets form at similar times and are seen to propagate at similar velocities. both jets are well collimated and accompanied by a halo plasma. On interaction with the target foil both systems produce a stationary shock, where the conditions across the shock are seen to be the same in both systems.

The anode-centric jet was seen to have a higher electron density than the cathode-centric jet. The higher electron density indicates the flow parameters of the jet are different, which may explain the absence of the reverse shock in the flow of the jet. The higher jet density is also suggested as an explanation for the improved collimation observed in the body of the anode-centric jet.

The production of the stationary shock indicates that electron beams from the cathode in the cathode-centric system did not play a significant role in the pre-heating of the target. The observed stationary shock shape is different closer to the jet in the anode-centric system, where the stationary shock is seen to fit to a radius of curvature of $\sim$ 45mm, though this is an arbitrary fit and relates to no physical distance in the system. The observed similarity of the stationary shock in the anode-centric and cathode-centric systems suggests the underlying mechanism of its creation is the same.

The next chapter will present experiments that investigate the shock structures produced when the two jets discussed in this chapter and the previous chapter are combined. This produces two supersonic, counter streaming flows of plasma that will collide producing shock structures similar to those observed in the jet into target experiments, including a stationary shock structure that will be used to evaluate the underlying mechanisms driving the formation of these shocks in the halo plasma.

Chapter 7

Colliding Aluminium Supersonic Jets

In chapters 5 and 6 the interaction of supersonic jets with stationary thin metallic foils was discussed. This chapter will introduce experiments that bring these two jet-creating systems together, producing a test-bed for studying shocks in supersonic flows. The colliding supersonic jets are expected to produce a series of shock features both in the flow from the jets and in the halo plasma around the jets.

The chapter will describe the result of preliminary investigations with the colliding jet system using the results of processed 532nm laser images and the fast-framing self emission camera.

7.1 Experimental setup

Figure 7.1 shows the experimental hardware used to create the colliding jet system. Figure 7.1a shows a schematic of the system with the different elements of the hardware labeled for reference. Figure 7.1b shows a photograph of the assembled hardware in the discharge chamber prior to the experiment, with the components labeled.

The jet-forming foils and their holders have the same dimensions and foil thickness as in the previous jet experiments. The diameter of the jet-forming foil and the diameter of the central connection are also kept the same. Figure 7.1a indicates the

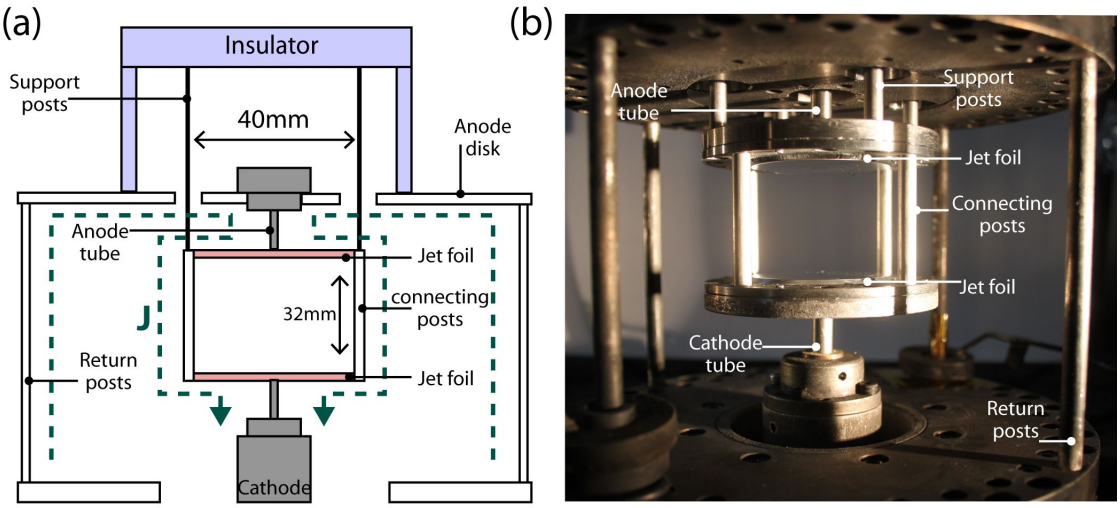

Figure 7.1: (a) schematic of the hardware for the colliding supersonic jets experiment. The jet-forming foils are indicated in red, and the anode and cathode connections indicated in grey. (b) a photograph of the hardware in the discharge chamber prior to the experiment.

two jet-forming foils in red and the electrical cathode and anode electrodes in grey. The path of the current, J, is indicated in dark green by a dashed line.

The current direction moves through the return posts first, and then along the anode disk as indicated in the figure 7.1a. The current then passes radially outwards through the the upper jet foil via an anode-tube. The current then moves along the connecting posts between the two foil holders to flow radially inwards across the bottom foil to the cathode-tube at its centre. The direction of the toroidal magnetic field under each jet-forming foil is in the same direction.

The anode-tube is a 6.35mm outer diameter stainless steel tube which makes electrical contact with the top foil at its centre. The foil that is centrally touching to the anode tube produces an anode-centric jet that moves downwards. The anode-centric jet-forming foil is suspended via four long support posts which are shown in the figure 7.1a. These are attached to an insulating plastic, this and the long length of the supporting posts ensures current is not diverted of out the two foil system. The supporting posts do not make contact with the anode plate and pass though a $\sim 15mm$ diameter hole in the anode plate before attaching to the foil holder.

The anode-centric jet-forming foil is attached via its holder to the second foil. The connecting posts provide the spacing of the two foils which is 32mm at their

edges. The jet-forming foil holders are identical and assembled as was described in section 5.1. The two jet-forming foil holders are spaced with 4 connecting posts. These are attached to the two foil holders in the same manner that the anode-centric jet-forming foil holder was attached to the target-forming foil in the previous chapter.

The foil at the bottom of figure 7.1a is electrically connected to the cathode at its centre via a 6.35mm outer diameter stainless steel tube. The anode and cathode-tubes are identical. The cathode-tube is then attached to the MITL. The bottom foil produces a cathode-centric jet that propagates upwards, towards the anode-centric jet.

In the experiments described in this chapter both of the jet-forming foils are $14\mu m$ thick with an outer diameter of 40mm. The surface of both the jet-forming foils forms a 'humped' profile which was described in section 5.1. The separation at the centre of the foils is 30mm, between the central cathode and anode contacts, and 32mm at the outer diameter of the foil.

Two experiments were conducted for the colliding jets investigation. The interaction was observed with the laser imaging suite and the self emission imaging systems in XUV and optical. The results presented here are intended as an overview of the system and a starting point for further investigation.

7.2 Overview of the jet-jet interaction observed in the experiment

Images of the colliding jet system will be presented in this section in order to provide an overview of the interaction between the two jets. A series of images in optical emission are captured by the fast-framing optical camera and provide a detailed first look at the system. Images in self-emission XUV and 532nm laser interferometry will be discussed with reference to the fast-framing camera images and the features observed in them, the interferometry will be discussed in greater detail for each of the features observed during the jet-jet interaction later in this chapter.

Figure 7.2a shows a frame from the fast-framing optical camera captured at 563ns after current start. The exposure used during these experiments is 5ns. The cathode-centric jet-forming foil is at the bottom of the image and the anode-centric jet-forming foil is at the top of the image. The system of structures visible in this image is summarised in figure 7.2b which shows a sketch of the jet-jet interaction.

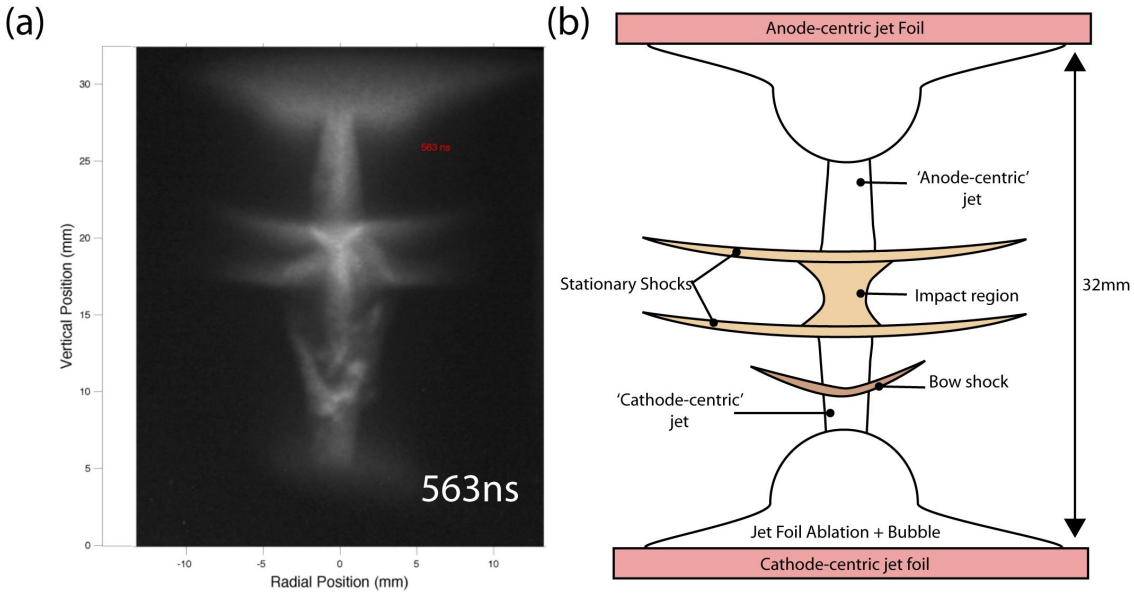

Figure 7.2: (a) a frame at 563ns after current start from the optical emission fast framing camera. From experiment s080612 (b) is a sketch of the features seen during the collision of the two supersonic jets. The features that will be discussed are indicated on the image.

Figure 7.2b indicates the orientation of the system with respect to the two jet-forming foil and the shock features observed. The two jets are marked in the figure along with the ablated dense material from the foils that form them. At this time after current start the jets and the accompanying flows of halo plasma have collided and produced two horizontal shock fronts seen to have a large radius. These shocks are formed approximately halfway between the two jet-forming foils and are similar to the stationary shocks seen in the 'jet into target' experiments described in the previous chapters. Another shock is seen below the stationary shocks in the flow from the cathode-centric jet which is labeled in the figure as a bow shock. This shock will be discussed later in this chapter.

7.2.1 Overview of the jet-jet interaction from the optical self-emission

The formation and evolution of the features indicated by the figure 7.2a can be seen in the sequence of images from the fast-framing optical camera shown in figure 7.3. The figure shows time sequences from two experiments. Figure 7.3a covers a time period from 353ns to 683ns and figure 7.3b covers a time period from 379ns to 709ns. For both image sequences time increases from left to right along the rows. The time the frame is taken is indicated in red on the image. The cathode-centric jet is at the bottom of all the frames and the anode-centric jet is at the top of all the frames.

The frames at 353ns and 383ns on figure 7.3a and the frame 379ns on figure 7.3b show the two jets prior to the collision of the emitting material in the jet body. It is apparent in these three frames that the anode-centric jet is brighter, both at the anode-centric jet-forming foil where the ablated material from the foil is visible, but also in the body of the anode-centric jet, which appears to have progressed further than the cathode-centric jet. The ablated material from the cathode-centric jet-forming foil is not readily visible by its emission. In frame 383ns, on figure 7.3a, the two jets are visible and, on first inspection, appear well collimated.

Frame 413ns in figure 7.3a and frame 409ns in figure 7.3b show the initial collision of the two jet streams. This is seen as a slanted bright shock occurring ∼14mm from the cathode-centric jet-forming foil. This collision does not happen at the halfway point between the two foils, and occurs closer to the cathode-centric jet-forming foils.

After the initial collision of the two jets a series of shock systems begin to form. Most clearly visible in frames 443ns to 593ns in figure 7.3a is the formation and progression of the bow shock. In frame 443ns the bow shock forms in the flow of material from the cathode-centric jet, below the position of the first shock formed when the jets collide (seen on frame 413ns). In frames 473ns to 593ns the bow shock progresses towards the cathode. The shock front of the bow shock is curved with its lowest point in the centre of the flow from the cathode-centric jet. The shock is initially well defined and smooth in frame 443ns, however as the shock

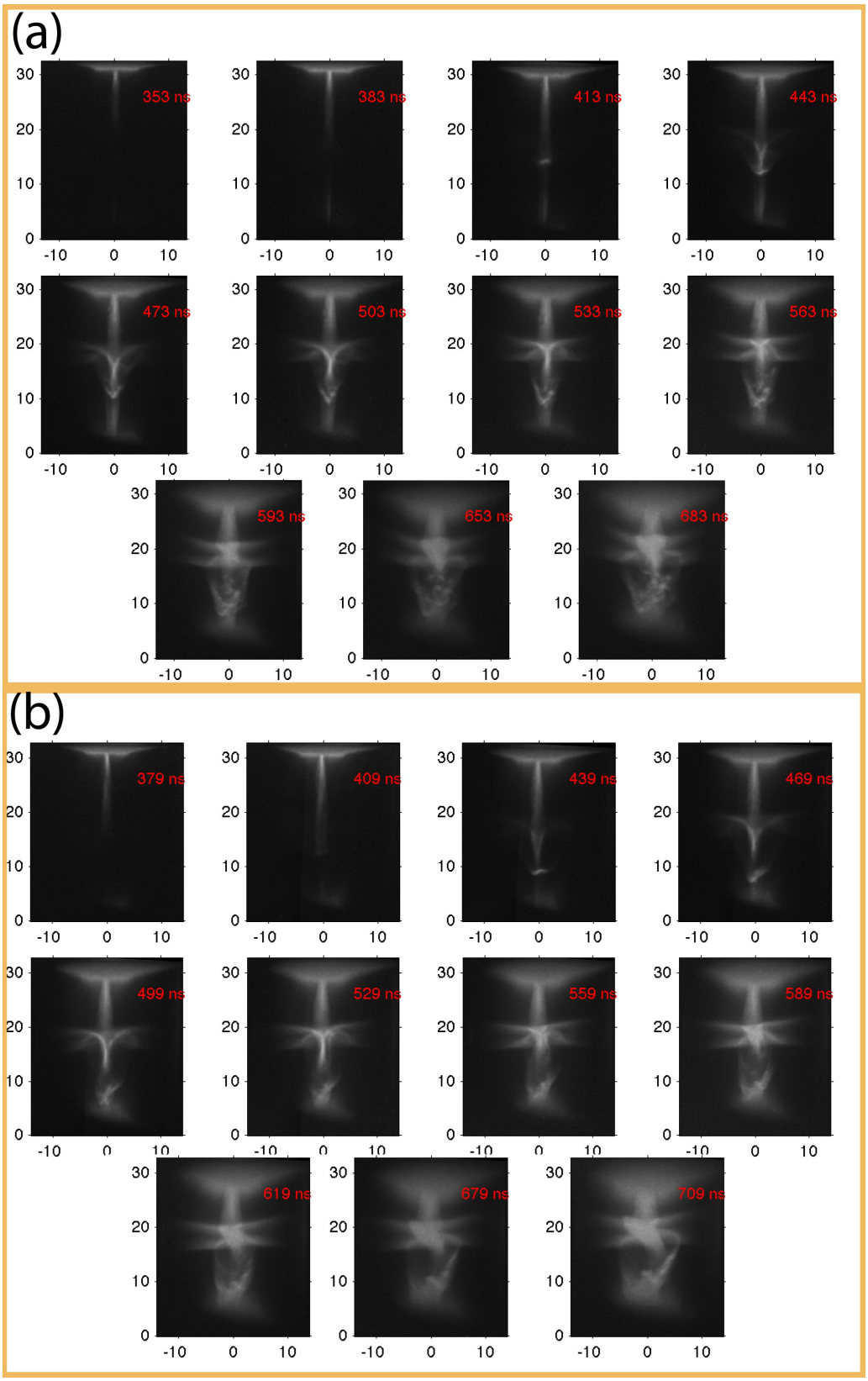

Figure 7.3: The sequence of images from the fast-framing optical camera from two experiments. The cathode-centric jet is at the bottom of the image, moving upwards towards the anode-centric jet. Time runs left to right along the rows of images, scale in mm. (a) from experiment s080612. (b) from experiment s080312. The experiment shows reproducibility, but there are variations in the development of some of the shock features.

moves through the jet body it becomes more unstable and less defined at its shock front. In the final two frames of figure 7.3a the shock front is no longer visible but the material that would form the cathode-centric jet is seen to be expanded and turbulent. The bow shock is also seen to develop in frames 439ns to 559ns in figure 7.3b. In comparison to figure 7.3a, the bow shock is wider and more unstable at its shock front in 7.3b in the cathode-centred jet flow. Formation of the bow shock at the front of the anode-centric jet indicates the anode-centric jet has a higher ram pressure, probably due to a higher density, velocity or both.

At the same time the bow shock is forming, two further shocks form around the half-way position between the two jet-forming foils and at radial positions away from the axis of the system, that create the stationary shock system. Visible from 443ns onwards on figure 7.3a, a parallel pair of shocks form at a position approximately midway between the two foils. The shocks have a smooth interface with the halo plasma, each shock front extents radially outwards up to 10mm from the centre of the two jets. The two shocks are separated by ∼3mm which is maintained for the duration of the interaction. The point between the foils about which the shocks is centred also appears not to move during the interaction. It is seen that the material emits most intensely at the boundary of these stationary shocks and in between the two fronts there is no detected emission, this is clearly visible on frames 533ns to 683ns in figure 7.3a and frames 529ns to 709ns in figure 7.3. The stationary shock features are most probably the product of the collision of the two halo plasmas surrounding the dense jets.

The point at which the two dense jets collide remains approximately midway between the two foils. A ‘Y’ shaped structure is observed at the collision site in frames 443ns to 563ns in figure 7.3a and frames 469ns to 529ns in figure 7.3b. This Y-shaped feature stays at the same axial position for the time periods indicated and appears to be connected at its base to the lowest point in the bow shock. After 563ns in figure 7.3a and 529ns in figure 7.3 the Y-shaped feature is no longer distinguishable and the collision region becomes a confined ball-like region of emitting material with no visible structure.

7.2.2 Overview of the jet-jet interaction from the XUV self-emission

The structures arising from the interaction of the two jets seen in optical emission are also seen on the XUV emission framing camera. Figure 7.4 shows a series of four images taken from the two experiments. Figure 7.4a shows the jet system at 431ns and 461ns. Figure 7.4b shows the system at 528ns and 558ns. The cathode-centric jet is at the bottom of each frame. The images were taken with an exposure of 5ns.

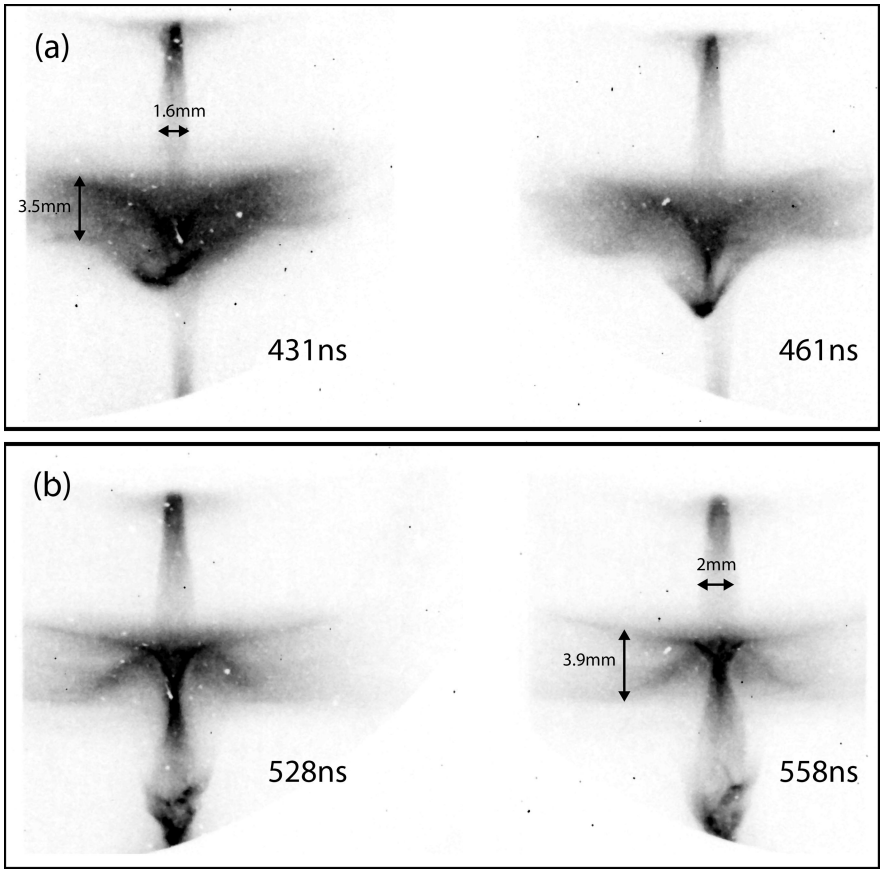

Figure 7.4: A time sequence of XUV self emission images. The cathode-centric jet is at the bottom of the image, moving upwards towards the anode-centric jet. A scale is indicated on the images. (a) from experiment s080612, (b) from experiment s080312.

The time sequence in XUV shows a similar development of the features as was observed in the optical emission shown in figure 7.3. Figure 7.4a at 431ns shows both jets are well collimated and the collision forming the stationary shock and the bow shock is developed. The anode-centric jet is brightest at its base as it emerges from

the jet-forming foil and the jet has a diameter of ∼1.5mm. The emission along the anode-centric jet is not uniform and becomes minimal close to the interaction region between the two jets. The cathode-centric jet is also visible and well collimated, and also shows a drop off in emission along its axial length. The stationary shock is not yet distinct as two separate shocks at 431ns or at 461ns however an emitting region with well defined edges and a spacing of ∼3.5mm is present in the position the stationary shocks will form.

Frame 461ns in figure 7.4b shows the bow shock in the flow from the cathode-centric jet. It has a 'V' shape as observed in the optical images. The front of the bow shock is very smooth in this image, and the brightest emission is at its lowest point in the flow from the cathode-centric jet. The bow shock will be discussed in more detail later in the chapter.

Frames 528ns and 558ns in figure 7.4b the cathode-centric jet has been disrupted and left turbulent by the progression of the bow shock though it. Emitting clumps of material in the region of the cathode-centric jet are visible in both frames. Figure 7.4b also show the two horizontal parallel stationary shocks with a slight upwards curvature to their shock fronts. The material in the stationary shocks is emitting in a narrow region at the shock front. In between the two shock fronts there is an intense emission at the interaction region of the two jets, however the emission deceases radially from this region until there is no emission between the two shock fronts.

In frame 558ns in figure 7.4b, the stationary shock fronts are ∼4mm apart. The anode-centric jet is ∼2mm in diameter. The anode-centric jet appears to be unperturbed by the presence of the cathode-centric jet and retains its good collimation in all four images shown in figure 7.4b.

7.2.3 Overview of the jet-jet interaction from interferometry

The diagnostics in XUV and optical self emission give a good overview of the emitting structures that develop during the jet-jet interaction. Additional information

can be found from laser probing. Figure 7.5 shows four 532ns interferometry images. (a) and (b) are from the same experiment and (c) and (d) and from a different experiment. They are arranged sequentially in time to show the evolution of the jet interaction. Interferometry is sensitive to the electron density in the plasma, and is able to detect even low electron density plasmas that may not be visible in the optical or XUV emission diagnostics. The interferometry system used is described in section 3.2. In all of the images the cathode-centric jet is at the bottom and the anode-centric jet is at the top. A scale is indicated by the distance between the ablated dense material seen from the two jet-forming foils.

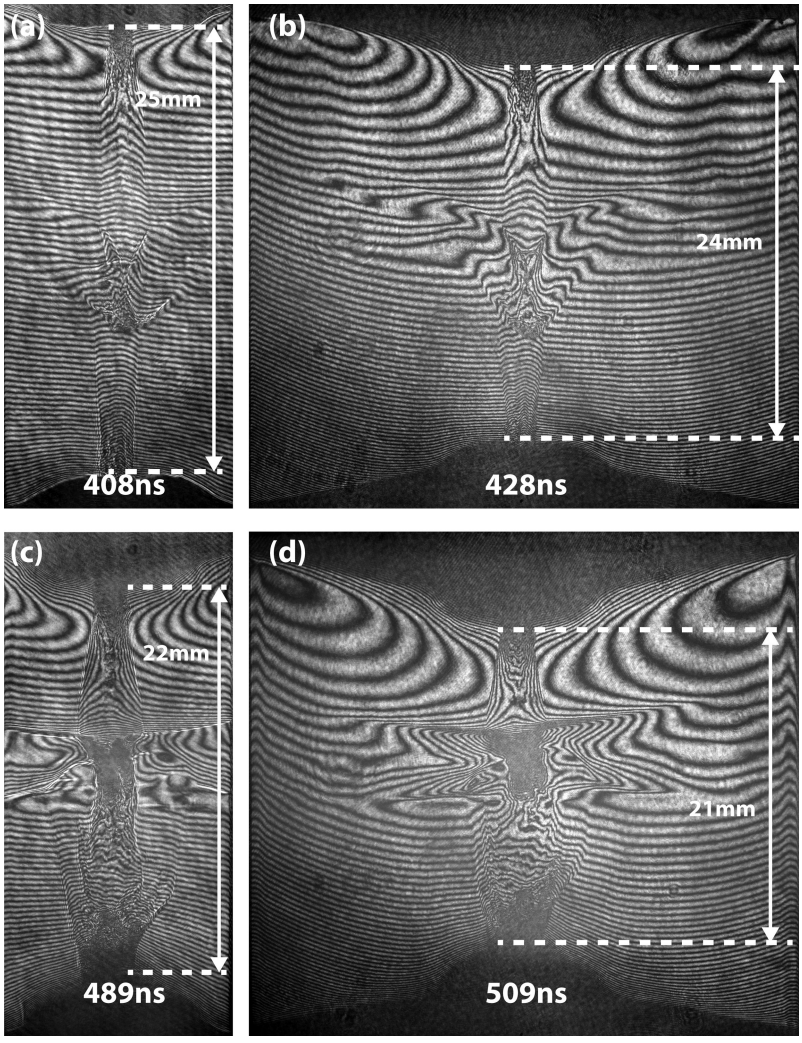

Figure 7.5: Four interferometry images at (a) 408ns, (b) 428ns, (c) 489ns and (d) 509ns from 532nm laser interferometry. The cathode-centric jet is at the bottom of all the images. From experiments s080312 and s080612.

On all the interferograms in figure 7.5 both jets are visible and appear with distinct edges and good collimation. In figure 7.5a and 7.5b both jets have collided and a denser region appears at the interaction point. In figures 7.5c and 7.5d the diameter of the plasma in the region of the anode-centric jet has increased. The cathode-centric jet is no longer narrow and well collimated as the flow is disrupted by the bow shock which has moved though it.

Figure 7.5a and 7.5b show the bow shock as a sharp bend in the fringes with a parabolic shape in the flow from the cathode-centric jet. This is a similar shape as seen in the XUV and optical images, the shock front of the bow shock is now observed to be well defined and extending to a larger radius than seen in the self emission images.

Figure 7.5c and 7.5d show the stationary shock structures as sharp horizontal bends in the fringes extending radially outwards from the interaction region of the two jets. At the shock front in frames 489ns and 509ns the fringes become discontinuous, indicating a large jump in electron density at this point.

The following sections will describe the specific features mentioned in the overview of the self emission and interferometry of the jet-jet interaction. A short discussion of the properties observed in the two jets, their velocity from emission and the electron density profile though the jets will be compared to the jets seen in previous chapters. The bow shock will then be discussed, finding its velocity and electron density contrast. Finally, the stationary shock structure will be discussed with reference to the electron density found form interferometry and then compared to the stationary shock structures seen in the previous chapters. A case will then be made for a dynamically significant magnetic field that develops midway between the two jets.

7.3 The dynamic behaviour of the jets during the jet-jet interaction

This section will look at the formation and propagation of the two jets and compare them to the jet systems discussed in the previous chapters. The velocity, radial expansion and the degree of collimation between the two jets will be discussed.

7.3.1 Formation of the jets

The two jet systems are observed to form and propagate in the same manner as seen in the anode-centric and cathode-centric jet systems. The anode-centric jet is observable for the duration of the experiment, however the cathode-centric jet is observable for a short period prior to the interaction of the bow shock though it.

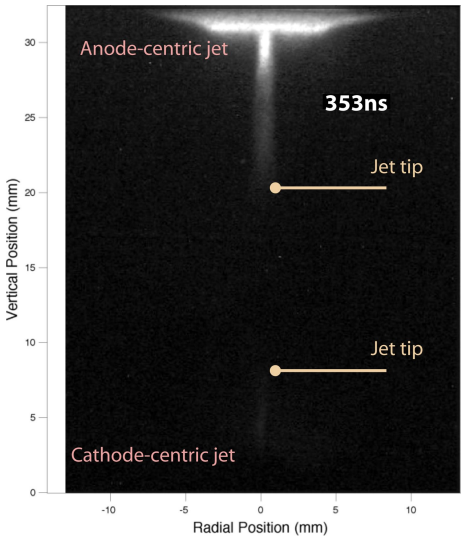

Figure 7.6: An optical emission image at 353ns from the fast framing camera. The emitting tip of the two jets is indicated. From Experiment s080612.

From inspection of the emission on the XUV and optical framing camera the velocity of the emitting regions in the jets can be found. The emission from the fast-framing camera at 353ns is shown in figure 7.6. The image indicates the position of the emitting jet tips. From the two experiments there are only four images prior to the collision of the jets of the emitting region at the jet tip. The average velocity of the anode-centric emitting jet tip is found to be $\sim 80 \pm 10$km/s, and the cathode-

centric emitting jet tip is found have an average velocity of $\sim$ 60$\pm$10 km/s. As these velocities are based on a couple of frames they are only indications of the initial velocities in the emitting flows from the jets. In the previous experiments the anode-centric jet had a velocity of 55$\pm$5km/s and the cathode-centric jet was found to have a velocity of 80$\pm$5km/s. The results do not match within error, though all the measurements are made on very few data points.

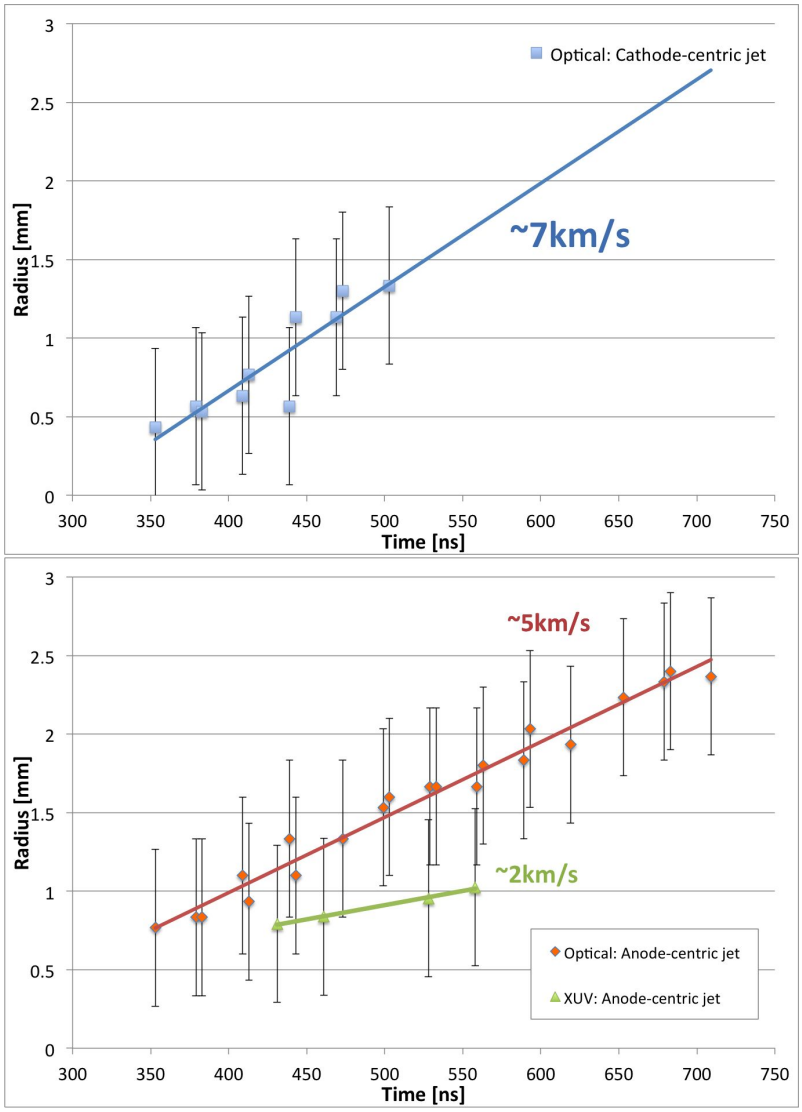

Figure 7.7: Radial expansion of the two jets as found from optical and XUV images. The cathode-centric jet is shown in blue. The optical emission from the anode-centric jet is shown in red and the XUV emission from the anode-centric jet is shown in green. From experiments s080312 and s080612.

Figure 7.7 summarises the radial expansion of the jet as measured from the

optical and XUV emission. The diameter of each jet is measured at a fixed axial position on the images and then this value is halved in order to find the radius. Figure 7.7 shows these measured radii against time for the anode-centric jet and the cathode-centric jet.

The radius of the cathode-centric jet is not recorded once the bow shock has passed through it. The velocity of the radial expansion of the anode-centric jet is found to be ∼5±2km/s from the optical emission images and found to be ∼2±2km/s from XUV emission. The radial expansion of the anode-centric jet is found to be ∼7±2km/s, this is consistent with results discussed in the previous chapters which were 6±2km/s for the cathode-centric jet and 5±2km/s for the anode-centric jet.

7.3.2 Density profile of the jets

The interferometry shown in figure 7.5b is processed to produce an electron line density map shown in figure 7.8a. The electron line density is processed to produce an electron density map which is shown in figure 7.8b.

Figure 7.8c and 7.8d shows the electron line density, $n_e l$, and the calculated electron density, n_e, profiles though the two jets. The profiles are colour coded and the regions that they were taken from indicated on the two density maps in figure 7.8a and 7.8b. The profile shown in figure 7.8c is though the cathode-centric jet. The density profile shown in 7.8d is through the anode-centric jet.

The profile though the cathode-centric jet shown in figure 7.8c indicates that the jet has a sharp density increase at its boundary to the halo plasma. The electron density in the body of the jet ranges between 4 to $9\times10^{18}\text{cm}^{-3}$. The halo plasma outside of the cathode-centric jet has a density of $\sim0.5\times10^{18}\text{cm}^{-3}$.

The profile through the anode-centric jet is shown in figure 7.8d. Comparing these profiles to figure 7.8c the jet appears to have a less abrupt increase in density between its interior and the halo plasma. The electron density in the body of the anode-centric jet ranges between 3 to 4 $\times10^{18}\text{cm}^{-3}$.

The electron line density $n_e l$, can be integrated across each jet in the $n_e l$ map in figure 7.8a and divided by the jet width to give the average axial electron density

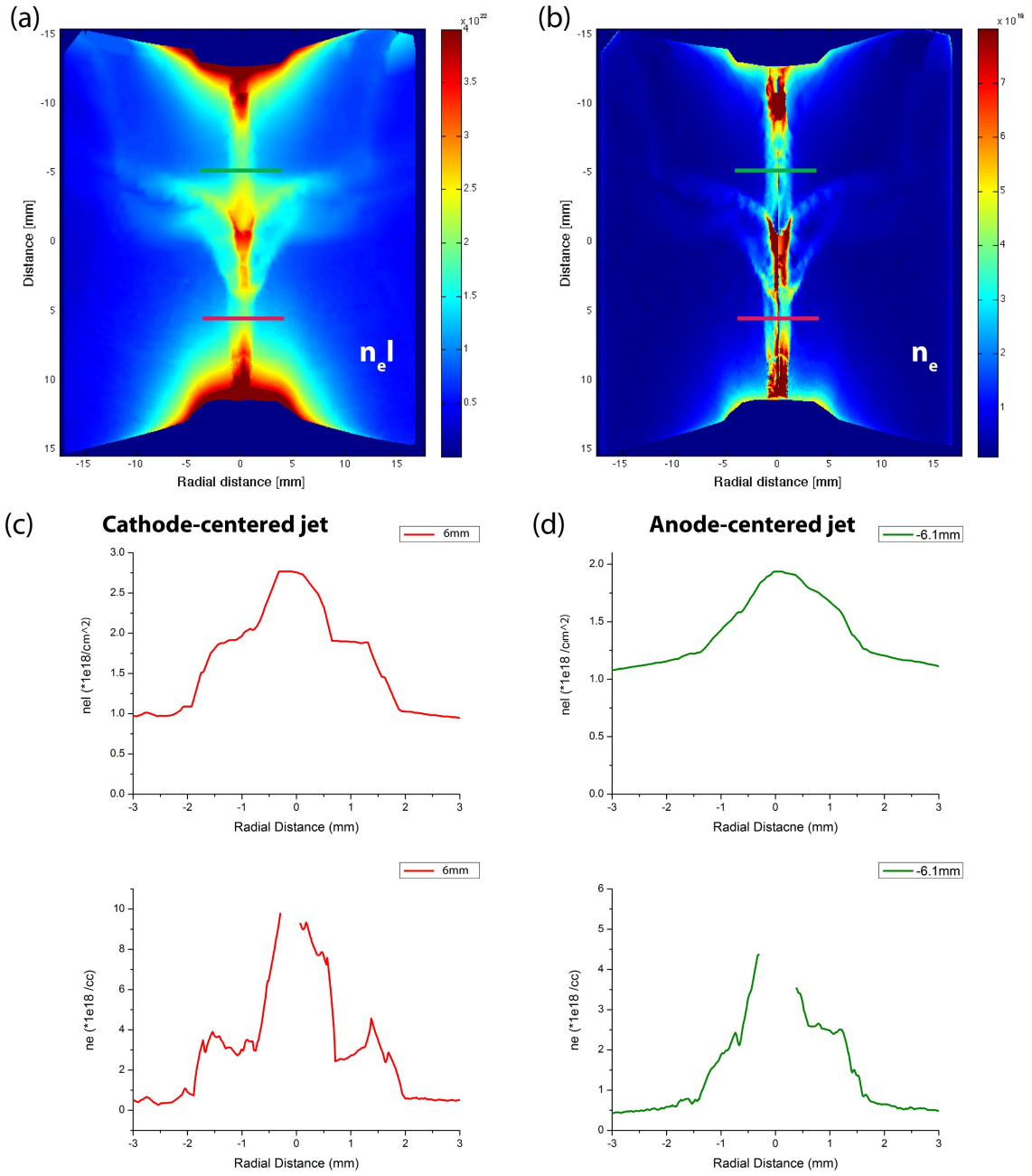

Figure 7.8: (a) Electron line density,$n_e l$, (b) electron density (c) & (d) density profiles through the stationary shocks. The region the profiles are taken corresponds to the coloured lines indicated on the $n_e l$ and n_e plots. Taken at 428ns from experiment s080612.

in each jet. This is plotted against the distance from the centre of the foil in figure 7.9. The anode-centric jet is shown in red and the cathode-centric jet is shown in blue.

The anode-centric jet is seen to have a higher ($\sim 2\times$) electron density closer to

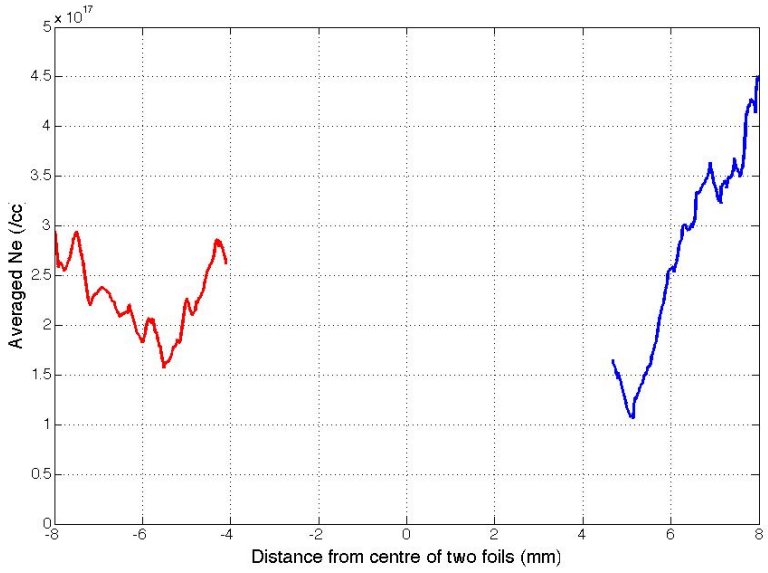

Figure 7.9: The electron line density map is radially integrated and divided by the jet width to give the axial average electron density. The anode-centric jet is shown in red and the cathode-centric jet is shown in blue.

the impact region of the two jets, which was shown previously in the comparison of the anode-centric jet-target system to the cathode-centric jet-target system. This is a possible indication of why the anode-centric jet moves though the cathode-centric jet producing the bow shock, as it will have a higher ram pressure than the cathode-centric jet, if the observed contrast in electron density is related to a similar difference in the ion density.

7.4 The bow shock

The bow shock is seen to form at ∼430ns on the optical images in figure 7.3 and is also visible in the XUV images shown in figure 7.4a and in the interferometry shown in figure 7.5a and 7.5b. The shock has a distinctive 'U' shape and moves downwards towards the cathode in all the time sequences. The front of the bow shock occurs in the body of the cathode-centric jet, however the shock front can be followed radially outwards into the halo plasma surrounding the cathode-centric jet, this is visible in the interferometry image at 428ns in figure 7.5b.

Figure 7.10 shows the position of the lowest emitting point of the bow shock in

both experiments. The positions of the emitting region at the anode-centric jet tip for these experiments is also plotted. The line drawn on the graph in figure 7.10 shows the projected positions of the jet tip from the initial positions. It can be seen that the bow shock appears to follow the anode-jet tip velocity before decelerating at later times. This gives an initial velocity for the bow shock that matches the averaged velocity for the emitting tip of the anode-centric jet at $\sim 80\pm10$km/s, the average velocity of the bow shock from the optical emission is then found to be 40 ± 10km/s.

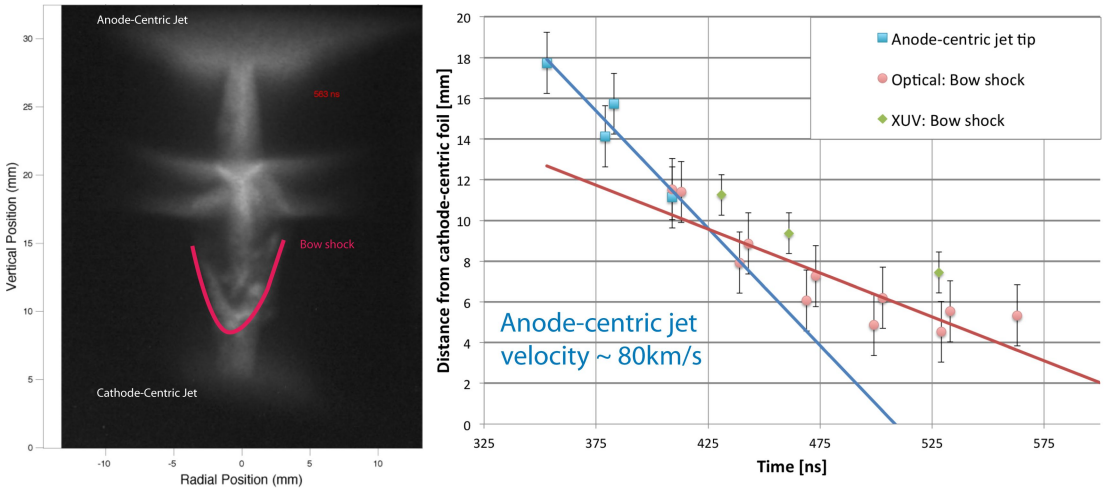

Figure 7.10: The position of the bow shock as seen in optical and XUV self emission images is plotted against time. The position of the optically emitting jet tip is plotted to give a projected position for the anode-centric jet tip if it had not collided with the cathode-centric jet. Image from experiment s080612 at 563ns. Graph from experiment s080312 and s080612.

7.4.1 Density profile of the bow shock

The interferometry shown in figure 7.5a is processed as described in appendix A to produce an electron line density map shown in figure 7.11a. Due to the asymmetry cylindrically in the region of the bow shock, an Abel inversion is not valid in this region. The image is taken at 408ns after current start and the bow shock has progressed ~4mm into the flow from the cathode-centric jet.

A selection of axial line outs are shown in figure 7.11b which are taken along the

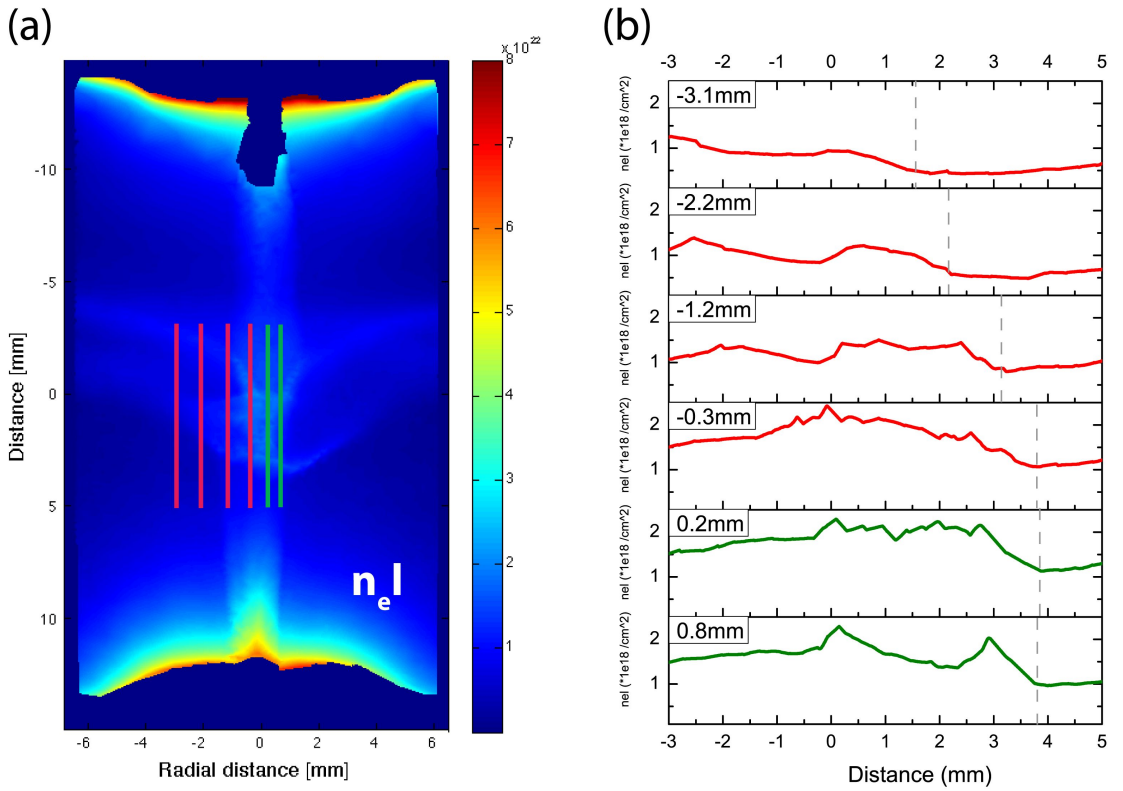

Figure 7.11: (a) the electron line density calculated from the interferometry shown in figure 7.5a. (b) six axial line outs taken at the positions indicated by the vertical lines on (a). The dashed grey line indicates the position of the bow shock. Taken at 408ns from experiment s080612.

coloured lines indicated on figure 7.11a. The front of the bow shock can be seen on all of the line outs. The bow shock is at z ~4mm in the profile at r=0.8mm from the jet centre, and at $z \sim$ 1mm in the profile at r=-3.1mm from the jet axis.

The material behind the front of the bow shock is seen to increase in electron line density. This corresponds to the $n_e l$ map which shows the region of the anode-centric jet behind the bow shock has an increased electron line density and appears narrow in comparison to the diameter of the anode-centric jet prior to the interaction region. This corresponds to the Y-shaped feature seen in the optical and XUV self emission, and indicates the material in the anode-centric jet is being compressed or shocked behind the bow shock.

Figure 7.12a shows the electron line density at the interaction region between the two jets taken 20ns after figure 7.11a from the same experiment. The scale on the image has been increased so that the interaction region and bow shock can be

seen in greater detail. Figure 7.12b shows four axial line outs through the bow shock which are taken at the positions indicated by the colour coded vertical lines in figure 7.12a.

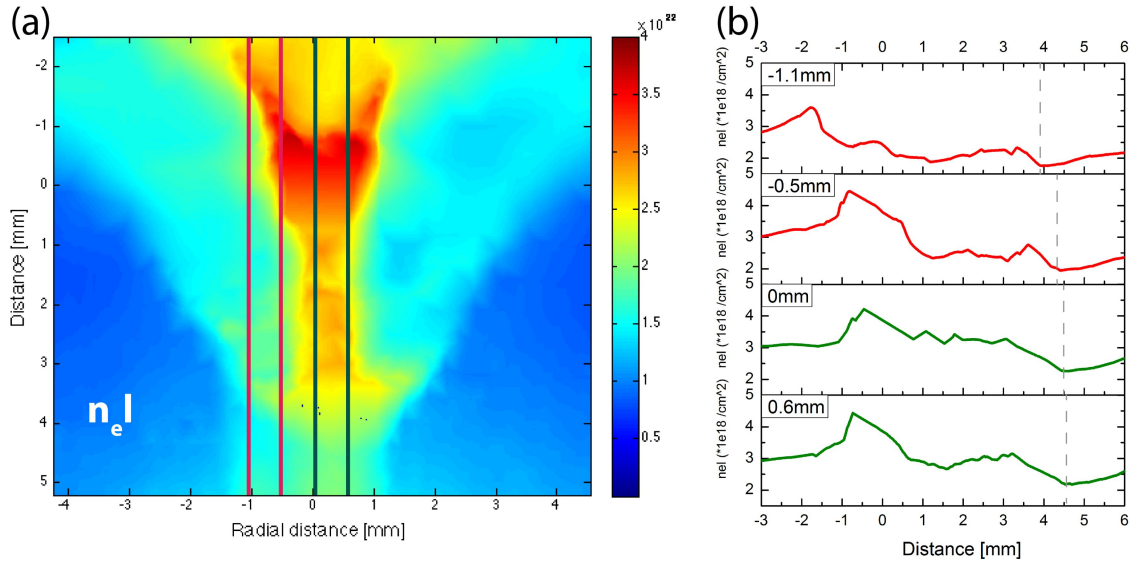

Figure 7.12: (a) the electron line density calculated from the interferometry shown in figure 7.5b. (b) four axial line outs taken at the positions indicated by the vertical lines on (a). The dashed grey line indicates the position of the bow shock. Taken at 428ns from experiment s080612.

From the axial line outs in figure 7.12 the bow shock is seen at $\sim$ 4mm from the central position between the two jet-forming foils. With comparison to the profiles shown in figure 7.11b, the bow shock increases to its peak density from the density in the cathode-centric jet over the same distance which is $\sim$ 0.5mm. As the electron line density has been used, the profile only gives an indication of the density contrast at the bow shock. From the profiles in figure 7.11b this is approximately a 2$\times$ increase and the profiles in figure 7.12b show a smaller increase of $\sim$ 1.5$\times$.

The region behind the bow shock in figure 7.12a is seen to be at a higher electron density and there is a narrow vertical column of dense plasma directly behind the bow shock.

7.4.2 The bow shock as a working surface

The bow shock can be viewed as a working surface at the front of the anode-centric jet moving into the material constituting the cathode-centric jet. The velocity of the bow shock can be estimated from the density contrast parameter η, which is the ratio of the density inside the jet to the density of the medium it is moving though, when η is low. For a jet of velocity ν_J the bow shock will move at velocity ν_{BS} as calculated by the following relationship (Blondin et al., 1990):

$$\nu_{BS} \approx \frac{\nu_J}{(1+\eta^{-1/2})} \tag{7.1}$$

Using the averaged electron densities in the anode-centric and cathode-centric jet to find $\eta \sim 2$, and assuming both jets are moving at ∼50km/s the expected velocity of the bow shock can be found. The above equation is valid in a frame of reference where the jet propagates into a stationary medium. From the frame of the material in the cathode-centric jet, the anode-centric jet approaches at 100km/s. For these approximations the bow shock velocity is expected to be ∼60km/s. In the lab fame this corresponds to a velocity of ∼10km/s.

This predicted velocity is slower than the observed progression of the bow shock into the cathode-centric jet. The exact density ratio is not known as there is not a measurement of the ion density, thus the velocity may be higher if $\eta >> 1$. For the bow shock to progress at the lower error boundary of ∼30km/s this would imply $\eta \approx 15$. If the anode centric jet has a larger velocity of 80km/s, the estimation of the density contrast can be reduced to $\eta \approx 2.5$. As the shock front is seen to decelerate in time, this implies that the jet is moving into a denser material, reducing the η for the jet and the surrounding material, and approaching the predicted velocity of the bow shock.

Figure 7.13 shows a cross section of a jet moving into an ambient medium. The jet is cocooned inside a shocked ambient gas that forms the inner boundary of the working surface. The outer boundary of the working surface is seen as the bow shock.

Previous investigations with the production of a working surface in a laboratory

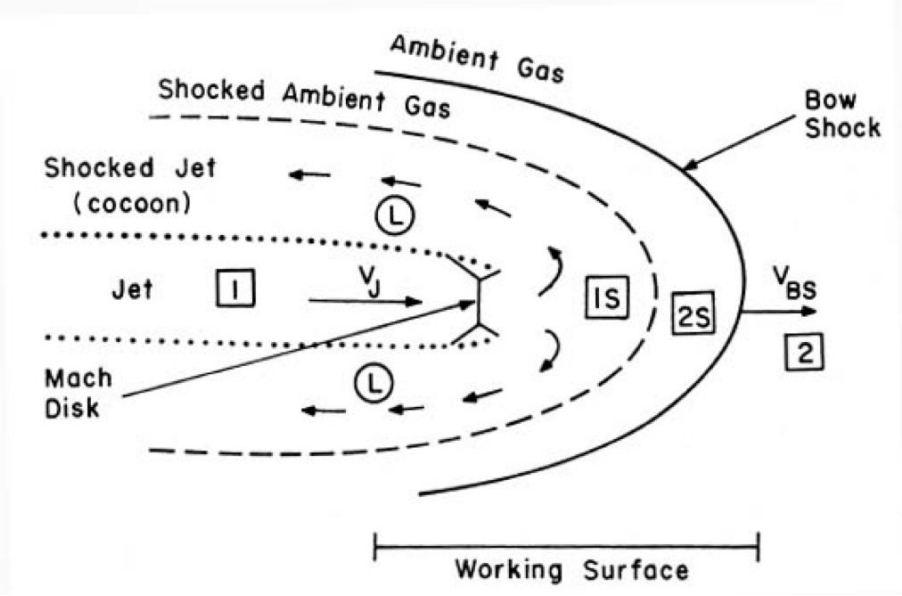

Figure 7.13: The working surface ahead of a supersonic jet propagating into an ambient medium. Reproduced from Hartigan, 1989.

supersonic jet moving into an ambient gas fill saw two effects on the dynamics of the jet as it interacted with the gas [19]. The pressure in the surrounding medium is shocked to match the pressure in the jet which acts to enhance the collimation of the jet. A working surface was produced at the head of the jet and a bow shock is formed ahead of the working surface in the ambient medium. The concept of a working surface is summarised in the schematic shown in figure 7.13.

The bow shock seen in the colliding jet experiments is a interesting feature for future study and the possibility of variation of the flow properties of the two jets may allow for a detailed investigation of the working surface formed.

7.5 The stationary shock feature

The two stationary shock features form after the collision of the jets, these shocks are visible from ∼430ns onwards in the optical emission sequences shown in figure 7.3. The shocks most likely arise from the collision between the two halo plasmas that accompany the dense jets. The shock fronts maintain their shape and rough position once they have formed. This is an interesting dynamic as the two shocks appear to be separate from each other and at larger radial distances from the centre

of the jets there is no detected emission in between the two shocks, for example in optical emission on frame 563ns in figure 7.3a or in XUV emission on frame 558ns in figure 7.4b.

7.5.1 Evolution of the stationary shock feature

The shape of the stationary shock as measured from the laser probing images at 509ns is shown in figure 7.14. The y-axis gives the distance from the centre point between the two jet-forming foils in millimetres. The points shown in red correspond to the shock front closer to the anode-centric jet and the points in blue correspond to the shock front closest to the cathode-centric jet.

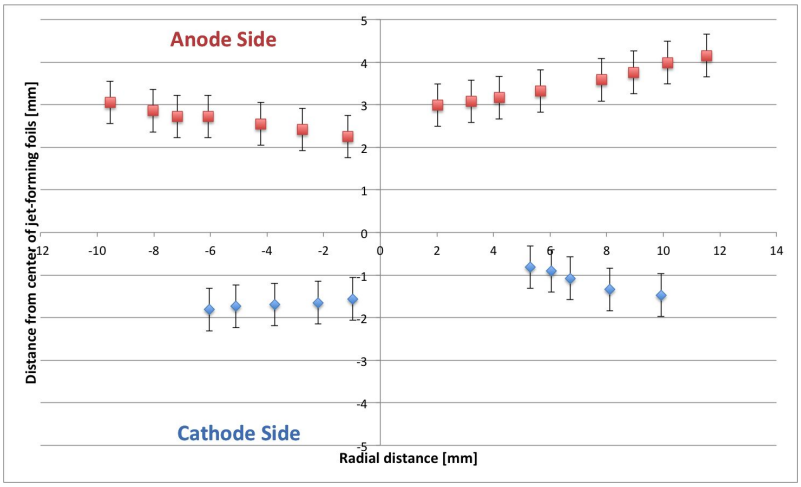

Figure 7.14: The position of the two stationary shock fronts at 509ns from shadowgraphy in experiment s080312. Note that the laser images show the two shock fronts curving away from each other, in contrast to the optical images which appears to show a curve in the same direction towards the anode. It is assumed the line of sight in the optical emission forms this initial impression.

In the case of both shock fronts the shape of the shock appears flat, sloping away from the central point between the two fronts. The shock is not perfectly symmetric, as was the case in the jet into target experiments, and the right hand portion of the graph shows both shock fronts with a steeper slope than the left hand shocks.

Figure 7.15 shows the separation between the shock fronts and the central position of the stationary shocks as measured from the optical emission and XUV

emission images shown in section 7.2. The figure shows a frame taken at 563ns which is annotated to show the position at which the separation of the shock was measured and the position that is used as the centre of the shock.

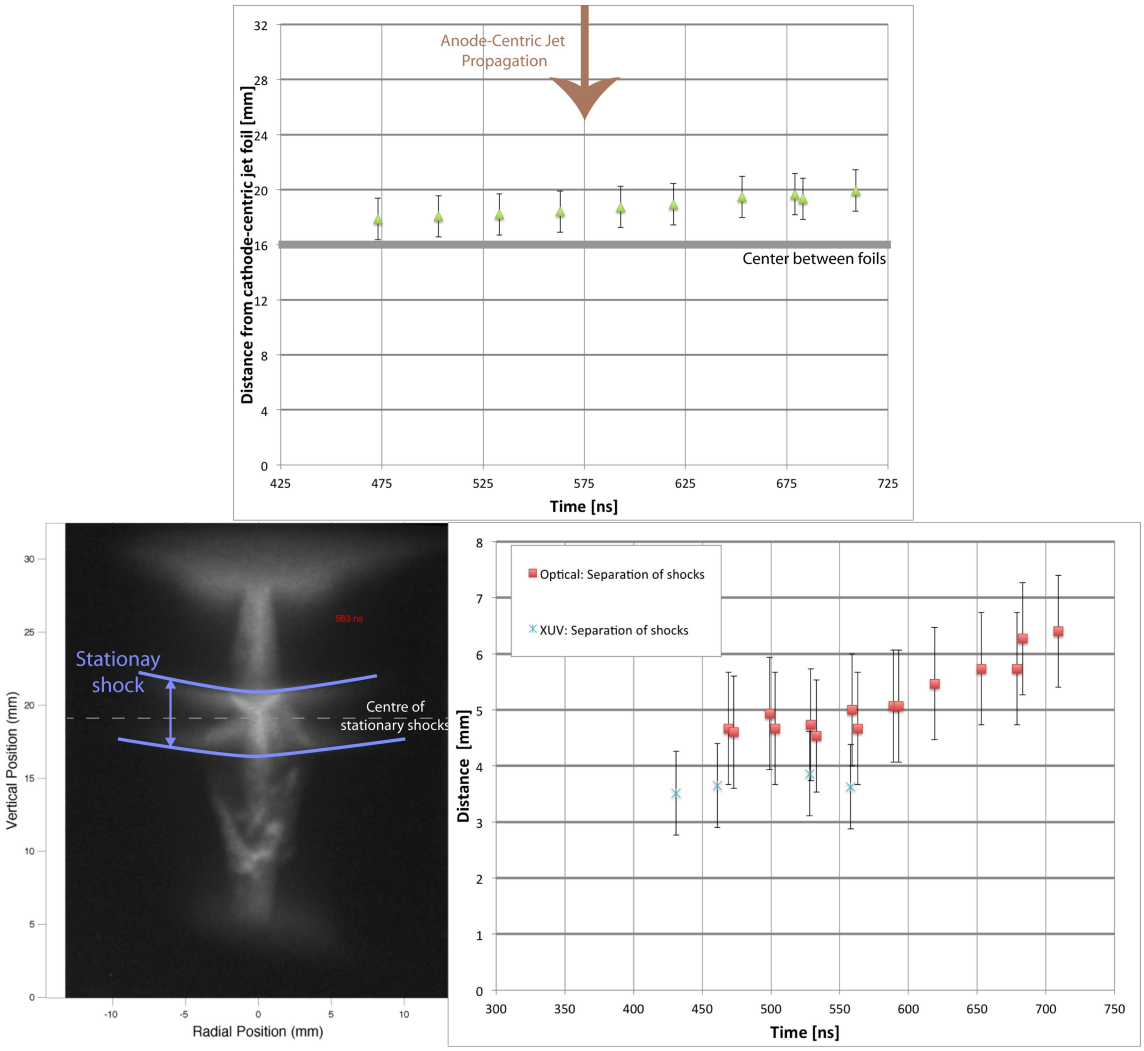

Figure 7.15: The position of the centre point between the two shock fronts and their separation measured from optical and XUV self-emission images. The annotated optical fast-frame image is from experiment s080612.

The separation of the shocks is measured in optical and XUV and shown on figure 7.15. The shock fronts increase their separation at a speed of $\sim 6 \pm 2$km/s. In XUV emission the separation is measured to increase at $\sim 1 \pm 1$km/s. The separation of the shocks appears to remain constant for ~ 150ns and the shocks then slowly move apart after this time.

The central position of the two stationary shocks is closer to the anode-centric

jet-forming foil. The central position of the shocks moves towards the anode-centric jet-forming foil at a velocity of $\sim 10 \pm 2$km/s.

The shape and movement of the shocks is similar to the shape observed in the previous experiments with the jet into a target foil, described in the previous chapters.

7.5.2 Density contrast across the stationary shock feature

The electron line density map for the interferogram shown in figure 7.5d, and taken at 509ns, is calculated as described in the appendix A. It has been stated previously that the stationary shock shows some asymmetry in the cylindrical symmetry plane. With this in mind, the Abel inversion was taken under the assumption that the asymmetry is reduced at larger radiuses from the jet-jet interaction region. For this reason the axial profiles taken through the stationary shock are chosen to be at radii over 5mm from the interaction region.

Figure 7.16a shows the calculated $n_e l$ map, 7.16b shows the n_e map. Figures 7.16c and 7.16d show the profiles though the n_e map taken in-between the corresponding coloured vertical bars on the density map shown in figure 7.16a and 7.16b.

At 509ns after the current start the stationary shocks are fully formed and seen to extend radially for r$\sim$ 10mm away from the central axis of the two jets. The bow shock has moved fully though the cathode-centric jet, and the flow from the cathode-centric jet is seen to be dispersed. As is seen on the density maps in figure 7.16, the stationary shock fronts have a region of higher density plasma on each front, but the region between the shocks has a lower density, forming a hollow axial density profile. This is most clearly seen in the electron density profile shown in figure 7.16c and 7.16d, as the profile takes a 'M' shape with a clear reduction in electron density between the two fronts.

In the axial profiles the anode-centric jet is on the left-hand side. The halo plasma electron density on the anode side is seen to be larger (e.g in the profile at 8.5mm, the halo plasma surrounding the anode-centric jet is $\sim 0.5 \times 10^{18}\text{cm}^{-3}$, in comparison to the halo plasma surrounding the cathode-centric jet which is $\sim 0.25 \times 10^{18}\text{cm}^{-3}$)

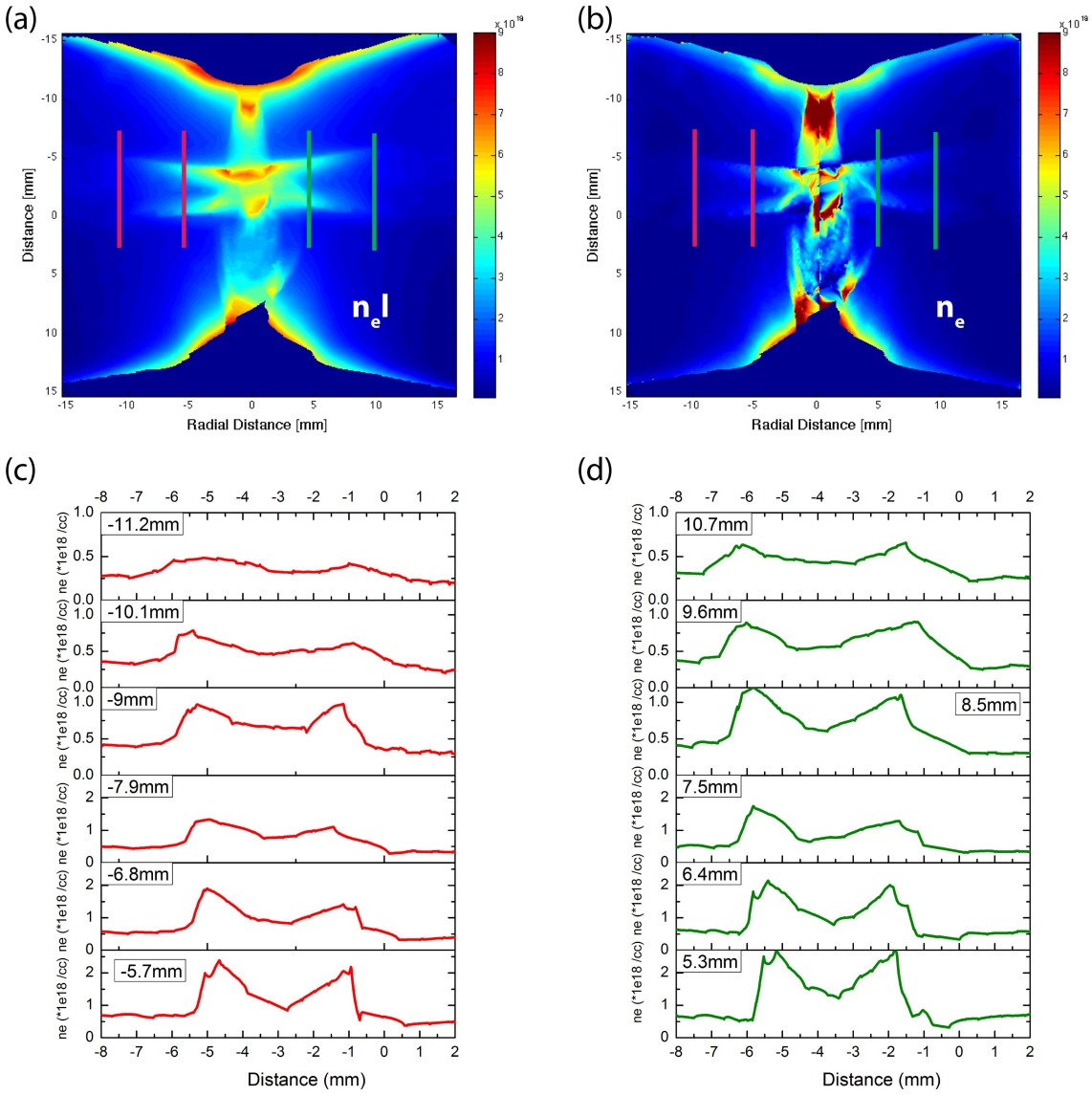

Figure 7.16: (a) Electron line density,$n_e l$, (b) electron density (c) & (d) electron density profiles through the stationary shocks. The region the profiles are taken in between the coloured lines indicated on the $n_e l$ and n_e plots. Note the density scale is doubled on the bottom three profiles in (c) and (d). Taken at 509ns from experiment s080312.

at almost all radial positions, which is consistent with the averaged electron density in the jets shown in figure 7.9 which suggested that the anode-centric jet is of a higher density than the cathode-centric jet. This observation was also seen in the jet into target experiments.

The width of the shocks is measured as the distance over which the electron

density observed in the halo plasma increases to the peak electron density measured in the shock. Figure 7.17 summarises the measured shock widths for both anode and cathode shocks.

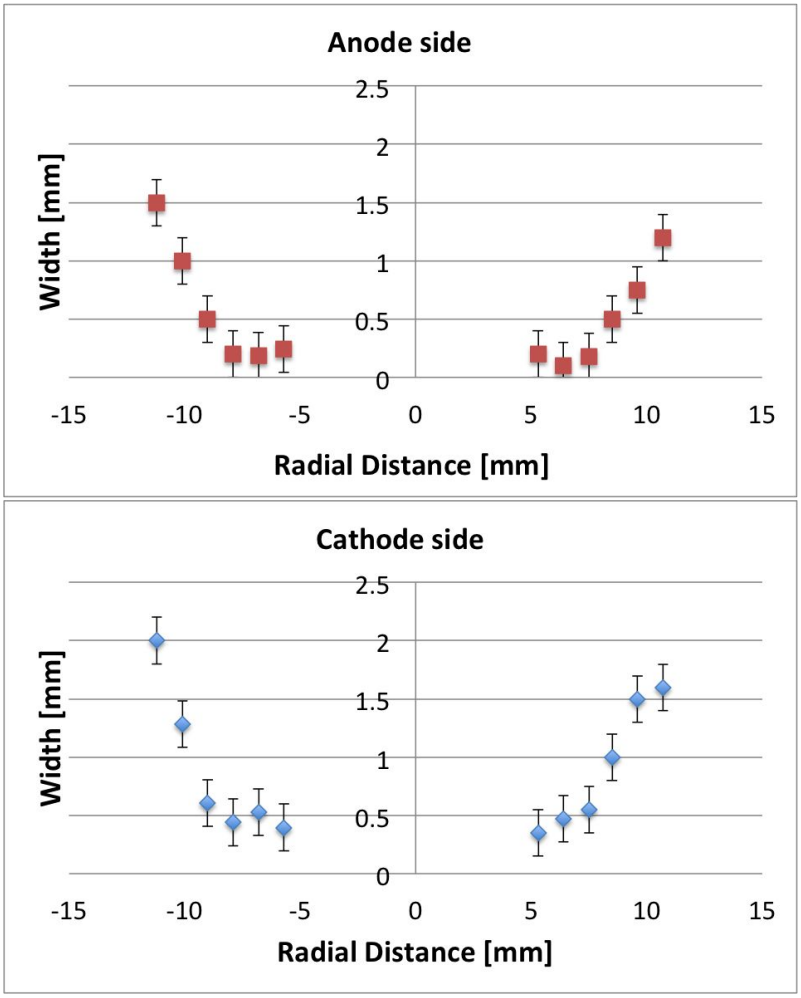

Figure 7.17: The width of the stationary shock front as measured from the electron density profiles shown in figure 7.16. The points in red are for the anode-side shock and the points in blue are from the cathode-side shock. Taken at 509ns from experiment s080312.

The shock width is seen to increase with radius, which is consistent with the measurements made for the previous jet into target experiments. The electron density contrast across the two shocks can also be found from the axial profiles shown in figure 7.16c and 7.16d.

Figure 7.18 shows the electron density contrast as measured from the density map in figure 7.16. The shock closest to the cathode is shown in blue and the shock

closest to the anode is shown in red. The ratio of the electron densities in the halo plasma and at the peak density in the shock is plotted against the radial distance from the centre of the two jets. It can be seen that the electron density is increased $\sim 3\times$ for both shock fronts at radial positions closest to the jet axis. The density contrast is decreased at larger radiuses from the jet centres. As the jump factors are taken at large radii (>5mm) the observed jump factor is similar to the previously observed density jumps for the jet-target experiments observed at similar radii.

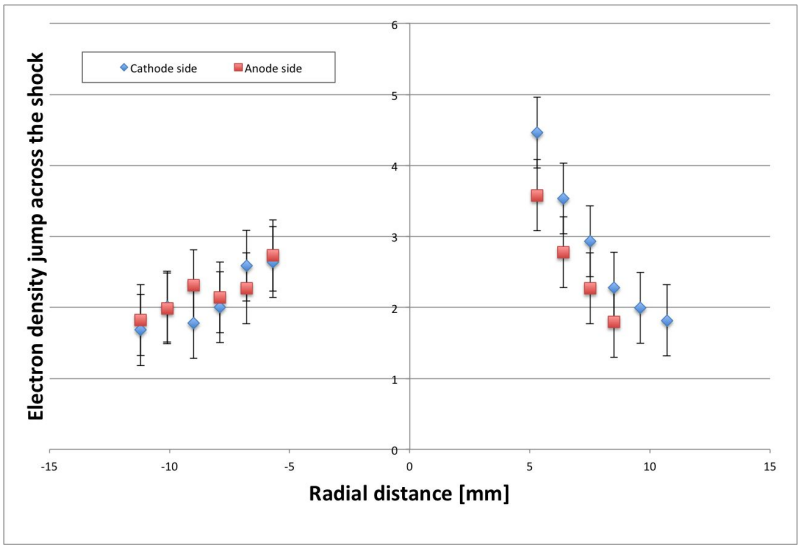

Figure 7.18: The electron density ratio is found by comparing the electron density at the peak of the shock front with the electron density in the halo plasma. This is plotted against the radial position of the shock front. The cathode-centric jet is shown in blue and the anode-centric jet is shown in red. Taken at 509ns from experiment s080312.

7.6 A comparison of the stationary shock structures observed in the jet into target experiments with the stationary shock structures observed in the colliding jet system

This section will attempt to analyse the origin of the stationary shock structures discussed in the previous section of this chapter by comparison with the equivalent

structures discussed in the previous chapters. The stationary shock structure seen in the cathode-centric jet interaction with a thin foil is presented in section 5.4, of the three systems discussed this was diagnosed the most extensively and many experiments were done that reproduced the discussed results. The stationary shock structure was also seen in the reversed polarity system and discussed in section 6.4.

The reproduction of the stationary shocks in the colliding jet system indicates ablation or plasma formation from the surface of the target plays only a small part in the stationary shock formation. For this analysis it is then assumed the stationary shock system in the colliding jet experiment can be halved at the midpoint between the two shock fronts and this will be an identical interaction concerning the stationary shock as seen in the jet into target systems. The cathode-centric jet into a thin foil target is compared to the half interaction of the anode-centric jet with the cathode-centric jet in the colliding jet system in figure 7.19.

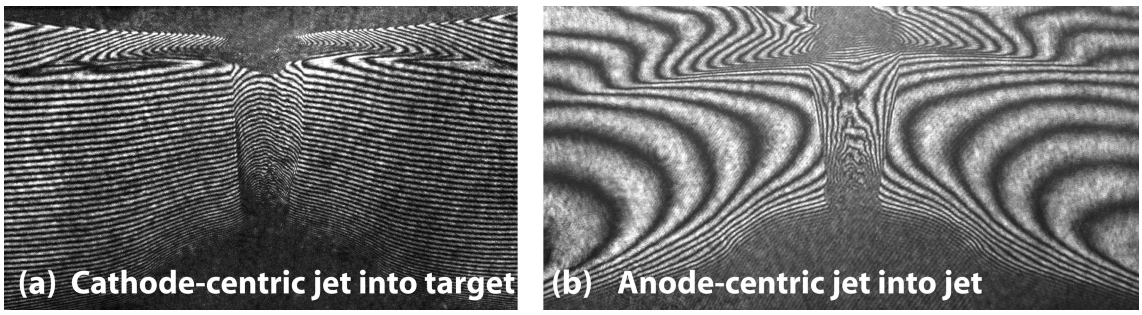

Figure 7.19: (a) Interferometry of the cathode-centric jet at 434ns after current start interacting with the thin metallic target. From experiment s052912 (b) the anode-centric jet interacting with the flow from the cathode-centric jet in the colliding jet system at 509ns, the image has been halved to show only the anode-centric jet. From experiment s080312

There are some noticeable differences between the two systems shown in figure 7.19, but their similarity is noteworthy. Apart from the absence of a target and reverse shock in figure 7.19b, the shock front also appears flatter and has a steeper angle. The shock however has a similar radial extension from the jet axis and a similar shock width from visual inspection of the phase lines.

7.6.1 The plasma properties in the stationary shock estimated from the experimental data

The similarity of the three shock systems will be used to create an idealised model of the plasma parameters in the shock front or 'test' version of the shock. This will allow the microscopic plasma parameters to be evaluated and the effects of magnetic fields and radiative losses in the shocked system to be discussed.

The density contrast across the test shock will be evaluated with the average values found for the halo plasma electron density of $\sim$0.5 to $1\times10^{18}\text{cm}^{-3}$, and the post shock electron density of $\sim 2\times10^{18}\text{cm}^{-3}$. The width of the test shock is assumed to increase radially and lay between 0.1mm and 1mm, as seen in the experiments. Density, both above and below the shock, is assumed to decrease radially. The idealised halo plasma before the test shock is assumed to have a uniform velocity between 50km/s and 70km/s. The electron temperature is assumed to not vary across the test shock and is evaluated at 25eV. Ionisation and ion density will be discussed where the values are needed.

The values chosen for the test shock are assumed to be a 'snapshot' in time of the development of the shock, when the front is fully formed. The temporal evolution of the parameters estimated will be discussed where it is of interest.

The test case above will be used as a bench mark to evaluate the nature of the shock in light of the experimental measurements.

7.6.1.1 Heating of the ions and equilibration length

At the shock front the kinetic energy of the ions in the flow of plasma forming the halo plasma is converted into the ionic thermal energy at the shock front. From previous work with the jet in vacuum, the cathode-centric jet was found to have a velocity of 50km/s from Thomson scattering. Measurements from optical and XUV emission give a higher estimate of $\sim$80km/s. For this discussion the ions in the halo plasma will be assumed to have an axial velocity of 50km/s, future experimental observations should attempt to measured this velocity more accurately. The maximum ionic heating of the ions in such a flow is given by [1]:

$$k_B T_i = \frac{2(\gamma - 1)}{(\gamma + 1)^2} u_s^2 \frac{A m_i}{(Z + 1)} \tag{7.2}$$

Where k_B is Boltzmann's constant, u_s is the axial velocity of the halo plasma, Z is the ionisation and γ is the compression factor of the material. The compression factor can be estimated from the ratio of ion densities in the shocked and unshocked material, assuming a strong shock. The ion density can be found from the electron density if the ionisation of the plasma is known, in the case of the stationary shock this can only be estimated. If it is assumed the shock is strong, then the density jump across the shock will be ∼4 if γ is assumed to be $\sim 5/3$. The ionisation is initially assumed to be equal to 1 in both the shock and the halo plasma, though it is most likely higher as the temperatures measured with Thomson scattering ($> 20eV$) were sufficient to multiply ionise aluminium. The effect of a higher ionisation of $Z \sim 3$ will be discussed alongside the lower ionisation estimate below.

From the above assumptions the maximum heating the ions can receive at the shock front is ∼ 70eV. If the ionisation is higher ($Z = 3$), then this becomes ∼ 30eV which reflects the kinetic energy of the flow being distributed between the ions and the electrons. Temperatures behind the shock front were observed though Thomson scattering to be $T_i \sim 55 \pm 10eV$ which suggests that both models do not accurately predict the measured temperature. Using a higher flow velocity of 70km/s and a ionisation of $Z = 3$ gives an ionic heating of $\sim 65eV$ which matches both the higher flow velocity observed in optical and XUV emission and the higher ionisation observed with Thomson scattering behind the shock front.

The ions will loose their thermal energy preferentially though collisions with electrons. The electrons will either rise in temperature uniformly until the ion and election temperature is matched, or they will stay at the same temperature and use the gained thermal energy to increase the ionisation, in which case the ion temperature decreases to the electron temperature which stays approximately constant through the shock.

From the Thomson measurements in section 5.4.3 the electron temperature was estimated to be ∼25eV at all the radial positions measured above the stationary shock. As the shock curved downwards, these measurements were made at increas-

ingly larger distances from the shock front (within a range of ∼0.5 to 1mm from the flock front). This observation indicated the extra energy given to the electrons by the ions is expended by increased ionisation and the ion temperature would then be expected to decrease to match the estimated electron temperature of 25 ± 5eV.

The distance over which the ions will give their thermal energy from the shock front to the electrons is the equilibration length. The ion-electron collision frequency and the ion velocity in the shock can be used to estimate the equilibration length. The ion-electron collision frequency, τ_{ei}, is given by [54]:

$$\tau_{ei} = \frac{AT_e^{\frac{3}{2}}}{3.2 \times 10^{-9} n_e Z^2 \ln \Lambda} \tag{7.3}$$

Where A is the atomic number (27 for aluminium), n_e is the electron density and $\ln \Lambda$ is the Coulomb logarithm, which is ≈ 6. The velocity of the ions in the shock can be found from the jump conditions for a strong shock that state:

$$\frac{u_2}{u_1} = \frac{(\gamma - 1)}{(\gamma + 1)} \tag{7.4}$$

The subscript '1' denotes the unshocked fluid velocity (in this case the halo plasma) and '2' denotes the shocked fluid velocity. If γ is estimated as 5/3, which gives a shocked fluid velocity of $\sim \frac{1}{4}u_1$. For a halo plasma velocity of 70km/s a shocked velocity of ∼18km/s is found.

The estimation of the equilibration length will use a shocked plasma density $n_e \sim 2 \times 10^{18}\text{cm}^{-3}$ and an ionisation, Z=3. This gives a electron-ion equilibration length of $\sim$ 0.2mm for a initial flow velocity of 70km/s and the electron temperature of 25eV. As the collision frequency depends on the inverse square of the ionisation, the cooling length will be greatly increased if there is a lower ionisation.

If the equilibration length is taken to be ∼0.2mm then the plasma in between the two shock fronts in the colliding jet system will have a plasma in local thermodynamic equilibrium of $\sim$ 25eV in between the two shock fronts.

7.6.1.2 The ion mean free path from the 'slowing down' length

The ions entering the shock front will also be decelerated by their interaction with the ions and electrons in the shock front. The ions approach the shock front with

a velocity of 70km/s and are then heated and decelerated such that they move through the shock front at a quarter of their initial velocity. At the shock front the relaxation length for ion-ion collisions is termed the 'slowing down' rate $\nu^{i|i'}$, and can be estimated in the 'fast' limit by [55]:

$$\frac{\nu^{i|i'}}{n_{i'}Z^2Z'^2\ln\Lambda} = 9\times10^{-8}\frac{2}{\sqrt{A}}\frac{1}{\epsilon^{3/2}} \tag{7.5}$$

For the ions entering the shock with an ionisation of $Z = 3$ and a kinetic energy $\epsilon \sim 690eV$ interacting with a shocked ion of $Z' = 3$ and $n_{i'} = 2\times10^{18}\text{cm}^{-3}$ gives a relaxation length, when combined with the pre-shock velocity of the ions, of $\lambda_{i|i'}$ ~0.1mm. For the lower estimate of the pre-shock ion velocity of 50km/s ($\epsilon \sim 350eV$), the relaxation length becomes $\lambda_{i|i'}$ ~0.04mm.

The interaction of the ion in the shock with the electrons can be estimated in the 'slow' limit to give the ion-electron relaxation rate $\nu^{i|e}$, from the following [55]:

$$\frac{\nu^{i|e}}{n_eZ^2\ln\Lambda} = 1.6\times10^{-9}\frac{1}{AT_e^{3/2}} \tag{7.6}$$

The post-shock ion velocity is found to be one quarter of the pre-shock velocity of the ions. Evaluating the ion-electron relaxation length in a similar manner to the ion-ion relaxation rate for a electron density of $n_e = 2\times10^{18}\text{cm}^{-3}$, $T_e = 30\text{eV}$ and $Z = 3$, it is found to be ~0.45mm. The ion-electron relaxation length is sensitive to the inverse square of the ionisation. For $Z = 2$ the ion-electron relaxation length is found to be $\lambda_{i|e}$ ~1mm.

The relaxation lengths give the mean free path of the ion through the shock front. The mean free path of the ions gives the physical shock width measured in the experiments between the halo plasma and the shocked material in the stationary shock. At radial positions close (~2mm from the axis) to the jet the shock width was measured to be ~0.1mm, at large radial distances (~8mm from the axis) the shock width was measured to be ~0.5mm which is shown in figure 5.31. Over the same radial distance the density jump from the halo plasma to the material above the stationary shock is observed to decrease from ~5 to ~2 times increase, shown in figure 5.30. The Thomson scattering measurements estimating the electron

temperature were taken in a similar radial interval (0mm to 6.4mm from the jet axis) and estimate a constant electron temperature in this region for $T_e = 25 \pm 5$eV. The ion-ion relaxation rate is much smaller then the ion-electron relaxation rate for similar parameters, indicating it dominates the measured shock width.

7.6.1.3 The hydrodynamic and radiative cooling times

The hydrodynamic and radiative cooling times can be estimated to find the effect of radiative cooling in the shock. The hydrodynamic time can be estimated as the distance between the two shock fronts in the colliding jet system divided by the post shock velocity which was estimated to be a quarter of the flow velocity in the halo plasma. For half the shock separation of $\sim \frac{4}{2}$mm, as seen at early times in figure 7.15, this gives a hydrodynamic time of ∼120ns.

The cooling time describes how quickly radiation escapes from the shock front. This is the ratio of the thermal energy per volume, E_t in the shock front, to the power radiated per volume, P_r, in the shock front.

$$E_t = \frac{3}{2} n_i (Z+1) k_B T \tag{7.7}$$

$$P_r = Z n_i^2 C(T) \tag{7.8}$$

In the equation for P_r, $C(T)$ is the cooling function found from Post et al., 1977 for a minimum temperature of 20eV to be $4{\times}10^{-20}$[ergcm^3/s]. For the previously stated parameters ($T_e \sim 30$eV, $\gamma = 5/3$, $Z = 3$ and $n_i = 2 \times 10^{18}$cm^{-3}) in the stationary shock this gives a cooling time of ∼1ns<<hydrodynamic time, hence, the stationary shock is radiatively cooled. This is summarised by the cooling parameter, χ, which is the ratio of the cooling time to the hydrodynamic time. For the stationary shock $\chi << 1$.

7.6.2 The ram pressure from the colliding halo plasmas surrounding the jet

The shock is created from the large ram pressure of the halo plasma colliding into a countering force. The shock is seen to stay in approximately the same position for the duration of the experiment and the shocks retain their separation from each other, which implies the force the ram pressure encounters is of equal magnitude. The ram pressure, p_R, is given by:

$$p_R = \rho u^2 \tag{7.9}$$

Where ρ is the density of the halo plasma. Thermal pressure, p_T is given by:

$$p_T = nk_BT \tag{7.10}$$

Where n is the number density and T is the temperature. Estimating at the 'test' shock front for an electron temperature of 30eV, this gives a thermal pressure of $\sim 1 \times 10^7$Pa. For a halo plasma of ion density $\sim 0.3 \times 10^{18}$cm^{-3}, as estimated from the electron density assuming $Z = 3$, and velocity 70km/s, this gives a ram pressure of $\sim 2 \times 10^7$Pa, which is two times larger than the thermal pressure.

In the case of the stationary shock in the colliding jet system, unless the thermal pressure matched the ram pressure from both halo plasmas, it would be expected that the shocks would move closer together. If the thermal pressure at the shock front matched the ram pressure, the density drop behind the shock front should correspond to a rise in plasma temperature equal to the decrease in density ($\sim 2\times$). Due to the calculated electron-ion equilibration length of the plasma and the lack of observed emission in between the shock that may indicate an increase in temperature, this is an unlikely scenario.

7.6.3 A magnetic field pressure that separates the two shock fronts in the colliding jet system

The presence of a magnetic field in-between the two shock fronts could exert a magnetic pressure to compensate the ram pressure of the colliding halo plasmas. The possibility of an azimuthal magnetic field in the halo plasma acting as a confining force for the jet was discussed in chapter 4. The observed improvement in the half-opening angle of the jet from the base to the body of the jet was strong evidence of this confining force. Simulations of the jet, discussed in section 4.5, suggested there was a magnetic field present above the foil.

The size of the magnetic field carried in the halo plasma is determined by the electron fluid conducting current. In this manner the magnetic field is said to be 'frozen' into the election density of the plasma. At the shock front the electron density is observed to increase by a large factor which was seen to vary between a jump of 2 at large radii and a jump >4 at radii closer to the jet axis. This leads to a hypothesis that the field advected by the flow of electrons though the shock can be accumulated in the region between the two shock fronts where the flow is assumed to stagnate. A possible direction of current in the plasma is shown in figure 7.20. This would then explain a reduced density between the shocks and produce a magnetic field that can balance the ram pressure from the flow in the halo plasmas.

The required magnetic field to balance the flows can be found through a comparison of the ram pressure from the flow to the magnetic pressure needed to match it. Magnetic pressure p_B, in gaussian units, is given by:

$$p_B = \frac{B^2}{8\pi} \tag{7.11}$$

For a field of 6T, this would exert a magnetic pressure of $\sim 2 \times 10^7$Pa which would match the ram pressure of a 70km/s fluid with ion density $\sim 0.3 \times 10^{18}\text{cm}^{-3}$. At larger radii from the jet axis the halo plasma is seen to decrease in density, which would also decrease the strength of the magnetic field needed to balance the ram pressure.

As material from the halo plasma continues to arrive at the shock front it is

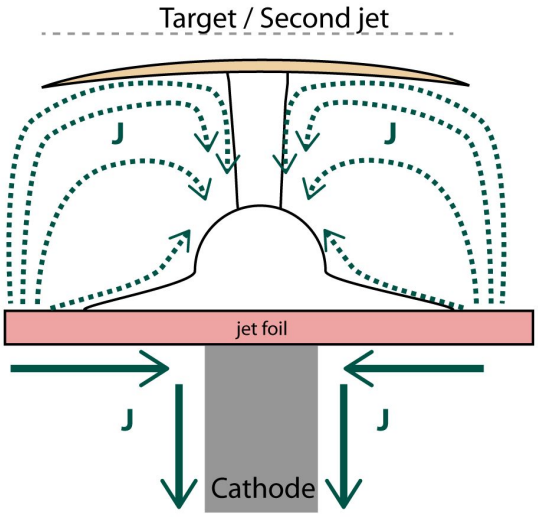

Figure 7.20: The green arrows marked 'J' indicate a possible direction of the current in the halo plasma for a stationary shock and jet system that is cathode-centric. The density of the current is expected to to be proportional to the electron density, and when the plasma is compressed in the shock front the current density will increase proportional to the compression.

expected that the density behind the stationary shock will increase in time, and this was seen in the processed interferometry images for the cathode-centric jet. If this is the case, it may also be expected that the magnetic field is increased at the shock front, strengthening the stationary shock structure.

The presence of a magnetic field introduces a new characteristic length in the shock front which originates from the orbit of the ions along the magnetic field lines, termed the Larmor radius. If a perpendicular magnetic field, to the jet, exists behind the shock front the ion Larmor radius R_L, can be found from:

$$R_L = \frac{v_i m_i c}{ZeB} \tag{7.12}$$

For the plasma parameters, $v_i = 70$km/s, $Z = 3$ and a magnetic field of $\sim$10T in the shock, then $R_L \sim 0.4$mm, which may play a part in the origin of the shock thickness, if there were to be a radially decreasing magnetic field, the Larmor radius would be expected to increase, possibly increasing the shock width. The estimate of R_L can be compared to the deceleration length of the ions, $\sim$0.45mm and their ratio is found to be $\sim$1. This implies both collisional and magnetic effects may play a role in the shock, and that at larger radius the magnetic field may dominate the

width of the shock front.

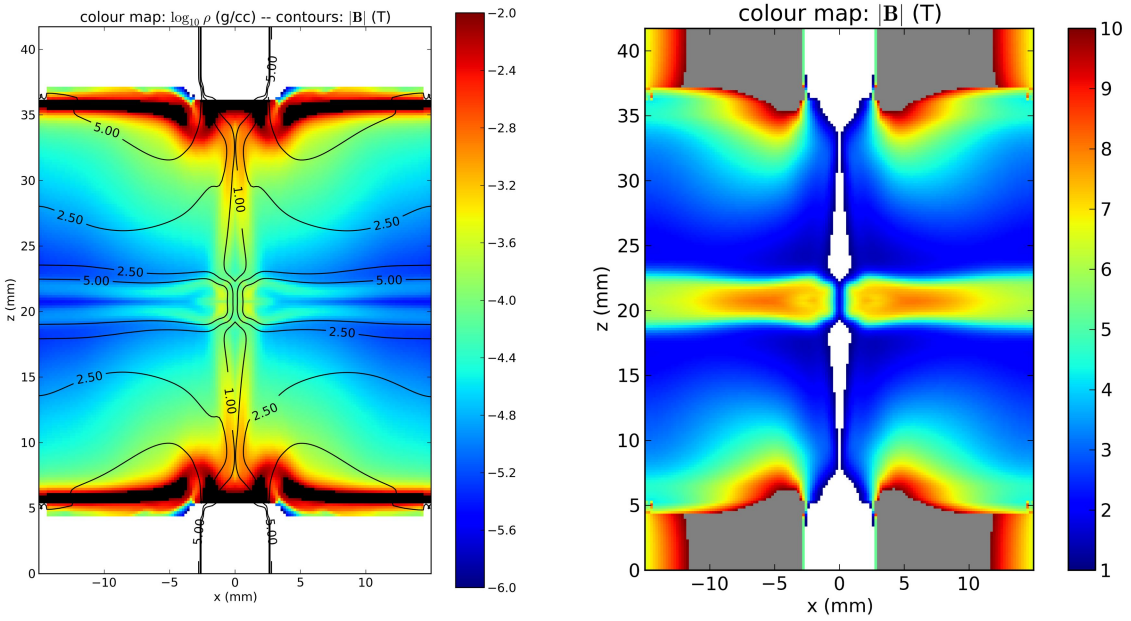

Figure 7.21: Density and magnetic field maps simulated for a colliding jet system. Thanks to Andrea Ciardi, Université Pierre et Marie Curie

Figure 7.21 shows preliminary simulation results from the MHD code GORGON of two identical jets colliding with each other. The jets propagate vertically in the image and are represented as white diverging columns in the magnetic field and density maps. The simulation reproduced the double stationary shock feature seen in the experiments, and the reduced density observed between the two shock fronts. The figure shows a magnetic field has developed between the two shock fronts, which is on the order of 10T near the jet axis.

This simulation result appears to be in agreement with the above analysis, which is strong motivation for continued experimental work with the colliding jet systems. A mechanism for measuring the magnetic field between the stationary shocks will be discussed in the next chapter as part of the suggested further experimental work.

Chapter 8

Conclusions and future work

In this thesis results from the studies of the interaction of supersonic plasma jets with planar foil obstacles and of the head-on collisions of two jets were presented. The interactions produce several shock features which were studied.

This chapter will summarise the results and analysis presented in chapters 5, 6 and 7 and discuss the future investigations which may be conducted to further support the observations made in this thesis and extend the presented work.

8.1 The formation and propagation of supersonic jets in the presence of a target foil

The results detailing the formation and propagation of a supersonic jet in vacuum originating from a radial foil set up were summarised in chapter 4. The jet in vacuum was found to have an electron density of 1 to $8\times10^{18}\text{cm}^{-3}$ with a surrounding low density halo plasma. The jet was found be well collimated and have a lower axial velocity of 50km/s from Thomson scattering and upper axial velocity of 85km/s from XUV self emission images.

The jet was used to study the formation of shocks by combining the jet set up with a thin metallic foil target placed ∼15mm from the jet-forming foil, this is described in section 5.1. The overview of the jet and target interaction, described in section 5.2, showed that the jet appeared to form and propagate in the same manner

as the jet in vacuum, with a uniform and dense central column surrounded by a low density halo plasma.

The optical emission from the jet-target interaction, observed on the fast-framing camera described in section 3.2.5.1, is used to measure the velocity of the jet tip, radial expansion and half opening angle of the jet. The jet created in the presence of the target is observed to have a tip velocity of $\sim 80 \pm 5$km/s. The jet expanded radially at 6±2km/s with a half-opening angle of 1° to 6° in the body of the jet. The base of the jet, in the region up to ∼5mm above the cathode, was observed to have a larger opening angle of 6° to 11°. These observations are summarised from section 5.3.1. These are seen to match within error similar measurements made from XUV emission of the jet propagating in vacuum.

532nm laser imaging interferometry measurements of the jet are used to find the electron density of the jet body and the halo plasma, these results are shown in figures 5.8 and 5.9. The jet body was found to have an electron density of ∼2 to 7×10^{18}cm^{-3}, with the highest values measured closest to the jet-forming foil. The halo plasma is found to have a density of $\sim 0.5 \times 10^{18}$cm^{-3}. These results appear consistent with the jet in vacuum measurements which showed an electron density in the body of the jet between ∼1 to 8×10^{18}cm^{-3}, with the highest value measured closest to the jet-forming foil and a halo plasma density of $\sim 1 \times 10^{18}$cm^{-3}. The density of both jets was seen to decrease axially, and the halo plasma is seen to decrease in density radially.

Thomson scattering measurements were made at several radial positions across the body of the jet and in the halo plasma to find the ion and electron temperatures and the radial velocity of the plasma, the results are discussed in section 5.3.3. The jet was found to have an ionic temperature of 55±10eV and a ZT_e, the product of ionisation and electron temperature, of 50 ± 10eV. The ionisation was predicted from a modified Saha model to be $Z \sim 3$ in the body of the jet. This is found to match the observed temperatures for the jet in vacuum which gave a temperature of $T_i \sim 45$eV, $ZT_e \sim 60$eV to 80eV and $Z \sim 4$. The ionisation is predicted to be lower in the jet into target experiment, this could be due to different probing times after the current start or the assumption of the temperatures in the Saha model.

The plasma in the jet was found to have a zero radial velocity at the edge of the jet. However in the central region of the jet a non-zero velocity was measured. By comparison with the shadowgraph images the measured velocity may result due to small, localised density gradients which may indicate some turbulence on the axis of the jet.

The estimated electron temperature in the jet allows an internal Mach number to be found as the speed of sound in the jet can be calculated. The internal Mach number for the jet is found to be $M \sim 2$ to 4, the range indicates the boundaries in the measured bulk axial velocity of the jet which is between 50km/s and 85km/s.

Thomson scattering was also used to estimate the temperature and radial velocity of the halo plasma. The halo plasma was found to have a radial velocity of 7±2km/s directed radially inwards, towards the centre of the jet. The observation of an axial velocity in the halo plasma confirms prediction of the MHD simulation shown in section 4.5 that showed a '$J \times B$' force directed towards the axis of the jet. The halo plasma was estimated to have a temperature of 20eV which matches the previous estimate in the halo plasma of the temperature, both measurements assumed local thermodynamic equilibrium.

A Thomson scattering measurement of the axial velocity in the presence of the target foil was not performed due to the geometry of the experiment, previous measurements of the axial velocity in the body of the jet in vacuum were made and have been used as a lower boundary for the material velocity in the jet and halo plasma of ∼50km/s, discussed in section 4.4. The use of this velocity is justified by the observed similarity between the two systems, despite the presence of the target foil.

8.1.1 The effect of reversed polarity on the formation of the jet

The investigation of a reversed current polarity jet set up was conducted in part as an investigation of the origin of the shocks seen in the jet-target interaction (which shall be discussed later in this chapter) and also as a proof of principle before the counter

streaming jet set up was used. The effect of reversing the current in the jet-forming foil should not change the dynamics that control the formation and propagation of the jet, which are discussed in section 4.2, from the examination of the single fluid MHD equations governing the motion of the plasma. The reversed polarity system produced a well collimated jet that was seen to be similar in behaviour to the 'normal' polarity system, however there were some differences which will be outlined below.

Both the jet into vacuum and jet into target experiments used a circular foil with a cathode electrode at the centre, so that the current propagated radially inwards from the outer diameter of the foil to the outer diameter of the cathode. In order to create a system where the propagation of current is reversed in the foil, a set up was designed that allowed an anode electrode to be positioned in the centre of the foil, where all other dimensions were kept the same, this is discussed in section 6.1. In order to distinguish the two systems easily during their comparison the reversed polarity jet it termed the 'anode-centric' jet and the previously discussed jet will be termed the 'cathode-centric' jet.

Measurements made from the optical self emission images of the jet, from section 6.3.1, by the fast framing optical camera showed the emission from the anode-centric jet tip propagated at 55±5km/s in comparison to the 85±km/s seen in the cathode-centric jet, however the radial expansion velocity of the emitting body of the jet was observed to be the same between the two systems. The anode-centric jet showed a smaller half opening angle in the jet body of 0° to 2°, however the half-opening angle in the 5mm at the base of the jet was observed to be the same as in the cathode-centric system. The anode centric jet was observed to have a better collimation in the jet body than the cathode-centric jet.

Comparison of the average electron density in the body of the anode-centric jet, shown in figure 6.8, to the cathode-centric jet, shown in figure 5.11, indicated that the anode-centric jet has a higher mass or ionisation in the jet body than the cathode-centric jet, resulting in a $\sim 2\times$ larger electron density than the cathode-centric jet. The electron density in the anode-centric jet is also seen to remain at an approximately constant value along the axial length of the jet, whereas the

	Unit	Jet in Vacuum	Jet with Target	Reversed Polarity Jet with Target
Axial velocity	[km/s]	50 to 80	80±5	55±5
Radial expansion velocity	[km/s]	5	6±2	5±2
Half opening angle at base of jet	[degrees]	5	6 to 11	6 to 8
Half opening angle in body of jet	[degrees]	2	1 to 6	0 to 2
Electron density in jet	[cm^{-3}]	1 to 8×10^{18}	2 to 7×10^{18}	7 to 9×10^{18}
Halo plasma electron density	[cm^{-3}]	1×10^{18}	1×10^{18}	1×10^{18}
T_i in jet	[eV]	45	55±10	
ZT_e in jet	[eV]	60	50±10	
T in halo plasma	[eV]	15 to 20	20	

Table 8.1: A comparison of the experimentally measured properties found in the jet between the jet in vacuum, the jet with a target and the reversed polarity jet with a target.

cathode-centric jet is seen to decrease in density along its axis.

The reverse polarity jet was also observed to have a halo plasma of electron density $\sim 1 \times 10^{18} cm^{-3}$ which is comparable to the cathode-centric jet in vacuum although larger than the values seen in the cathode-centric jet system with a target.

Table 8.1 shows a summary of the measured properties found for the jets in both polarities in the presence of a target foil, with reference to the measured values found for the jet propagating in vacuum, discussed in chapter 4. It can be seen from the table that the two cathode centric systems are similar within errors. The reversed polarity (or anode centric) system, discussed in section 6.3, is seen to display several differences from the cathode centric system, discussed in section 5.3, including better

collimation and a higher electron density.

8.2 The observed shock structures from the interaction of the jet and target foil

Both current polarity jets produced a shock in the halo plasma, that remained stationary throughout the experiment, ∼2mm below the target-forming foil. The cathode-centric jet also produced a reverse shock in the flow of the jet, this reverse shock was not seen in the anode-centric jet-target interaction.

8.2.1 The reverse shock

The reverse shock was seen to propagate counter to the flow direction of the cathode-centric jet and moved though the body of the jet. A detailed investigation of the reverse shock was inhibited by the large density gradients behind the reverse shock, which diverted the laser interferometry beam.

The reverse shock in the cathode-centric jet was seen to propagate at 9 ± 2km/s counter to the flow of the jet, shown in figure 5.47. The shock front was seen to be 'V' shaped and initially had a smooth shock front with the lowest point of the shock in the central flow of the jet. The shock can be seen on the optical framing images shown in figure 5.4. At the later times in the experiment (>500ns) the reverse shock front is seen to develop a 'bumpy' front, which may indicate an instability growth as it progresses into the jet due to a cooling parameter that is <<1.

The region behind the reverse shock had a very high refractive index gradient which inhibited the measurement of the electron density conditions across the shock front with the laser interferometry set up. Figure 5.48 showed the electron line density across the shock, these showed a large electron line density behind the shock front $> 6 \times 10^{18}\text{cm}^{-2}$.

The absence of the reverse shock in the anode-centric jet system may be due to the higher density in the anode-centric jet, which may inhibit the reverse shock propagation or formation at the target surface.

8.2.2 The stationary shock

The stationary shock was observed to form in a similar manner in both current polarity systems and is clearly visible in the optical emission images shown in figure 5.4. It is observed to have little axial velocity (∼3±2km/s) and extend radially away from the centre of the jet for >10mm with a downwards curvature shown in figures 5.23, for the cathode-centric jet, and figure 6.10, for the anode-centric jet. The stationary shock forms early in the experiments and is observed to retain a smooth shock front for all the time points it is observed thereafter.

The electron density is seen to jump, or sharply increase, across the shock front with a stepped density profile, shown in figures 5.27, 5.28 and 5.29, for the cathode-centric jet, and figure 6.14, for the anode-centric jet. The increase in the electron density varies radially along the shock front and is seen to be the highest closest to the jet where ∼6× increases in density are seen at r∼3mm from the jet axis. Increases of ∼2× are seen at r∼6mm from the jet axis, shown in figure 5.30 for the cathode-centric jet. The stationary shock forming in the anode-centric jet system shows the same electron density increases for similar radial positions.

The shock is seen to have a width that increases radially, ∼ 0.1mm at r∼3mm from the jet and ∼0.5mm at r∼6mm from the jet, this is shown in figure 5.31 for the cathode-centric jet. Similar measurements are also made for the anode-centric jet and match the shock width found in the cathode-centric jet system.

The temperature above the shock is found for the cathode-centric jet system using Thomson scattering, discussed in section 5.4.3. The temperature was found at seven axial positions ∼1mm below the target-forming foil. The temperatures found for the ions and electrons is shown in figure 5.36. The ion temperature was seen to decrease radially away from the jet axis from 90±18eV to 40±8eV. The electron temperature was estimated to remain approximately constant at the same radial positions, at 25 ± 5eV for a estimated ionisation of $3 < Z < 5$ which was found from the assumption of thermal equilibrium and a simple ionisation model.

Using the observation that the shock curves downwards and the electron temperature is estimated to remain constant as the ion temperature is reduced lead to the

suggestion that the ions were heated in the shock front and equilibrated to the electron temperature through collisions. The energy gained by the electrons is predicted to be lost to increased ionisation, and as such remains close to the values measured before the shock (20eV). In section 7.6 the maximum ionic heating at the shock front is estimated to be 65eV and the equilibration length for the ions is predicted to be 0.2mm from the values measured in electron density and temperature.

The formation of the stationary shock was investigated further by varying the target geometry to eliminate the role of the jet and the role of the target, discussed in section 5.4.4. Placing a hole on the axis of the target allowed the jet to pass though target, ruling out the flow of material radially from the jet stream at the target surface to accumulate behind the shock. It was observed that the stationary shock formed in the same manner as a target with no hole, the reverse shock was however absent.

The use of a widely spaced mesh target inhibited the formation of a stationary and reverse shock indicating the target does play a role in the formation of both shocks by interacting with the halo plasma surrounding the jet, or in the case of the reverse shock, the jet itself. The dynamics of the thin foil target are contrasted with the mesh target and hole-on-axis target in figure 5.41.

Preheating of the target via electron beams from the cathode-centric jet system was investigated as a possible mechanism for the creation of counter streaming ablation from the target surface, in section 5.4.5. A small, 100A, electron beam was measured, but the magnitude of energy, 1.6J, estimated is too small to be significant in heating the whole surface of the foil. The beam may pre-condition the area directly above the cathode which may form part of the formation of the reverse shock in the cathode-centric jet system, as this beam will be absent in the anode-centric jet system where the reverse shock is not observed.

8.3 Colliding jets

The interaction of a pair of counter streaming jets produces a test-bed for studying shocks in supersonic flows. The colliding supersonic jets were seen to produce a

series of shock features both in the flow from the jets and in the halo plasma around the jets, as described in chapter 6.

In order to create a system where two jets will collide, the anode-centric and cathode-centric jets are combined as described in section 7.1, with a distance of 32mm between the two jet-forming foils. The jets are seen to form and propagate towards one another, then collide near the centre point between the two foils. The anode-centric jet continues to move forward into the cathode-centric jet producing a prominent bow shock. At approximately the centre point between the two foils a stationery shock structure forms, such that two shock fronts are visible and separated by ∼3mm. The interaction of the two jets is shown from optical emission in figure 7.3 and described in more detail in section 7.2. The two stationary shock fronts appear to behave in the same manner as the stationary shocks seen in the jet-target systems.

Observation of the two jets indicates that they form in the same manner as in the jet systems with a target. The same velocity for the jet tip and radial expansion is measured from the optical emission for the two jets, as seen in figures 7.10 and 7.7. The average electron density along the two jets is shown in figure 7.9. The density of the anode-centric jet is seen to be $\sim 2\times$ larger than the cathode-centric jet, which is consistent with the comparison of the average density in the two jets when they propagate into a target. The increased electron density in the anode-centric jet may indicate the jet also has a higher mass density which would be the cause of the bow shock as the anode-centric jet moves though the cathode-centric jet due to a higher ram pressure.

8.3.1 The bow shock

The bow shock is seen to form at the head of the anode-centric jet as it moves into the cathode-centric jet, it is observed on both optical and XUV imaging systems. The bow shock has a 'U' shape as it propagates though the cathode-centric jet and the halo plasma and is not axially symmetric with the jet. The bow shock is seen to develop a clumpy structure as it moves through the cathode-centric jet, which is

disrupted by the path of the bow shock though it. The observed instability on the front of the bow shock may be an instability growth due to a low cooling parameter in the cathode-centric jet.

From optical self emission observed on the fast framing camera, the bow shock is seen to move at a velocity, which is initially comparable to the measured velocity of the anode-centric jet tip, of 80±10km/s. The bow shock is then seen to decelerate as it encounters the dense region at the base of the cathode-centric jet, shown in figure 7.10. From the optical emission an average velocity of the bow shock is found to be 40±10km/s.

The electron line density profile of the bow shock, shown in figures 7.11 and 7.12, shows the region behind the bow shock front has an increase in density and the anode-centric jet appears to narrow and improve its collimation directly behind the bow shock. The electron line density indicates a density increase of $\sim 2\times$ between the material in the cathode-centric jet and the material behind the bow shock.

Using the equation for a working surface, (7.1), for two counter propagating jets with a velocity of 50km/s, and a density contrast of 2, gives a bow shock velocity of ∼10km/s. To meet the observed average velocity of ∼30km/s a density contrast of ∼15 is needed for matched jet velocities of 50km/s, If the anode-centric jet velocity is increased to 80km/s (as observed in the optical emission) the density contrast needed to match the observed bow shock velocity becomes 2.5. More measurements need to be made of the ion density and plasma parameters in order to fully characterise the bow shock as it moves though the flow from the cathode-centric jet. The density contrast and temperature measurements indicate the bow shock is radiatively cooled, which may cause an instability growth in the shock front at later experimental times, which causes the observed deterioration in the smoothness of the shock front.

8.3.2 Collision of the counter propagating halo plasmas

The collision of the counter propagating halo plasmas forms two stationary shock features near the half-way point between the two jet-forming foils. The two station-

ary shock fronts are seen to have a smooth front, with a slight curvature, the shape is shown in figure 7.14. The two shock fronts are separated by ∼3mm and move apart at a velocity of $\sim 6 \pm 2$km/s. The shock is observed for a period of 300ns after its formation.

The electron density profile axially through the two stationary shock fronts shows a sharp increase in density at each shock front and then a decrease in the density between the shock fronts, forming a 'M' shaped, or hollow, profile, shown in figure 7.16. The measured density increase, shown in figure 7.18, from the halo plasma to the shocked plasma shows a $\sim 4\times$ increase at r∼5mm from the jet axis and a increase of $\sim 2\times$ at r∼10mm from the jet axis, which is comparable to the electron density increase seen in both jet-target systems. The absolute electron density in the shock is found to be ∼1 to 2.5×10^{18}cm^{-3}. The measured shock width is found to be the same as the jet-target systems when the radial distance from the jet is matched, the shock width is shown in figure 7.17.

From the electron density measurements and the observed behaviour in optical and XUV emission, the stationary shocks seen in the colliding jet system are probably governed by the same plasma parameters as the stationary shocks in the jet-target interaction. This would allow the effect of the target to be ignored. Using this idea, the data for the three systems is used to inform a model to estimate some of the plasma parameters inside the shock and before the shock which is discussed in section 7.6. From this discussion the shock is estimated to be radiatively cooled, with $\chi << 1$, collisional and the shock width is likely to be dominated by the ion-ion and ion-electron relaxation lengths (estimated to be ∼0.1mm to ∼0.5mm).

8.4 Supporting analysis for a magnetic field above the stationary shocks

The largest force on the stationary shock front will be from the ram pressure of the halo plasma. As the shock is observed to be stationary, it is assumed there is an equal force to balance the ram pressure. This is expected to be the thermal pressure

in the shock. However, the ram pressure is estimated to be five times larger than the thermal pressure in the shock. However, more importantly it is also seen that the density in-between the two shock fronts in the colliding jet system is reduced significantly.

The reduction in density is inconsistent with pressure balance in the post shock region, where the material is found to be radiatively cooled. The radiative cooling should reduce the temperature, reducing the thermal pressure, which should allow greater compression to be achieved. If density decreases it would be expected that the temperature would increase after the shock, although this is not seen in the Thomson measurements or in the self emission from the region between the shocks.

These observations are strongly indicative of a magnetic field pressure which balances the pressure of the colliding halo plasmas and inhibits the two shock fronts from moving closer together over the course of the experiment. It was estimated in section 7.6 that this field should be on the order of ∼6T near the jet and would be lower as the density of the halo plasma decreases radially away from the axis of the jet, decreasing the ram pressure.

This magnetic field could occur due to magnetic field lines 'frozen' into the electron density of the plasma. As the plasma is compressed there is an increase in the magnetic field. This observation is supported in preliminary simulation work shown in figure 7.21, and from the observation of improved collimation of the reverse polarity jet with a higher observed electron density. The stationary shock is also predicted to be highly radiatively cooled, however no instability is seen to arise from this as may be expected, which indicates instability growth may also be mitigated by the presence of a magnetic field, in contrast to the bow shock where instabilities were seen to grow in the shock front.

8.5 Comparing the observed shock structures to astrophysical shocks

The shocks observed in the colliding jet systems were radiative and collisional and the magnetic field may play a dynamic role in the stabilisation of the stationary shock. Similar systems are known to exist in astrophysical interactions of supersonic flows.

Radiatively cooled and collisional shocks can be seen in the structure of jets for young stars, such as Hebig-Haro (HH) jets. These may occur when the flow does not have a uniform velocity in the direction of the jet propagation. This causes faster regions of plasma to catch up to slower regions and collide forming observable shock fronts in the jet.

The shocks discussed in this thesis provide a useful set of conditions which may in future be investigated further with relation to a specific astrophysical system once they have been fully characterised.

8.6 Future work

8.6.1 Imaging the ion line density with X-ray radiography

In order to compare the shocks observed in the experiments to the theoretical predictions from the shock equations, the density of the ions in the plasma needs to be diagnosed. The ion density can be found through X-ray radiography.

Radiography requires an intense backlight with a known frequency range. If the source is point-like in comparison to the object being probed, it can form an imaging system. The X-ray source can be produced via an laser interaction [56, 57] or with an X-pinch [58, 59] producing an intense and short-lived (<1ns) burst of high energy (∼2.5keV) blackbody X-rays. The radiation pulse gives good time resolution in comparison to the temporal scale of the jet and is very intense in comparison to the self-emission from the jet or shock which do not emit in 'hard' X-ray.

The radiation source needs to be well characterised so that the range of fre-

quencies is known. This can be achieved by choosing a narrow band source (Such that the emission is from one line in its spectrum, this is most common in hard X-ray backlighting where a single k-shell line can be used) or through the use of filters, such as Ti which is transparent to 3 to 5keV, which provide a 'window' of wavelengths from the source. The filter can be placed over the film (which itself may filter the radiation in a known range of frequencies) and the thickness varied to provide a 'step wedge' which gives some indication of observed absorption through the experimental load [60].

For an ion density of $2 \times 10^{19}\text{cm}^{-3}$ in a 2mm thick plasma the 2.5keV radiation will be absorbed by 0.5%, for 1.5keV absorption is seen to be 2%. This density is much larger than observed in the jet or the shocked plasma. The density behind the reverse shock in the cathode-centric jet into target experiments, where the density was unresolved by the interferometry system due to high refractive index gradients maybe $> 1 \times 10^{20}\text{cm}^{-3}$ but this depends on ionisation in the region. A sensitive detection scheme would need to be devised to see small changes in intensity, though typical radiography used on Z, based at Sandia National Laboratories, have a transmission of $\sim$95%, which may allow a conventional X-ray backlight system to be used in the denser regions of the jet-target interaction, especially later in the time development.

A lower energy back lighter could be designed, for example in the 400-1000eV range, where absorption in the densities seen in the jet and shock would be 5% to 20%. This would allow the density in the halo plasma and the early time development of the jet to be probed. However the jet and shock might have bright self emission in this energy region, though experiments with 2μm polycarbonate filters on the XUV imaging system did not detect any radiation suggesting the XUV emission of the jet is not very intense or predominantly below 100eV in this energy band. Preliminary experiments with X-pinches using W wires suggest broadband emission in this region is possible, however the intensity of the emission from the pinch in this energy band is not comparable to the intensity in higher energy bands seen in Mo pinches. Also, the size of the emitting area is seen to be larger than $\sim$1μm which will decrease the resolution of the system.

8.6.2 Imaging the magnetic field with Faraday rotation

The magnetic field present in the stationary shock structures is estimated to be on the order of 10T. This would be a measurable magnetic field for the B-dot probe, discussed in section 3.2.6. The first experimental attempts to field the B-dot probes above the jet-forming foil have encountered large electric fields from which the signal due to the magnetic component is indistinguishable, further work in this area with varied probe size and shielding is promising. The B-dot gives a point measurement of the field varying in time, and if the probe is large, will disturb the formation of the system locally around the probe.

The laser imaging system can be modified to take advantage of the Faraday rotation effect. This will provide a 2D map of the magnetic field in the system at the time the probe laser is triggered. This could be useful in conjunction with B-dot measurements to find the origin of the magnetic pressure between the stationary shocks in the colliding jet system and their time variance.

The Faraday effect arises from the interaction of a probe light beam propagating in a medium where there is a magnetic field. The field induces a change in the polarisation of the light beam via the medium which is proportional to the strength of the magnetic field. The external magnetic field induces a circular birefringence in the medium which is due to the introduction of a $\vec{v} \times \vec{B}$ force on the orbit of the electrons as they interact with the rotating optical field of the probe beam.

A working equation for the rotation of the polarisation, in a probe beam, by an angle ϕ, from a magnetic field B, on a linearly polarised light source of wavelength λ is given in SI units by [47]:

$$\phi = \frac{e^3 \lambda^2}{8\pi^2 \epsilon_0 m_e^2 c^3} \int n_e B \cdot dl \tag{8.1}$$

This can be evaluated for a magnetic field of 10T, with a plasma of electron density 1 to $8{\times}10^{18}\mathrm{cm}^{-3}$ and a thickness of 2mm to give a rotation of 0.1° to 0.8°, which may be expected in the body of the jet. This is a very small change in the rotation of the polarisation and requires a very sensitive measuring system. A measurement of the rotation in a wire array plasma on MAGPIE has been previously

made for a plasma with magnetic field on the order of 4T and an electron density of $1 \times 10^{19}\text{cm}^{-3}$, for these conditions a rotation of $\sim 0.5°$ was found and measured [61], This implies the range of expected rotations in the jet can be measured.

This can be used to produce a 2D map by splitting the expanded imaging laser beam into two channels through a Glan-Taylor polariser where the initial beam is split into two beams with different polarisation, such that the effect of the magnetic field will rotate the total polarisation of each beam in opposite directions. The intensity of the split probe beams will change with the additional rotation to the initial polarisation such that one arm experiences a darkening and the other a brightening to the intensity of the beam. This effect is given by the following, where θ is the initial polarisation:

$$I_{Bright} = I_0 cos^2(\theta - \phi)$$

$$I_{Dark} = I_0 cos^2(\theta + \phi)$$

This scheme can be used in conjunction with a laser imaging system as described in section 3.2. Where a magnetic field is measured, darkening and brightening will be observed on the two images produced, such that one is dark when the other is light. Such a system requires good beam quality and an intense probe beam where the shadowgraph effects are limited by the use of a high acceptance-angle imaging system. The detector is also required to be sensitive to intensity changes in small spatial scales.

8.6.3 Axial velocity of the plasma

The axial velocity of the plasma under the target could be found with an alternate scheme for the Thomson probing diagnostic. The axial velocity for the jet in vacuum was described in section 4.4. This scheme used a side on probe beam and a viewing angle which was directly above the jet.

By punching a small hole in the target, that is large enough for the focused beam to pass through (<3mm), the beam can interact with the halo plasma from above and the scattered light viewed from a port on either side of the diagnostic chamber.

The scattering angle can be kept at 90° and the measured velocity will be sensitive to axial velocity and to the radial velocity.

The scheme can be used to find the temperature change across the shock and the pre and post shock axial velocity. The hole needs to be sufficiently small to not disturb the symmetry or formation of the stationary shock, and off axis to avoid interaction with the jet.

8.6.4 Effect of radiative cooling in the jet though varying the jet material

Some preliminarily investigations were done to explore the effect of the jet-forming foil material on the formation and dynamics of the jet. These results are shown in figure 8.1. The figure shows the interferometry and XUV images for two different materials. On the left hand side of the image the material and the thickness of the foil used is indicated. It can be seen that with this increase of atomic mass number the thickness of the foil has not been adjusted to conserve the same mass distribution, this will effect the permeability of the magnetic field through the foil. The formation of the jet with thicker foils may be inhibited by less penetration of the magnetic field though the foil to drive ablation. All the experiments were performed with a aluminium target placed 15mm from the jet-forming foil, which further complicates the dynamics observed, and the shock formation is also seen to be effected by the parameters of the jet.

The Cu and W experiments formed a well collimated jet, although, turbulence or instability is seen along the length of both jets. In the case of the Cu jet the interferometry is blocked by large density gradients in the central column of the jet, however the interferometry for the W jet shows the phase lines can be followed though the body of the jet. The observed instability or turbulence in the jets may result from a change in the cooling parameters. In the case of the W jet the XUV image indicates a form of shock is evident on the target foil, which is not visible in the interactions of the Cu jet.

This data could form an interesting investigation line for further experimentation,

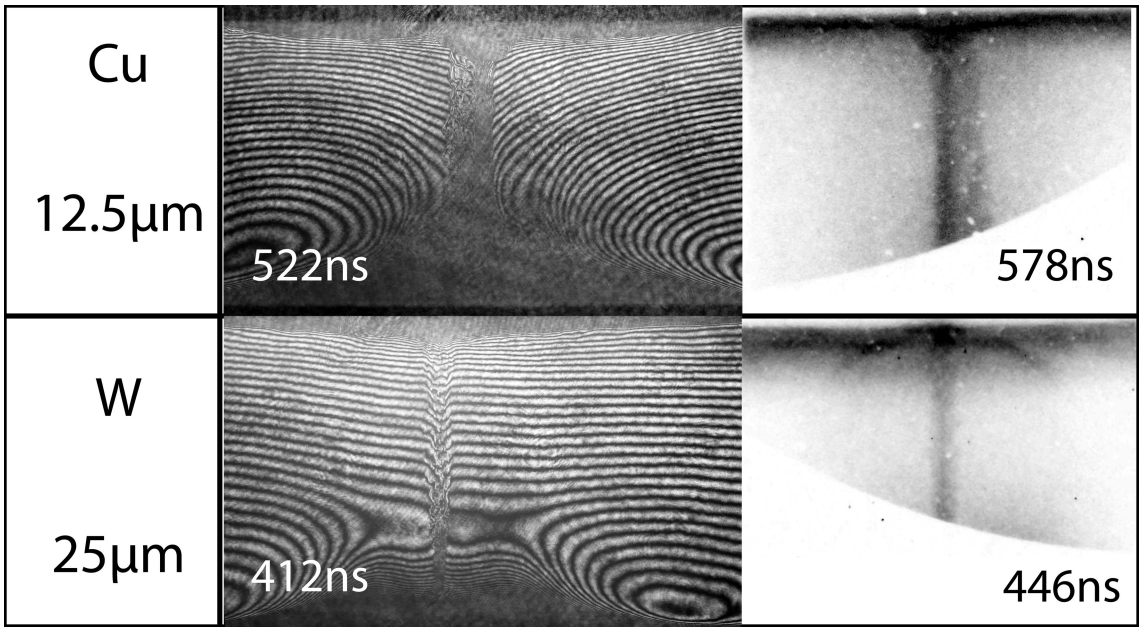

Figure 8.1: Selection of experimental data for different jet materials. The element and foil thickness used are on the left hand side of the rows, the timing of the interferometry or XUV is on the image. From experiments s053112B and s060812B.

allowing the control of the flow properties in the jet. An investigation of different materials forming the jets, where the radial mass of the jet-forming foil is matched to the aluminium experiments and propagating in vacuum, could set a bench mark for such parameters as Mach number, jet velocity and the presence, or otherwise, of a halo plasma. This can then be used to investigate the shocks discussed in this thesis where the flow parameters will be different.

Appendix A

Processing the interferometry images to find the electron line density

This appendix will describe the analysis of the interferograms presented in this thesis with a MATLAB code written by Dr. G. Swadling. The necessary processing of the interferograms and the running of the code was performed by the author. The interferogram that is processed here is from experiment s052912. The origin of the phase lines forming the interferogram is discussed in chapter 3.2 in the laser diagnostics section.

Figure A.1 shows examples of the 'raw' interferograms. The 'background' interferogram, taken prior to the experiment, is shown on the left and the experiment interferogram is shown on the right. The background image is made up of a series of relatively straight fringes. The pattern corresponds to a linearly increasing phase from the top of the image to the bottom.

The quality of the interferograms is dictated by the beam quality, which is often subject to intensity variations across the image and also artefacts from the optics producing dark spots on the image. Around the regions corresponding to large refractive index gradients brightening and darkening can be observed causing secondary shodowgraph effects.

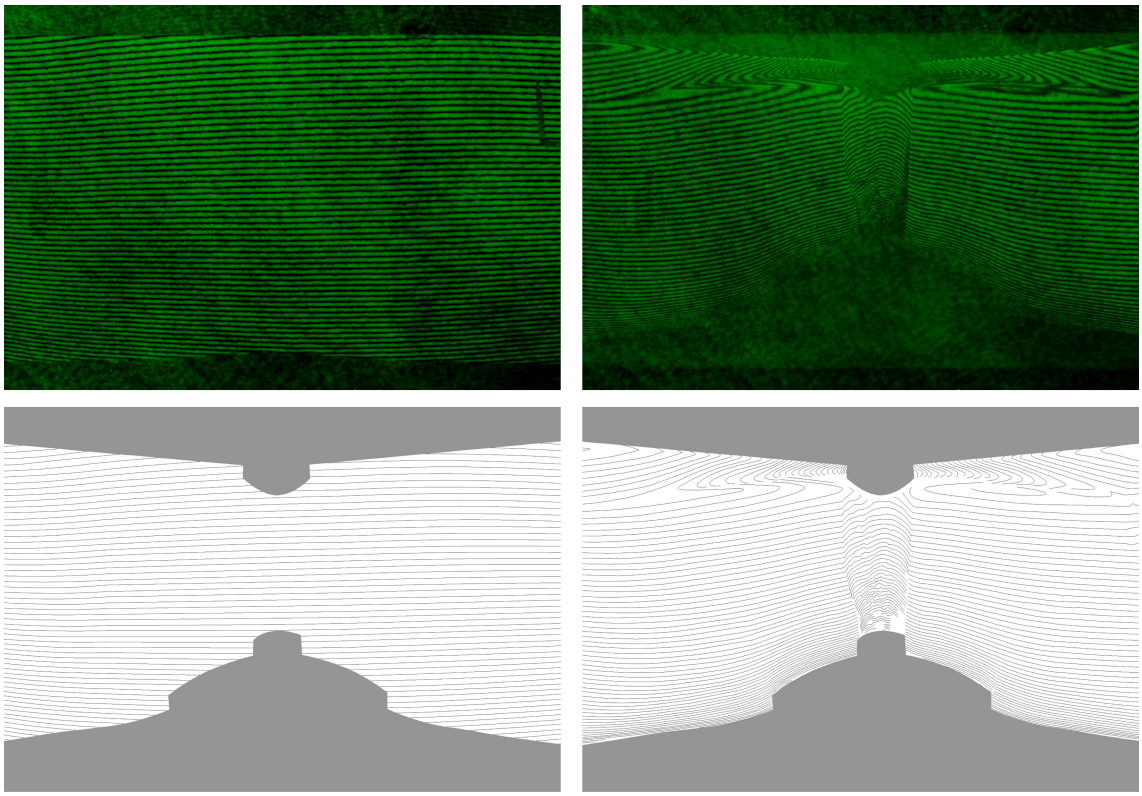

Figure A.1: The raw interferograms and the traced dark fringes from them. The grey area on the traced fringes marks where the probe beam was blocked due either to the hardware or a large refractive index gradient in the plasma.

The fringe lines need to be traced for the MATLAB program. Due to the effects of the laser beam and large refractive index gradient mentioned above, the automation of fringe tracing has proven difficult. The fringes are then traced along the 'dark' fringes in Adobe Photoshop. Figure A.1 shows the contour maps resulting from the tracing process of the background and experiment interferograms. Where the hardware or large refractive index gradients are observed a mask, shown in grey, is used. These images can then be directly used in the MATLAB code. The fringe tracing can be time consuming for large images as in the case here, or for very complex interactions as in the case of the colliding jets.

Once the fringes are traced the phase needs to be numbered. The contour maps are imported to the program and the processing from this point to the electron line density map is performed there. The numbered fringes from the contour map are shown in figure A.2. The colour of the line corresponds to their numbering with blue being low and red high. The program then needs to take the discontinuous

contour map, and create an interpolated phase map for both of the images. This uses a Delaunay triangulation algorithm and a built-in class of MATLAB called 'triscatterdintep'.

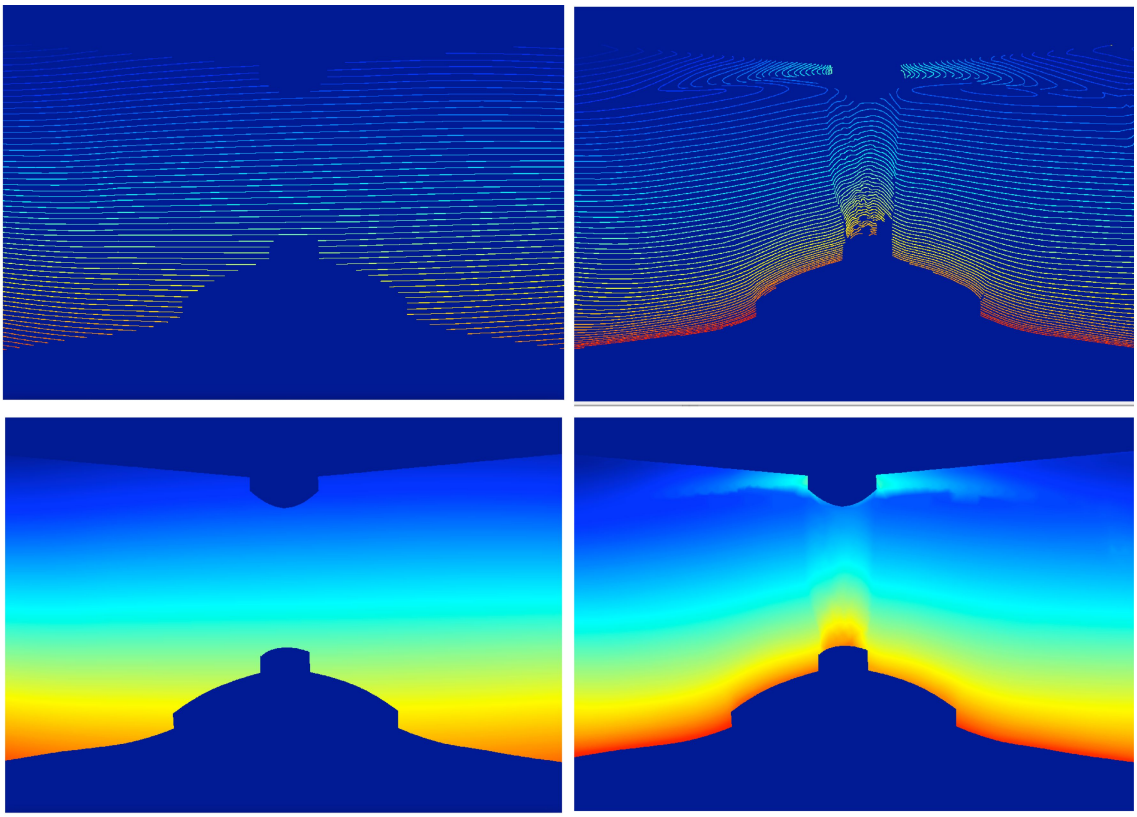

Figure A.2: The traced fringes are numbered, then interpolated.

When the interpolation is complete the phase maps can be subtracted to produce a map of the phase imparted by the plasma. If the area traced in the contour map is sufficiently radially far from the plasma, the outer fringes will have a zero phase shift. If there is plasma at all points of the tracing the lowest number fringe will not correspond to a zero fringe shift. This introduces a linear shift in the calculated electron densities, but can be accounted for if the electron density is known or can be modeled for a position in the $n_e l$ map.

A calibration factor that accounts for the user given magnification of the image, the wavelength of the probe beam and the line depth of the plasma is applied to produce the electron line density map shown in figure A.3.

Some corrections need to be added to the calculated electron line density if

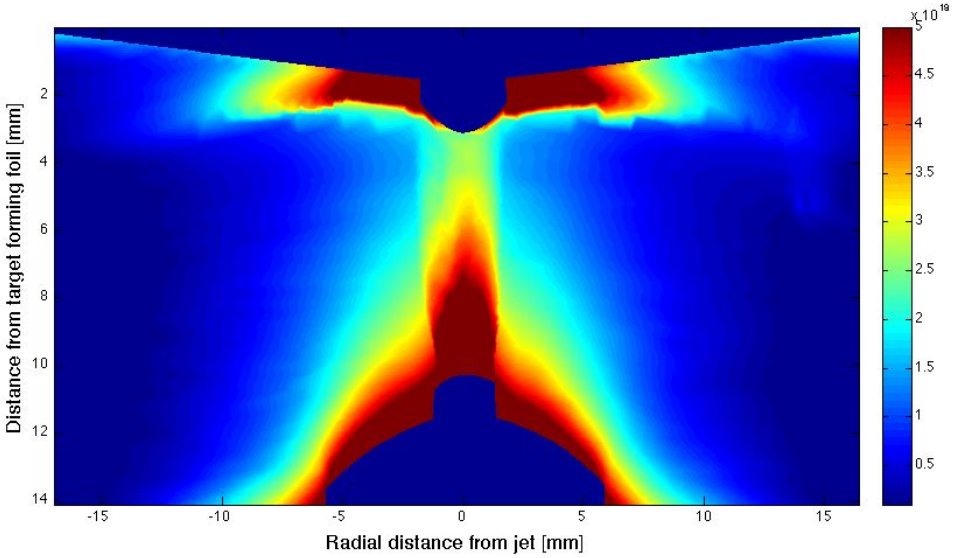

Figure A.3: The final electron line density, $n_e l$ map as calculated from the phase map.

there is an observed 'tilt' in the density across the map. This arrises from thermal vibrations in the imaging optics used that change the position of the background fringes. This is accounted for by another MATLAB routine written in part by J. Skidmore, F. Suzuki-Vidal and the author. The tilt is subtracted from the density map by creating a zero density plane from three points on the density map which are known to have the same density. This is easily done for systems with a high degree of symmetry. If needed, this will be applied prior to the Abel inversion which gives the election density map.

Bibliography

[1] R.P. Drake. *High-Energy-Density Physics*. Shock wave and high pressure phenomena. Springer, 2006.

[2] C. Busschaert, C. Michaut, E. Falize, B. Loupias, A. Ravasio, A. Dizere, H.C Ngyen, and M. Koenig. Numerical modelling of the accretion column in magnetic cataclysmic variables. *SF2A*, 2011.

[3] B.T. Draine and C.F. McKee. Theory of interstellar shocks. *An. Rev. Astron. and Astrophys.*, 31:373–432, 1993.

[4] D. Ryutov, R. P. Drake, J. Kane, E. Liang, B. A. Remington, and W. M. Wood-Vasey. Similarity Criteria for the Laboratory Simulation of Supernova Hydrodynamics. *The Astrophysical Journal*, 518:821–832, 1999.

[5] F.A. Suzuki-Vidal. *Experimental Study of Radiatively Cooled Magnetically Driven Plasma Jets*. PhD thesis, Imperial College London, 2009.

[6] S. V. Lebedev, J. P. Chittenden, F. N. Beg, S. N. Bland, A. Ciardi, D. Ampleford, S. Hughes, M. G. Haines, A. Frank, E. G. Blackman, and T. Gardiner. Laboratory Astrophysics and Collimated Stellar Outflows: The Production of Radiatively Cooled Hypersonic Plasma Jets. *The Astrophysical Journal*, 564:113–119, 2002.

[7] A. Ciardi. Laboratory studies of astrophysical jets. *Lect. Notes Phys.*, 793:31–50, 2010.

[8] B. Reipurth and J. Bally. Herbig-Haro Flows: Probes of Early Stellar Evolution. *An. Rev. Astron. and Astrophys.*, 39:403–455, 2001.

[9] William K. Teets, David A. Weintraub, Joel H. Kastner, Nicolas Grosso, Kenji Hamaguchi, and Michael Richmond. Detection of a cool, accretion shock-generated x-ray plasma in ex lupi during the 2008 optical eruption. *Astrophysical Journal, http://arxiv.org/abs/1210.1250*, 2012.

[10] Doron Kushnir and Eli Waxman. Hard x-ray emission from accretion shocks around galaxy clusters. *JCAP*, 25(1002), 2010.

[11] E Endeve, C Y Cardall, R D Budiardja, and A Mezzacappa. Magnetic field generation by the stationary accretion shock instability. *Journal of Physics: Conference Series*, 125(012006), 2008.

[12] I. Stevens, J. Blondin, and A. M. T. Pollock. Colliding winds from early-type stars in binary systems. *Astrophysical Journal, Part 1*, 386:265–287, February 1992.

[13] D. Falceta-Goncalves and Z. Abraham. Mhd numerical simulations of colliding winds in massive binary systems- i. thermal versus non-thermal radio emission. *MNRAS*, 423(1562-1570), 2012.

[14] B. H. Ripina, C. K. Mankaa, T. A. Peysera, E. A. McLeana, J. A. Stampera, A. N. Mostovycha, J. Gruna, K. Kearneya, J. R. Crawforda, and J. D. Hubaa1. Laboratory laser-produced astrophysical-like plasmas. *Laser and Particle Beams*, 8(1-2), 1990.

[15] D.R. Farley, K. G. Estabrook, S. G. Glendinning, S. H. Glenzer, B. A. Remington, K. Shigemori, J. M. Stone, R. J. Wallace, G. B. Zimmerman, and J. A. Harte. Radiative jet experiments of astrophysical interest using intense lasers. *Phys. Rev. Lett.*, 83:1982–1985, September 1999.

[16] Shigemori, Kodama, Farley, Koase, Estabrook, Remington, Ryutov, Ochi, Azechi, Stone, and Turner. Experiments on radiative collapse in laser-produced plasmas relevant to astrophysical jets. *Physical Review E*, 62:8838–41, 2000.

[17] B. Loupias, M. Koenig, E. Falize, S. Bouquet, N. Ozaki, A. Benuzzi-Mounaix, T. Vinci, C. Michaut, M. Rabec le Goahec, W. Nazarov, C. Courtois, Y. Aglit-

skiy, A. Ya. Faenov, and T. Pikuz. Supersonic-jet experiments using a high-energy laser. *Phys. Rev. Lett.*, 99(265001), December 2007.

[18] C. D. Gregory, J. Howe, B. Loupias, S. Myers, M. M. Notley, Y. Sakawa, A. Oya, R. Kodama, M. Koenig, and N.C Woolsey. Astrophysical jet experiments with colliding laser-produced plasmas. *The Astrophysical Journal*, 676:420–426, March 2008.

[19] D. J. Ampleford, S. V. Lebedev, A. Ciardi, S. N. Bland, S. C. Bott, J. P. Chittenden, G. N. Hall, C. A. Jennings, J. Armitage, Blyth. G., S. Christie, and L. Rutland. Formation of Workings Surfaces in Radiatively Cooled Laboratory Jets. *Astrophys. and Space Science*, 2005.

[20] D. J. Ampleford, S. V. Lebedev, A. Ciardi, J. P. Chittenden, S. N. Bland, S. C. Bott, J. Rapley, M. Sherlock, C. Jennings, A. Frank, and T. Gardiner. Laboratory Modeling of Radiatively Cooled Jets Using Conical Wire Array Z-pinches. *AIP Conf. Proc. 703: Plasmas in the Laboratory and in the Universe: New Insights and New Challenges*, pages 443–446, 2004.

[21] T. A. Gardiner, A. Frank, E. G. Blackman, S. V. Lebedev, J. P. Chittenden, D. Ampleford, S. N. Bland, A. Ciardi, M. Sherlock, and M. G. Haines. MHD Models and Laboratory Experiments of Jets. *Astrophys. and Space Science*, 287:69–74, 2003.

[22] A. Frank, E.G. Blackman, A. Cunningham, S.V. Lebedev, D. J. Ampleford, A. Ciardi, S.N. Bland, J.P Chittenden, and M.G. Haines. A hed laboratory astrophysics testbed comes of age: Jet deflection via cross winds. *Astrophys. and Space Science*, 294:107–114, 2004.

[23] A. Ciardi. *PhD thesis: Modelling of hypersonic jets in wire array z-pinch experiments.* Imperial College London, 2003.

[24] A. Ciardi, S.V. Lebedev, A. Frank, E. G. Blackman, J.P Chittenden, C. J. Jennings, D. J. Ampleford, S.N. Bland, S. C. Bott, J. Rapley, G. N. Hall,

F. Suzuki-Vidal, A. Marocchino, T. Lery, and C. Stehle. The evolution of magnetic tower jets in the laboratory. *Physics of Plasmas*, 14(056501), 2007.

[25] F. Suzuki-Vidal, S. V. Lebedev, S. N. Bland, G. N. Hall, G. Swadling, A. J. Harvey-Thompson, J. P. Chittenden, A. Marocchino, A. Ciardi, A. Frank, E. G. Blackman, and S. C. Bott. Generation of episodic magnetically driven plasma jets in a radial foil z-pinch. *Physics of Plasmas*, 17(112708), November 2010.

[26] F. Suzuki-Vidal, S. V. Lebedev, M. Krishnan, J. Skidmore, G. Swadling, A. J. Harvey-Thompson, S. Patankar, M. Bocchi, M. Bennett, S. N. Bland, G. C. Burdiak, J. P. Chittenden, P. de Grouchy, G. N. Hall, E. Khoory, L. Pickworth, R. A. Smith, S. J. P. Stafford, L. Suttle, A. Ciardi, A. Frank, R. Madden, K. Wilson-Elliot, and P. Coleman. Interaction of radiatively cooled plasma jets with neutral gases for laboratory astrophysics studies. *High Energy Density Physics*, June 2011.

[27] F. Suzuki-Vidal, S. V. Lebedev, M. Bocchi, M. Krishnan, G. Swadling, G. Burdiak, S.N. Bland, P. de Grouchy, A. J. Harvey-Thompson, E. Khoory, L. Pickworth, J. Skidmore, J.P Chittenden, K. Wilson-Elliot, R. Madden, and A. Ciardi. Experimental study of shock waves from the interaction of a supersonic plasma jet with an ambient gas. *Shock waves*, October 2011.

[28] F. Suzuki-Vidal, S.V. Lebedev, M. Krishnan, J. Skidmore, G. Swadling, A. J. Harvey-Thompson, S. Patankar, M. Bocchi, M. Bennett, S. N. Bland, G. C. Burdiak, J. P. Chittenden, P. de Grouchy, G. N. Hall, E. Khoory, L. Pickworth, R. A. Smith S. J. P. Stafford, L. Suttle, A. Ciardi, A. Frank, R. Madden, K. Wilson-Elliot, and P. Coleman. Interaction of radiatively cooled plasma jets with neutral gases for laboratory astrophysics studies. *High Energy Density Physics*, June 2012.

[29] C.M. Krauland, R.P. Drake, C.C. Kuranz, B. Loupias, R.P. Young, C.M. Huntingdon, S. Klein, E. Falize, and T. Plewa. Radiative reverse shock laser experiments. Conference Poster HEDLA, 2011.

[30] N. L. Kugland, D. D. Ryutov, P-Y. Chang, R. P. Drake, G. Fiksel, D. H. Froula, S. H. Glenzer, G. Gregori, M. Grosskopf, M. Koenig, Y. Kuramitsu, C. Kuranz, M. C. Levy, E. Liang, J. Meinecke, F. Miniati, T. Morita, A. Pelka, C. Plechaty, R. Presura, A. Ravasio, B. A. Remington, B. Reville, J. S. Ross, and Y. Sakawa. Self-organized electromagnetic field structures in laser-produced counter-streaming plasmas. *Nature Physics*, 8:809–812, September 2012.

[31] J. M. Blondin, B. A. Fryxell, and A. Konigl. The structure and evolution of radiatively cooling jets. *The Astrophysical Journal*, 360:370–386, 1990.

[32] Gallagher and Pearmain. *High Voltage; Measurement, Testing and Design*. John Wiley and Sons, 1983.

[33] I. H.Mitchell. A high impedence mega-ampere generator for fiber z-pinch experiments. *Review of Scientific Instruments*, 67(4):9, April 1996.

[34] D. Pellinen, M. Di Capua, S. Sampayan, H. Gerbracht, and M. Wang. Rogowski coil for measuring fast, high level pulsed currents. *Review of Scientific Instruments*, 51(11), November 1980.

[35] G. S. Settles. *Schlieren and Shadowgraph Techniques*. Springer, 2001.

[36] A. Colaïtis. Thomson scattering diagnostics for z-pinches in magpie. Master's thesis, Imperial College London, September 2010.

[37] J. Sheffield. *Plasma Scattering of Electromagnetic Radiation*. Academic Press, 1975.

[38] W. Lochte-Holtgreven. *Plasma Diagnostics*. American Institute of Physics, 1968.

[39] E.E. Salpeter. Electron density fluctuation in a plasma. *Physical Review*, 120(5), December 1960.

[40] George Swadling. Development of a high current time resolved electron spectrometer for use in z-pinch wire array implosion experiments on magpie. Master's thesis, Imperial College London, May 2007.

[41] K. Kanaya ans S. Okayama. Penetration and energy-loss theory of electrons in solid targets. *J. Phys. D: Appl. Phys.*, 5, 1972.

[42] F. Suzuki-Vidal, M. Bocchi, S.V. Lebedev, G. Swadling, G. Burdiak, P. de Grouchy, G. N. Hall, E. Khoory A.J. Harvey Thompson, S. Patankar, L. Pickworth, J. Skidmore, R. Smith, J. P. Chittenden, M. Krishnan, R. E. Madden, K. Wilson-Elliot, A. Ciardi, and A. Frank. Interaction of a supersonic, radiatively cooled plasma jet with an ambient medium. *Physics of Plasmas*, 19(022708), February 2012.

[43] P.-A. Gourdain, J. B. Greenly, D. A. Hammer, P. F. Knapp, B. R. Kusse, S. A. Pikuz, P. C. Schrafel, and T. C. Shelkovenko. The impact of cathode diameter on radial foil explosions. *IEEE Transactions on Plasma Science*, 38(12), December 2010.

[44] F. Suzuki-Vidal, S.V. Lebedev, A. Ciardi, S.N. Bland, J.P. Chittenden, G.N. Hall, A. Harvey-Thompson, A. Marocchino, C. Ning, C. Stehle, A. Frank, E.G. Blackman, S.C. Bott, and T. Ray. Formation of episodic magnetically driven radiatively cooled plasma jets in the laboratory. *Astrophys. and Space Science*, 322:19–23, January 2009.

[45] P-A. Gourdain, I. C. Blesener, J. B. Greenly, D. A. Hammer, P. F. Knapp, B. R. Kusse, S. A. Pikuz, and T. C. Shelkovenko. High energy density plasmas generated by radial foil explosions. *Plasma Phys. Control. Fusion*, 52(055015), April 2010.

[46] J. Canto, G. Tenorio-Tagle, and M. Rozyczka. The formation of interstellar jets by the convergence of supersonic conical flows. *Astron. and Astrophys.*, 192:287–294, 1988.

[47] Principles of Plasma Diagnostics. *I. Hutchinson*. Cambridge University Press, 2nd edition, 2002.

[48] J. P. Chittenden, S. V. Lebedev, C. A. Jennings, S. N. Bland, and A. Ciardi. X-ray generation mechanisms in three-dimensional simulations of wire array Z-pinches. *Plasma Physics and Controlled Fusion*, 46:B457–B476, 2004.

[49] P-A. Gourdain, I.C. Blesener, J.B. Greenly, D. A. Hammer, P.F. Knapp, B.R. Kusse, and P. C Schrafel. Initial experiments using radial foils on the cornell beam research accelerator pulsed power generator. *Physics of plasmas*, 17(012706), 2010.

[50] F. Suzuki-Vidal. In experiment discussion. 2012.

[51] A.J. Harvey Thompson, S.V. Lebedev, S.Patankar, S.N. Bland, G. Burdiak, J.P Chittenden, A. Colaitis, P. de Grouchy, G. N. Hall, E. Khoory, M. Hohenberger, L. Pickworth, F. Suzuki-Vidal, R. A. Smith, J. Skidmore, L. Suttle, and G. Swadling. Optical thomson scattering measurements of plasma parameters in the ablation stage of wire array z pinches. *Phys. Rev. Lett.*, 108(145002), April 2012.

[52] D.E. Post, R.V. Jensen, C.B. Tarter, W.H. Grasberger, and W.A. Lokke. Steady-state cooling rates for low-density, high-temperature plamas. *Atomic Data and Nuclear Data Tables*, 20:397–439, 1977.

[53] F.A. Suzuki-Vidal, S. Lebedev, S.N. Bland, G.N. Hall, G. Swadling, A. J. Harvey-Thompson, G. Burdiak, P. de Grouchy, J. P. Chittenden, A. Marocchino, M. Bocchi, A. Ciardi, A. Frank, and S. C. Bott. Experimental studies of magnetically driven plasma jets. *Astrophys. and Space Science*, 336:41–46, 2011.

[54] Y.B. Zel'dovich and Y.P. Raizer. *Physics of shock waves and high-temperature hydrodynamic phenomena*. New York: Academic Press, 1967.

[55] J. D. Huba. NRL plasma formulary, revised. Technical Report NRL/PU/6790-07-500, Naval Research Laboratory, 2007.

[56] G. R. Bennett, O. L. Landen, R. F. Adams, J. L. Porter, L. E. Ruggles, W. W. Simpson, and C. Wakefield. X-ray imaging techniques on z using the z-beamlet laser. *Rev. Sci. Instrum.*, 72(657), 2001.

[57] B. Loupias, F. Perez, A. Benuzzi-Mounaix, N. Ozaki, M. Rabec, L.E. Gloahec, T.A. Pikuz, A.Ya. Faenov, Y. Aglitskiy, and M. Koenig. Highly efficient, easily spectrally tunable x-ray backlighting for the study of extreme matter states. *Laser and Particle Beams*, 27(601-609), July 2009.

[58] S. V. Lebedev, F. N. Beg, S. N. Bland, J. P. Chittenden, A. E. Dangor, M. G. Haines, M. Zakaullah, S. A. Pikuz, T. A. Shelkovenko, and D. A. Hammer. X-ray backlighting of wire array Z-pinch implosions using X pinch. *Review of Scientific Instruments*, 72:671–673, 2001.

[59] T. A. Shelkovenko, D. B. Sinars, S. A. Pikuz, and D. A. Hammer. Radiographic and spectroscopic studies of X-pinch plasma implosion dynamics and x-ray burst emission characteristics. *Physics of Plasmas*, 8:1305–1318, 2001.

[60] I.C. Blesener, J. B. Greenly, S. A. Pikuz, T. A. Shelkovenko, S. Vishniakou, D. A. Hammer, and B.R. Kusse. Axial x-ray backlighting of wire-array z-pinches using x pinches. *Rev. Sci. Instr.*, 80(12):123505– 123505–5, December 2009.

[61] S. N. Bland, D. J. Ampleford, S. C. Bott, A. Guite, G. N. Hall, S. M. Hardy, S. V. Lebedev, P. Shardlow, A. Harvey-Thompson, F. Suzuki, and K. H. Kwek. Use of faraday probing to estimate current distribution in wire array z pinches. *Rev. Sci. Instr.*, 77(10E315), October 2006.